Characterization of anisotropy in a karstified carbonate platform using seismic and electrical resistivity methods : a joint approach

Jan Beres

▶ **To cite this version:**

Jan Beres. Characterization of anisotropy in a karstified carbonate platform using seismic and electrical resistivity methods : a joint approach. Earth Sciences. Université Paris Sud - Paris XI, 2013. English. NNT : 2013PA112214 . tel-00880759

HAL Id: tel-00880759

https://theses.hal.science/tel-00880759

Submitted on 6 Nov 2013

HAL is a multi-disciplinary open access archive for the deposit and dissemination of scientific research documents, whether they are published or not. The documents may come from teaching and research institutions in France or abroad, or from public or private research centers.

L'archive ouverte pluridisciplinaire **HAL**, est destinée au dépôt et à la diffusion de documents scientifiques de niveau recherche, publiés ou non, émanant des établissements d'enseignement et de recherche français ou étrangers, des laboratoires publics ou privés.

Université Paris Sud

Département des Sciences de la Terre
Hydrogéologie, hydrogéophysique
Interactions et Dynamique des Environnements Sédimentaires (IDES)
UMR 8148 UPS / CNRS

École doctorale MIPEGE 534
Modélisation et Instrumentation en Physique, Énergies, Géosciences et Environnement

Discipline: Géophysique

Thèse de doctorat de l'Université Paris Sud

CARACTÉRISATION DE L'ANISOTROPIE D'UNE PLATE-FORME CARBONATÉE KARSTIFIÉE: APPROCHE MÉTHODOLOGIQUE CONJOINTE SISMIQUE ET ÉLECTRIQUE

présenté par:
MSc. BEREŠ Ján

Directeur de thèse: Prof. ZEYEN Hermann
Co-directeur de thèse: Dr. GAFFET Stéphane

soutenue le 11 Octobre 2013 à Orsay devant le jury composé de:

Prof. GUERIN Roger (Université Paris 6 - UPMC)	rapporteur
Prof. GRANDJEAN Gilles (BRGM - Orléans)	rapporteur
Prof. TUCHOLKA Piotr (Université Paris Sud)	examinateur
Dr. SENECHAL Guy (Université de Pau et des Pays de l'Adour)	examinateur
Dr. CHALIKAKIS Konstantinos (Univ. d'Avignon, et Pays de Vaucluse)	examinateur

University Paris Sud

Department of Earth Sciences
Hydrogeology, hydrogeophysics
Interactions et Dynamique des Environnements Sédimentaires (IDES)
UMR 8148 UPS / CNRS

Ecole doctorale MIPEGE 534
Modelling and Instruments in Physics, Energies, Geosciences and Environment

Discipline: Geophysics

PhD thesis of University Paris Sud

CHARACTERISATION OF ANISOTROPY IN A KARSTIFIED CARBONATE PLATFORM USING SEISMIC AND ELECTRICAL RESISTIVITY METHODS - A JOINT APPROACH

presented by:
MSc. BEREŠ Ján

Supervisor: Prof. ZEYEN Hermann
Co-supervisor: Dr. GAFFET Stéphane

defended October 11th 2013 in Orsay in front of a jury composed of:

Prof. GUERIN Roger (Université Paris 6 - UPMC)	reviewer
Prof. GRANDJEAN Gilles (BRGM - Orléans)	reviewer
Prof. TUCHOLKA Piotr (Université Paris Sud)	examiner
Dr. SENECHAL Guy (Université de Pau et des Pays de l'Adour)	examiner
Dr. CHALIKAKIS Konstantinos (Univ. d'Avignon, et Pays de Vaucluse)	examiner

Acknowledgements:

I would like to thank anyone who contributed to this thesis, might it be by scientific knowledge, moral support, cooking or by making me doubt my own thoughts. My unending gratitude goes to my supervisor who made me work on my way of thinking, who had lot of nerves to review my manuscript and maybe one day I will be as half a scientist as he is.

I would like to dedicate this thesis to him and to my family.

Ďakujem.

This manuscript is submitted in fulfilment of the requirements for the degree of Doctor of Philosophy in geophysics.

Abstract:

Seismic and electrical resistivity anisotropies of a fractured karstic limestone massif in sub-parallel underground galleries are studied. As the fractures are mostly vertically oriented, the seismic properties of the massif are approximated by horizontal transverse isotropy (HTI). Several data inversion methods were applied to a seismic datasets of arrival-times of P and S-waves and a resistivity datasets of electrical potential measurements in a pole-pole configuration.

For the seismic datasets (four campaigns), the applied methods include: isotropic tomography, approximative cosine function fit, homogeneous Monte-Carlo anisotropic inversion for the parameters of the stiffness matrix of HTI and anisotropic tomography for tilted transversely isotropic bodies. All methods lead to the conclusion that there is indeed an anisotropy present in the rock massif and confirm the direction of maximum velocity parallel to the direction of fracturing. Strong anisotropy of about 15% is found in the studied area.

For the resistivity datasets (two campaigns), the applied methods include approximative cosine function fit, homogeneous Monte-Carlo anisotropic inversion for the longitudinal resistivity ρ_L, transversal resistivity ρ_T and angle of orientation of model with respect to the reference system. Two maxima of apparent resistivities with respect to the azimuth of measurement over 180° are found in the data, which cannot be modelled by conventional approaches. A conceptual modelling of a network of conductive wires in a non-conductive medium shows promising results, where the two maxima were successfully modelled.

Repeated measurements show slight variations of apparent resistivity and variations of the P-wave parameters. The variations of the S-wave parameters are not pronounced, which is reflecting a change in water saturation. Porosity of 10-15 % is estimated from the seismic measurements.

Keywords: anisotropy, horizontal transverse anisotropy, seismic anisotropy, electrical resistivity anisotropy, inversion, karstified limestone massif, analog of carbonate reservoir, LSBB

Résumé:

Les résultats présentés dans ce document portent sur les anisotropies sismique et électrique d'un massif calcaire fracturé dans des galeries parallèles souterraines. Les fractures étant orientées verticalement, leurs propriétés sont approximées par isotropie transverse horizontale (HTI). Plusieurs méthodes d'inversion ont été étudié pour traiter les données sismiques (temps d'arrivée des ondes P et S); et pour traiter les données de résistivité électrique mesuré dans une configuration pôle-pôle (valeur de potentiel mesuré).

Pour traiter les données sismiques (quatre campagnes), les méthodes étudiées dans ce document sont: une tomographie isotrope, une approximation de cosinus, une inversion anisotrope basée sur l'algorithme Monte-Carlo pour les paramètres de la matrice de rigidité (de l'isotropie transverse horizontale) et une tomographie anisotrope pour un milieu avec une isotropie transverse inclinée. Toutes les méthodes conduisent à la conclusion qu'il y a effectivement une anisotropie présente dans le massif rocheux et confirment la direction de la vélocité maximale parallèle à la direction de la fracturation. Une forte anisotropie de 15 % est présente dans la zone étudiée.

Pour traiter les données électriques (deux campagnes), les méthodes étudiées sont une approximation de cosinus et une inversion anisotrope basée sur l'algorithme Monte-Carlo pour les paramètres de résistivité transversale ρ_T, de résistivité longitudinale ρ_L et de l'angle d'orientation du modèle par rapport au système de référence. La présence à 180° de deux maxima de résistivité apparente par rapport à l'azimut de mesure ne peuvent être modélisés par des approches conventionnelles. Une modélisation conceptuelle d'un maillage des fils conducteurs dans un milieu non conducteur a été développé et montre des résultats prometteurs, avec le succès de la modélisation des deux maxima.

Des mesures répétées montrent de légères variations de résistivité apparentes et des variations des ondes P. Les variations des ondes S ne sont pas prononcés, ce qui reflète un changement de la saturation en eau. La porosité de 10-15% est estimé à partir des mesures sismiques.

Mots clés: anisotropie, anisotropie transverse horizontale, anisotropie sismique, anisotropie de résistivité électrique, inversion, massif calcaire karstifié, analogue de réservoir carbonaté, LSBB

Table of Contents

1 Introduction....7
2 Geology of studied area....21
3 Theoretical background....28
3.1 Anisotropy....28
3.1.1 Triclinic and monoclinic anisotropy....32
3.1.2 Orthogonal / orthorhombic anisotropy....32
3.1.3 Transverse isotropy....33
3.2 Modelling in general....38
3.2.1 Seismic modelling....40
3.2.2 Electrical modelling....43
3.3 Inversion procedures and tomographic inversions....48
3.3.1 Linear problem....49
3.3.2 Non-linear problem....51
3.3.2.1 Method of the Non Linear Least Squares (NLLSQ)....51
3.3.2.2 Gradient methods....52
3.3.2.3 Monte-Carlo algorithms....53
3.3.3 Seismic inversion....54
3.3.4 Electrical resistivity inversion....56
3.4 Fracture characterisation....57
4 Methodology and results....61
4.1 Seismics – Real data....61
4.1.1 Geometry – Equipment....62
4.1.2 Isotropic cross hole tomography....65
4.1.3 Approximative cosine fit function....69
4.1.4 Homogeneous anisotropic Monte-Carlo Markov Chain inversion....75
4.1.5 Anisotropic tomography program ANRAY and other software....92
4.1.6 Anisotropic tomography "3Dray_gTI0"....92
4.2 Electrical resistivity – Real data....102
4.2.1 Geometry – Equipment....102
4.2.2 Data treatment....104
4.2.3 Homogeneous anisotropic Monte-Carlo Markov Chain inversion....110
4.2.4 Anisotropic tomography "3Dres_GQG"....116
4.2.5 Network of conductors....116
5 Discussion....124
5.1 The seismic data....125
5.1.1 Structural interpretation....125
5.1.2 Hydrological interpretation....126
5.1.3 Fracture characterisation....128
5.2 The electrical resistivity data....129
5.3 Structural interpretation....131
6 Conclusions and outlook....132
7 References....135
8 Index of Tables....141
9 Index of Figures....142
10 Résumé étendu français....149
11 Annexe....161
12 Appendix....177

1 Introduction

In recent years in the oil prospecting industry, but not limited only to it, more and more importance is given to the interpretation of seismic data taking anisotropic rock properties into consideration. Assuming only isotropic properties in the interpretation often results in false estimations of medium properties and dimensions (e.g. Winterstein, 1990; Pain et al., 2003). Anisotropy could be also the indication of reservoirs containing shale gas, as in recent years the big oil reservoirs are being depleted, the search for oil is focusing on porous shales and fractured rock reservoirs (e.g. Maultzsch et al., 2003; Agosta et al., 2010).

But what actually is anisotropy? To the uninterested reader, someone who doesn't have to deal with it, the anisotropy might be just a fancy word, but everybody is observing anisotropy in everyday situations. For instance looking at a plank of wood, or a wooden table, one can notice that the structure is not the same from the left to the right and from the rear to the front of the table. If it was to be broken into two equal pieces, one direction would be easier than the other. The table would break easier along the fibre direction. The same applies for propagation of seismic signal. The signal travels faster along the lines of wood fibre than across them.

The simplest anisotropic media, where the velocity dependence on the direction of propagation follows an ellipse, hence named elliptically anisotropic, has been studied by Gurvich (1940), but because of the non-uniqueness, this approach failed to deliver satisfactory results (Grechka, 2009b).

There are different symmetry systems of anisotropy. They are based on symmetry classes used for crystals (Winterstein, 1990). For a brief introduction, in the nature, one can observe transverse isotropy, orthorhombic or orthogonal anisotropy and monoclinic anisotropy. The

easiest way for a geoscientist to imagine anisotropy, is to look at horizontal layering of different soils (e.g. limestone and clay), sea bed or compacted shales. If the layering is horizontal, without any dipping of the layers, properties of the subsoil, when measured at the surface seem to be isotropic, therefore rotationally invariant. This azimuthal isotropy (Winterstein, 1990) which is only apparent, because the signal always goes through the same layers before it comes back to the surface, has been named transverse isotropy. In this symmetry system, the only symmetry axis, which is the vertical axis, gives the name to this anisotropy (Fig. 1.1). Therefore it has been named vertical transverse isotropy (VTI) and has been known and investigated from the middle of the last century.

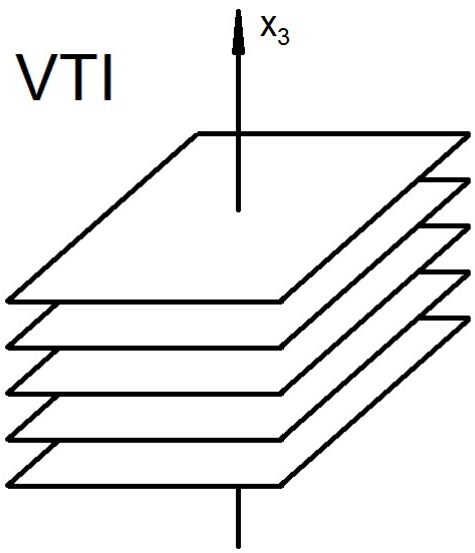

Fig. 1.1: Example of horizontal layering having vertical symmetry axis - VTI medium

Already then, in exploration geophysics, the term of transversely isotropic media was used (e.g.: Stoneley, 1949; White and Sengbush,1953). In an anisotropic medium, the S-waves undergo a change that is not present in an isotropic medium. They are divided into two waves that are polarised differently and with this polarisation their properties differ from each other. This polarisation is called splitting of S-waves, because one of the main differences is the splitting into fast and slow S-waves (Grechka, 2009a). Jolly (1956)

investigated two differently polarized shear waves caused by shear wave splitting and showed different anisotropic behaviour for the S-waves and for the P-waves in shales in terms of group velocities, their directions and amplitudes. Before 1980, the majority of sedimentary rocks were found to be vertically transversely isotropic and terminology and concepts for this special case of transverse isotropy became well known (Winterstein, 1990).

For an example purpose, just consider two layers of same thickness; one where the seismic wave propagates with velocity of 6 km/s and another one, with velocity of 3 km/s. If the signal passes across both layers, the resulting apparent velocity will be between 3 and 6 km/s. The same would apply if there was several sequences of these two layers. It is quite logical that if there was a layer of first material covered with a layer of second material, and so on several times, the resulting velocity across these layers would be around 4.5 km/s. However, the apparent velocity along the interface of these two materials would be nearer to 6 km/s. That is because the signal would have travelled faster through the fast layers and transmit the energy to the slower layers along the passage. The signal propagating inside the slow layers would arrive later, but would be difficult to see in the recording. This apparent velocity dependence with respect to the angle between propagation direction and isotropy axis can be mathematically expressed and therefore a modelling can be done.

However, from the middle to the end of the last century, the computations for anisotropic media were cumbersome and approximations were used. Even though the standard hyperbolic approximation of Dix (1955), is exact only for isotropic and homogeneous media and a planar reflector, it was an acceptable approximation for short offsets even for anisotropic media. Based on this approximation, several other models were build, some using correction terms, some more complicated (sixth order equations, Taylor series, orthogonal polynomials), but for larger offsets they were inaccurate (Aleixo and Schleicher,

2010).

In order to reconstruct the subsurface properties, modelling became the basic tool and computer programs were designed that would invert the measured data for the medium properties. Seismic tomography, from its conception in the 1960's and 1970's until nowadays, is the primary source of information on the Earth's interior from local to global scale (Fichtner et al., 2013). With the boom of computational resources, it became gradually easier to invert huge amounts of data. Seismic ray tomography, based on ray tracing methods were used successfully for isotropic media (Zhou et al., 2008). Červený (1972) extended the kinematic inversion to heterogeneous anisotropic media, which has been applied by many geophysicists since. Nevertheless, they have been using the assumption of weak anisotropy, a slight disturbance from isotropic background medium, allowing to use a linear inversion solver with constant Jacobian matrix (Zhou et al., 2008).

The assumption of weak anisotropy became an acceptable approximation and by the year 1985, Thomsen (1986) published his paper on weak elastic anisotropy, which introduced the terminology and a new parameter set for weakly anisotropic media and has been used ever since for VTI media. A few years later, Tsvankin (1997a) modified the terminology for horizontally transversely isotropic media.

Later that year (1986), at the Society of Exploration Geophysicists (SEG) annual meeting, presentations based on multicomponent recordings showed that another type of symmetry was needed to describe all observations and since general anisotropy is intrinsically complicated, there was a need to for a glossary on the subject and Winterstein (1990), published an article containing a unified terminology.

There were different groups that were studying anisotropy and their contributions helped understanding of anisotropic modelling. For the advances in seismic anisotropy, a short

overview follows.

Vlastislav Červený belongs to the scientists who conducted tremendous research in the theory of anisotropic media since the 1960's and 1970's. Alone or in association with his colleagues at Czech Charles University in Prague, he published 3 books and about 200 scientific articles. His work led to the foundation of a scientific group: Seismic Waves in complex 3-D structures (SW3D), in association with Charles University and consortium of some oil companies and renowned research groups. SW3D focuses primarily on the fundamental issues of high-frequency seismic wave propagation in complex 3-D isotropic and anisotropic structures. Červený laid the basics for the theory of kinematic inversion in anisotropic media and his work among many other topics involves: detailed study of ray theory in heterogeneous anisotropic media, study of head waves, transmission and reflection of seismic energy on the interfaces of different media, study of seismograms, and many different aspects connected with forward modelling and inversion; whether it was for theoretical background or numerical studies. Among other members of the group that contributed to the study of seismic anisotropy are: Pšenčík, Jech, Klimeš, Bulant, Vavryčuk and others. The list of all publications and contributions of the SW3D group is too big, the reader is invited to visit their site: http://sw3d.cz/, which is in English.

Another extensive work in the field of seismic anisotropy has been started and is continued ever since by Ilya Tsvankin (1980's-present) and his colleagues at Centre of Wave Phenomena (CWP), which is associated with the Department of Geophysics at Colorado School of Mines – a public research university. Tsvankin was interested in all aspects of seismic data treatment that considered anisotropic properties of the media, especially for oil prospection. Whether it was wave propagation, reflection move-out, velocity analysis, time-to-depth conversion, imaging and modelling of complex structures, parameter estimation or

inversion procedures, he was involved in every aspect of the data treatment.

Among other publications, Tsvankin and Thomsen (1994) and Alkhalifah and Tsvankin (1995) proposed a new modified approximation for travel-time calculations, which is valid for longer offsets. Douma and Calvert (2006) proposed a new approximation based on their work and on the Padé approximation. There were also other attempts to approximate the travel-time. The reader is invited to look up the article by Aleixo and Schleicher (2010) for a more detailed list of approximation methods.

Grechka was similarly a member of CWP for some time and co-authored also many publications. Among his many contributions, one that stands out, is a complete and easy to understand handbook on applications of seismic anisotropy in the oil and gas industry (Grechka, 2009a).

Yet another team that started to tackle the anisotropic media and also succeeded to create 2.5-D / 3-D inversion programs, at first modelling with ray tracing methods in time domain (Zhou and Greenhalgh, 2008) and later within the frequency domain (e.g. Zhou et al., 2012), and recently going into the investigation and modelling of electric resistivity anisotropy (e.g. Wiese et al., 2013) is situated at the Australian Adelaide University and at Swiss ETH Zurich. Another branch of ETH is also interested in full waveform inversion (e.g. Fichtner et al., 2013).

In honour of the new millennium (Y2K), the SEG Research Committee invited a series of review articles and tutorials in order to summarize the advances in geophysics. Advances in seismic modelling were published by Carcione et al. (2002). They divided the methods into three different categories: direct methods, integral-equation methods and ray-tracing methods. The first category, also called grid methods or full-wave equation methods do not have restrictions on material variability and can be very accurate, but require much more

memory and computer time, than the other two. The integral-equation methods are more restrictive, but can be applied well for specific geometries, such as boreholes or bounded objects in a homogeneous embedding. Ray tracing methods have their limitations, they are approximative or asymptotic, since they do not take the complete wave-field into account. On the other hand, they are perhaps the most efficient for large 3-D models and due to their efficiency, they have played a very important role in seismic imaging (Carcione et al., 2002). The majority of these methods were nevertheless usable only for isotropic media. The reader is invited to read this article by Carcione, for a more detailed list of applications.

Robertsson et al. (2007) issued another supplement on seismic modelling for "Geophysics" journal. The consideration of anisotropy is already included in several cited articles.

In 2010-2012, when we started treating our data, the full 3-D elastic waveform inversion (FWI) was still in its infancy, required an excellent calibration system, knowledge of source signal and still is computationally very demanding. Most methods did not take anisotropy into account. Therefore, to treat our data acquired in LSBB (the Laboratoire Souterrain à Bas Bruit - Low-Noise Interdisciplinary Underground Science & Technology Laboratory), we used a non-linear inversion scheme based on first-order travel-time perturbation (Zhou and Greenhalgh, 2008). The ray tracing method is based on 'shortest ray-path method', used for isotropic media by Moser (1991). We also gained the access to the code, therefore we were able to test this code extensively and we applied some modifications necessary to our needs, like e.g. implementing the uncertainty matrix (C_D^{-1}) of acquired data into the calculation.

In recent years anisotropic FWI are starting to emerge (e.g. Warner et al., 2013; Fichtner et al., 2013). Virieux and Operto (2009) presented a review of used FWI in exploration geophysics. With the boom of calculation power and new processors, many scientists might

converge towards the FWI, as it calculates the model with as little approximations as possible comparing to the other methods.

The journal “Geophysics” dedicates every two years one whole special section to seismic anisotropy. It is following the International Workshops on Seismic Anisotropy (IWSA) which started in 1980's (Tsvankin et al., 2009; Bóna et al., 2011). The section is usually divided into several sub-sections that are dealing with imaging, modelling, inversion and rock physics.

Aleixo and Schleicher (2010) gave an overview of a collection of travel-time approximations and compared their quality. They also proposed some new single-parameter travel-time approximations based on existing ones, found in the literature.

Even though in exploration geophysics, main interest is focused on local data and reservoir assessment, the anisotropy was first observed and studied for seismic data in global and mega-scale samples such as the upper crust. The research still continues in the Earth's examination. To name a few: the azimuthal anisotropy is quantified by surface wave anisotropic inversions (e.g. Adam and Lebedev, 2012), the structure of mountain chains in Central Europe is investigated (Babuška et al., 2008), or the full resolution of small-scale structures in crust and mantle is studied (e.g. Fichtner et al., 2013).

There are many more geophysicist that contributed to the research of anisotropy, be it in theoretical work (e.g. singularity assessment of S-waves, parameter estimations, etc.), in numerical studies (e.g. study of boundary conditions) or in modelling and inversion (e.g. approaches in space and frequency domain, strategies for best minimum search, combination of algorithms). To list a few authors: Gerhard Pratt, Mathew Yedlin, Stuart Crampin (all since 1980's), Mark Chapman (last few years) and increasingly more geophysicist will be studying the anisotropy, as it is receiving increasingly more well deserved attention.

The research that has been conducted in the electrical resistivity anisotropy also dates

before the 50's of last century. The effect of anisotropy was known since the 1930's. In geophysical literature Slichter (1933) and Pirson (1935) were dealing with uniform transversely isotropic media (Yin and Weidelt, 1999).

Calculations for apparent resistivities of dipping beds in the early periods were also aware of the anisotropic effects, but the calculations were assuming isotropy of the layers and it was advised to use correction factors, that were obtained empirically dependent on each site (Unz, 1953).

Zhao and Yedlin (1996) classified the direct current (DC) resistivity modelling into basically three principal numerical techniques: integral equation approach, finite-element (FE) methods and finite-difference (FD) methods, each one being suitable for different geometries.

The integral equation method, represented by Lee (1975) was used for calculation of the potential of a cylinder in layered earth. Pal and Dasgupta (1984) used this method to derive analytically the electrical potential due to a surface point source over an inhomogeneous, anisotropic VTI media. Later Xu et al. (1988) used this method for 3-D terrain effects for DC resistivity surveys, yet over isotropic media. Yin and Weidelt (1999) modelled anisotropic half-space with different layers, each containing their own resistivity tensors.

Finite-difference algorithm are good for arbitrary structures with rather simple node repartition. Dey and Morrison (1979) developed a numerical method to solve the 3-D potential distribution over isotropic media. Zhao and Yedlin (1996) presented the combination of two modifications based on existing FD algorithms to better treat the singularity problem of the source.

The finite-element method is suitable for complex geometries. Representatives of this method are modelling isotropic media such as Coggon (1971), Pridmore et al. (1981),

Holcombe and Jiracek (1984), and also anisotropic media in recent years (Pain et al., 2003). Zhou et al. (2009) developed a new numerical scheme for heterogeneous anisotropic media based on the Gaussian quadrature theory (Abramowitz and Stegun, 1964) and modified spectral element method. This method differs from usual spectral methods, but retains the main advantages of this advanced numerical method. The gaussian quadrature gridding (GQG) method was used for our purposes.

Other algorithms based on analytic solutions were developed, the reader is invited to read the paper by Greenhalgh et al. (2009b) for a brief yet quite exhaustive list of different algorithms, whether numerical or analytic, for isotropic and anisotropic media. The explicit expressions for Fréchet derivatives is described in accompanying paper by Greenhalgh et al. (2009a).

Anisotropy can be found also within certain minerals and has also been studied for almost a half century now for their piezoelectric properties (e.g. Musgrave, 1970). Different materials or minerals, depending on the symmetry class, have different properties. Therefore, depending on the composition of the rocks in the studied area, the physical properties measured in one direction could have different values than in another direction. This is particularly true, if the crystals are well organised and aligned in the area (e.g. metric hexagonal poles of cooled lava). In fact most geological materials exhibit some degree of anisotropy (e.g. Grechka, 2009a).

Another possible cause of anisotropy is a systematically oriented fracturing of otherwise homogeneous isotropic medium. Fractures in host rock (or material) and their influence on elastic (seismic) properties, have been studied in a simplified way as penny shaped fractures for over a half century (e.g. Bristow, 1960). If oriented horizontally, they can be regarded as thin layers of very slow material and therefore create a medium with vertical transverse

isotropy. Oriented vertically, they result in a medium with horizontal transverse isotropy (e.g. Tsvankin, 1997b). Multiple sets of fractures, with exact spacings, could result in a medium with a monoclinic or triclinic symmetry (Winterstein, 1990), but mostly (because of irregular spacing) they result in a medium with orthorhombic anisotropy. This is valid also for the improbable regular orthogonal sets of fractures but also for a material with any orientation of fracture sets (Grechka and Kachanov, 2006).

Characterisation of the fractures in an otherwise homogeneous material in terms of elastic properties were done by Schoenberg (1980) and Hudson (1980). Schoenberg's theory approximates the fractures by infinite linear fractures, without assumption about the shape. It is based on physically intuitive relations between stress and discontinuity in displacement, formulated in terms of the fracture compliances or weaknesses (Bakulin et al., 2000a). Hudson's model sees the fractures as idealised penny-shaped fractures with specific geometry. They were giving almost the same results for media, with fluid-filled fractures, but they differed when the fractures were dry. For more than 20 years, geophysicists were using one of these two models for the description of fractured reservoirs. Grechka and Kachanov (2006) revised these two methods and showed that Schoenberg's theory is more accurate.

The studied site (LSBB) contains sub-horizontal galleries drilled inside a mountain. In one part, the tunnels form a big U-shape, where the two sub-parallel tunnels are 100 m apart (Fig. 1.2). The first idea was to do cross-hole tomography. Therefore, the geophones were placed in one of the galleries and the shots were executed in the other, parallel gallery (Figs. 2.2 and 4.2).The first data acquired in the galleries (measured in 2005) showed two branches for two velocities in the travel-time vs. offset graph (Fig. 1.3). For an isotropic medium, one would expect only one straight line for one velocity.

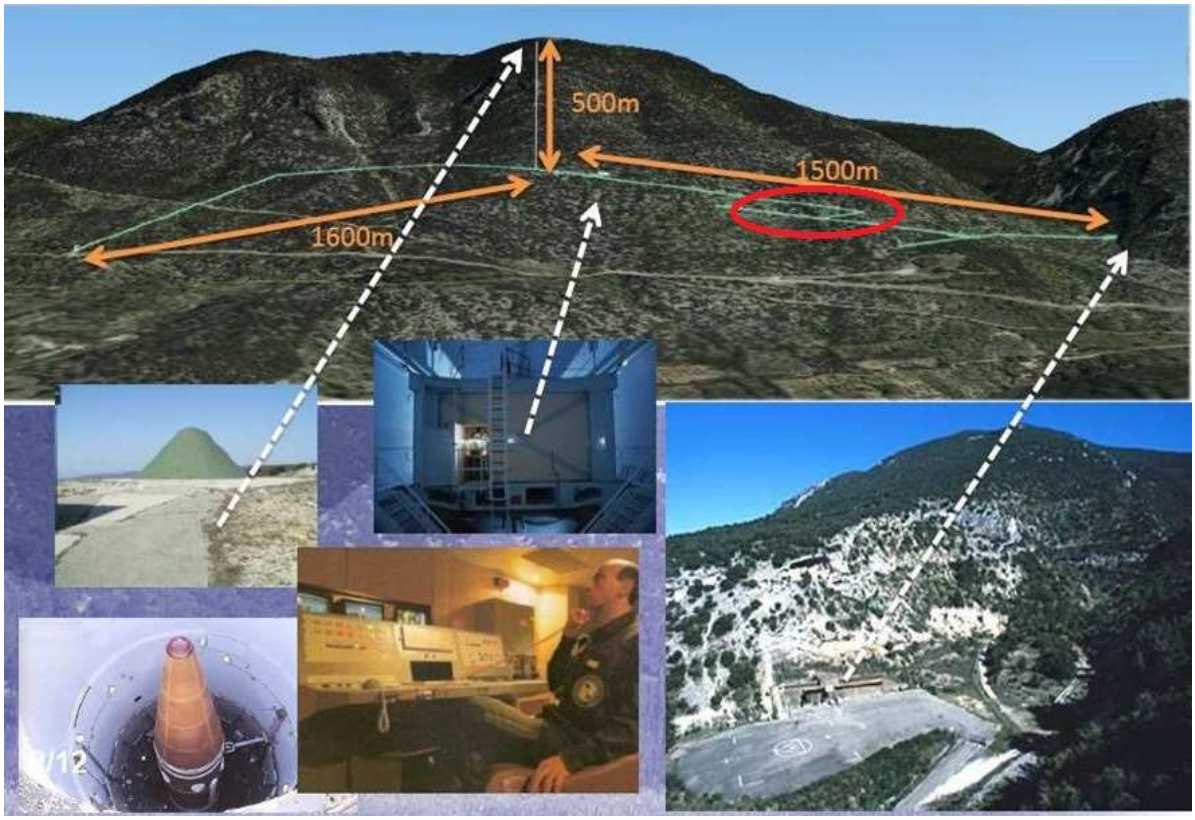

Fig. 1.2: Layout of tunnels inside the mountain (green) with the rocket tubes (left bottom), launching centre (centre bottom) and the entry (right bottom). Red ellipse represents the area of interest with two sub-parallel tunnels.

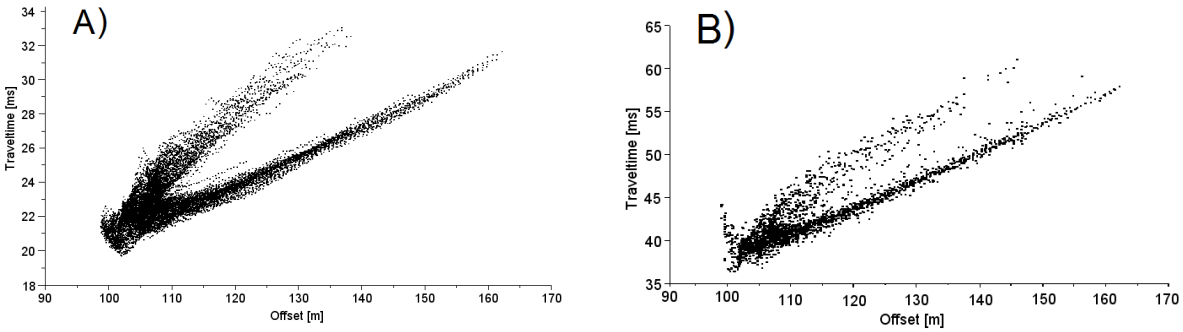

Fig. 1.3: Travel-time vs. offset for first campaign in May 2005 P-waves (A), S-waves (B).

Once it was clear that anisotropy was the cause of the branching of the two velocities, Monte-Carlo inversions were started and soon it became necessary to pick also the S-wave first arrival times, because the P-waves on their own, were not sufficient to constrain the

model. After the data was treated with satisfactory results and the two branches were modelled and matched the measured data, new questions arose. Could be the anisotropy detected also with other geophysical method that we had instruments for? Ground penetrating radar (GPR) would not have sufficient penetration because of a metallic grid inside the concrete walls (GPR measurements were conducted on the floor of galleries with no metallic grids inside – Sénéchal et al., 2013), the magneto-telluric methods might not provide sufficient information about the structure in horizontal directions between the galleries, majority of the electro-magnetic methods could be difficult to set up. The gravimetric measurements are of no use for two reasons: first they would not be sensitive to anisotropy, but maybe only slightly to increased fracture densities, and second they would not be able to screen the horizontal plane between the galleries. Therefore, the obvious choice was the electrical resistivity. Next question was, how anisotroy would be visible in the measures and how the two methods could be combined? It is said that one geophysical method equals zero geophysical methods, therefore the information of the two combined, provides more information and constraints than a single one.

The following chapters contain the description of work conducted on the acquired data and on some synthetic models in order to quantify the anisotropy of the studied area.

In the second chapter, the geology of the studied area is described in more details.

In the third chapter, the basic theory is described. In the first part, the different kinds of anisotropy are explained in more detail. Later comes the description of modelling in general. Basic governing equations are explained in little more detail and the description of inversion procedures for seismic and electrical resistivity methods follows. In this part, the common routines used for inversions are described. Finally, the chapter concludes on possible fracture characterisation methods.

The fourth chapter – methodology and results – describes the actual data treatment conducted on both data types. Preliminary, intermediate step and final results are in this chapter.

The fifth chapter will sum up the results collected during the research, discusses them and will attempt an interpretation of the data.

The final chapter will draw some conclusion and suggest the next steps as an outlook for future work needed in this field.

2 Geology of studied area

The LSBB (geographical location: N43.928472, E5.487048), is a system of underground tunnels in southern France that was built for the command of French nuclear forces and after dismantling converted into a research laboratory in 1998 (Fig. 2.1). It belongs to the Albion plateau, a karstic unit of the southern French Alps, drained by the Fontaine-de-Vaucluse (FdV) spring located 30 km west of the site - figure 2.2 (Maufroy, 2010). FdV is the biggest karst spring in the Europe with an average discharge of 19 m^3/s from 1970 to 2006 (Cognard-Plancq et al., 2006 in Carrière et al. 2013).

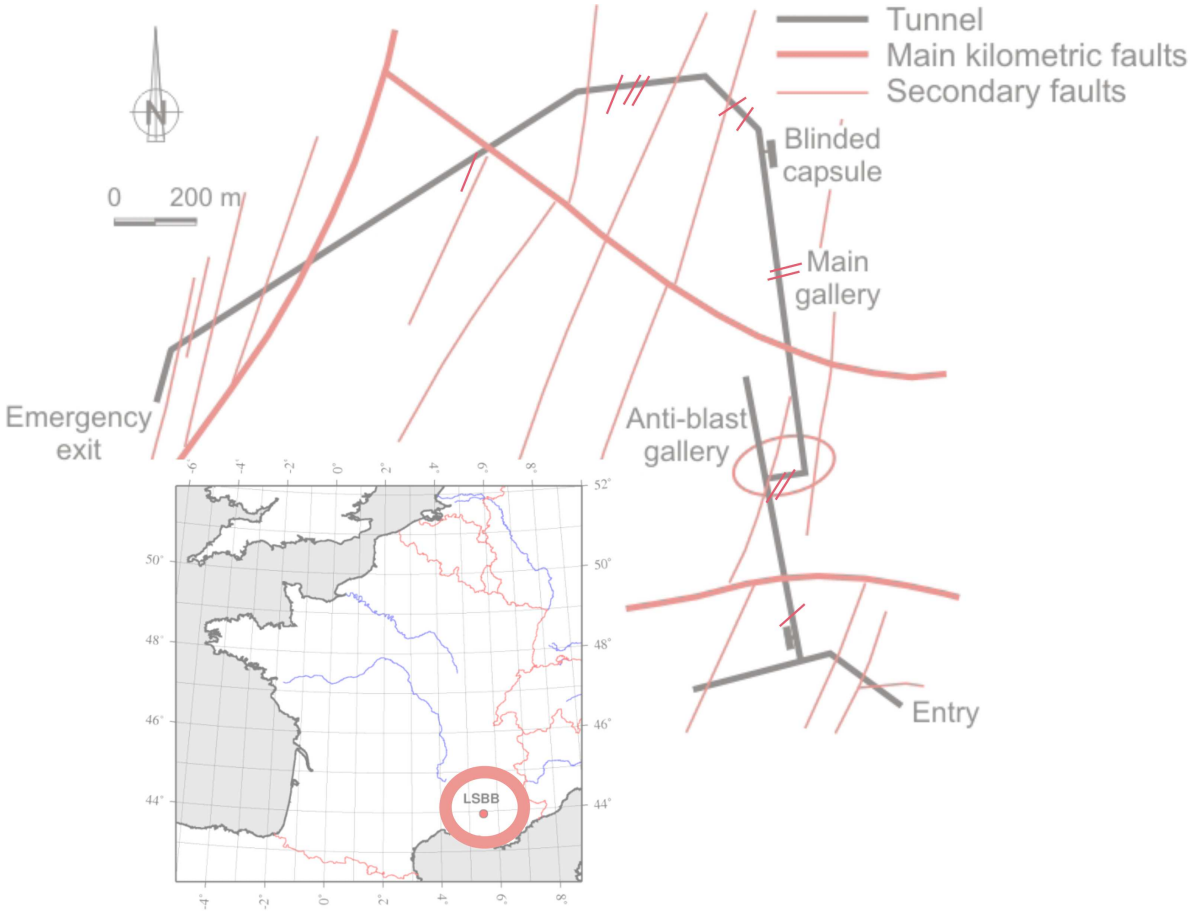

Fig. 2.1: : Location of the study area and fracture/faults setting. Faults visible at the surface are shown with long red lines (thick lines: major faults, thin lines minor ones). Short red lines indicate fractures visible in the galleries. The red oval represents the investigation zone.

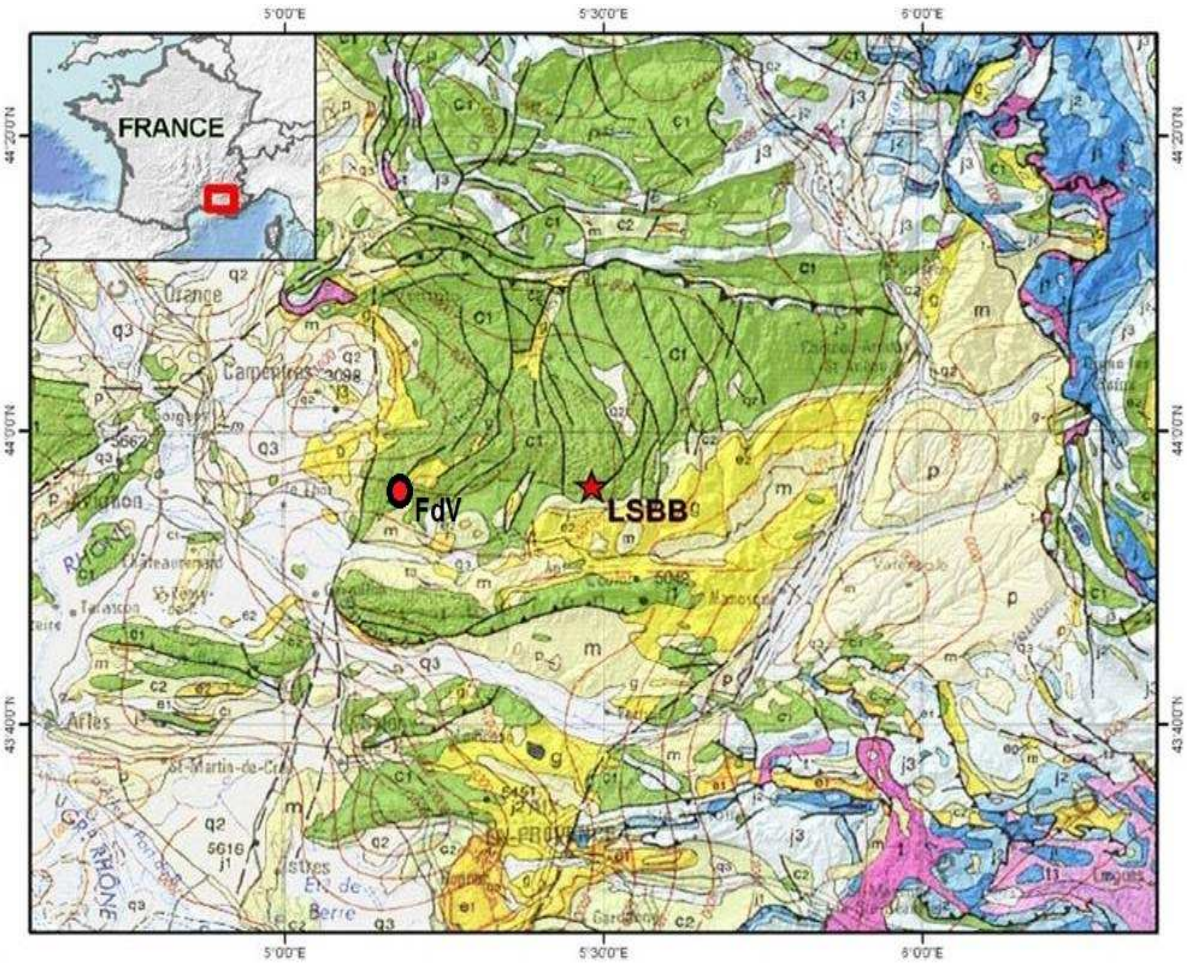

Fig. 2.2 Geographical location of LSBB (star) and Fontaine-de-Vaucluse (FdV - dot) on a geological map of the region.

The laboratory's position is very unique. Firstly, it is drilled inside one of the biggest karstified platform in the Europe, that is considered as an analogue of Middle-East carbonate reservoirs. Secondly, it is situated far away from any town and big communication routes, providing noise-free environment and therefore many different disciplines use it as study area (http://lsbb.oca.eu/).

The laboratory is located in a karstic limestone massif containing fractures and faults with a predominant N30°E direction (Thiébaud, 2003) in a 1000-1500 m thick succession of Lower Cretaceous carbonates (Maufroy, 2010). The studied area (the U-shaped structure) is completely within a 150 to 200 m thick layer of Urgonian sediments - U1 (Upper Barremian

to Aptian – ca. 125-115 Ma) (Fig. 2.4) composed of bio-calcarenitic carbonates with an average porosity of 10% (Masse, 1993). The properties of the investigated part of the massif are influenced mostly by minor fractures, major faults are not present. However, the rock is intensely deformed by sub-vertical and sub-parallel cracks (Fig. 2.2 and 2.4).

Sub-horizontal alternations of massive banks and friable layers (dipping with 25° in N120-130° direction) are interrupted by sub-vertical reef structures striking in E-W to WNW-ESE direction (Thiébaud, 2003).

The laboratory is situated in the vadose zone of the karstified limestone massif with the aquifer table being about 100-200 m below the galleries (Gaffet et al., 2003). The elevation of the galleries is around 500 m.a.s.l. and the karstification of the limestone layers is recorded well underneath the permanent water table (Fig. 2.5). Measurements conducted in the FdV spring confirmed a depth of around 225 m.b.s.l. - thickness over 700 m (Staigre 1983, in Garry, 2007).

Studied area in the laboratory is situated from around 900 to 1000 m from the entry point inside the mountain, and 200-300 m below the surface. Therefore the seasonal variations of temperature (either of the air, or infiltrating water) are not influencing the mechanical properties of rock.

Mechanical properties of the rock are influenced only by the variations of water content, which will be attempted to qualify during this work. From the work of Thiébaud (2003), who characterised the fractures, by examining the seepages in the galleries, one can observe that some of the fractures are sufficiently open to allow free flow of the water (some permanent seepages along the tunnels (Fig.2.3), others are correlated with the sufficient precipitation), some of them only allow water to fill the free space. Above the permanent water table, there are some seasonal unmapped water collectors that are supplying the seepage areas with

water even when there is no rainfall (Sénéchal et al., 2013).

A master thesis in progress (Ollivier, 2013) tries to quantify a relation between the rainfall and water content, however their study site is situated at the end of escape gallery near the emergency exit (Fig. 2.2), close to the surface. Nevertheless, their findings could help us understand the variations within the galleries buried 200 m below the surface.

The studied galleries are not constructed the same way. The walls of TG and MG are covered by a concrete of thickness of about 30 - 40 cm, which is fortified with metallic grids. These galleries were used by military. Therefore, their walls are smooth and straight (Fig.2.3). The ABG is not fortified, contains only sprayed concrete mixture on the ceiling and top part of the walls. The height and the width of this gallery vary as the drilling loosened some bigger chunks of rock. As the walls have not been treated, they are not straight.

Fig. 2.3: Example of seepages inside the tunnels.

These two types of structures influence the seismic and resistivity measurements in different ways. In the ABG, the geophones for the seismic measurements were not planted always perpendicularly to the wall, although we tried to plant them parallel to one another, in directions perpendicular to the direction of the gallery. The two remaining fortified galleries posed problems for the

resistivity measurements as initially, using short electrodes, the current entering the surface of the gallery was dissipated in the metallic grids. The construction of long (50 cm) insulated electrodes planted directly into the limestone solved this problem.

Karstic limestone is a product of mechanical and/or chemical erosion of limestone. The process of karstification is connected to favourable climatic and geologic conditions necessary to start and sustain the process (e.g. Garry, 2007). Karstic limestone will eventually lead to free water flow and thus become a good conductor for the water. It is however, still hard to quantify the water flow, especially in the vadose zone, as the fractures and open spaces created by the karstification processes are not evenly spread; and therefore a representative sample that could be studied at laboratory scale is hard to obtain. Quantification is usually done by examining the springs that are draining the studied areas. Nevertheless, the LSBB can be considered as a representative sample of these karstified limestone formations supplying the water for FdV (Garry, 2007). From the examination of seepages (Thiébaud, 2003), it is clear that the variations of water content in the massif are to some degree related to the precipitation and some fractures can become dry during some periods of the year. However, the amount of water trapped in the collectors are difficult to quantify and research on this subject in LSBB is still in progress (e.g. Ollivier, 2013) .The rainfall data is represented in the figure 2.6, collected and studied by Perineau et al. (2011).

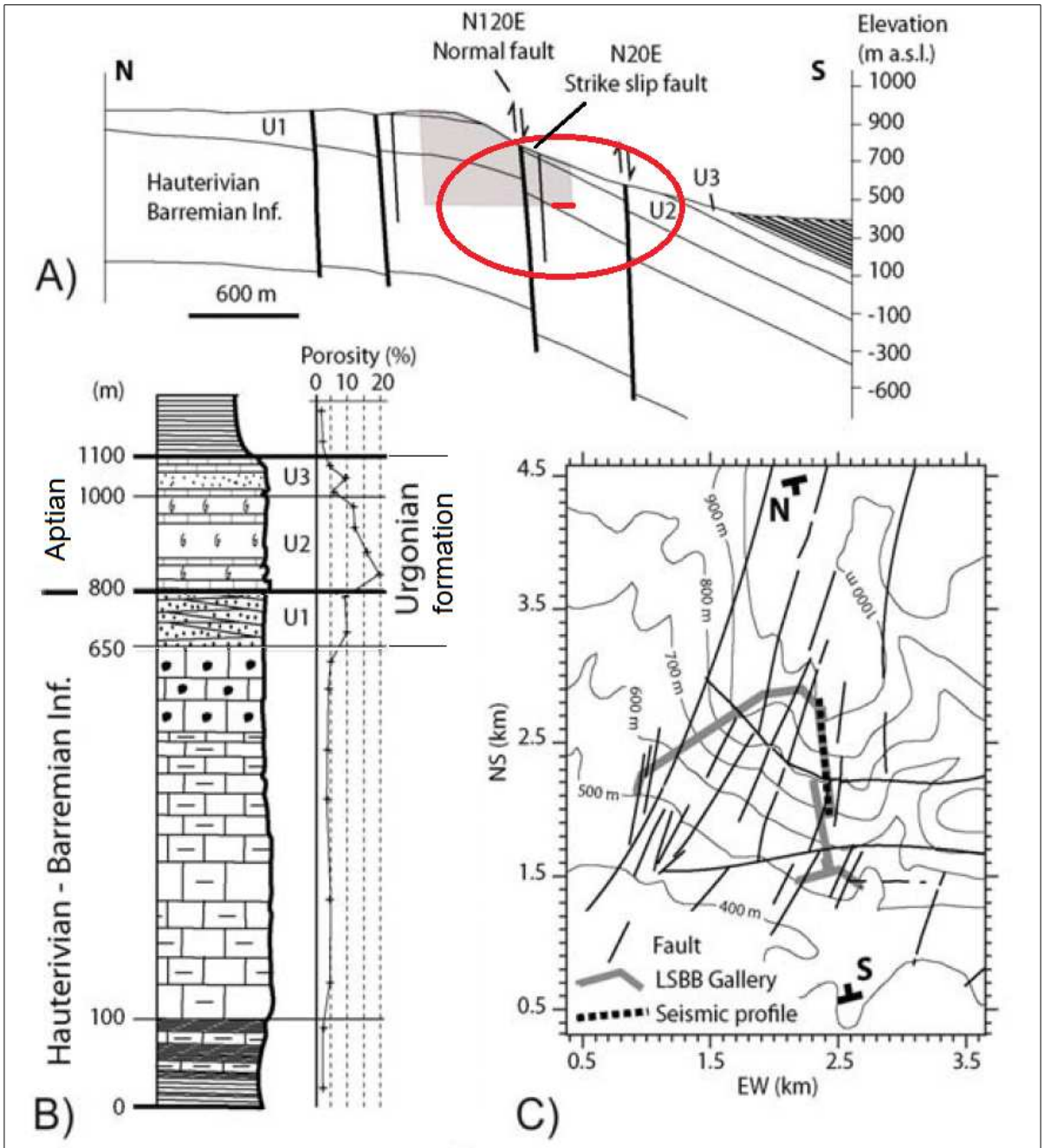

Fig. 2.4: A) Schematic N-S geological cross section of LSBB site with the zone of interest marked with red segment within the red ellipse; B) Lithostratigraphic succession and porosity variation of the carbonate rocks; C) Representation of the galleries with topographic information superposed (Modified from Maufroy, 2010)

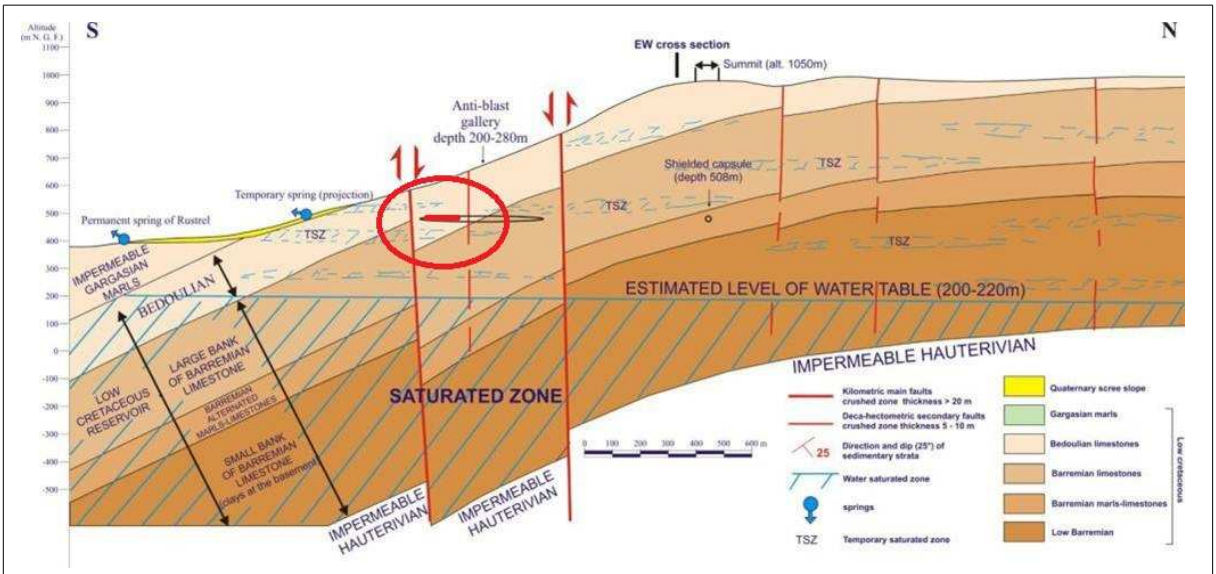

Fig. 2.5: Geological cross section of LSBB with permanent water table and schematic seasonal zones filled with water above some impermeable layers that entrap the water. Modified from Sénéchal et al., 2013

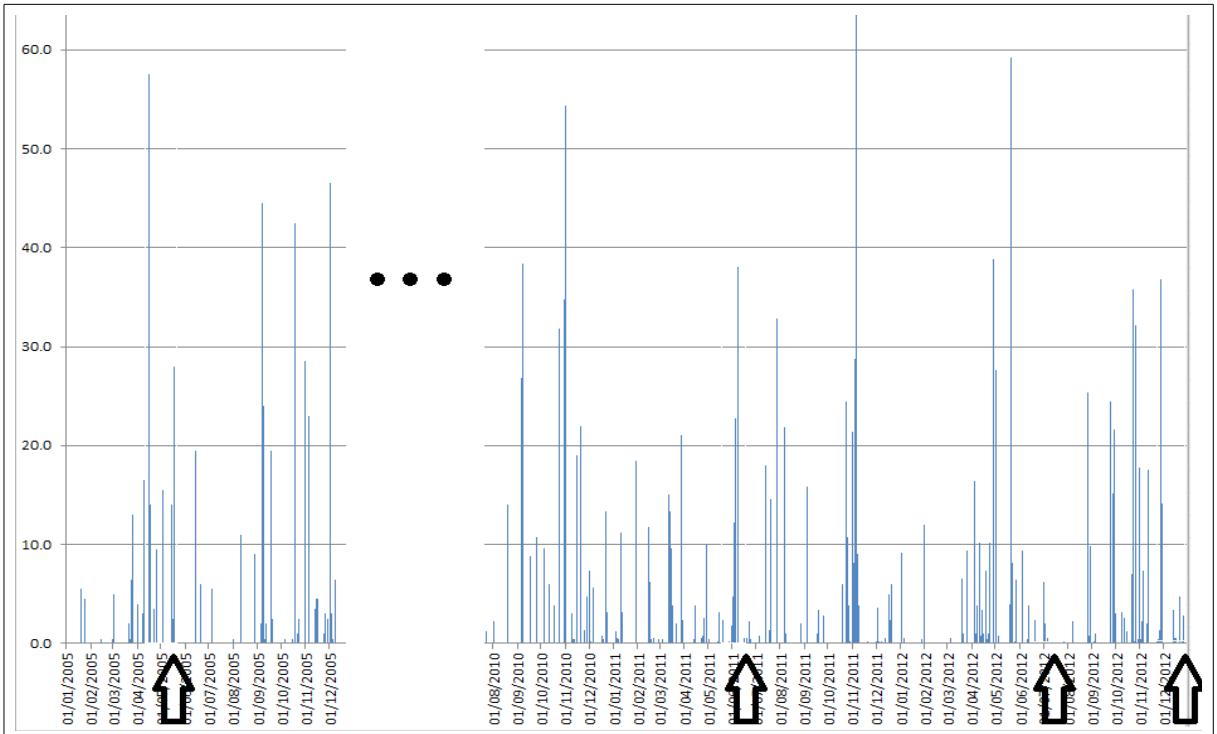

Fig. 2.6: Rainfall data recorded at the station: St Saturnin lès Apt, 10 km east from the LSBB site. The arrows represent the dates of four seismic campaigns.Modified from Perineau et al., 2011.

3 Theoretical background

3.1 Anisotropy

The word “anisotropy” describes the property of a material, that has no (an-) equal (-iso-) value in all directions (-tropos = way). Coming back to the difference of scales mentioned in the introduction, there can be confusion between the anisotropy and the heterogeneity. As Grechka (2009a) pointed out, these two are related: “Ordered heterogeneity on micro-scale results in anisotropy on macro-scale”. The same applies for the layered subsoil (thickness of layers of few centimetres) with the signal wavelength is far greater (meters) than the layering (Fig. 3.1)

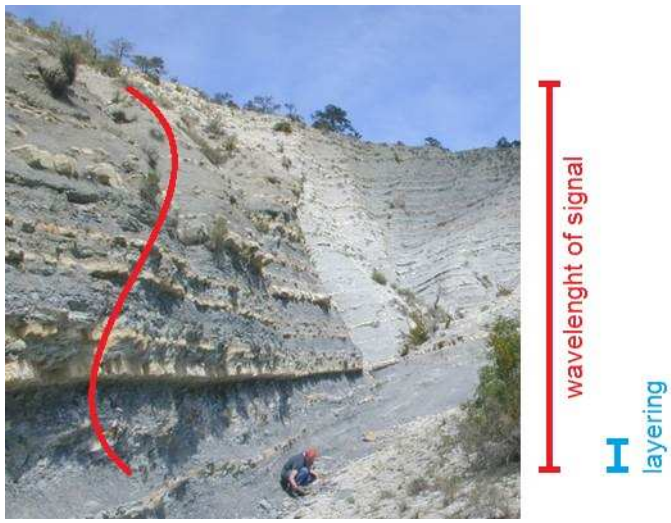

Fig. 3.1: Example of difference between the size of signal wavelength and layering

There are different systems of anisotropy, which are based on symmetry systems of crystals (Winterstein, 1990). However, not all of the 32 crystal symmetry classes can be found at the scale of rock samples or at the scale of several tens or hundreds of meters of the acquisition geometry. The reason for that, as described by Winterstein (1990), is that the causes for the anisotropy (namely layering, in situ stresses, orientation of microscopic

particles such as clays in shales (Grechka, 2009a) and last but not the least oriented planar cracks and fractures) cannot be naturally so structured as to produce a complicated symmetry.

If more planar fractures and cracks dispersed in a medium are oriented in the same direction, they create an anisotropic medium. The oriented voids can be considered as layers of different material, heterogeneities (within the matrix of a rock) that depending on the infill of the fractures, influence the medium in the following way: For a dry medium, the compressional P-wave velocities parallel to the fractures propagate as fast as in the matrix without the fractures. Perpendicular to the fractures, the velocity changes depending on the size and aperture of the fractures. For a medium with fractures filled with water, the ratio between the fast and slow velocity is smaller, yet the same rules as to the directions apply (higher velocity parallel to the fractures than across). The difference of the infill is manifested for P-wave velocity perpendicular to the fractures. Filled with water, it is higher than a velocity of the same medium with dry fractures.

The S-waves do not propagate either in void, or in the water, therefore are unchanged for dry or wet medium. Similar to the P-waves, direction parallel to the fractures has higher velocity than the one perpendicular to them. However, as in anisotropic medium two S-waves are created that are polarised parallel and perpendicular to the fractures, in addition to directional dependence, their behaviour around the fractures depends on the polarisation they acquire during the S-wave splitting. Those polarised parallel to the fractures propagate faster than those that are polarised perpendicularly.

Mathematically, the resulting elastic properties of anisotropic medium can be calculated by summing up the compliance matrices (inverse of stiffness matrices) of background medium and those of the fractures and their infill (e.g. Bakulin et al., 2000a; Grechka and

Kachanov, 2006).

If there is only one set of oriented planar fractures, the resulting medium will have properties of transversely isotropic medium. Horizontal fractures will result in VTI medium, similar to horizontal layering of different layers explained earlier.

Also the electrical resistivities change for dry and wet media yet the change is different to the seismic changes. If the medium is dry, the resistivity parallel to the fractures, also called longitudinal, is lower than the resistivity perpendicular, also called transversal. For water filled media, the ratio between the longitudinal and transversal resistivities increases with the infill as it is mainly the longitudinal resistivity that is decreasing furthermore with mineralised water content.

The reconstruction of the properties of a material or area is done by modelling. The modelled sample is then subjected to forward calculation (description later in this chapter) and the resulting modelled response is compared to measured data. In order to quantify the difference / error between the modelled and measured data, there is a need of parametrisation of the properties of the sample / area by a set of parameters. The changes of these parameters are then reflected into the final difference between the two datasets.

As for the seismic modelling, these properties are physically expressed by a stiffness C_{ijkl} (or compliance S_{ijkl}) tensor of 4^{th} rank. This tensor contains 81 (3x3x3x3) coefficients, but because of symmetry of this tensor, only 21 coefficients are independent (e.g. Grechka, 2009a). It has been common practice to express these coefficients in terms of a modified two-dimensional symmetric matrix (6x6) in Voigt notation (Winterstein, 1990).

Although not all structures belonging to all 32 symmetry classes are possible at macroscopic scale, it is possible to observe in nature the following structures. The examples are given by one of the causes, namely fracturing, where the addition of compliances of all

fracture sets will result in media with different symmetry system. Along with the description of different configurations, the number of parameters needed for modelling is displayed (modified from Winterstein, 1990):

a) no cracks at all, therefore homogeneous body, expressed by 2 coefficients of the stiffness matrix, equivalent to coefficients of Lamé, creating isotropic symmetry.

b) one set of oriented planar cracks in a homogeneous body, creating transversely isotropic symmetry with 5 independent coefficients.

c) two sets of oriented planar cracks, either not orthogonal but equidistant, or two orthogonal sets with different spacings, or one single set of vertical crack within VTI media (Bakulin et al., 2000b), or multiple vertical fracture sets in VTI media (Grechka, 2007), creating the orthorhombic symmetry in the medium with 9 independent coefficients.

d) two sets of oriented planar cracks not orthogonal and not equidistant to each other, creating monoclinic symmetry, with 13 independent coefficients of the stiffness matrix, and with a favourable orientation within the reference system, their number decreases to 12.

e) three sets of oriented planar cracks not orthogonal and not equidistant (=different spacing between the parallel cracks) to each other, creating triclinic symmetry, where all 21 coefficients of the stiffness matrix are independent. If the orientation of the cracks is aligned with the reference system, only 18 of them are independent.

As for the electric resistivity, there are not so many possible ways in expressing these different anisotropies, electrical potential following the Poisson equation, implementing a conductivity tensor of 3rd rank, results in an ellipsoid with only three different axes, therefore it is possible to model only orthorhombic, transversely isotropic and purely isotropic media.

In resistivity measurements, however, anisotropy should be strongly reduced when the

rock is dry. Dry limestone is almost as good insulation as is the air within. The medium is therefore very resistive and anisotropy is only clearly manifested when the fractures are filled with water. The water is dissolving the rock matrix and becomes therefore mineralised and conductive. The current then has preferential flow along the fractures. Different water content should in theory have an influence on the conductivities.

3.1.1 Triclinic and monoclinic anisotropy

For the reasons of computational limitations, time and complexity vs. simplicity of model, it is hard to model many parameters. Having to search for 12 or 18 coefficients of the sample stiffness matrix of geological material is, if not impossible, then definitely futile. However, Grechka et al. (2000) showed that it is possible for monoclinic media, if wide azimuth reflection data is combined with multi-azimuth walk-away vertical seismic profiles (VSP) or known vertical velocity or depth of the reflector. Modelling of a monoclinic medium has been done by e.g. Winterstein and Meadows (1991).

In addition, with the acquisition geometry on geological sites, it is very unlikely to screen ('illuminate') the whole volume of studied material from all angles in order to find out all of the parameters. This is only possible for small laboratory samples that will not be representative of the whole volume of a studied area, because of other heterogeneities. Also, having no way of expressing the electrical potential distribution in another than orthogonal reference system, these two configurations of anisotropies are not used in electric interpretations and they are not very common in seismic interpretation.

3.1.2 Orthogonal / orthorhombic anisotropy

Because of the complexity of the two former anisotropy geometries, some simplifications are introduced into the modelling. It is also more probable for a material on a bigger scale to

have properties of orthorhombic anisotropy than the previous two and in fact existing geological and geophysical data indicate that orthorhombic media are rather common for naturally fractured reservoirs (Bakulin et al., 2000b). Orthorhombic material is in the seismic modelling expressed by a stiffness matrix with 9 independent coefficients. Nevertheless, nine is still too large to be routinely used in seismic data processing (Grechka, 2009a), but some a priori information might facilitate their use. The stiffness matrix in Voigt notation has the form:

$$C^{(ORT)} = \begin{pmatrix} c_{11} & c_{12} & c_{13} & 0 & 0 & 0 \\ c_{12} & c_{22} & c_{23} & 0 & 0 & 0 \\ c_{13} & c_{23} & c_{33} & 0 & 0 & 0 \\ 0 & 0 & 0 & c_{44} & 0 & 0 \\ 0 & 0 & 0 & 0 & c_{55} & 0 \\ 0 & 0 & 0 & 0 & 0 & c_{66} \end{pmatrix} \tag{3.1}$$

The stiffness matrix contains information about elastic properties dependent on direction of propagation. These could be translated into directional velocities. The parameter c_{XY} in the first sub-matrix (3x3) contains information about the P-wave velocity in X-axis with influence of the Y direction. The fourth sub-matrix with only diagonal elements c_{44} - c_{66} contains information about the S-waves velocities.

Also for the electrical anisotropy, three different semi-axes of resistivity / conductivity ellipsoid (stemming from the conductivity tensor σ with three orthogonal eigenvectors) are a measure of different properties perpendicular to each other and therefore are possible to model.

3.1.3 Transverse isotropy

Increasing further the symmetry of anisotropy, thus making two of the three directions equal in seismic and resistivity properties, one comes to a transversely isotropic medium,

where properties do not change, if only the angle around the symmetry axis is changing, hence the name.

In the general case, where the direction of the symmetry axis is not aligned with the reference system, the system is called tilted transverse isotropy (TTI). If the symmetry axis is vertical and the properties do not change with the horizontal azimuth, we are dealing with VTI. In the second extreme case, where the symmetry axis is horizontal, we are talking about horizontal transverse isotropy (HTI).

The stiffness matrix of a vertically transversely isotropic medium is expressed as:

$$C^{(VTI)}=\begin{pmatrix} c_{11} & c_{12} & c_{13} & 0 & 0 & 0 \\ c_{12} & c_{11} & c_{13} & 0 & 0 & 0 \\ c_{13} & c_{13} & c_{33} & 0 & 0 & 0 \\ 0 & 0 & 0 & c_{55} & 0 & 0 \\ 0 & 0 & 0 & 0 & c_{55} & 0 \\ 0 & 0 & 0 & 0 & 0 & c_{66} \end{pmatrix} \tag{3.2}$$

The matrix contains six parameters, but only five of them are independent. The parameter is a linear combination of two others:

$$c_{12}=c_{11}-2c_{66} \tag{3.3}$$

For comparison, to show the difference between matrix (3.2) and the stiffness matrix of horizontally transversely isotropic media with axis x_1 as the symmetry axis, the reader is invited to compare with matrix (3.10) later in this chapter.

In practice, the programs to model this type of anisotropy use a VTI approach and two rotation angles to rotate the reference system, allowing the modelling of TTI and HTI media by simulating VTI geometry.

As it is rather cumbersome to understand the properties of a VTI medium by examining

the stiffness matrix, Thomsen (1986) introduced dimensionless coefficients that help the interpreter to visualise the properties in a more comprehensible and faster way.

The parameter ε contains information about the ratio between the fast and slow velocities of P-waves:

$$\varepsilon \equiv \frac{c_{11} - c_{33}}{2c_{33}} \tag{3.4}$$

Similarly the parameter γ contains the information about the ratio between the fast and slow velocities of S-waves:

$$\gamma \equiv \frac{c_{66} - c_{55}}{2c_{55}} \tag{3.5}$$

If these parameters are positive, the velocity on the symmetry plane is faster than the velocity in the direction of the symmetry axis. If they are negative, it is the opposite. These parameters vanish in isotropic media.

The parameter δ describes the curvature of the P-wave velocity function at the vertical, it has key importance for seismic reflection data, because it governs the P-wave normal-moveout velocities from horizontal reflectors and is therefore used for seismic reflection processing (Grechka, 2009a):

$$\delta \equiv \frac{(c_{13} + c_{55})^2 - (c_{33} - c_{55})^2}{2c_{33}(c_{33} - c_{55})} \tag{3.6}$$

The parameter δ has no use for our data, as we are not dealing with reflection data.

Various authors designed different parameters, or modified the Thomsen's parameters in order to facilitate their interpretation and to gain insight into the form of phase velocity function. The list of these parameters can be found in Grechka (2009a). The phase velocity function for isotropic media, when represented in space will have a form of a sphere. For

VTI media and P-waves, this form is near to an ellipse (with a fortunate parameter combination it is a perfect ellipse), however because of parameter c_{13}, this form can deviate from an ellipse (Fig. 3.2). When represented with respect to the angle of departure, the phase velocity function will have the form of a constant line for isotropic media and will be near to a trigonometric function for VTI media in the isotropy plane cross section (Fig.3.3).

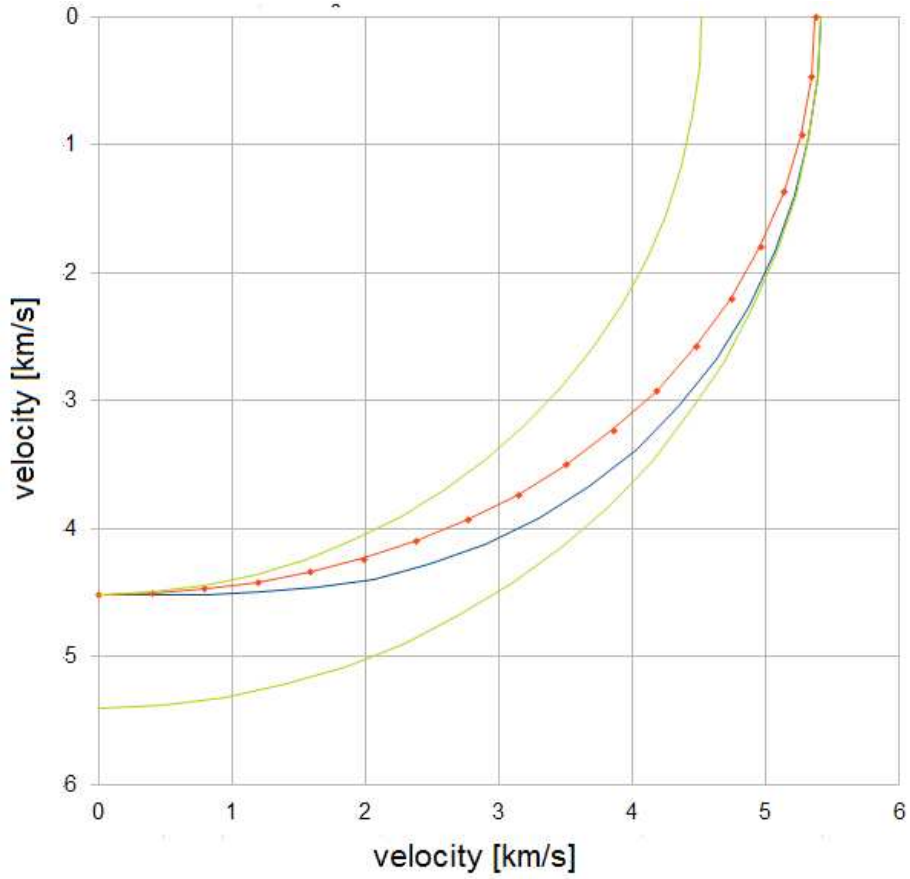

Fig. 3.2: Phase velocity function for P-waves of VTI medium, represented in one quadrant of a section between isotropic axis (vertical) and isotropic plane (horizontal). Red dotted curve represents the perfect ellipse. Blue curve represents an example of another anisotropic phase velocity, with different parameter c_{13} from the red curve. Both of the anisotropic media have the same maximum and minimum velocities. Green lines represent the isotropic velocities situated at maximum and minimum of the anisotropic examples.

The phase velocity functions for S-waves differ from P-waves, as one of the S-waves (polarised perpendicular to the layering) is modified only in the non-axial directions (role of parameter c_{13}) with the same velocities in axial directions (role of parameter c_{55}) and the

other S-wave (polarised parallel to the layering) is modified only in the isotropic plane direction (role of parameter c_{66}) – figure 3.4.

For the electrical anisotropy, there are only two different resistivity / conductivity values and they are oriented perpendicular to fractures (transversal resistivity) and parallel to fractures (longitudinal resistivity).

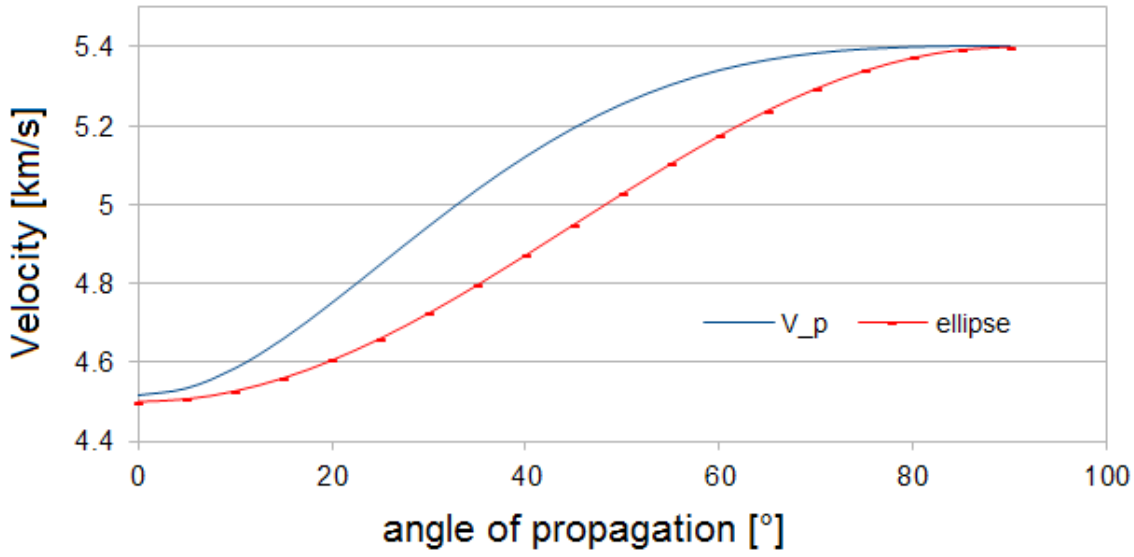

Fig. 3.3: Phase velocity function for P-waves of VTI medium with respect to angle of departure. Two combinations of parameters are shown, red curve form an exact ellipse, the blue deviates from ellipticity. Maximum and minimum velocities are the same for both of them.

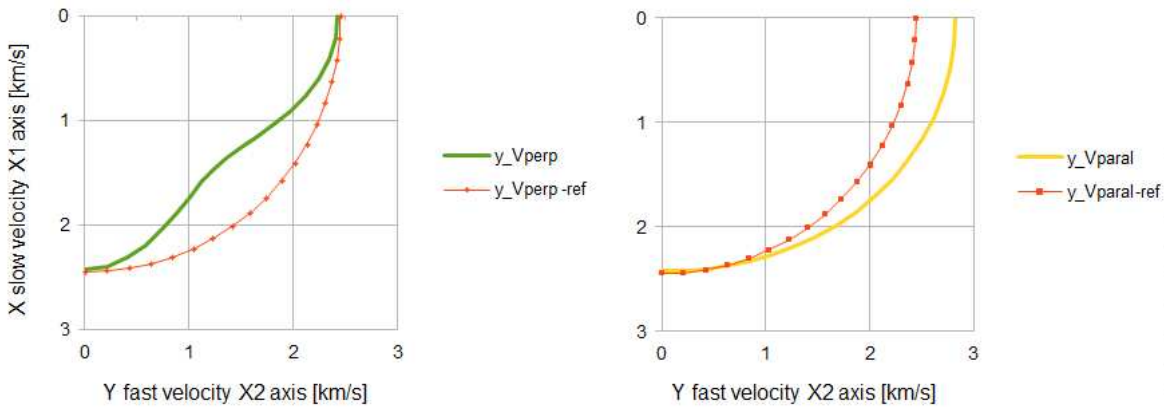

Fig. 3.4: Phase velocity function for S-waves of VTI medium, represented in a section of a quadrant of space. Green curve represents the S-waves polarised perpendicular to layering, Yellow curve represents S-wave polarised parallel to layering. Red curves represent the isotropic reference velocity.

3.2 Modelling in general

As mentioned in previous sub-chapter, the modelling needs to be done in order to reconstruct the properties of studied area/sample. Reconstruction is also called inverse modelling or for short inversion, because the properties that created the measured data are searched from the data. During the inversion (described in more detail later in this chapter), the forward modelling procedure is repeated several times.

During the forward modelling the properties of the modelled medium are known and the physical response they produce will be also known after the calculation. The physical properties of the model (e.g. velocity of seismic wave, resistivity) are then expressed in the modelled physical responses (e.g. travel-time data from source to receiver for seismic waves, or potential distribution from modelled current injection) which can then be compared to real data during the inversions and in order to find the best possible match between the modelled and acquired data, it is necessary to conceive different models, that would have a response similar to the acquired data.

Some simplifications for the models are welcome, provided they do not influence the quality of the data fit. For instance, our seismic model (described later) could be well explained by orthorhombic as well as transversely isotropic symmetry. In the former, some of the coefficients of the stiffness matrix would not have any influence on our data whatsoever as we are dealing with data, that has been collected in one plane containing only two major axes of the symmetry coordinate system. Nine coefficients instead of five would slow down the calculation and because they don't influence the data, the inversion would become unstable.

The simplest modelling case is when the medium is considered homogeneous. During the

modelling that tries to simulate measured data, the acquisition geometry is set to the one used for real data and the modelled signal for a given source-receiver combination is calculated by governing equation.

During modelling, even if it can be very complex, the model is always a simplification of the real medium. In our case, the transversely isotropic (TI) model could explain the seismic data sufficiently well.

As there are various possible approaches to model the physical properties of a medium, based on different algorithms (space domain, frequency domain, different approximations, etc.) it is advisable to compare more approaches in order to verify the result. If this is not possible, at least a comparison with analytical formulas is recommended. In our case, we compared the results of seismic modelling with analytical solutions for isotropic medium and also for the anisotropic medium with different sets of parameters in order to validate the algorithm. For the electrical modelling, we compared the forward modelling program with analytical solutions and models calculated with Comsol Multiphysics.

Once the results are satisfactory, i.e. there is a combination of parameters that can explain the data well enough with this homogeneous approximation, the model can be divided into different blocks and their variations are introduced into the model. In this way the heterogeneities are modelled. The FD routines, FE routines or finite-volume routines (FV) can be employed (Virieux and Operto, 2009)).

3.2.1 Seismic modelling

Modelling the velocities in any (elastic) media requires the ability to express the propagation of seismic signal in the media in a mathematical form. This can be achieved by the equation of motion, which binds together the displacement of particles within the medium with stresses applied to the medium (Grechka, 2009a):

$$\rho \frac{\partial^2 \boldsymbol{u}}{\partial t^2} = \frac{\partial \sigma_{ij}}{\partial x_j} + f_i \quad (i = 1,2,3) \tag{3.7}$$

where **ρ** is the density of the medium, ***u*** represents the displacement vector, t is the time, σ is the stress tensor, **x** is the position in a cartesian coordinate system and **f** is the vector of body forces.

The actual displacement of particles depends on the relationship between the stress vector and deformation (strain), expressed by (Hook's law):

$$\sigma_{ij} = C_{ijkl}\, \varepsilon_{kl}, \tag{3.8}$$

where the C_{ijkl} is the 4th rank stiffness tensor and ε_{kl} represents the strain tensor:

$$\varepsilon_{ij} = \frac{1}{2}\left(\frac{\partial u_i}{\partial x_j} + \frac{\partial u_j}{\partial x_i} \right) \quad (i, j = 1,2,3) \quad , \tag{3.9}$$

It is difficult to express and visualise the physical properties using a tensor with four dimensions, with 81 coefficients. Because many coefficients of the stiffness tensor are inter-dependent due to symmetry requirements, it has been common practice to transform the tensor (Voigt notation) into a two-dimensional symmetrical matrix of 6x6 = 36 coefficients with 21 independent entries, since also this matrix is symmetric.

For each symmetry system, there is a different stiffness matrix (as seen in equations 3.1 and 3.2). For horizontal transversely isotropic media the stiffness matrix $C^{(HTI)}$ has five

independent coefficients, in Voigt notation expressed as (Winterstein, 1990):

$$C^{(HTI)}=\begin{pmatrix} c_{11} & c_{12} & c_{12} & 0 & 0 & 0 \\ c_{12} & c_{22} & c_{23} & 0 & 0 & 0 \\ c_{12} & c_{23} & c_{22} & 0 & 0 & 0 \\ 0 & 0 & 0 & c_{44} & 0 & 0 \\ 0 & 0 & 0 & 0 & c_{66} & 0 \\ 0 & 0 & 0 & 0 & 0 & c_{66} \end{pmatrix} \tag{3.10}$$

Similar to the equation (3.3), one of the coefficients is a linear combination of two others:

$$c_{23}=c_{33}-2c_{44} \tag{3.11}$$

Equation 3.8, becomes in the Voigt notation (Grechka, 2009a):

$$\sigma_i = C_{ij}\,\varepsilon_j, \qquad (i,j= 1, \dots , 6) \tag{3.12}$$

where σ and ε tensors became six-dimensional vectors with the following components:

$$\begin{bmatrix} \sigma_1 \\ \sigma_2 \\ \sigma_3 \\ \sigma_4 \\ \sigma_5 \\ \sigma_6 \end{bmatrix} = \begin{bmatrix} \sigma_{11} \\ \sigma_{22} \\ \sigma_{33} \\ \sigma_{23} \\ \sigma_{13} \\ \sigma_{12} \end{bmatrix} \qquad \begin{bmatrix} \varepsilon_1 \\ \varepsilon_2 \\ \varepsilon_3 \\ \varepsilon_4 \\ \varepsilon_5 \\ \varepsilon_6 \end{bmatrix} = \begin{bmatrix} \varepsilon_{11} \\ \varepsilon_{22} \\ \varepsilon_{33} \\ 2\varepsilon_{23} \\ 2\varepsilon_{13} \\ 2\varepsilon_{12} \end{bmatrix} \tag{3.13}$$

Substituting equation 3.8 and equation 3.9 into the equation of motion 3.7, results after neglecting the terms of body forces in:

$$\rho \frac{\partial^2 u_i}{\partial t^2} - C_{ijkl} \frac{\partial^2 u_l}{\partial x_j \partial x_k} = 0, \quad (i = 1,2,3) \tag{3.14}$$

Its solution is a harmonic plane wave ***u****:*

$$\boldsymbol{u} = \boldsymbol{U} \exp\left[i\,\omega \left(\frac{\boldsymbol{n}\cdot\boldsymbol{x}}{V} - t \right) \right] \tag{3.15}$$

where U is the polarisation vector, $i=(-1)^{-1/2}$ is the imaginary unity, ω is the angular frequency, n is the unit wavefront normal and V is the phase velocity.

Substituting equation 3.15 again into the equation of motion 3.7 leads to the Christoffel equation (Grechka, 2009a):

$$[G_{il}(n)-V^2\delta_{il}]U_l=0 \quad (i=1,2,3) \tag{3.16}$$

where δ is the Kronecker delta function and $G_{il}(n) = \alpha_{ijkl}\ n_j\ n_k$, (i,l = 1,2,3) is the Christoffel matrix with α being the density normalised stiffness tensor α=c/ρ.

In an HTI medium, this leads to a system of equations, which, when solved, leads to the following equations for velocities (modified from Grechka's VTI coefficients, 2009a):

$$V_{\mathrm{P}}^2=\frac{1}{2\rho}\{F+\sqrt{[(c_{11}-c_{66})\cos^2\varphi-(c_{22}-c_{66})\sin^2\varphi]^2+4(c_{12}+c_{66})^2\cos^2\varphi\ \ \sin^2\varphi}\}$$

$$V_{\mathrm{S_prp}}^2=\frac{1}{2\rho}\{F-\sqrt{[(c_{11}-c_{66})\cos^2\varphi-(c_{22}-c_{66})\sin^2\varphi]^2+4(c_{12}+c_{66})^2\cos^2\varphi\ \ \sin^2\varphi}\}$$

$$V_{\mathrm{S_paral}}^2=\frac{1}{\rho}\left\{c_{66}\cos^2\varphi+c_{44}\sin^2\varphi\right\} \tag{3.17}$$

where

- *V_{s_prp} stands for the S-wave velocity, polarised in a plane normal to fractures, (Rüger, 1997) for which the particle movement with respect to fractures depends on the propagation direction;*
- *V_{s_paral} stands for the S-wave velocity, with particle movement within the fracture plane;*
- *$F = (c_{11} + c_{66}) \cos^2 \varphi + (c_{22} + c_{66}) \sin^2\varphi$;*
- *ρ is the rock density and φ represents the angle between the propagation direction and the isotropy axis.*

These equations are then used within a program that is used as a modelling tool. The program then takes account of the geometry and calculates the travel-time for a given source-receiver combination. Calculated travel-times can then be compared to the real measured travel-times.

3.2.2 Electrical modelling

Electrical resistivity measurements are done by injecting the current into the studied area between two electrodes and the potential difference is measured between two other electrodes. The potential distribution in any media is governed by Poisson's equation and mathematically given by:

$$\vec{\nabla}\cdot(\bar{\bar{\sigma}}(\vec{r})\vec{\nabla}U(\vec{r}))=I\,\delta(\vec{r}-\vec{r}_s),\quad \vec{r},\vec{r}_s\epsilon\,\Omega \tag{3.18}$$

where U is the potential, r and r_s are the position vectors for measuring point and source point, respectively, Ω is the domain, where the measurements are taking place, I is the current injected at position r_s, δ is the Kronecker delta function and σ is the conductivity tensor, dependent on the position:

$$\bar{\bar{\sigma}}(\vec{r})=\begin{pmatrix}\sigma_{xx} & \sigma_{xy} & \sigma_{xz}\\ \sigma_{xy} & \sigma_{yy} & \sigma_{yz}\\ \sigma_{xz} & \sigma_{yz} & \sigma_{zz}\end{pmatrix} \tag{3.19}$$

The matrix can be diagonalised to produce the three eigenvalues σ_1, σ_2, σ_3, which yield the principal conductivities in the directions of the three principal axes of the studied medium (e.g. Greenhalgh et al., 2009b):

$$\bar{\bar{\sigma}}'(\vec{r})=\begin{pmatrix}\sigma_1 & 0 & 0\\ 0 & \sigma_2 & 0\\ 0 & 0 & \sigma_3\end{pmatrix} \tag{3.20}$$

Modelling is conducted by simulating the geometry of the studied site, injecting the

nominal current and retrieving the calculated potentials at the positions of the potential electrodes.

For isotropic medium, the tensor (3.20) can be geometrically expressed as a sphere as all the principal conductivities are the same. Therefore the potential distribution (best expressed in equipotential surfaces) around a point source located in the medium has a form of a sphere. For injections at the surface of a medium, it has the form of a half-sphere. Therefore any planar representation of potential distribution, such as surface map of potential distribution around a point source, will have the form of a circle (half circle - e.g. for cross-section into the medium).

Within an anisotropic medium, the tensor (3.20) is geometrically expressed as an ellipsoid with three principal semi-axes of values equal to the inverse square roots of the principal conductivities (Greenhalgh et al., 2009a). Therefore the equipotential surfaces form also an ellipse with bigger semi-axis in the direction of higher conductivities. This shape has an effect on apparent conductivities / resistivities. For VTI media caused by layering of different beds, the conductivity along the layering (also called longitudinal) is higher than the conductivity across the layering (also called transversal). However, the apparent longitudinal conductivity appears to be lower than the apparent transversal conductivity. This is called the paradox of anisotropy.

The paradox of anisotropy is best observed on a surface measurement of vertically dipping beds (HTI medium), with higher longitudinal conductivity. In terms of resistivity (inverse of conductivity), the longitudinal resistivity ρ_L is lower, than the transversal resistivity ρ_T.

The equipotential surfaces for HTI media with direction of symmetry axis in x_1-direction are expressed by the equation for an ellipsoid:

$$\frac{x_1^2}{\frac{K}{\rho_T}}+\frac{x_2^2}{\frac{K}{\rho_L}}+\frac{x_3^2}{\frac{K}{\rho_L}}=1 \tag{3.21}$$

The analytical formula for potential in homogeneous transversally isotropic body is (modified from Greenhalgh et al., 2009b):

$$U(R,\Phi)=\frac{I\rho_m}{4\pi R(1+(\lambda^2-1)\cos^2(\Phi-\Phi_0))^{1/2}} \tag{3.22}$$

where R is the distance between measurement point and injection point, I is the current, Φ_0 is the zero azimuth, normal to layering and the angle, Φ is the observation angle from the source, ρ_m is the geometric mean resistivity, (also sometimes referred as the equivalent isotropic medium resistivity value, Wiese, 2012) defined as:

$$\rho_m=\sqrt{(\rho_L\cdot\rho_T)} \tag{3.23}$$

and λ is the coefficient of anisotropy defined as:

$$\lambda=\sqrt{\frac{\rho_T}{\rho_L}} \tag{3.24}$$

If the measurements are taken in the direction of layering Φ=90°, then the resulting potential, using the equation (3.22) is calculated as:

$$U(R,90)=\frac{I\rho_m}{4\pi R} \tag{3.25}$$

and the medium has the apparent longitudinal resistivity equal to ρ_m and not the real longitudinal resistivity. For the measurements taken in the direction perpendicular to the layering, the potential is again calculated using the equation (3.22):

$$U(R,0)=\frac{I\rho_m}{4\pi R\lambda}=\frac{I\rho_L}{4\pi R} \tag{3.26}$$

where the medium appears to have transversal resistivity equal to real longitudinal resistivity, which is lower than the apparent longitudinal resistivity.

The equation (3.22) is then used within a program to model the properties of medium. We were using a program called "3Dres_GQG" designed by Dr. Zhou from Adelaide University (Wiese et al., 2013), and we compared its forward modelling results (Fig. 3.5) with Comsol Multiphysics and results from analytical formulas (Fig. 3.7).

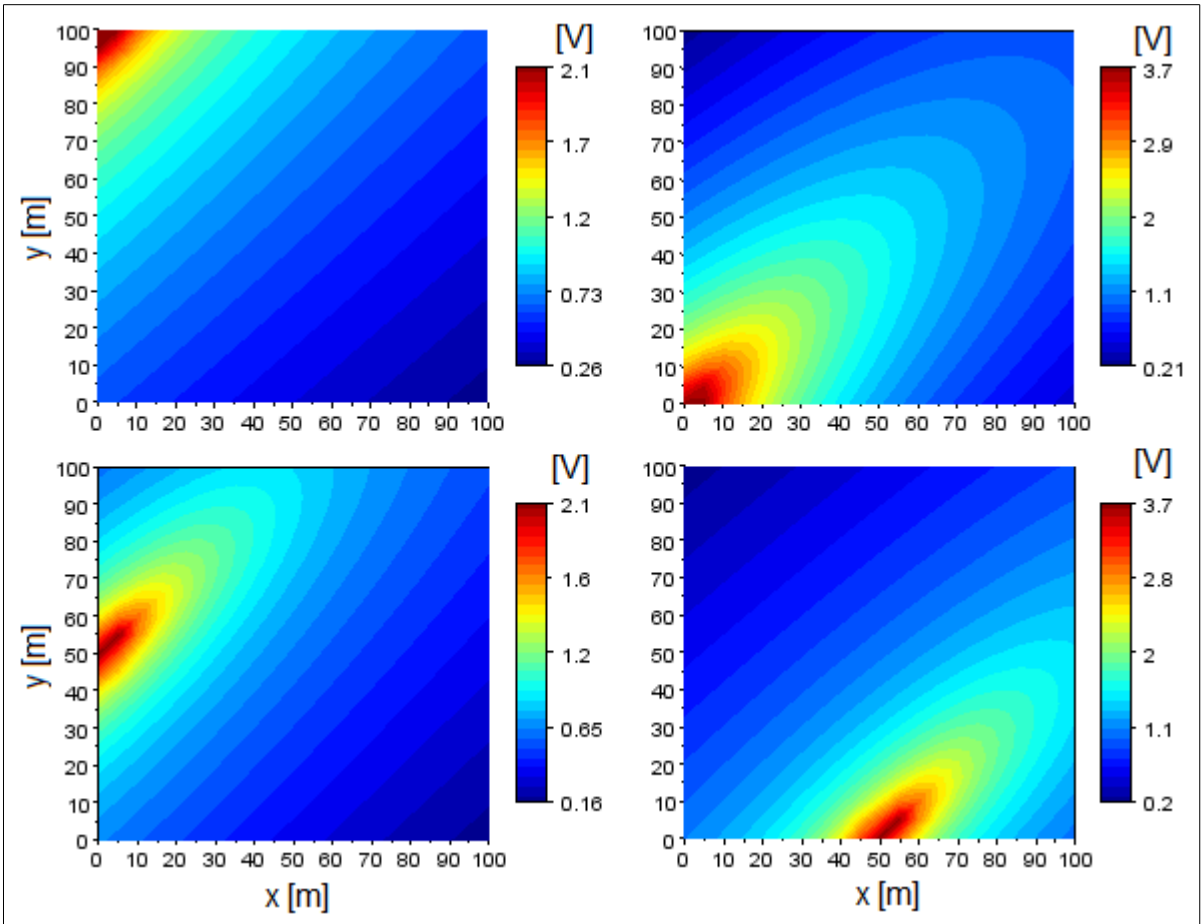

Fig. 3.5: Potential distribution (coming from 3Dres_QGQ) in a block of 100 x 100 m at four injection points (imposed nominal current) located at the maxima of potentials (red zone, with second current electrode in the infinite distance with negative nominal current) with transversal resistivity of 1000 Ω.m and longitudinal resistivity of 100 Ω.m and angle of rotation of anisotropy of Φ_0=-45° from the reference system (angle 0° is parallel to x-axis).

The modelling using Comsol Multiphysics program was done by simulating the injections inside a homogeneous block of dimensions 900 x 1400 x 800 m (width, length, height) with defined conductivity tensor and with nominal injections at specified points (Fig. 3.6). The distribution of potential on a studied grid was then exported and compared with the analytical formulas and the results from 3Dres_GQG (Fig. 3.7).

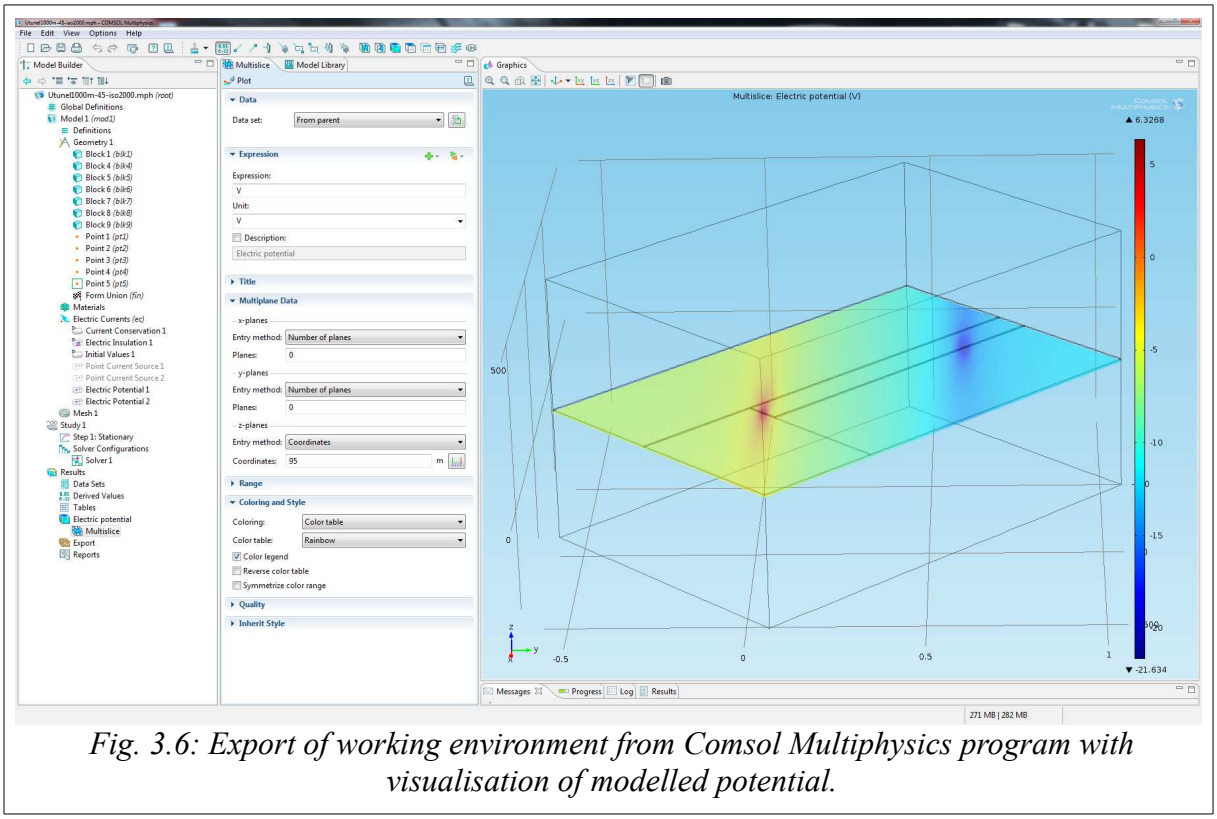

Fig. 3.6: Export of working environment from Comsol Multiphysics program with visualisation of modelled potential.

The figure (3.7) shows the comparison between the three forward programs used. We observed the same evolution of the potentials, however the potential from analytical formula was always smaller compared to the other methods by a constant value. We tested the forward calculation on several models and this behaviour was always the same with constant difference between the methods for offsets bigger than 25 m. We could therefore predict the real resistivity from the calculated. This would have a small effect on inversion

(consideration of this difference), but finally was not needed, because the real data was impossible to invert. The detailed steps of data treatment will be listed in the chapter dealing with methodology and results.

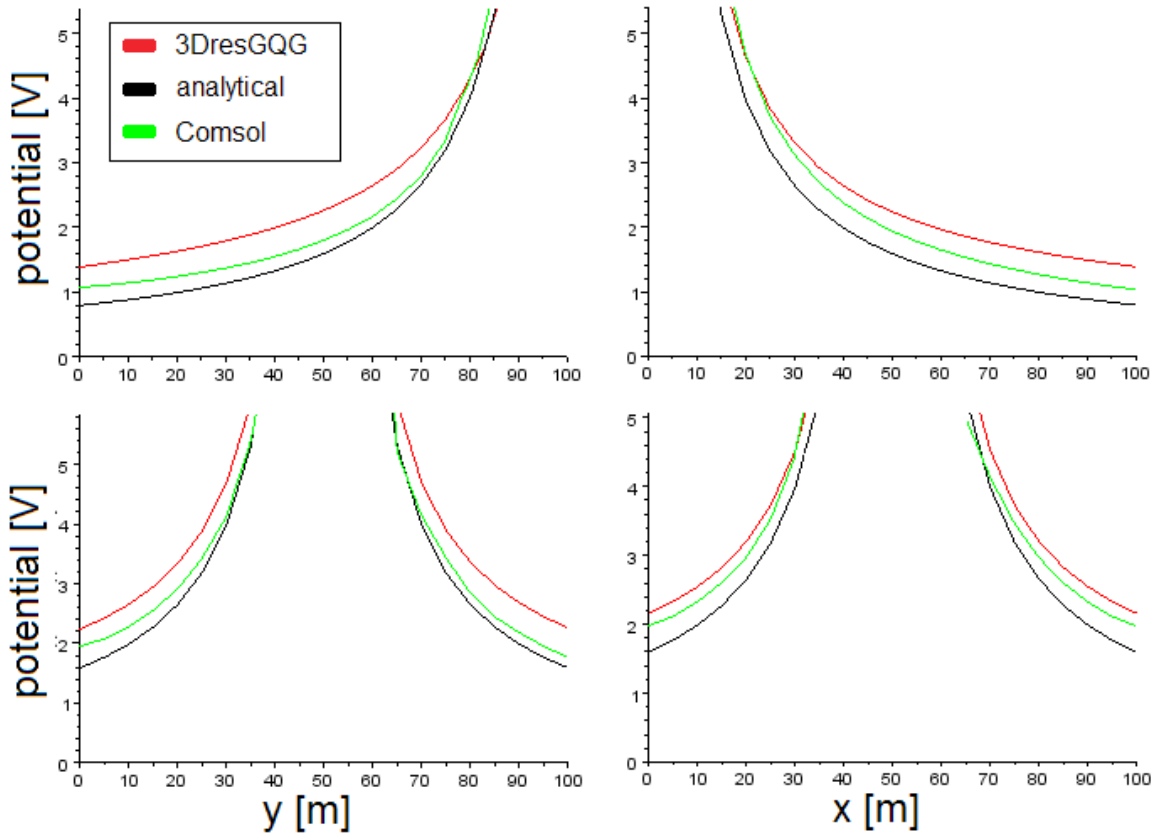

Fig. 3.7: Comparison of selected profiles for each of the four modelled injections from figure 3.5 (passing through the injection point), coming from three different forward calculations.

3.3 Inversion procedures and tomographic inversions

If the forward calculation is working, and gives satisfactory results, finding the correct combination of parameters that matches the measured data, in other words, reconstructing the properties of the medium, is the next step. To the two basic steps of the forward modelling: 1) calculation, 2) comparison, a third one is added: 3) updating the model

parameters. There are various methods how the update can be done:

- by incrementing each parameter and therefore eventually testing all possible combinations, which might me impossible due to the huge number of combinations

- by randomly testing combinations of parameters for a given number of iterations and then choosing the best combination

- by examining the sensitivity of each measured data with respect to parameter changes and updating the parameter towards the direction of expected better result.

All three steps are repeated until some condition of quality is fulfilled (e.g. sum of squared or absolute differences has reached a specified acceptable value) or number of iterations reached the maximum.

3.3.1 Linear problem

For a linear problem, the solution is found by the method of ordinary least squares (LSQ). The method is based on minimising the sum of squares of the residuals between the measured and calculated data (e.g. Menke, 1984):

$$L_2=\sqrt{\Sigma_{i=1}^{M}(\Delta d_i)^2}=\sqrt{\Sigma_{i=1}^{M}(d_m-d_c)_i^2}=\sqrt{\Sigma_{i=1}^{M}(d_m-F(\vec{p}))_i^2} \qquad (3.27)$$

where L_2 is the norm, that describes the squared residuals, Δd is the vector or residuals, d_m is the measured data vector of M values, d_c is the vector of calculated data, p is the vector of parameters used in the forward calculation and F is the forward operator.

The inversion process for a linear problem could be written in matrix equation form:

$$\vec{p}=\boldsymbol{G}^{-1}\vec{d}_m \qquad (3.28)$$

where G is the sensitivity matrix connecting the calculated data with the parameters. In the general case, G contains the partial derivatives of the forward operator F for all data with

respect to each parameter:

$$G_{ij}=\frac{\partial F_i}{\partial p_j} \quad (i=1,..,M\,;\, j=1,..,N) \tag{3.29}$$

where N is the total number of parameters.

To calculate the residuals, expressed in L_2-norm, in matrix form, eq. (3.27) becomes:

$$L_2^2=(\vec{d}_m-\boldsymbol{G}\cdot\vec{p})^T(\vec{d}_m-\boldsymbol{G}\cdot\vec{p}) \tag{3.30}$$

where T stands for transposed matrix. In order to minimise the norm:

$$\frac{L_2^2}{\partial\vec{p}}=\boldsymbol{G}^T(\vec{d}_m-\boldsymbol{G}\cdot\vec{p})=0 \tag{3.31}$$

needs to be found. The solution of equation 3.31 is:

$$\vec{p}^{\,est}=(\boldsymbol{G}^T\boldsymbol{G})^{-1}\boldsymbol{G}^T\vec{d}_m \tag{3.32}$$

where (-1) stands for inverse matrix and p^{est} is the estimated final set of parameters, best describing the measured data. If data have variable uncertainties, it can be used to assign different weights to the residuals. Equation (3.27) expressed with different weights then becomes:

$$L_2=\sqrt{\Sigma_{i=1}^{M}\frac{1}{\sigma_i^2}(d_m-F(\vec{p}))_i^2} \tag{3.33}$$

where σ represents the standard deviation, therefore the weight is the inverse of estimated or measured variance. In matrix form the equation (3.30) becomes:

$$L_2^2=(\vec{d}_m-\boldsymbol{G}\cdot\vec{p})^T\cdot C_D^{-1}\cdot(\vec{d}_m-\boldsymbol{G}\cdot\vec{p}) \tag{3.34}$$

where C_D is a data covariance matrix. It is a square diagonal matrix of dimension M where the variance of the i-th data point is stored in position C_{ii}.

The solution of a linear problem then becomes (modifying equation 3.32):

$$\vec{p}^{\,est} = (\boldsymbol{G}^T \cdot C_D^{-1} \cdot \boldsymbol{G})^{-1} \boldsymbol{G}^T \cdot C_D^{-1} \cdot \vec{d}_m \qquad (3.35)$$

The linearity of the problem means that there is only one best solution and the process of calculating the best solution is by nature convergent (provided the inverted matrix - in parentheses - is not singular).

3.3.2 Non-linear problem

The linear problem cannot be assumed in our case, because the forward operator F is non-linear. Therefore we need to be solving a non-linear problem. For a non-linear problem, as opposed to the linear problem, there might be not only one solution to minimising the L_2, the process cannot be solved by simple inversion of matrix (G^TG) and therefore needs to be solved by a series of iterations.

3.3.2.1 Method of the Non Linear Least Squares (NLLSQ)

The non-linear problem can be solved iteratively by updating the parameter vector p and by decomposing the forward problem into a Taylor series:

$$\vec{d}_{c(k+1)} = F(\vec{p}_k + \Delta\vec{p}) = F(\vec{p}_k) + \frac{\partial F(\vec{p}_k)}{\partial \vec{p}} \Delta\vec{p} + \ldots \approx F(\vec{p}_k) + \boldsymbol{G}\,\Delta\vec{p} \qquad (3.36)$$

where k is the k-th iteration, Δp is the increment of the parameter vector between iteration k and k+1 and G is the sensitivity matrix, showing the perturbation of a measured quantity with respect to a unity perturbation of the modelled properties of the medium (e.g. Menke, 1984).

By neglecting the higher order terms of the Taylor decomposition of equation (3.28), the problem is linearized. The aim of the inversion is to minimise the residuals between d_m and

$d_{c(k+1)}$, therefore equation (3.27) becomes:

$$L_2 = \sqrt{\Sigma_{i=1}^{M} (d_m - F(\vec{p}_k) - \boldsymbol{G}\,\Delta p)_i} \qquad (3.37).$$

The solution of linearised problem can then be found by solving:

$$\vec{p}^{\,est}_{(k+1)} = \vec{p}^{\,est}_{(k)} + (\boldsymbol{G}^T \cdot C_D^{-1} \cdot \boldsymbol{G})^{-1} \boldsymbol{G}^T \cdot C_D^{-1} \cdot (\vec{d}_m - F(\vec{p}_k)) \qquad (3.38)$$

The weighed solution of the non-linear problem by the series of approximations has the form:

$$\vec{p}^{\,est}_{(k+1)} = \vec{p}^{\,est}_{(k)} + (\boldsymbol{G}^T \cdot C_D^{-1} \cdot \boldsymbol{G} + \gamma\, C_P^{-1})^{-1} \cdot [\boldsymbol{G}^T \cdot C_D^{-1} \cdot (\vec{d}_m - \vec{d}_{c(k)}) + \gamma\, C_P^{-1} \cdot (\vec{p}^{\,est}_{(k)} - \vec{p}_0)] \quad (3.39)$$

where matrix C_P^{-1} stands for the inverse of the covariance matrix of parameters, dependent on a priori information. This matrix is squared diagonal with dimension equal to the number of parameters N. γ represents the damping factor that determines the trade off between the data fit and a priori information.

Usually if the a priori information does not exist, the p_0 is updated to $p_{(k)}^{est}$ and the last term disappears, leaving:

$$\vec{p}^{\,est}_{(k+1)} = \vec{p}^{\,est}_{(k)} + (\boldsymbol{G}^T \cdot C_D^{-1} \cdot \boldsymbol{G} + \gamma C_P^{-1})^{-1} \cdot [\boldsymbol{G}^T \cdot C_D^{-1} \cdot (\vec{d}_m - \vec{d}_{c(k)})] \qquad (3.40)$$

3.3.2.2 Gradient methods

The LSQ algorithms might not be the fastest and the search for the minimum of a misfit function can be done by other more sophisticated methods. The mostly used algorithms are the gradient algorithms. The gradient algorithms are based on the fact that the misfit function has a global minimum at the correct set of parameters and therefore in their vicinity the misfit function has a slope. This is easy to imagine in the case, where the interpreter is looking for two parameters (Fig. 3.8, central depression is where the best solution is). There are several variations of gradient methods; such as e.g. conjugate gradient, steepest descent

method, etc. They might differ in the way the parameter perturbations are calculated and in the speed of convergence towards the best solution. Problems with gradient methods could arise, when the starting model is not near the best solution, but near another partial solution, expressed as a local minimum in the misfit function (as in figure 3.8 on the right side), and the algorithm might end up in the wrong local minimum.

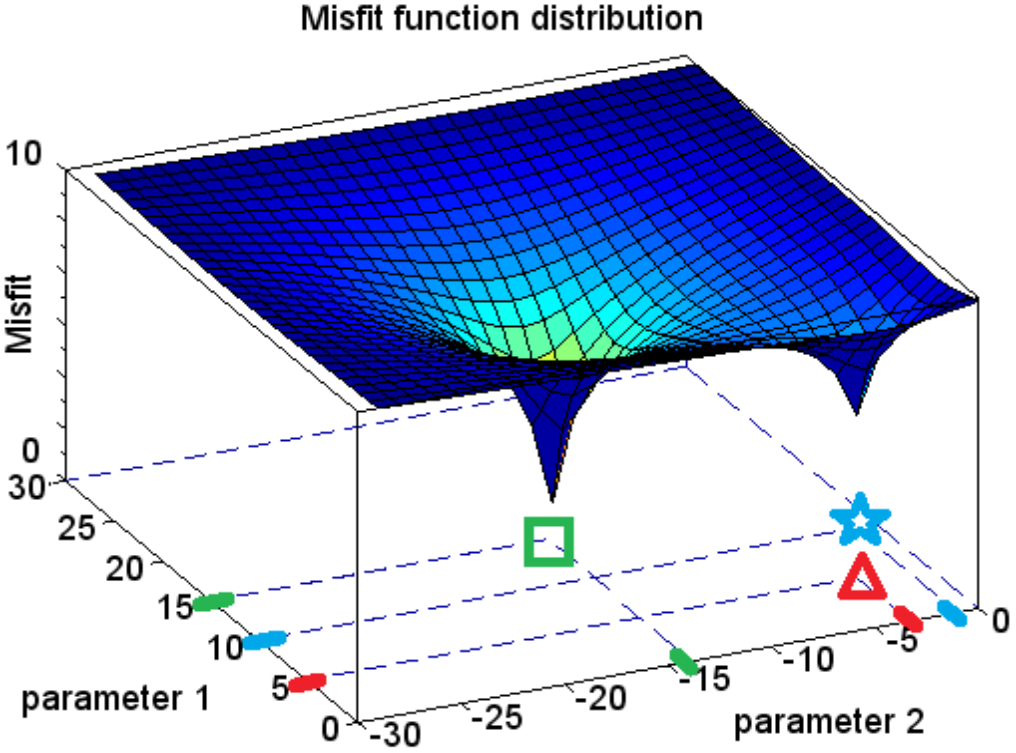

Fig. 3.8: Example of a misfit function for two parameters (on the axes). The global minimum in placed in the centre of the searched parameter boundaries (green square). The local minimum on the right side (red triangle) may attract the inversion process if the starting points for the inversion is located at wrong place (indicated with a blue star). In this case, the result would be at wrong combination of parameters 1 and 2.

3.3.2.3 *Monte-Carlo algorithms*

Another widely used algorithm is based on stochastic processes and therefore it is called Monte-Carlo. The forward modelling is done with a set of initial parameters. The difference between the modelled and calculated data is computed as for the LSQ method. In the next

step, the parameters are modified in a predefined model space and the difference is computed again. If this new difference is better (smaller) than the previous one, it means that the new set of parameters was closer to the solution (or to a local minimum). The model is accepted into the assemblage of results, and the next iteration is started. If the new misfit it is not better, it still could be accepted with a certain probability, thus creating the opportunity to leave a local minimum and 'climb' the slope of the misfit function and later be able to find the global minimum (Fig. 3.8). If this worse misfit is not accepted, the previous model is integrated into the assemblage of results and next iteration is started.

This scheme of updating of parameters is called Markov chain as the next update depends only on the current state and does not retain any memory of previous iterations. After the last iteration, the assemblage of results is searched for the best misfit, in the case the last solution ended up near a local minimum.

3.3.3 Seismic inversion

Testing and inverting a homogeneous block with only 5 parameters is a simple task. However, introducing heterogeneities into the model requires the use of tomographic inversion. The tomography program that we used for seismic data is called '3Dray_gTI0' written by Zhou and Greenhalgh (2008) and will be described in more detail in the next chapter. As explained in the modelling part, it has become a good practice in all natural sciences to compare the measured data with data coming from models of known properties. The validation of the program was achieved by forward modelling, and also by inverting synthetic datasets. In the synthetic case, the scientist knows both measured and modelled data.

The inversion algorithm should reconstruct the values of the synthetic model. As a first step a simple forward problem is calculated. The results of this forward calculation are used as if they would come from a measuring campaign. Errors are usually added to the synthetic model in order to simulate the real acquisition. In the next step, the inversion process is started, where initially only one parameter is allowed to update at a time before doing a full inversion of all parameters together in order to test all parts of the inversion algorithm.

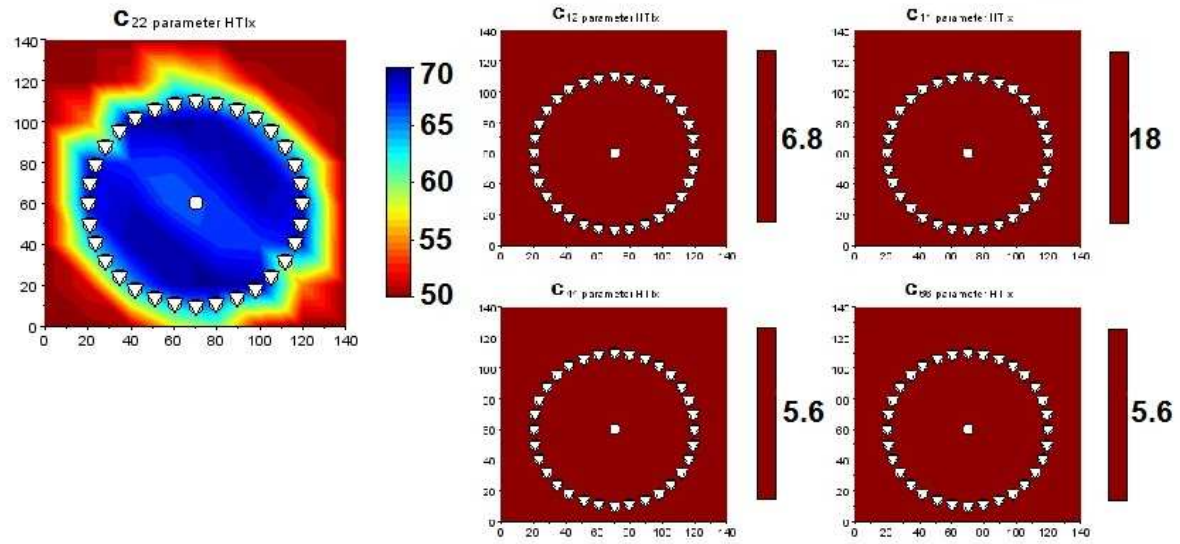

Fig. 3.9: Example of a step in a process of validation of inversion by allowing to update only one parameter c_{22}, with other parameters fixed. Figure shows the result after the inversion. The parameter c_{22} was inverted, the remainder of parameters (c_{12}=6.8, c_{11}=18, c_{44}=c_{66}=5.6) were unchanged (the brown plots of starting parameters). Note that the inside of the circle contains the updated, correctly found values of the parameter, while at the rims, with no travel-time data, the input parameters stayed unchanged.

For example purpose, this is explained on one parameter and is done in the following way: a travel-time dataset is created coming from a model with value for c_{22} = 67.5, (fast velocity $v=(c_{22}/\rho)^{-1/2}$=5.2 km.s^{-1} , see equations 3.17 for P-wave with density ρ=2500 kg.m^{-3}). The values of other parameters are not important for this step. Next, the inversion procedure is started with a value of c_{22} = 50 and only this parameter is allowed to update during the inversion. At the end of the inversion process, the initial value of 50 remains unchanged for

the rims outside of the circle (no passing rays) whereas the inside of the circle contains the correctly inverted values (Fig. 3.9). In another test, the initial parameter is set to be higher than the synthetic value and a similar result is observed (not shown here). This time, the outside of the circle contains the unchanged higher values of the initial parameter and the inside of the circle has correctly inverted values.

Seeing that the parameter on its own is reacting according to expectation, led to testing all of the parameters which were tested separately and also together. The validation of the inversion program was successful, because the synthetic properties were inverted correctly from the synthetic data.

If the model is more complicated and many heterogeneities are inverted from the synthetic data, it is possible, to apply some additional operations such as applying regularisation filters, smoothing filters, introducing a priori information about the studied area (minimum or maximum velocities, zones of known velocities, etc.). Treatment of the real data is presented in the chapter dealing with methodology and results.

3.3.4 Electrical resistivity inversion

The same procedure as for seismic inversions applies for the electrical resistivity inversions. Although, the used program 3Dres_GQG did work well for forward modelling, it failed to invert the synthetic data properly.

We tried to model with different ratios between the longitudinal and transversal resistivities of one order of magnitude (100 and 1000 Ω.m, respectively) and also with higher ratios (e.g. 100 and 10.000 Ω.m), with different starting models, but the parameters were not updated correctly.

Due to a lack of time it was not possible to build a successful inversion, and even though

the authors of the program did supply us with some of their models, we were unable to follow their results. Possible reason for this failure might be due to the use of different compilers for the program creation from the source code. We tested the compilation under Windows 7 with Microsoft Visual Studio, using the Intel compiler and under Linux Ubuntu 12.04 with Eclipse IDE using GNU Fortran compiler and did not succeed building a working inversion program.

3.4 Fracture characterisation

In the case where the fractures are the reason for anisotropy, attempts have been made to quantify them in terms of spatial distribution, volume and fluid saturation. The characterisation derived from the linear slip theory by Schoenberg (1980) is based on added weakness (compliance) of the fractures to the compliance (inverse of stiffness) of the background medium. The TI medium is modelled by compliance of isotropic background rock with compliance tensor $\mathbf{s}_b = \mathbf{c}^{-1}$ and the effect of one set of coplanar fractures, expressed by the compliance tensor $\mathbf{s}_f$. For vertically oriented fractures with normals in x_1-direction (HTI medium), with the assumption of purely isotropic micro-structure on the surface of the fractures and no interaction between the stresses and shear strains, $\mathbf{s}_f$ has the form:

$$\boldsymbol{s}_f = \begin{pmatrix} K_N & 0 & 0 & 0 & 0 & 0 \\ 0 & 0 & 0 & 0 & 0 & 0 \\ 0 & 0 & 0 & 0 & 0 & 0 \\ 0 & 0 & 0 & 0 & 0 & 0 \\ 0 & 0 & 0 & 0 & K_V & 0 \\ 0 & 0 & 0 & 0 & 0 & K_H \end{pmatrix} \tag{3.41}$$

where K_N has the physical meaning of normal compliance, K_V and K_H are the tangential compliances added by the fractures to the host rock (also called K_T).

For Hudson's penny-shaped fractures (1980), using some predefined dimensionless

quantities, dependent on the boundary conditions on the crack faces, infill parameters, possible interaction of cracks and some other factors, the compliance (stiffness) tensor has the same form as the one resulting from linear slip theory (Bakulin et al., 2000a).

Hsu and Schoenberg (1993) introduced dimensionless quantities Δ_N and Δ_T called normal and tangential weaknesses (Bakulin et al., 2000a):

$$\Delta_N = \frac{(\lambda + 2\mu) K_N}{1 + (\lambda + 2\mu) K_N} \tag{3.42}$$

$$\Delta_T = \frac{\mu K_T}{1 + \mu K_T} \tag{3.43}$$

where λ and μ are the Lamé coefficients.

The fracture characterisation might be done using ratio K_N/K_T alone (Schoenberg and Sayers, 1995). For dry cracks this ratio approaches unity, for fluid filled cracks it almost vanishes.

Alternatively, the characterisation might be done using the weaknesses. For dry (gas-filled) fractures they are expressed as:

$$\Delta_N = \frac{4e}{3g(1-g)} \tag{3.44}$$

$$\Delta_T = \frac{16e}{3(3-2g)} \tag{3.45},$$

and for fluid-filled fractures:

$$\Delta_N = 0 \tag{3.46}$$

$$\Delta_T = \frac{16e}{3(3-2g)} \tag{3.47},$$

where e is the crack density (number of cracks per unit volume) and $g = V_S^2/V_P^2$ (V_S and

V_P are velocities of P- and S-waves of the isotropic background medium).

For an orthorhombic medium, there are two approaches how to characterise the fractures. In the first one, the host rock might be simulated by an isotropic medium with two perpendicular fracture sets. Each fracture set is then characterised separately as it would create a TI medium. In the second case, it is simulated by a VTI medium with one set of vertical fractures. The properties of a VTI medium and fracture weaknesses are calculated. Estimates of the fractures can vary slightly between these two approaches. In addition, both approaches are based on the assumption of weak anisotropy and might therefore prove ineffective for strongly anisotropic media.

To our knowledge, there have been no attempts to quantify the fractures by means of electrical resistivity data. The azimuthal resistivity surveys can serve only qualitatively to assess the number of fracture sets by inspecting the polar representations. A simple ellipse represents one fracture set with the fractures oriented in the direction of the longer semi-axis. Deformed ellipse, with additional peaks represents fracture sets oriented in the azimuth of the peaks (Fig. 3.10).

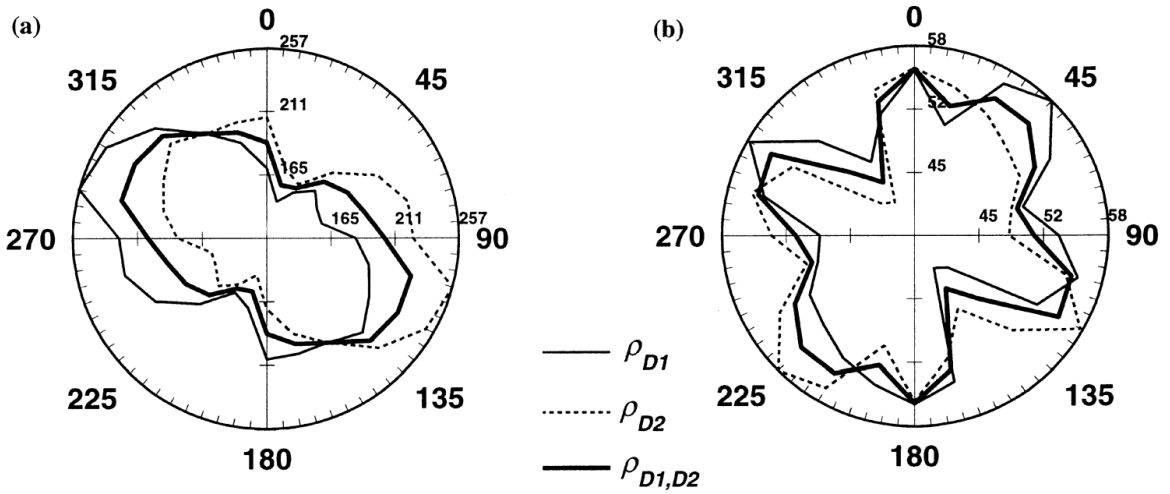

Fig. 3.10: Polar representations of azimuthal apparent resistivity surveys after removal of the datum for better distinction of the peaks. A) single-peaked ellipse with orientation of fractures in azimuth 120° and B) multiple-peaked ellipse indicating possible direction of two fracture sets in direction 10-20° and 120°. Alternatively depending on interpretation, three fracture sets in directions 0°, 45° and 120°. ρ_{D1} and ρ_{D2} represent measurements with different Wenner offsets. $\rho_{D1,D2}$ is the combination of the two (Busby, 2000).

4 Methodology and results

The following sub-chapters describe the work flow that has been conducted on real data collected in the LSBB.

4.1 Seismics – Real data

In 2005, seismic data were collected in the two sub-parallel sub-horizontal galleries. The aim was to examine the massif between the two galleries like a cross-hole tomography. When the data was first treated, one could distinguish two branches in the travel-time-offset graph of P-wave arrival times (Fig. 4.1) that turned out to be due to seismic anisotropy.

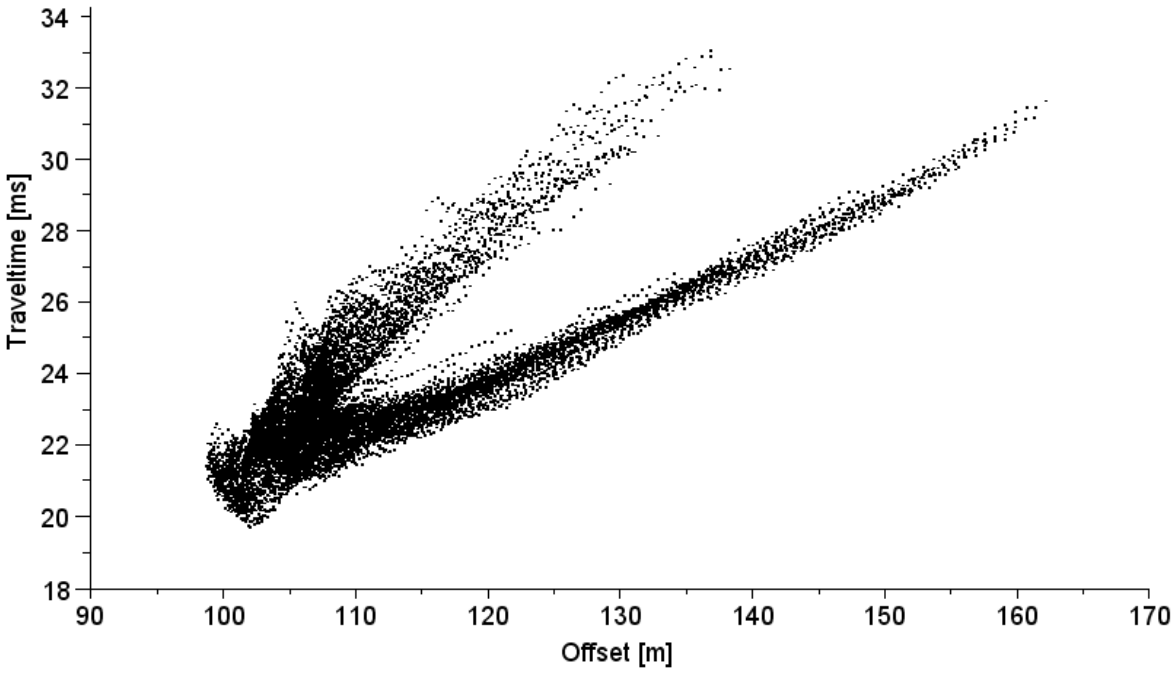

Fig. 4.1: Travel-time vs. offset for first campaign in May 2005.

4.1.1 Geometry – Equipment

Altogether, we were treating the data from four campaigns: May 2005, June 2011, July 2012 and December 2012.

To facilitate the orientation in our model, we constructed a local coordinate reference system in the studied area based on the direction of the galleries (Fig. 4.2). The x-axis corresponds to the direction of the TG and the y-axis corresponds to the ABG. The origin of the reference system was chosen to be in the corner where the ABG and TG meet. The zero azimuth in this reference system is therefore parallel to TG, oriented from ABG to the MG. The azimuth of +90° is the direction from the origin into the ABG.

In 2005, the data was collected in the first 120 m of the ABG and MG galleries. In this configuration, the central area between the two galleries was 'illuminated' by rays with an aperture of around 100°, from around -50° to +50°. Other areas, such as the corners between

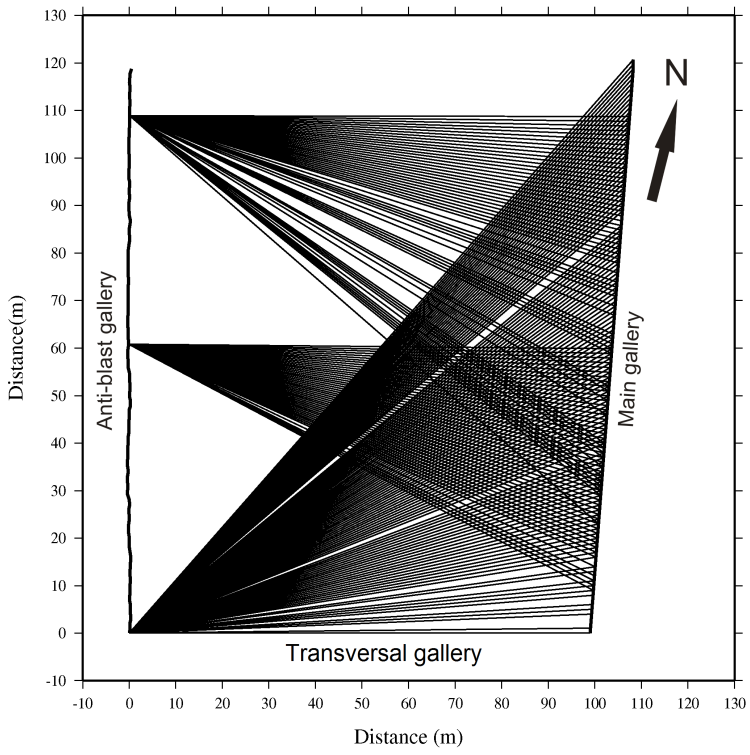

Fig. 4.2: Example of rays coming from 3 shots performed in the ABG, recorded in the MG conducted in May 2005. Missing rays are due to noise at the corresponding receiver.

the TG and ABG had an aperture of only around 50°, from 0° to around 50° (Fig. 4.3a). Because of the limitations of acquisition geometry, the 'illumination' of the massif cannot be homogeneous. It would be ideal if the whole block between the two sub-parallel galleries were surrounded by shot-receiver combinations. However, this is not possible, unless an additional tunnel is drilled that would connect ABG and MG some 100 m from their beginnings.

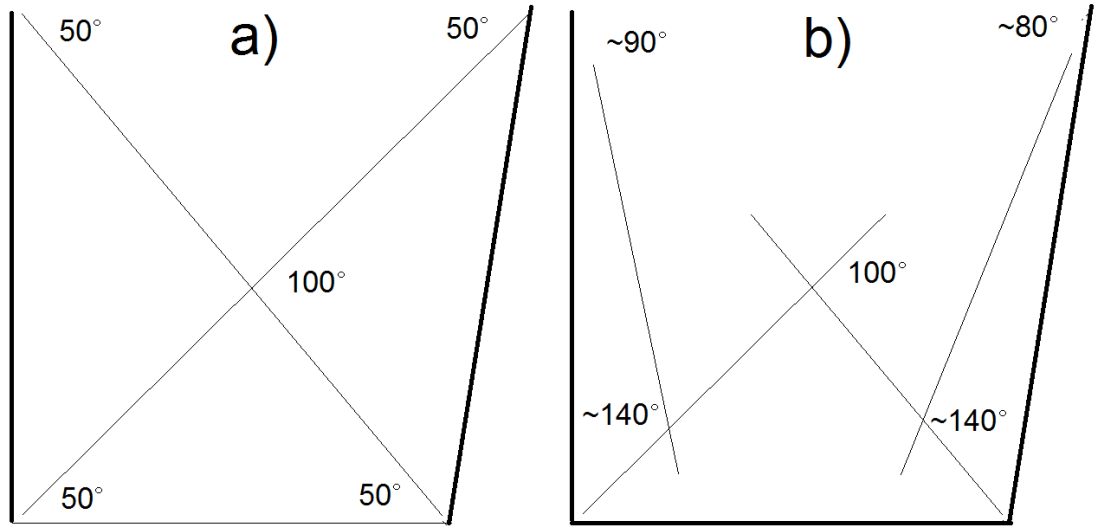

Fig. 4.3: Visualization of angle coverage before additional shots in TG, coming from a) only the shots from the sub-parallel galleries ABG and MG in May 2005, and angle coverage b) with additional shots in TG. The lines represent samples of shot-receiver couples and the angles at the chosen locations

Therefore, the only possible option to help increasing the angle coverage is to add shots in the TG. During the repeated measurements conducted in 2011, additional shots were executed in the TG. In this way at least the borders of the block profited from better illumination (Fig. 4.3b). The setting with additional shots in TG was kept for both campaigns in 2012.

For the seismic acquisition, geophones of 50 Hz were used, with Summit seismic

acquisition system from DMT. In 2005, the geophones were mounted on the walls recording only the horizontal movement perpendicular to the wall. Since we had no access to three-component geophones, in 2011, single-component geophones were placed in a way that simulated three component geophones. They were mounted in groups of three. The main interest for that was the attempt to quantify the S-wave splitting. However, because of the inhomogeneities and excessive noise at distances above 50 m, the splitting was not observed and for the measurements in 2012, again single-component geophones in direction normal to the walls was used. Despite the fact that this installation should not be sensitive to all waves, coming from all different directions (S-wave coming from the direction perpendicular to the wall, and P-wave coming along the wall), the first arrival times are visible for all wave types for all measurements. The source for the signal was a blow of 4 kg hammer.

A summary of all campaigns in terms of geometry of acquisition is given in table 4.1. An example of a record section is shown in figure 4.4, examples of different campaigns from the same shot points are shown in the annex.

Table 4.1: Summary of acquisition geometries for each campaign.

acquisition date	receiver positions	rec. spacing [m]	total distance [m]	shot positions	shot spacing [m]	total distance [m]	stack
May 2005	ABG	1	120	MG	1	122	1
	MG	1	120	ABG	1	122	1
June 2011	ABG	1 (4)*	90	MG, TG	1	122 + 99	1
	MG	1 (4)*	90	ABG, TG	1	122 + 99	1
July 2012	ABG	2	80	MG, TG	1	120 + 99	1 , 4
	MG	2	78	TG	1	99	1 , 2 , 4
Dec. 2012	ABG	2	80	MG, TG	1	100 + 99	1 , 4
	MG	2	80	TG	1	99	1 – 4

** represents the experimental mounting of geophones, alternating between each component (vertical, perpendicular to wall, parallel, 1 m no geophone).*

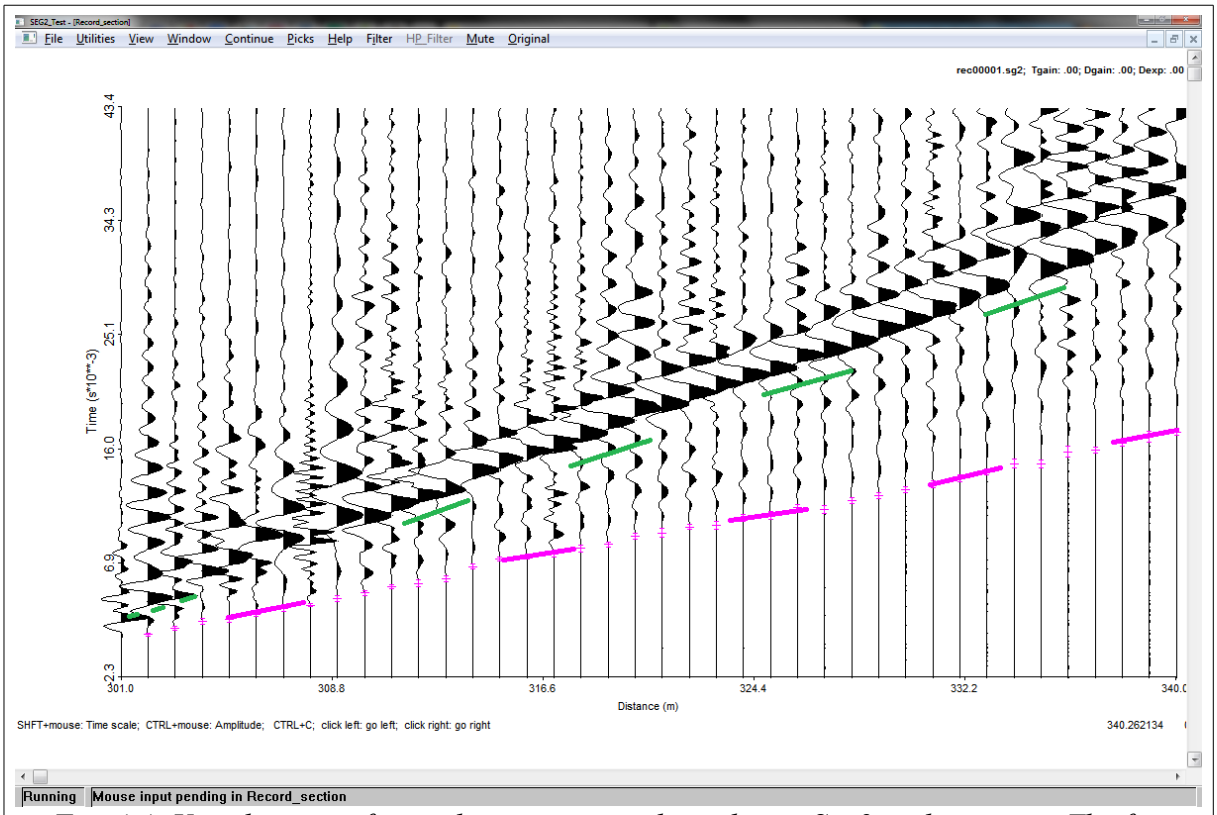

Fig. 4.4: Visualization of record section using the in-house Seg2read program. The first arrivals of P-waves are recorded with pink picks, allowing also the interpreter to choose the uncertainty of his/her pick. The green dashed line represents the onset of the S-waves (not picked in this figure. (The horizontal axis: receiver position number, vertical axis: travel-time (ms).

4.1.2 Isotropic cross hole tomography

Fig. 4.11 shows all measured P-wave and S_{paral}-wave arrival times from May 2005 as function of offset. For an isotropic and homogeneous velocity distribution, one should expect all points lying on a straight line. The scatter of the arrival times shows that the rocks must be inhomogeneous in the area. As a first step, we did standard isotropic cross-hole tomography using the code pstomo_eq (Tryggvason and Linde, 2006). Since the galleries are

not parallel and do not have the same slope, we had to use a 3-D program that takes the real geometry into consideration. The resulting model (Fig. 4.5) explains the data well with a standard deviation of 0.29 ms, however, it shows clear artefacts (red ellipse areas), especially in the NE and SW corners, where velocities are unrealistically high for limestones (e.g. Fournier et al., 2011; Jeanne et al., 2012). This result can be explained by the fact that rays travelling in SW-NE direction have smaller travel-times than those travelling in NW-SE direction. The tomographic inversion algorithm gives realistic velocities in the centre, where the ray density is highest (Fig. 4.6). However, it tries to compensate the travel time differences in the areas that are less well constrained due to smaller ray density. This result indicates presence of anisotropy. It is well known that P-wave travel-times corresponding to an anisotropic medium may be explained also by a more complicated isotropic velocity distribution, but the resulting velocities are then usually not geologically meaningful (e.g. Grechka, 2009a). Also the two well distinguished branches in figure 4.11 indicating two different velocities can be explained by anisotropy.

Similar results and conclusions were drawn by Neau (2005) who treated the data with isotropic tomography and attempted the first anisotropic inversions.

Subsequent datasets from 2011 and 2012 were not treated with the isotropic inversion any more, as they would not provide any additional useful information.

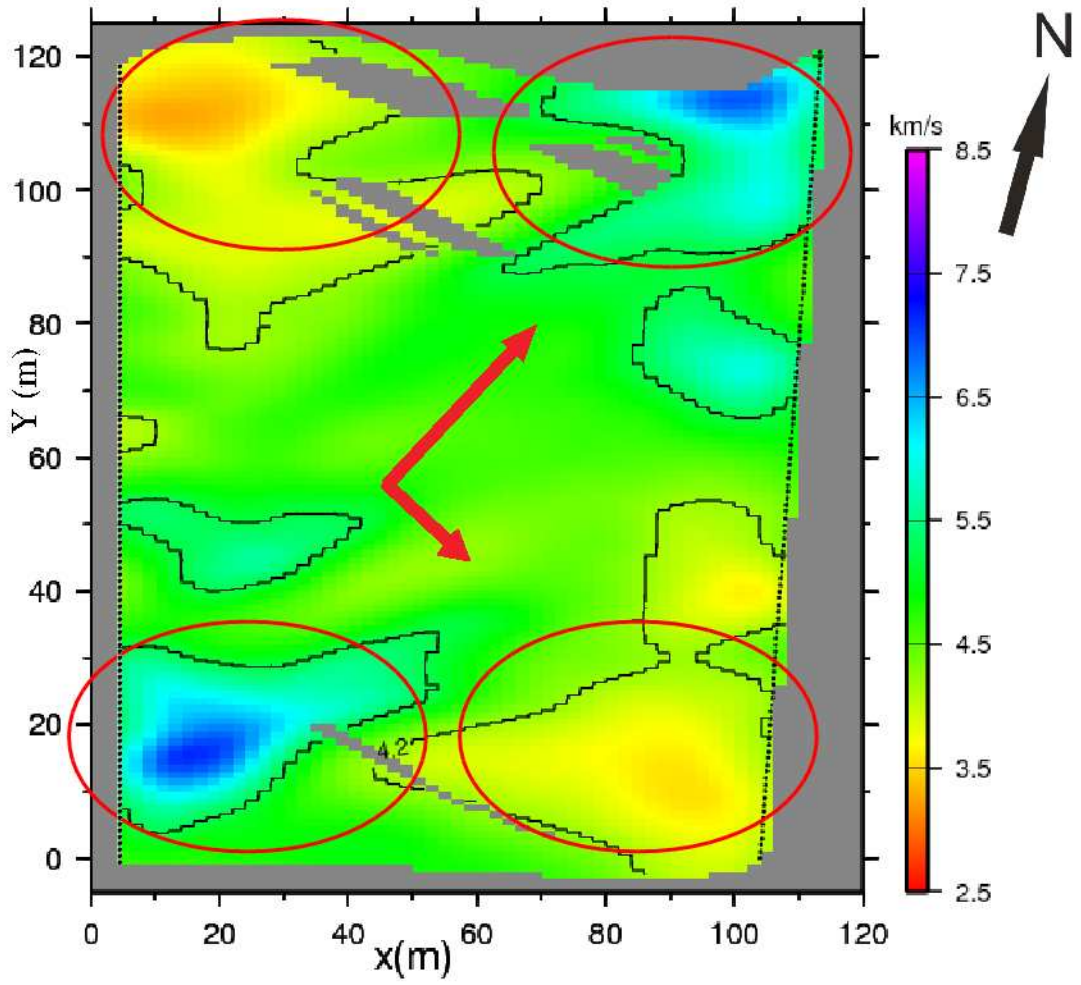

Fig. 4.5: P-wave velocity distribution obtained from 3-D isotropic cross-hole tomography using the real field geometry - cross section in the plane of the galleries. The very high velocities in the upper right and lower left corners and the low velocities in the opposite corners are artefacts due to neglecting anisotropy. The black dots correspond to the positions of shots (left) and receivers (right). Long red arrow: direction of high velocity, short red arrow: direction of low velocity obtained from cosine fit described later.

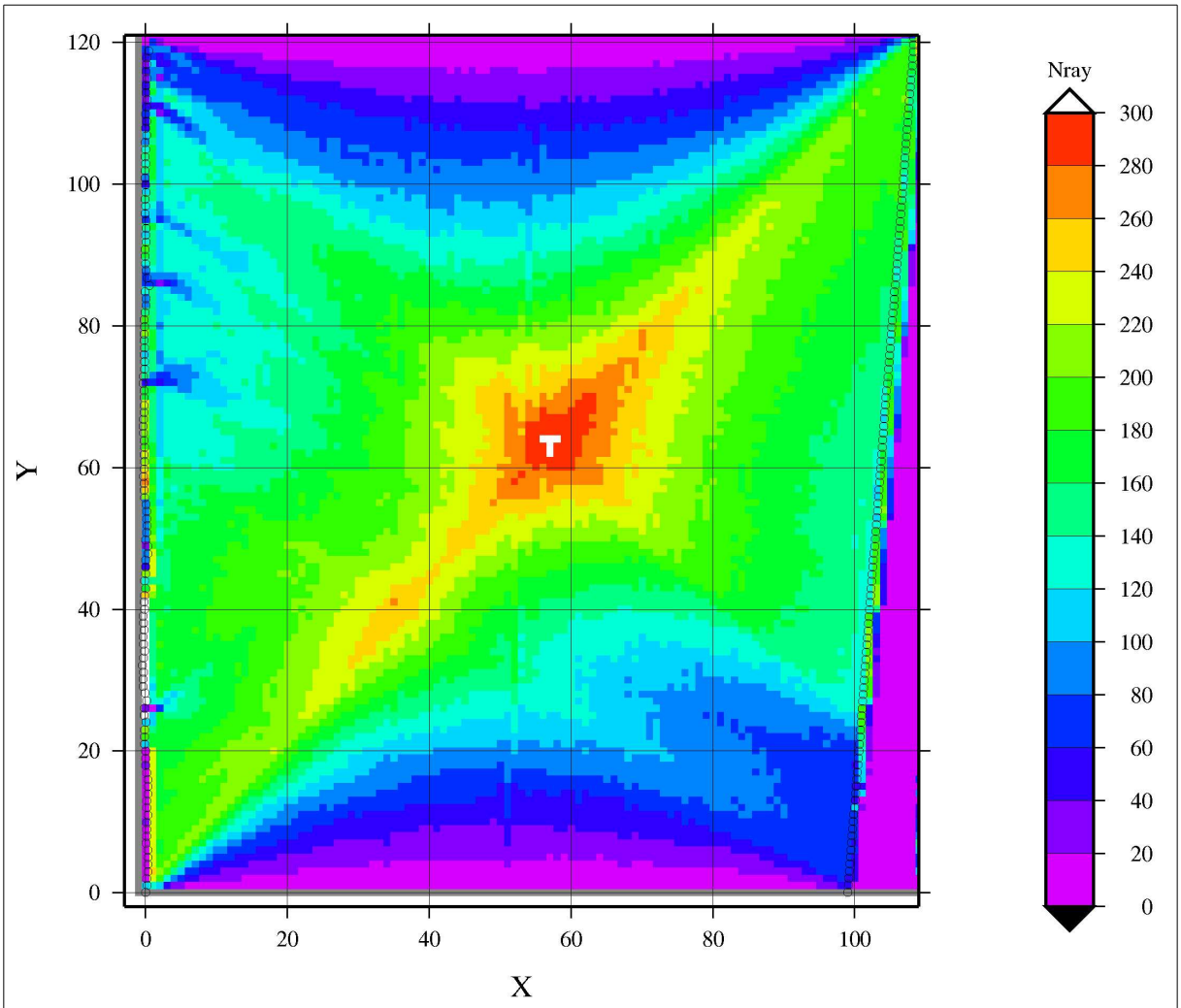

Fig. 4.6: Ray coverage for isotropic tomography. Nray represents density of rays per m²

4.1.3 Approximative cosine fit function

As a first test of anisotropy, we fitted the observed travel-times to a simple cosine function assuming seismically homogeneous material (i.e. straight rays):

$$t(d,\phi)=\frac{d}{v_0+dv\cdot\cos[2(\phi-\phi_0+90)]} \qquad (4.1)$$

where t is the travel time [ms], d – the offset [m], ϕ – the angle of ray departure (ϕ=0 is perpendicular to the wall of the ABG), v_0 – the average velocity [km/s], dv – the amplitude of anisotropy [km/s] and ϕ_0 – the low velocity direction with respect to the direction perpendicular to the ABG. The 90° shift the minimum velocity to angle ϕ_0, as the cosine function has there the maximum value.

The cosine fit can be used only as a first approximation. It is valid only for fast S_{paral}-waves (polarised parallel to the isotropic plane) and only for a perfectly elliptic phase velocity function of P-waves. As the combination of stiffness parameters for perfectly elliptic P-waves is rare, the majority of combinations will be non-elliptic.

The resulting best fitting parameters for P- and S_{paral} -waves are given in table 4.2. The overall data misfit (fourth column in Tab. 4.2 for each year) corresponds to 60% travel time variance reduction with respect to the best fitting isotropic model and >99% with respect to the measured data. We also calculated the average velocity for all rays departing within bins of 5° and plotted these data for P- and S-waves of all years as function of departure angle (Figs. 4.7 to 4.10) together with the best fitting cosine approximations. Slightly bigger uncertainty bars for the year 2011, especially for the S-waves are due to a different experimental mounting of the geophones on the walls which produced some additional noise due to geophone vibrations after the first arrival. Also the bigger σ in the table 4.2 reflects this fact.

Table 4.2: Summary of best fitting parameters for simple cosine fit.

Wave type	May 2005				June 2011			
	v_0 [km/s]	dv [km/s]	ϕ_0 [°]	σ [ms]	v_0 [km/s]	dv [km/s]	ϕ_0 [°]	σ [ms]
P	4.69	0.46	- 47 †	0.55	4.68	0.51	- 49	0.91
S_{paral}	2.61	0.17	- 47	0.98	2.57	0.15	- 64	2.01
	July 2012				December 2012			
P	4.72	0.24	- 46	0.59	4.89	0.3	- 38	0.54
S_{paral}	2.51	0.08	- 67	1.34	2.52	0.10	- 37	1.62

- † 0° in reference system represents N15°W in absolute coordinates (NNW)

where σ represents the standard deviation calculated as:

$$\sigma = \sqrt{\frac{1}{N-1} \Sigma_{i=1}^{N} \left(t_{calc} - t_{meas} \right)^2} \qquad (4.2)$$

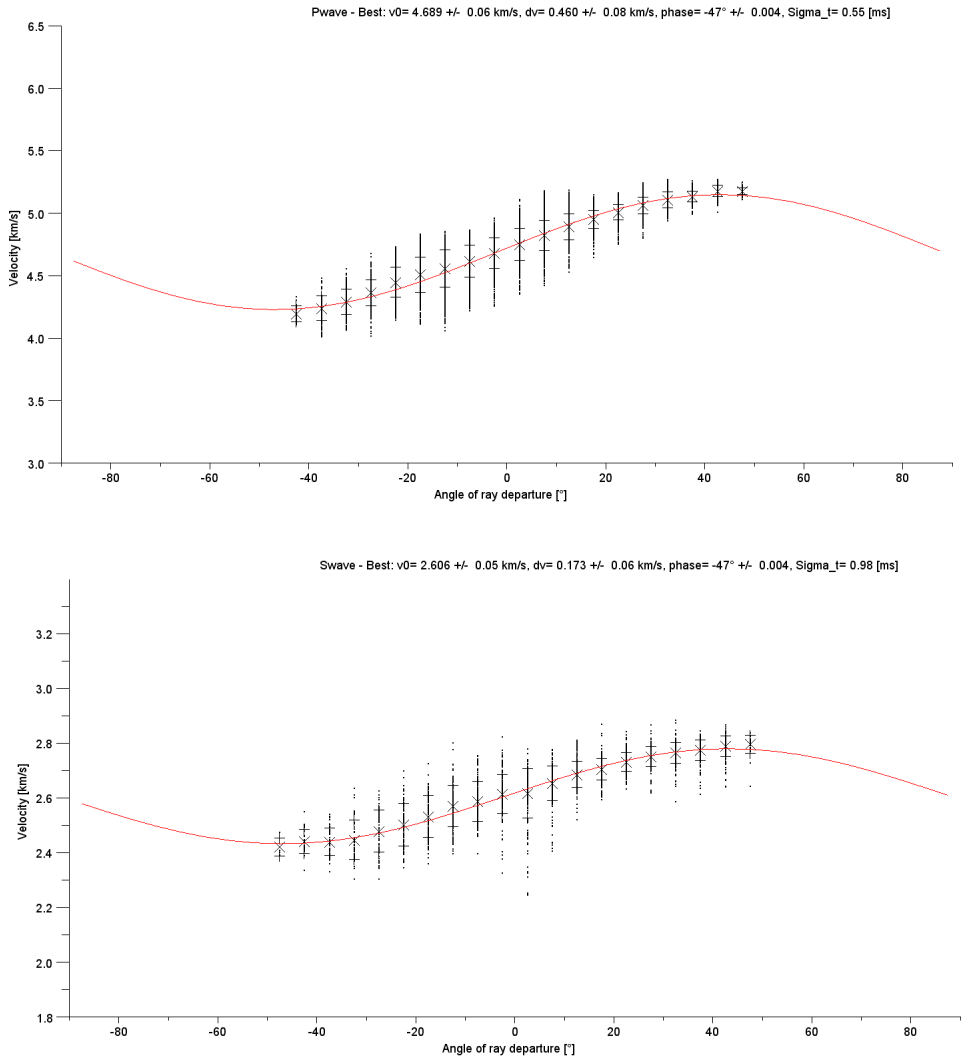

Fig. 4.7: May 2005. Velocities for all rays departing from the shot points within a range of angles of +/- 2.5° (dots), along with averaged velocities (X), standard deviation of averaged velocities (error bars) and with optimum velocity adjustments from cosine fit function (red curve - title of each graph contains the information about the equation of the curve). 0° departure corresponds to the direction perpendicular to the ABG. Top figure velocities P-waves, bottom figure velocities S-waves.

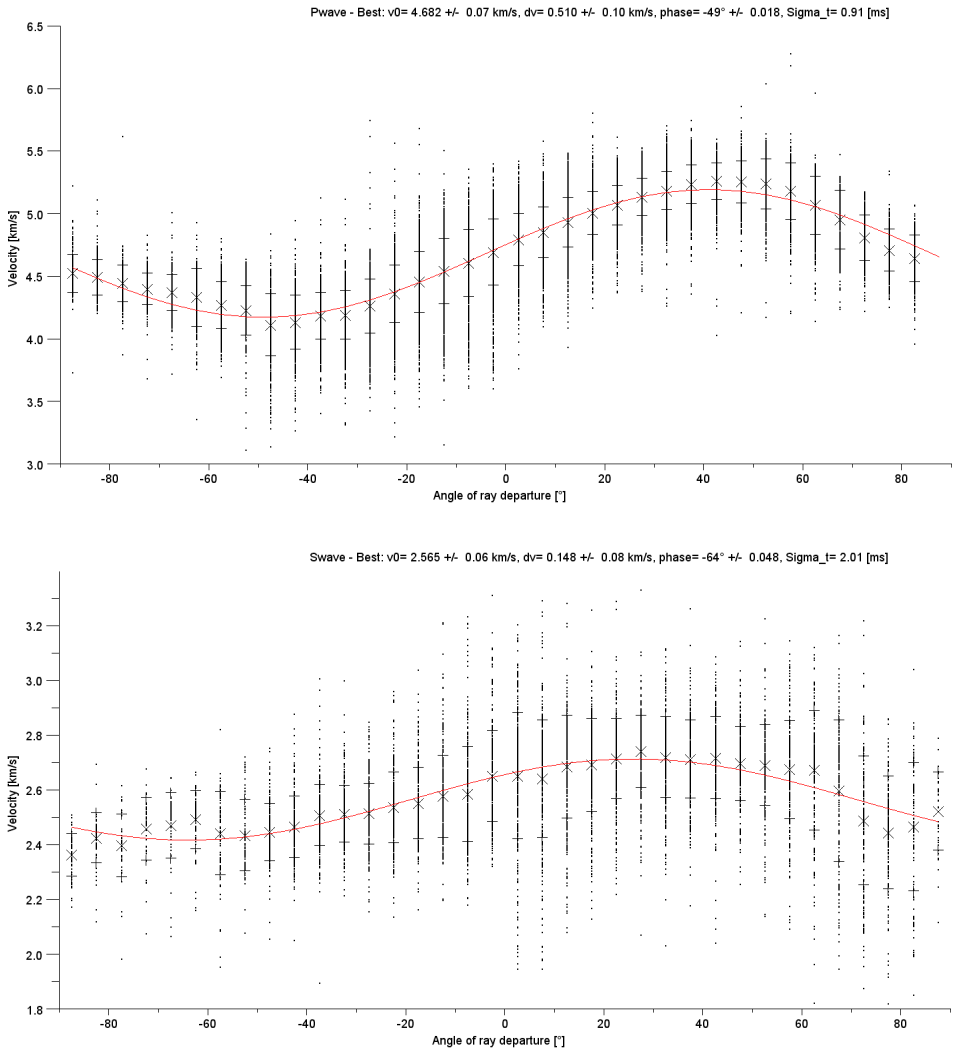

Fig. 4.8: June 2011.Velocities for all rays departing from the shot points within a range of angles of +/- 2.5° (dots), along with averaged velocities (X), standard deviation of averaged velocities (error bars) and with optimum velocity adjustments from cosine fit function (red curve - title of each graph contains the information about the equation of the curve). 0° departure corresponds to the direction perpendicular to the ABG. Top figure velocities P-waves, bottom figure velocities S-waves.

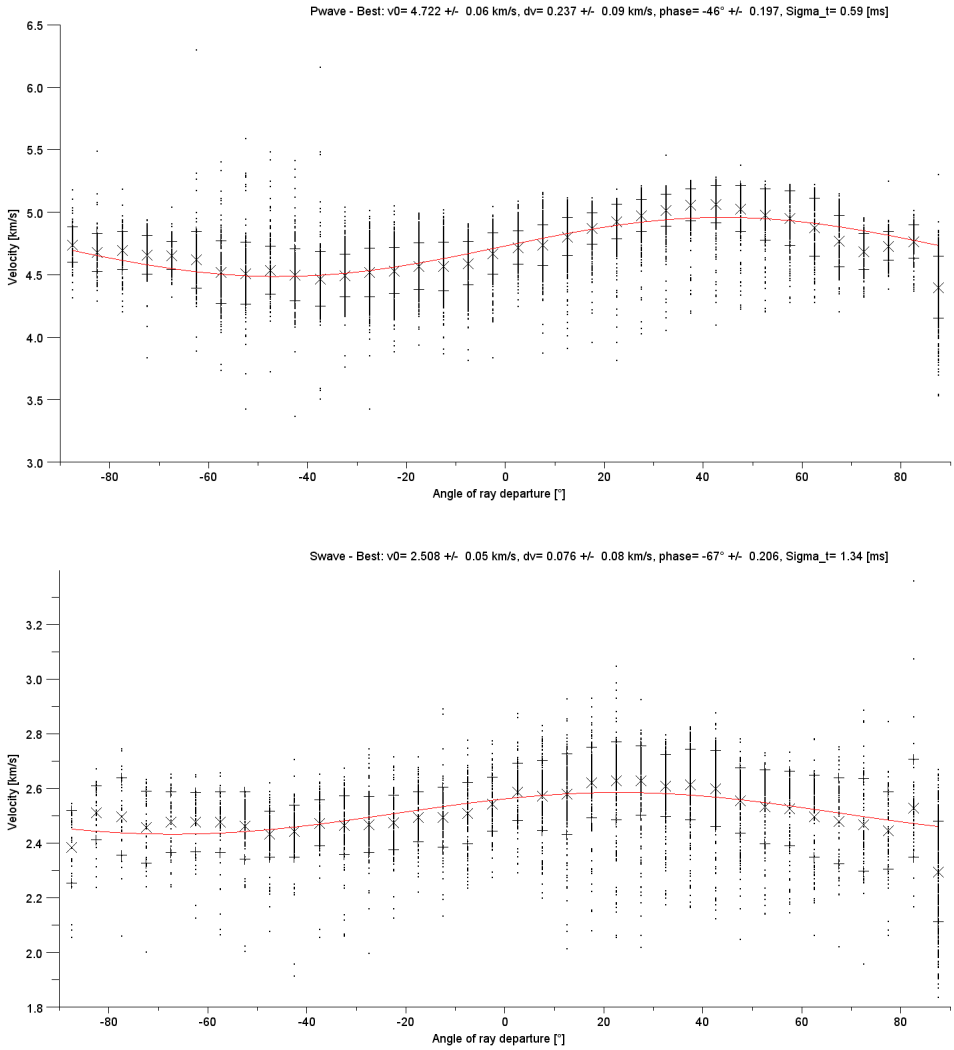

Fig. 4.9: July 2012. Velocities for all rays departing from the shot points within a range of angles of +/- 2.5° (dots), along with averaged velocities (X), standard deviation of averaged velocities (error bars) and with optimum velocity adjustments from cosine fit function (red curve - title of each graph contains the information about the equation of the curve). 0° departure corresponds to the direction perpendicular to the ABG. Top figure velocities P-waves, bottom figure velocities S-waves.

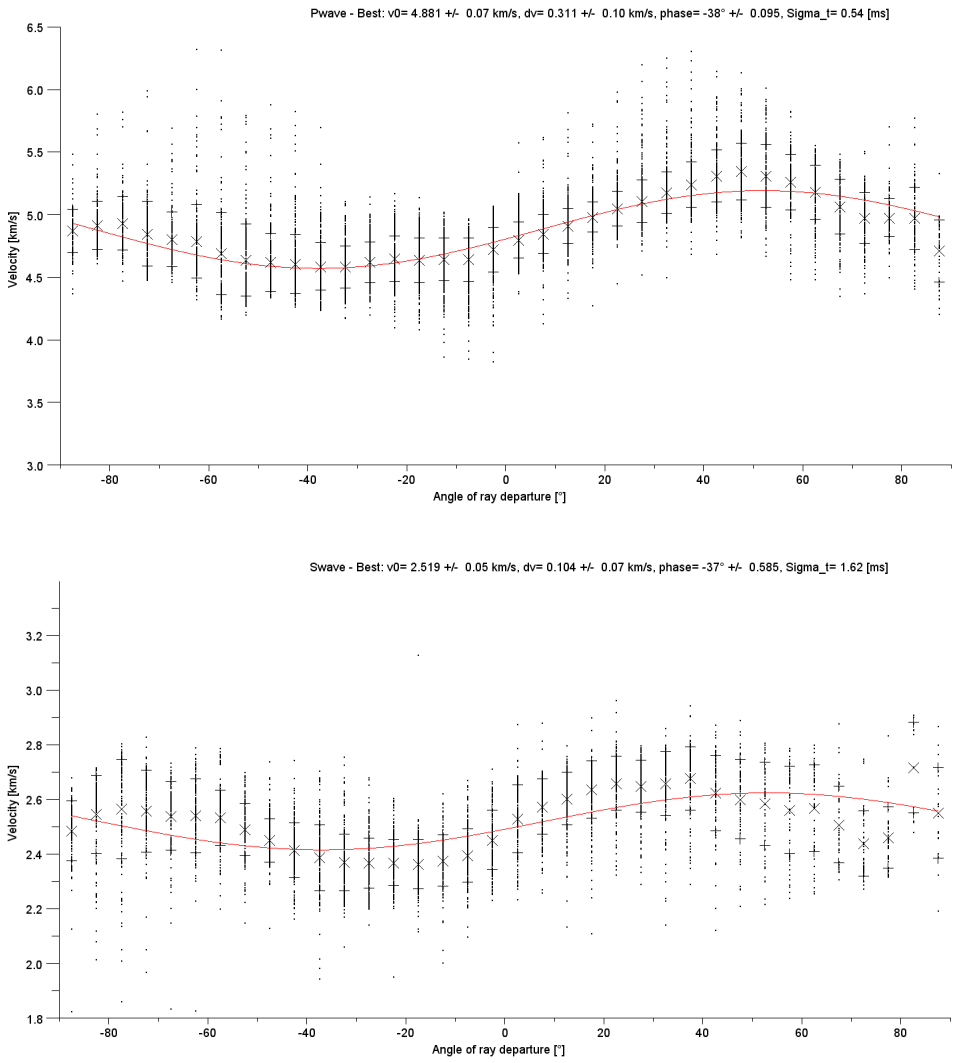

Fig. 4.10: December 2012. Velocities for all rays departing from the shot points within a range of angles of +/- 2.5° (dots), along with averaged velocities (crosses), standard deviation of averaged velocities (error bars) and with optimum velocity adjustments from cosine fit function (red curve - title of each graph contains the information about the equation of the curve). 0° departure corresponds to the direction perpendicular to the ABG. Top figure velocities P-waves, bottom figure velocities S-waves.

4.1.4 Homogeneous anisotropic Monte-Carlo Markov Chain inversion

In order to determine more precisely the anisotropic seismic properties of the rock massif, we developed a Monte Carlo program based on the Markov chain algorithm (MCMC). In the most general case, 21 independent stiffness coefficients are needed to describe anisotropic seismic velocity distribution (e.g. Grechka, 2009a). Grechka and Kachanov (2006), examined the media with penny shaped cracks and came to the conclusion that when the cracks are not co-planar, resulting anisotropy is orthorhombic. The number of independent stiffness coefficients for such a medium decreases to 9.

However, as mentioned earlier, having to consider only one plane, perpendicular to the plane of fractures, it makes sense to take into account only two dimensions and consider the massif as transversely isotropic, where the number of independent stiffness coefficients decreases furthermore to 5. The third dimension does not influence the velocities in the two studied dimensions, and the third orthorhombic plane and its respective coefficients have no effect on the studied dimensions. If the fractures would not be oriented vertically, but with an important angle, using this simplification of transversely isotropic medium, would lead to an error of maximum velocity estimation. The real velocity would be higher if the velocity in the direction of the unused orthorhombic axis was higher, and smaller in the other case. As Grechka and Kachanov (2006) state, there is virtually no effect on the stiffness matrix if the crack faces are corrugated or not.

Therefore, the massif is considered as a medium with an isotropy plane parallel to the principal fracture planes (Tsvankin et al., 2010) containing the maximum velocity. The minimum velocity is parallel to the symmetry axis perpendicular to the fractures. In the studied area, sub-vertical cracks lead to a horizontal transversely isotropic medium approximation (HTI).

This simplification leads to six unknowns, five independent stiffness coefficients and the direction of the symmetry axis. In the coordinate system of anisotropy, we define the direction of the isotropy axis and therefore also of low velocity as X_{HTI}. The isotropy plane of high velocity is then parallel to Y_{HTI} and Z_{HTI}. This coordinate system of anisotropy is rotated with respect to the reference system defined earlier (the X-axis defined perpendicular to the ABG), by an angle ϕ_0 in the X-Y plane. This angle of rotation is one of the unknowns in the inversion. The Z axis of the laboratory and the anisotropy coordinate systems are the same due to the essentially 2-D configuration of the data acquisition.

Although it is common to express anisotropy in reflection seismics in terms of Thomsen's parameters (Thomsen, 1986) or Thomsen's type parameters derived for HTI media (Rüger, 1997 or Tsvankin, 1997a), we were inverting for the stiffness coefficients as they provide the direct physical information about the medium. If only P-wave information were available, Thomsen's parameters ε and δ could be uniquely resolved, whereas the stiffness coefficients c_{12} and c_{66} would be linearly dependent. However, the joint inversion of P and S-wave arrival times allows a unique resolution of all five stiffness parameters necessary for HTI anisotropy and the rotation angle. Thomsen's parameters can then easily be calculated from the stiffness parameters (eqs. 3.4 - 3.6), as well as the velocities in the direction of the symmetry axis, V_{P0} and V_{S0}.

Apart from the angle of rotation ϕ_0, the independent coefficients needed to be calculated for this model are in Voigt notation: c_{11}, c_{22}, c_{12}, c_{44} and c_{66} (Grechka, 2009a), as shown in equations 3.17. Coefficients c_{11} and c_{22} are the coefficients that relate to the velocities of P-waves parallel to the anisotropy axes, where c_{11} is related to the minimum velocity and c_{22} to the maximum velocity. The coefficients c_{44} and c_{66} are mainly controlled by the S-wave velocities, where c_{44} is related to the maximum velocity of S_{paral}-waves and c_{66} is related to

minimum velocity for S_{paral}-waves and axial velocities of S_{perp}-waves. The parameter c_{12}, is related to non axial velocities of S_{perp}-waves and P-waves. For the P-waves it is controlled by the ellipticity (Fig. 3.2 and 3.3), for the S_{perp}-waves it is controlled by the variations of non axial velocity with respect to the axial ones (Fig. 3.4). As c_{66} enters also the equation for P-wave velocities where, it is related to c_{12}, it leads to a strong linear dependency between these two parameters in the absence of S-wave travel-times.

During the inversion, beginning with an arbitrary starting model, the program modifies randomly all parameters at the same time within a predefined model space and with a gaussian probability-density function around each actual model parameter. The fit of the new model measured in a least squares sense with respect to measured and calculated travel-times is compared with the one of the former model. If the new model fits the data better than the former model, it is introduced in an assemblage of accepted models and the following model is searched around the new model (i.e., the centre of the probability-density function is shifted from the former to the new model); if, however, the new model fits worse than the former, the new model can be accepted with certain probability (to allow the solution to climb out of the local minimum) but otherwise it is rejected and the former model is repeated in the mentioned assemblage. The area was supposed to be homogeneous, i.e. no ray bending was considered and we inverted only for the average stiffness parameters. As output, the program gives a list of all coefficient combinations with their respective misfits (expressed as standard deviations σ - Tab 4.3).

For the MCMC inversion we used two approaches. At first we tried to fit each data point from the dataset, meaning that for each measured data point we calculated the theoretical velocity and then compared with the measured value. This process can become very lengthy and the inversions in terms of calculation time can last several hours. In order to speed up the

process, we first calculated the average directional velocities from the measured data for each degree, and then compared with the calculated theoretical velocities. As only 180 averaged values were inverted, the inversions were completed within tens of minutes. The results of these two approaches are almost the same (Table 4.3).

Table 4.3: Best fitting parameters MCMC after 500.000 iterations, showing results for inversion of all travel time data, for inversions of averaged directional velocities and manual fit with respective standard deviations (σ) for all velocities. In order to compare the two different approaches, the standard deviations are expressed in both [ms] and [km/s], as they have been recalculated with the resulting parameters from the inversion.

year		c_{11}	c_{22}	c_{12}	c_{66}	c_{44}	ϕ_0 [°]	σ[ms]	σ[km/s]
May 2005	all data	46.5	65.9	25.3	15.2	19.3	-42.5	0.769	0.031
	averaged	45.1	66.2	26.0	14.8	19.4	-43.7	0.768	0.023
	manual	44.5	66.5	26.0	14.8	19.4	-44.0	0.771	0.024
June 2011	all data	43.5	67.3	20.2	15.2	18.2	-49.2	1.490	0.068
	averaged	43.9	68.1	20.1	14.8	17.7	-48.9	1.575	0.066
	manual	43.0	68.0	28.0	14.5	19.5	-36.0	1.710	0.151
July 2012	all data	52.0	63.1	18.0	14.8	16.6	-53.2	0.992	0.071
	averaged	51.9	63.5	19.5	14.9	16.6	-49.8	0.992	0.069
	manual	48.0	65.0	30.0	14.5	19.0	-40.0	1.034	0.139
Dec. 2012	all	52.0	69.0	29.1	14.6	17.8	-35.1	1.041	0.086
	averaged	53.1	68.5	26.1	14.9	17.1	-36.7	1.126	0.081
	manual	48.0	67.0	33.0	13.5	18.5	-35.0	1.064	0.119

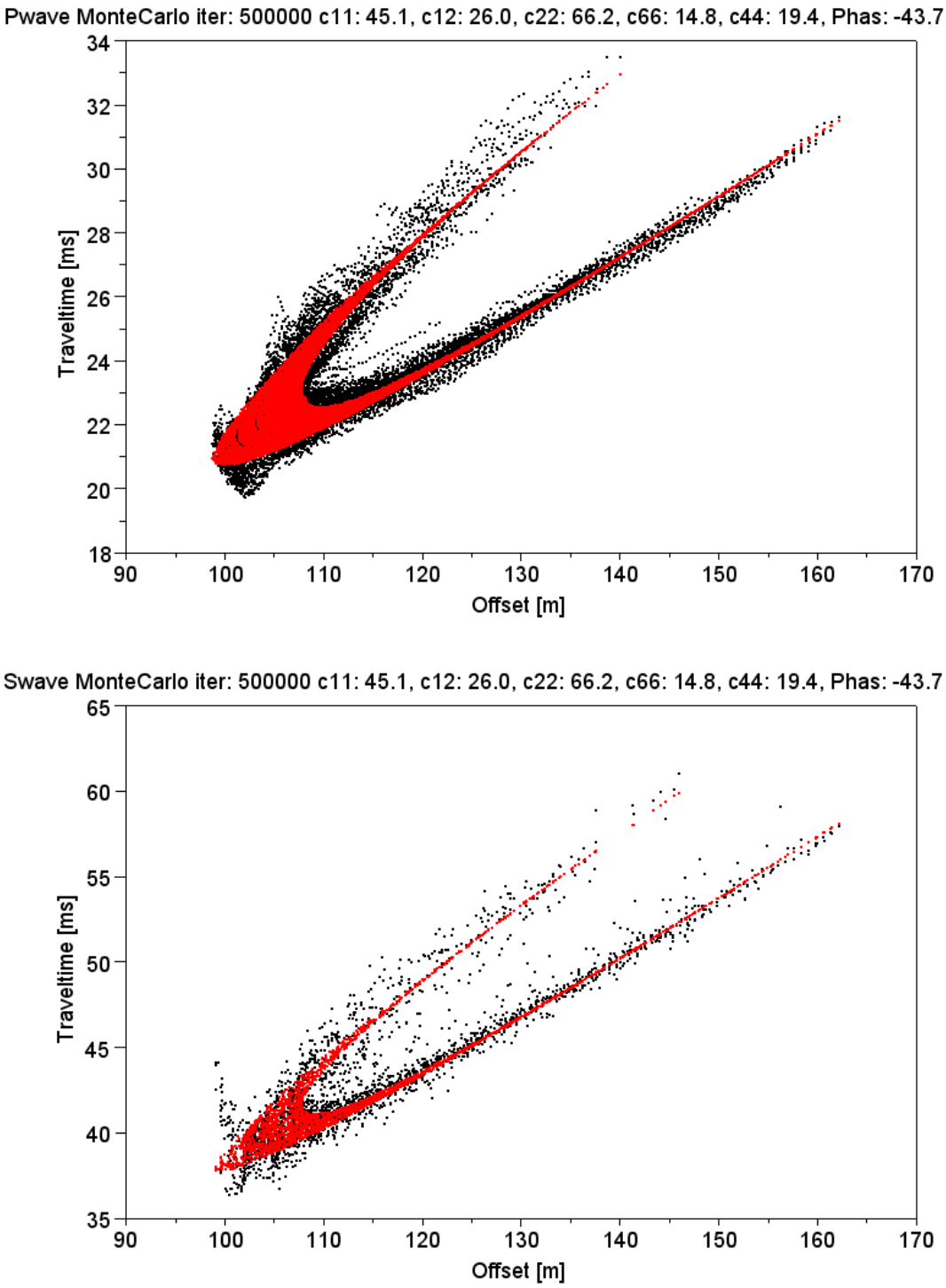

Fig. 4.11: Best fit for MCMC May 2005 with resulting parameters. P-waves above, S-waves below. Black dots - measured data, red dots - calculated data

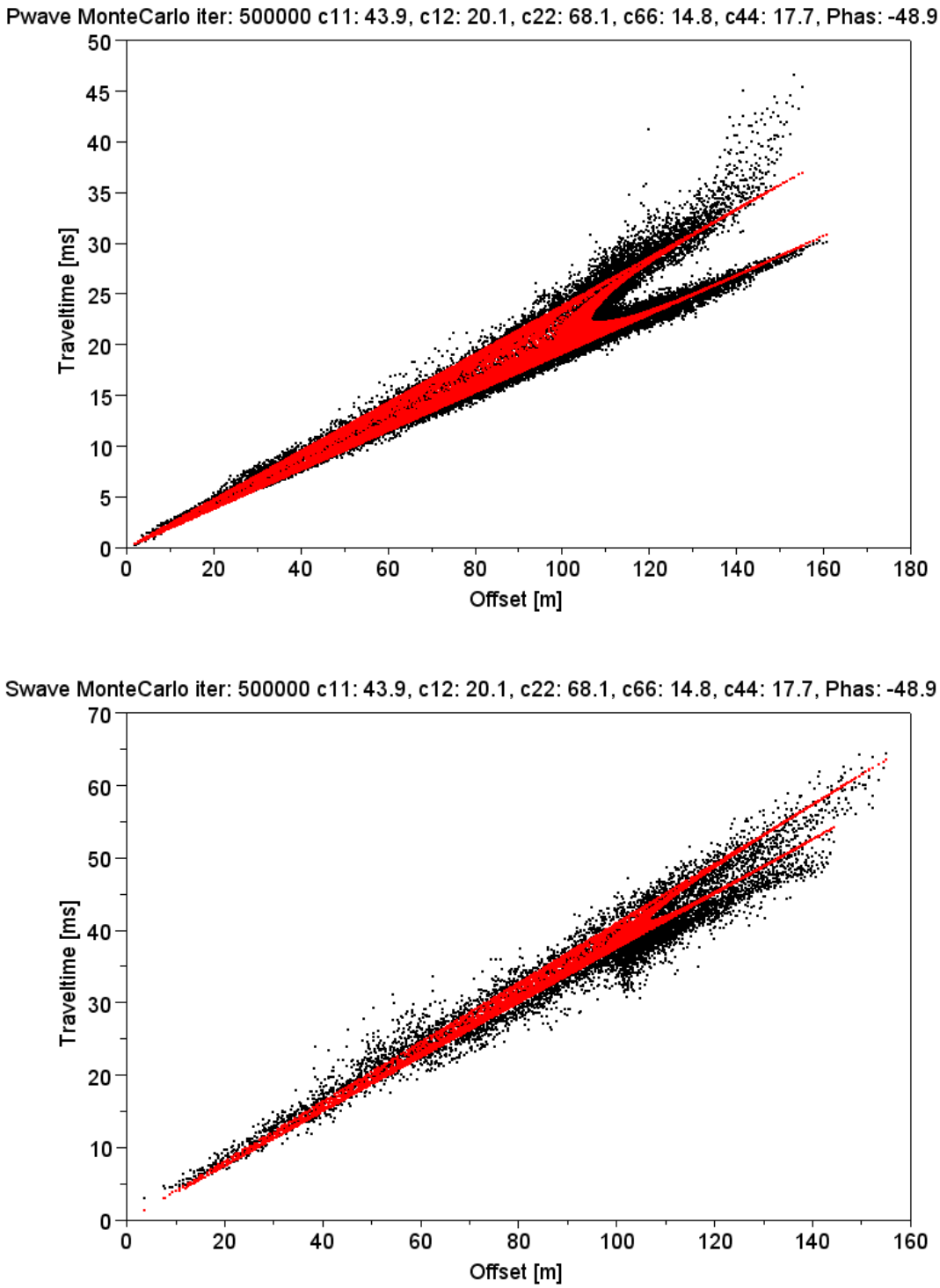

Fig. 4.12: Best fit for MCMC June 2011 with resulting parameters. P-waves above, S-waves below. Black dots - measured data, red dots - calculated data

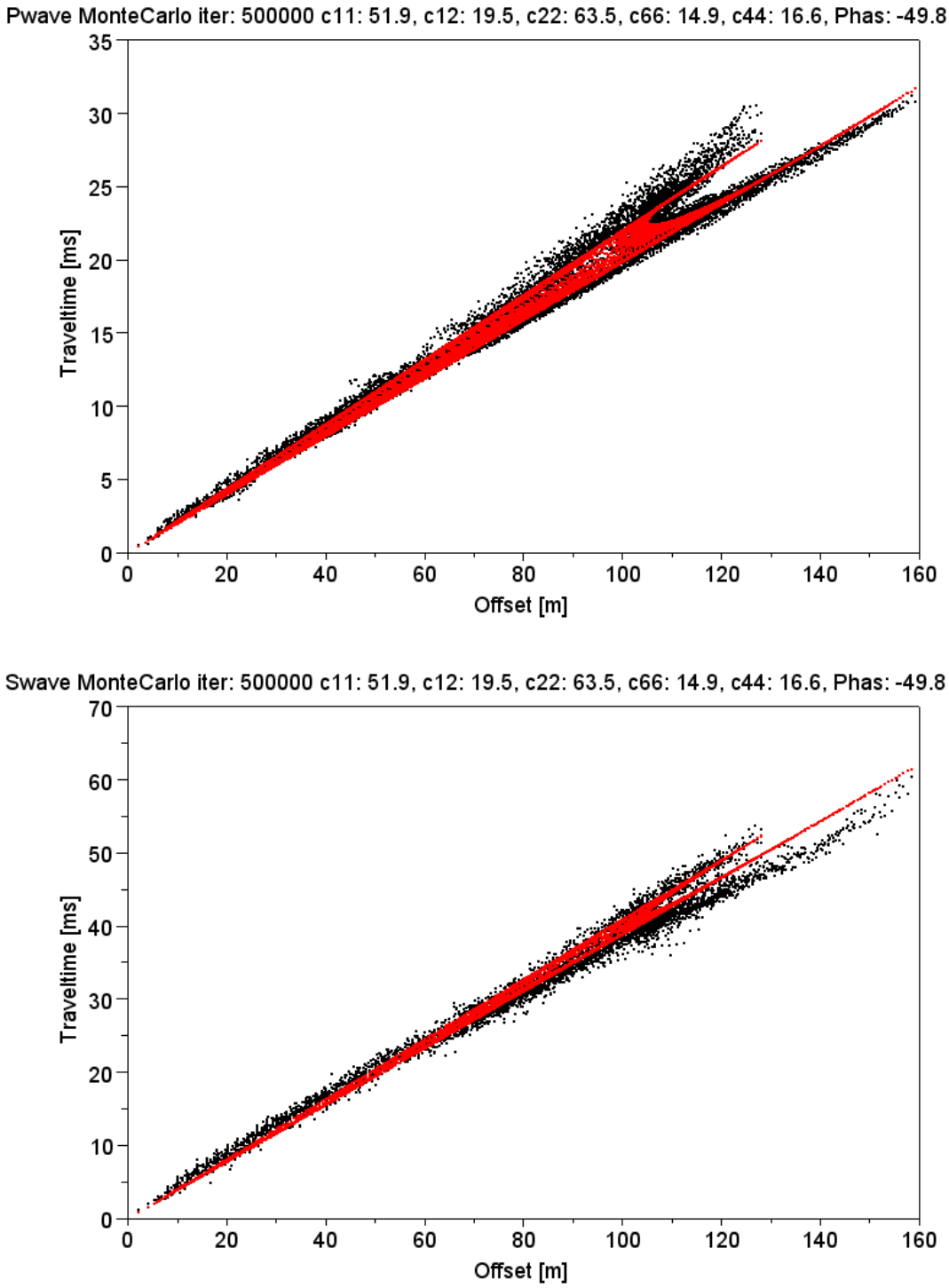

Fig. 4.13: Best fit for MCMC July 2012 with resulting parameters. P-waves above, S-waves below. Black dots - measured data, red dots - calculated data

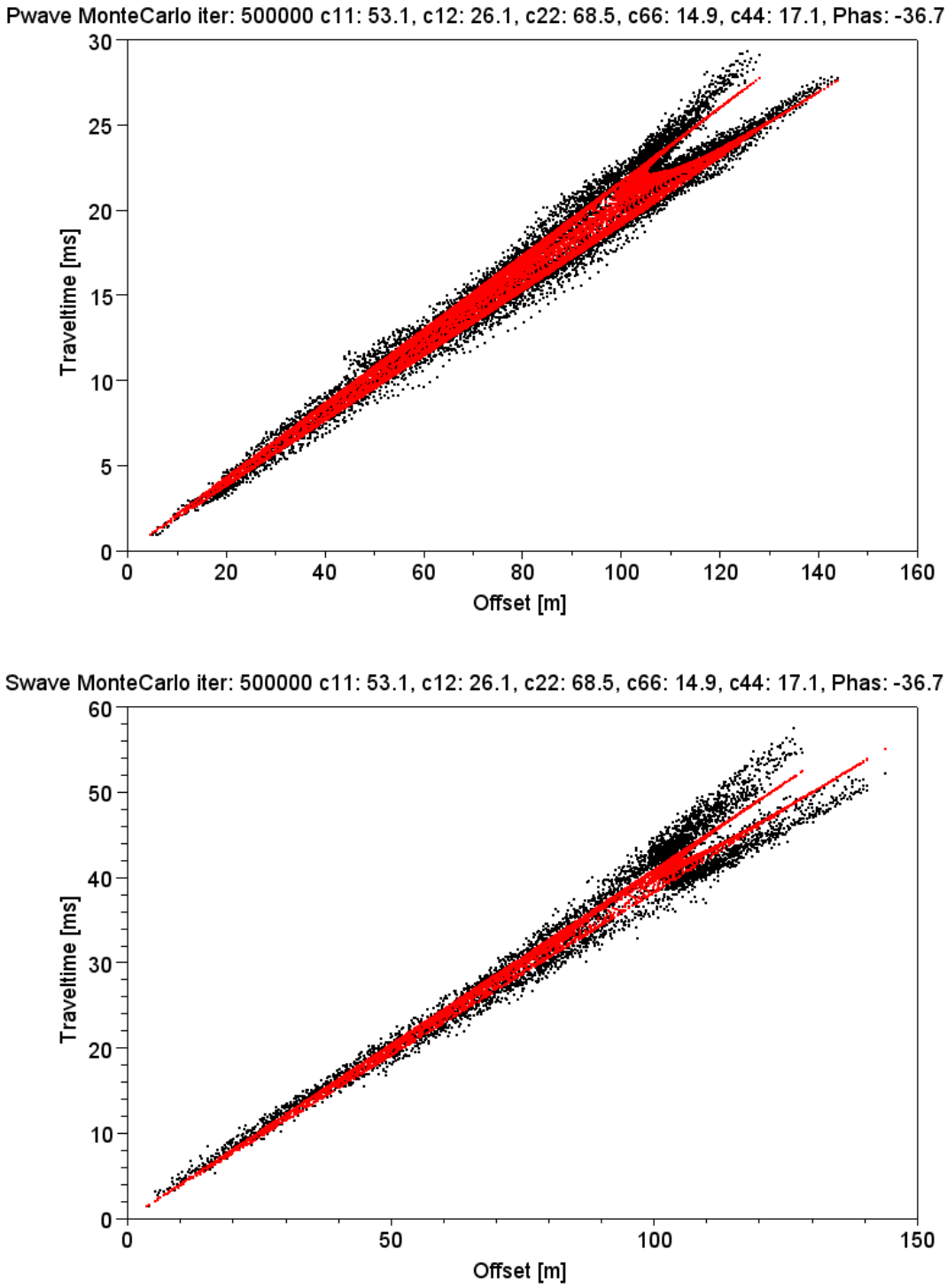

Fig. 4.14: Best fit for MCMC December 2012 with resulting parameters. P-waves above, S-waves below. Black dots - measured data, red dots - calculated data

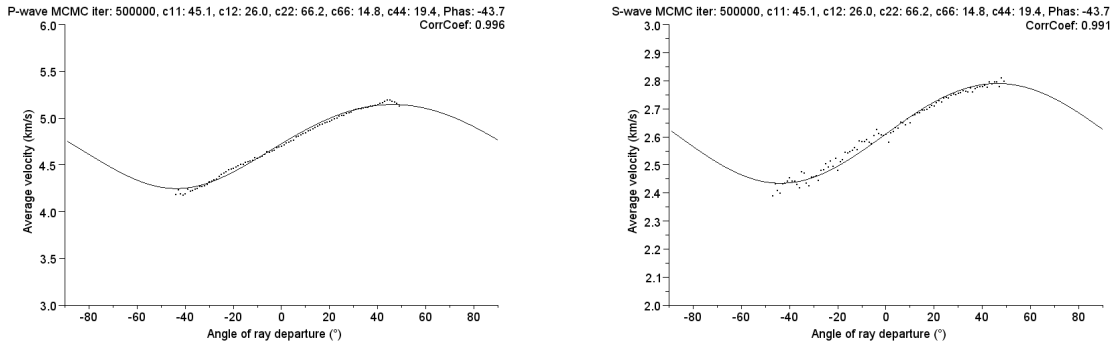

Fig. 4.15: Result of MCMC May 2005. Velocity vs. angle dependence with resulting best parameters. P-waves left, S-waves right.

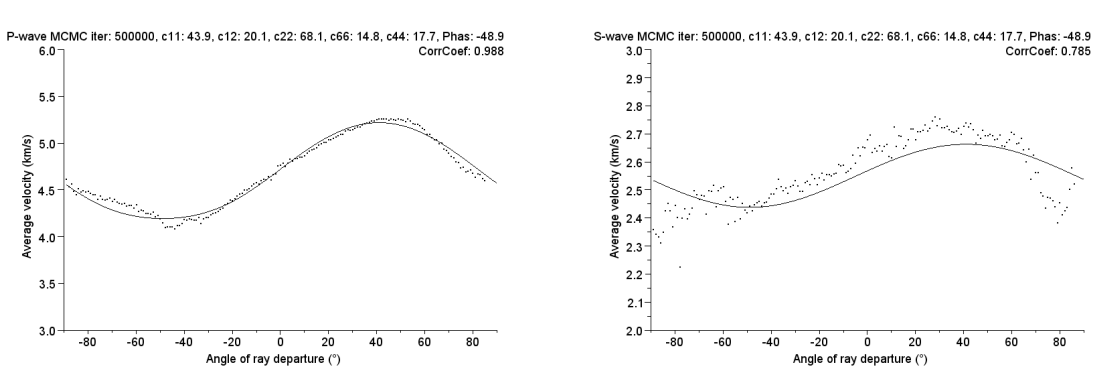

Fig. 4.16: Result of MCMC June 2011. Velocity vs. angle dependence with resulting best parameters. P-waves left, S-waves right.

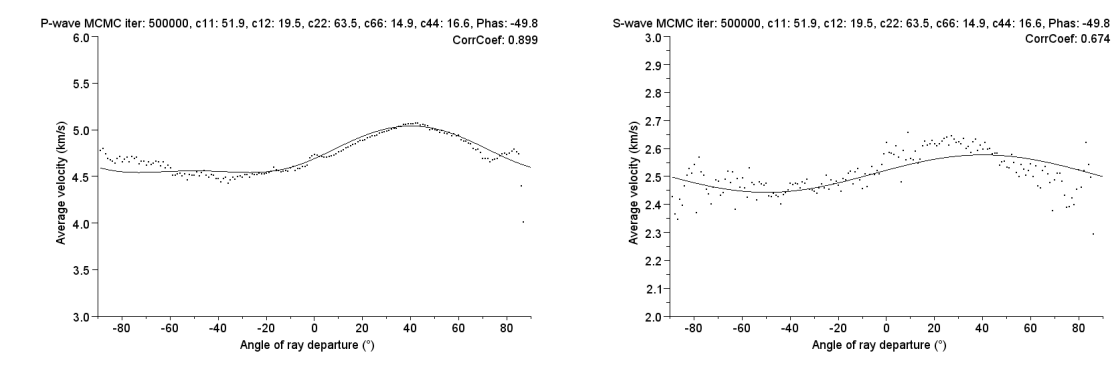

Fig. 4.17: Result of MCMC July 2012. Velocity vs. angle dependence with resulting best parameters. P-waves left, S-waves right.

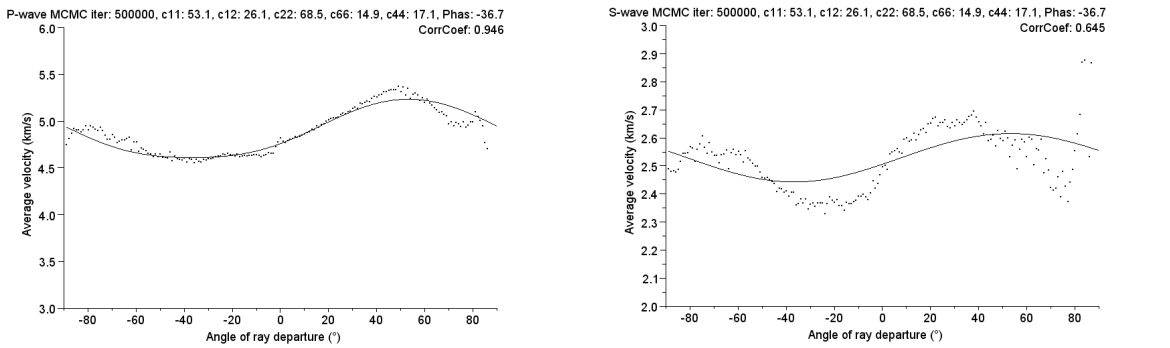

Fig. 4.18: Result of MCMC December 2012. Velocity vs. angle dependence with resulting best parameters. P-waves left, S-waves right.

The best fitting models after 500,000 iterations for all campaigns are displayed in figures 4.11 (May 2005), 4.12 (June 2011), 4.13 (July 2012), 4.14 (December 2012). The calculated theoretical velocity vs. angle dependence with the averaged velocities for each campaign are shown in figures 4.15 (May 2005), 4.16 (June 2011), 4.17 (July 2012), 4.18 (December 2012). The figures display the results from the inversions that calculated the average velocities for all angles and then performed the search for the parameters. The results from inversion that considered all points from dataset are not displayed as the results differ only slightly from the ones shown (Tab. 4.3).

It can be observed that the branches of the velocities (4.11-4.14) are not fitting entirely for the last two campaigns in 2012 and to some degree for S-waves for the year 2011. The reason for that is the influence of the whole dataset on the inversion process at short offsets. The best visual fit for the branches can be achieved by manual fitting (Fig. 4.19), where the interpreter can modify successively each parameter and observe the fit of each branch in the figure, but this process is highly subjective. Only the data from July 2012 is shown in the figure, the results for other campaigns are in the table 4.3). It can be seen that the branching in offset vs. travel-time graph fits better, however the averaged velocities is worse than during the automatic process. The reason for this misfit can be too many data at short offsets,

or too noisy data at offsets around 100-120 m, that are influencing the final average velocities, preventing an acceptable fit.

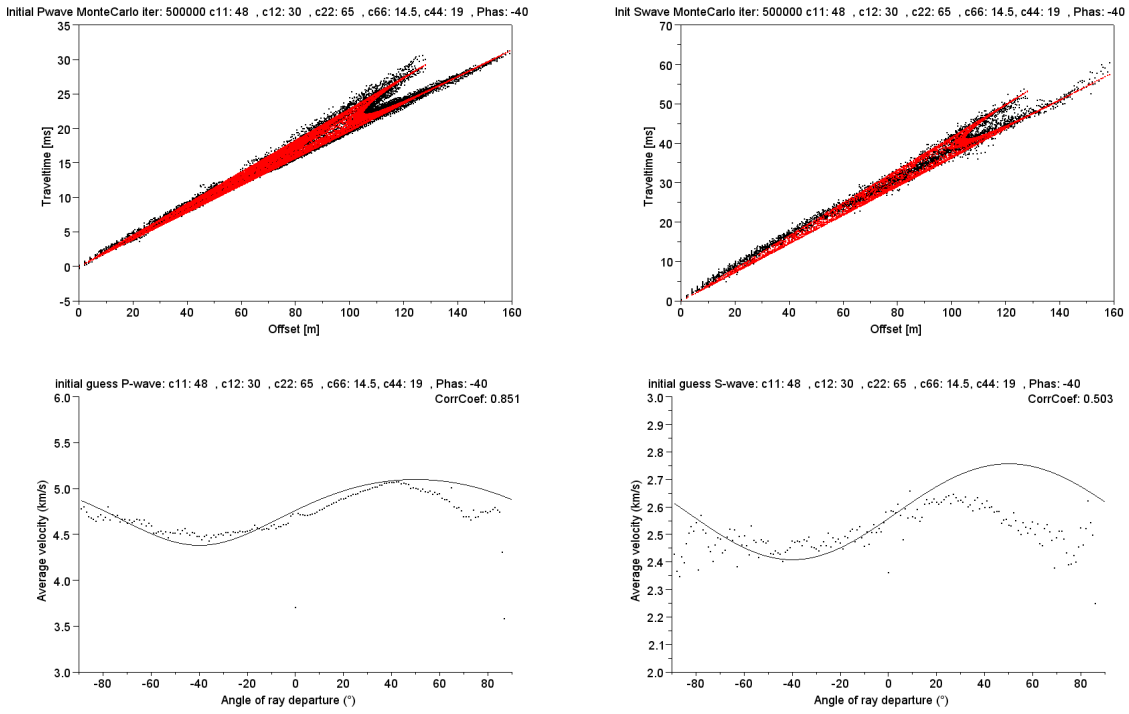

Fig. 4.19: Example of possible best fit from visually fitting the fork of velocities (July 2012). P-waves left, S-waves right. Travel-time data fits above, velocity vs. angle below.

In order to have an automatic process, we tried first reducing graphically the number of points in the figure and running the inversion again. The automatic graphical reduction of points was done by dividing the plot area into several small cells of predefined size and choosing randomly one point found in that cell. This way, in travel-time vs. distance areas, where the points were scarce, all or most of the points were retained for the new selection and where the points were 'overlapping', only one point out of the specified cell was accepted. However, the results of this procedure did not bring any improvement neither for selection of 60% nor 40% of the points out of the dataset and the results are not shown.

The search for the best fitting parameters, retaining 100% of the data points, was executed in two steps. A first inversion was run with large boundaries, even for the

combinations of parameters that would not have any physical meaning for a limestone massif, such as unrealistically high velocities for P or S-waves, or combinations of parameter c_{12} with c_{11} that create unrealistic jumps in phase velocities for certain angles. In the second inversion, the boundaries were set around the peak of accepted parameters from the first inversion. Figure 4.20 shows the histogram of tested parameters from the first inversion step with marked narrow boundaries for the second inversion in order to reduce the number of searched parameters and have a better chance to find the best combination.

The inversions for all years correspond quite well to their cosine approximations for both wave types even though cosine approximation is for elliptic phase velocity and the results of the MCMC are non-elliptic. Comparison of the resulting corresponding parameters for each year is given in table 4.4.

Table 4.4: Comparison of all parameters of stiffness matrix from MCMC inversion with the best cosine fits for all years

year	inversion	wave type	v_0	dv	φ_0	vmax	vmin	c_{22}	c_{11}	c_{44}	c_{66}
May 2005	cos.fit	P	4.7	0.5	-47.0	5.2	4.2	66.3	44.7	-	-
		S	2.6	0.2	-47.0	2.8	2.4	-	-	19.3	14.9
	MCMC	-	-	-	-43.7	-	-	66.2	45.1	19.5	14.8
June 2011	cos.fit	P	4.7	0.5	-49.0	5.2	4.2	67.3	43.5	-	-
		S	2.6	0.2	-64.0	2.7	2.4	-	-	18.5	14.6
	MCMC	-	-	-	-49.0	-	-	68.1	44.0	17.7	14.9
July 2012	cos.fit	P	4.7	0.2	-46.0	5.0	4.5	61.5	50.2	-	-
		S	2.5	0.1	-67.0	2.6	2.4	-	-	16.8	14.8
	MCMC	-	-	-	-49.9	-	-	63.5	52.0	16.6	14.9
Dec. 2012	cos.fit	P	4.9	0.3	-38.0	5.2	4.6	67.3	52.7	-	-
		S	2.5	0.1	-37.0	2.6	2.4	-	-	17.2	14.6
	MCMC	-	-	-	-36.7	-	-	68.5	53.1	17.1	14.9

Figures 4.21 and 4.22 display the histograms of all inverted parameters for all models within the smaller chosen boundaries for each year (second inversion). Figures 4.23 and 4.24 display the histograms of accepted inverted parameters.

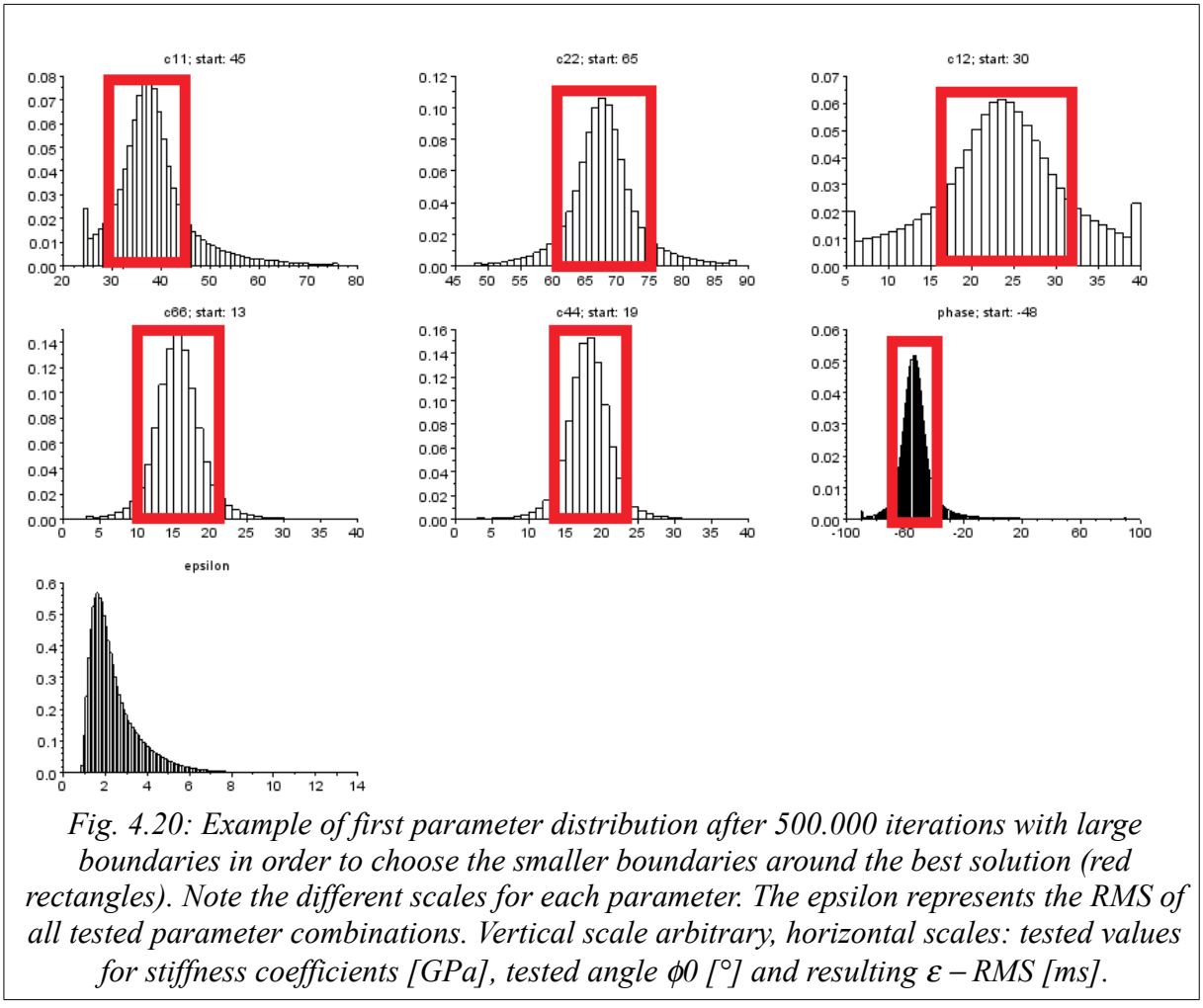

Fig. 4.20: Example of first parameter distribution after 500.000 iterations with large boundaries in order to choose the smaller boundaries around the best solution (red rectangles). Note the different scales for each parameter. The epsilon represents the RMS of all tested parameter combinations. Vertical scale arbitrary, horizontal scales: tested values for stiffness coefficients [GPa], tested angle $\phi 0$ [°] and resulting ε – RMS [ms].

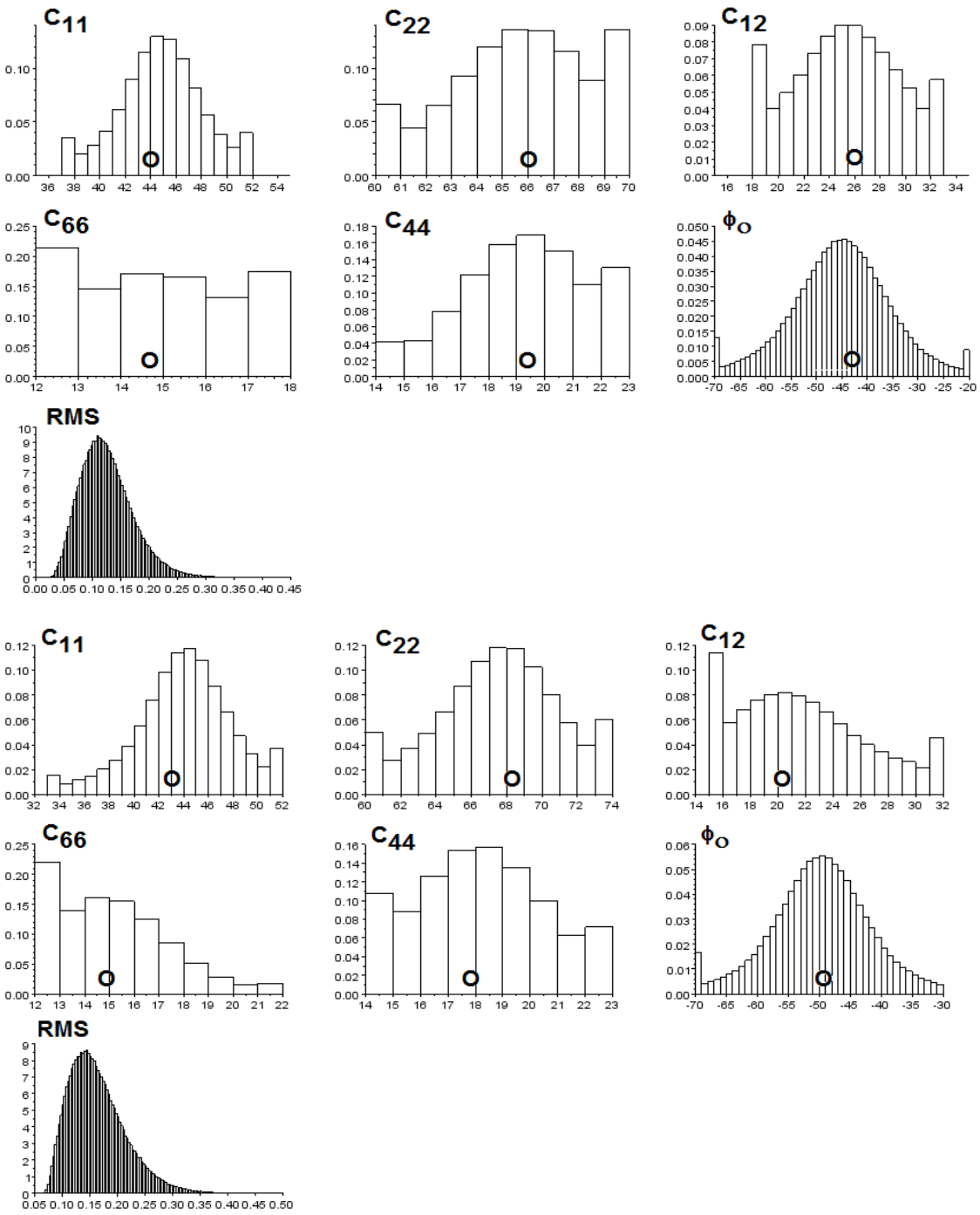

Fig. 4.21: Histograms of all tested parameters within the chosen tighter boundaries. Top May 2005, bottom June 2011. Circles represent the best results. Note the different scales for each parameter. Vertical scale is arbitrary, horizontal scales: tested values for stiffness coefficients [GPa], tested angle ϕ_0 [°] and resulting RMS [ms].

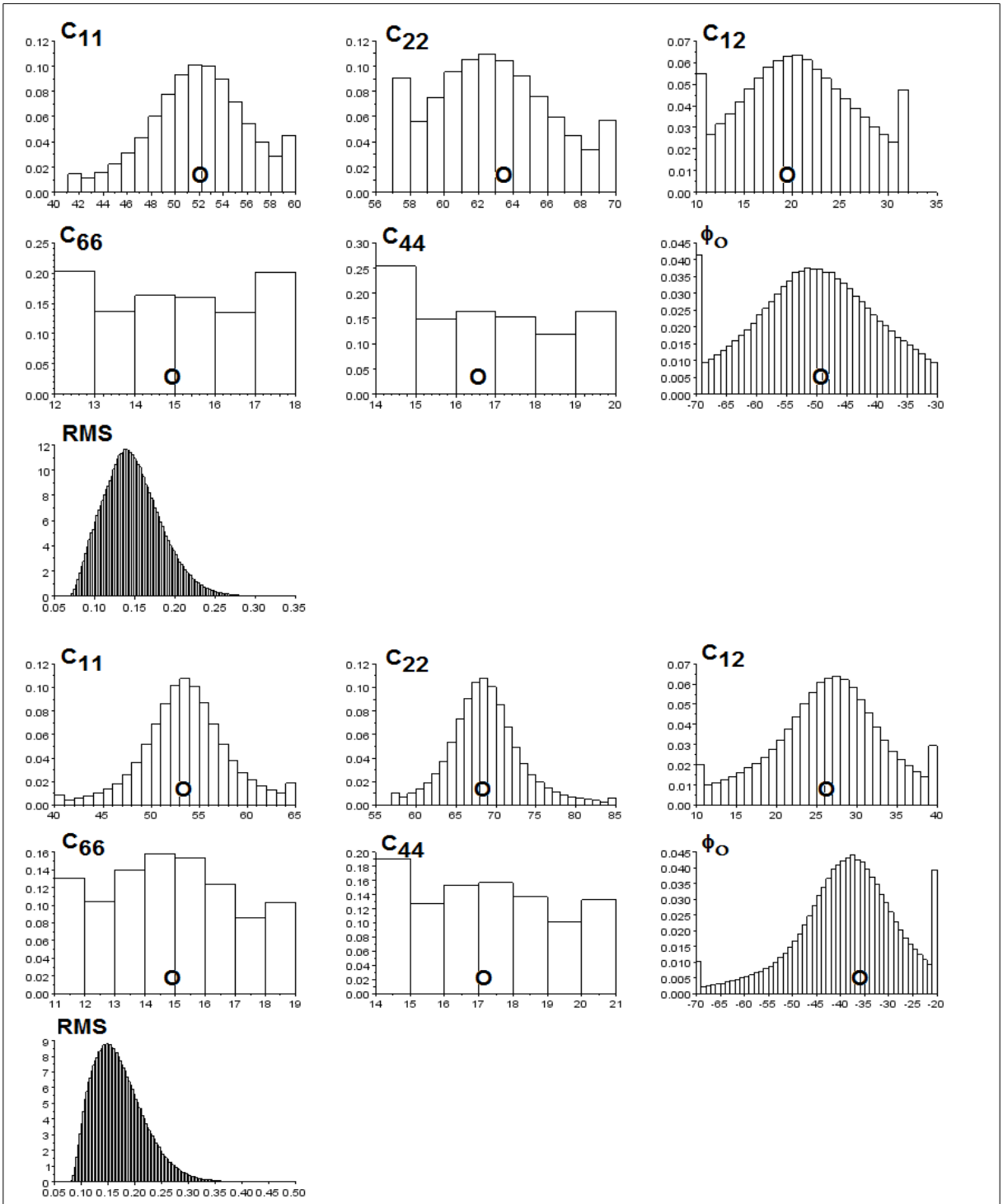

Fig. 4.22: Histograms of all tested parameters within the chosen tighter boundaries. Top July 2012, bottom December 2012. Circles represent the best results. Note the different scales for each parameter. Vertical scale arbitrary, horizontal scales: tested values for stiffness coefficients [GPa], tested angle ϕ_0 [°] and resulting RMS [ms].

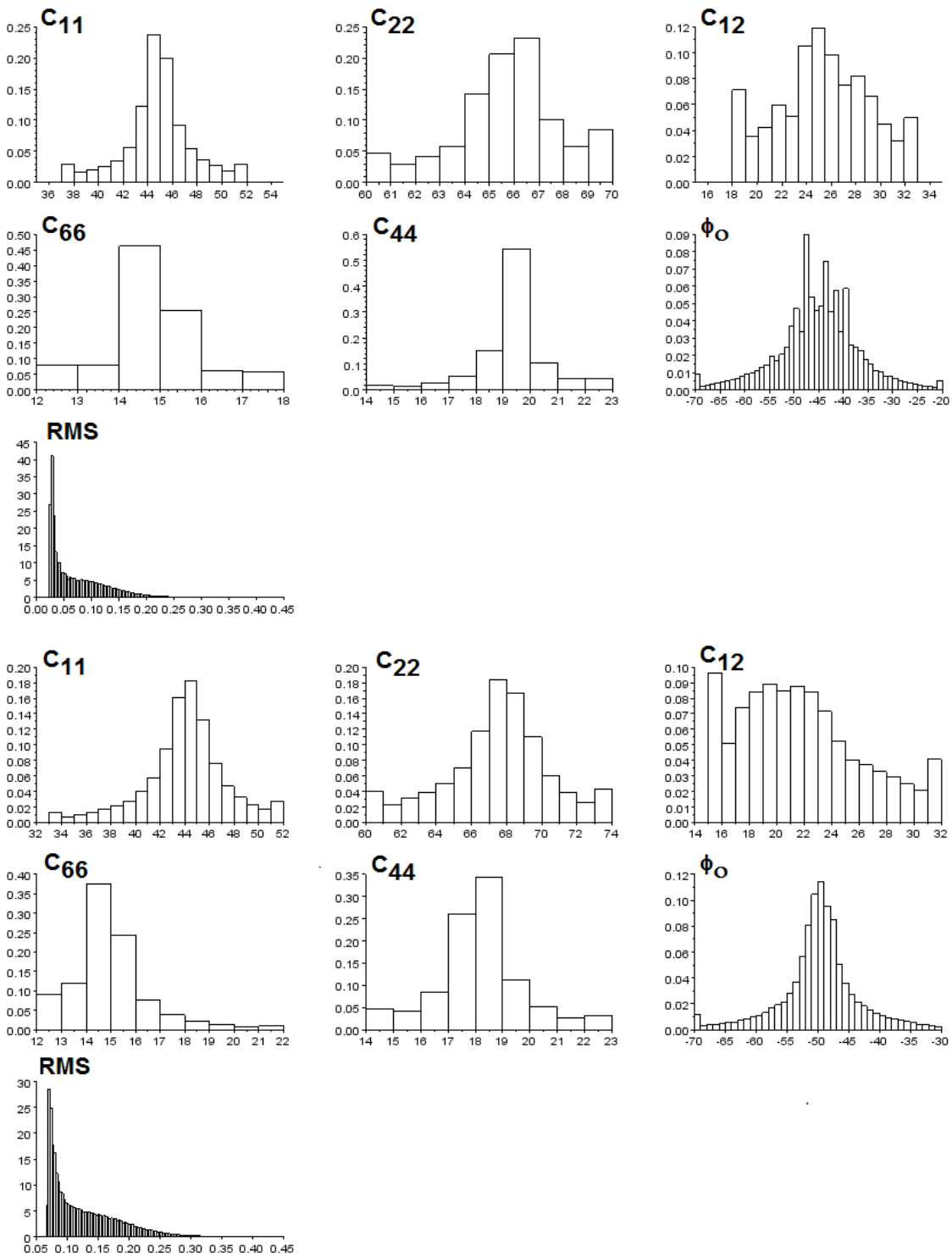

Fig. 4.23: Histograms of accepted parameters. Top 2005, bottom 2011. Note the different scales for each parameter. Vertical scale arbitrary, horizontal scales: tested values for stiffness coefficients [GPa], tested angle ϕ_0 [°] and resulting RMS [ms].

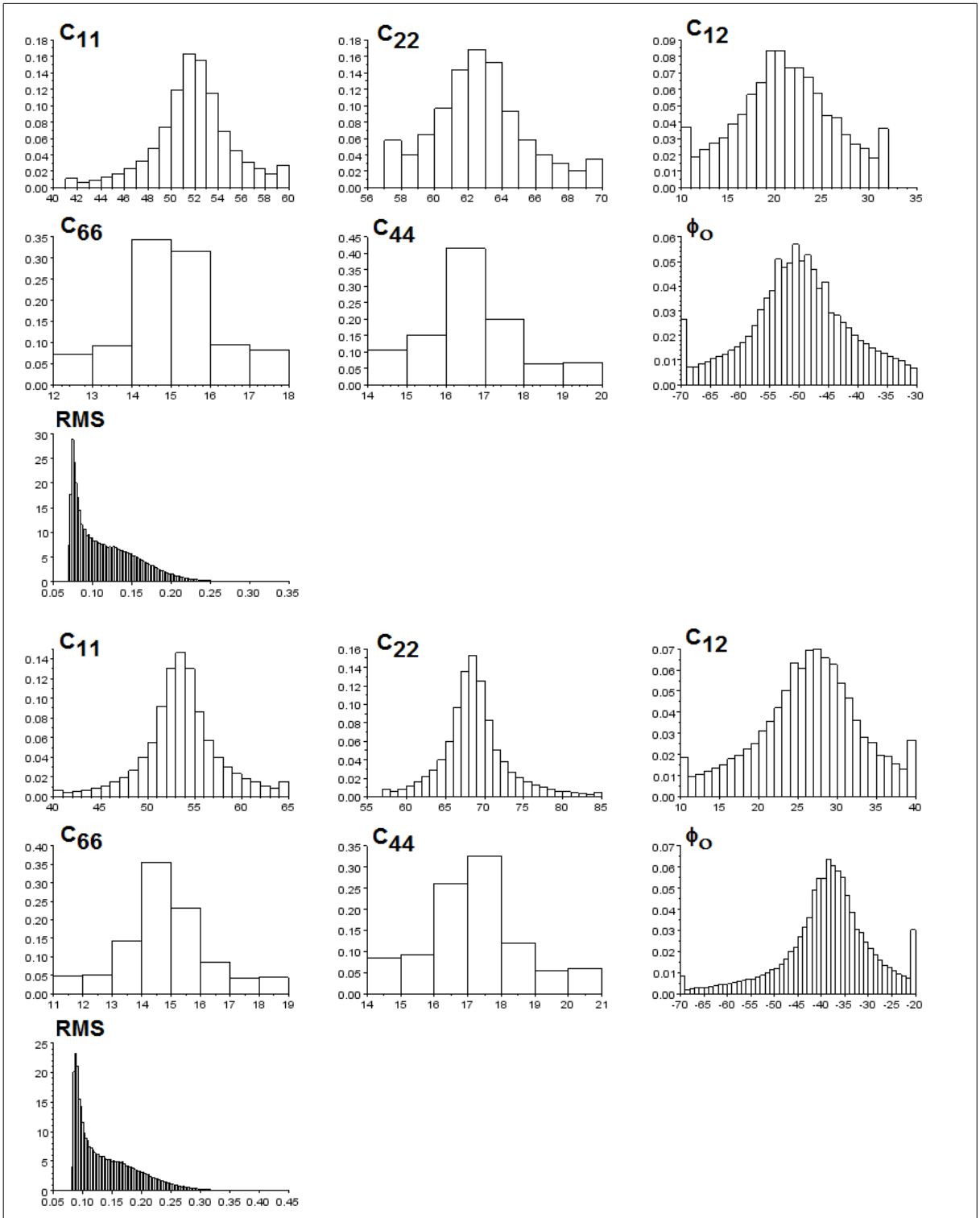

Fig. 4.24: Histograms of accepted parameters. Top July 2012, bottom December 2012. Note the different scales for each parameter. Vertical scale arbitrary, horizontal scales: tested values for stiffness coefficients [GPa], tested angle ϕ_0 [°] and resulting RMS [ms].

4.1.5 Anisotropic tomography program ANRAY and other software

The previous results show that the approximation of the rock by an HTI medium explains most of the data; however, the spread of the measured travel-times around the synthetic ones shows that the area is not homogeneous. Also, due to the inhomogeneities, the RMS for MCMC inversions is higher than the RMS for isotropic tomography (inversion for all data from table 4.3). During the analysis of data from LSBB, several computer codes were tested in order to do the modelling and inversion of the data. Among them was the Fortran code Anray designed by Gajewski and Pšenčík (1990) from the SW3D Group. As the majority of seismic processing deals with reflected or refracted data, this code is not very suitable for data acquired at LSBB. The interpreter has to specify which waves he/she is looking for, e.g. converted PS waves, reflected PP, etc. and the use of the program for direct waves is counter-intuitively rather cumbersome.

Other softwares were examined, but were found unsuitable because of lack of some features, e.g. FDWaveAni by Boyd (2006) lacked the inversion part as it is only a forward problem calculation tool.

4.1.6 Anisotropic tomography "3Dray_gTI0"

Out of the available codes for the seismic data treatment, we chose to use the 3-D seismic anisotropy tomography program “3Dray_gTI0” (Zhou and Greenhalgh, 2008), designed for TTI media in order to invert for the distribution of stiffness parameters. Tilting in 3-D is done using two rotational angles in spherical coordinates. The first rotation (angle θ) rotates the VTI model from the z-axis around the y-axis of the reference system set in the laboratory. The second angle φ rotates then the model into the specified azimuth. Since we are dealing with an HTI medium, the first rotation of the symmetry axis of the TI media is set to $\theta=90°$

with respect to a reference system, and the second angle φ was fixed as previously obtained from the Monte-Carlo inversion. As the massif is rather homogeneous and the direction of the fractures does not show important changes in the studied area, we did not invert for the angles because the sensitivity of velocity with respect to the angle is very small around the optimum angle and small changes in angles would not affect the result (Golikov and Stovas, 2012).

We modified the program for our needs, implementing a data weighing matrix (C_D^{-1} in equation (3.38), that allows for taking into account variable data uncertainties for the model construction (Menke, 1984). These data uncertainties were measured during picking of arrival times and depend on visually determined data quality. P-wave picks have in average smaller uncertainties than S-wave picks. The bigger the uncertainty for a given point during the picking, the smaller the importance of this point during the inversion.

The inversion is non-linear and it is therefore done by a series of iterations. The parameters of the starting model were set to the output values of the homogeneous Monte-Carlo anisotropic inversion on a 10 m x10 m grid. Each node of the grid represents a point at which the parameters are set.

The forward modelling part uses the ray tracer based on 'shortest path' method (Zhou and Greenhalgh, 2005). Going through all the nodes of the model, the tracer calculates all possible ray-paths for each source-receiver combinations (for each data) and chooses the fastest travel-time. For the inversion part, after each iteration, the program updates the Jacobian matrix based on the first-order travel-time perturbation (Zhou and Greenhalgh, 2008) and uses a conjugated gradient method to calculate the inverse matrix in eq. 3.39 (Greenhalgh et al., 2006).

We tried several configurations with different weights between the precision of data

fitting and smoothness of the result, defined in the input file by a damping factor and the inversion stabilized after 15-20 iterations. The configurations with too small damping factor showed big oscillations between neighbouring nodes, which could not be physically possible. The configurations with too big damping factor were smoothed to that extent, that the final result contained no visible structures. We chose the configuration that was smoothed, yet it contained some structures that could be physically possible.

The size of the inversion cells (10 m x 10 m) was chosen in a way that would be reasonable from the geological point of view. It is possible to expect that the geological properties could vary in cells of 5 m as well, but for our data the results for the cells of 5 m did not improve the overall RMS, nor was the distribution of resulting parameters very different from the one using 10 m cells. These distributions are shown in figures 4.25 (May 2005), 4.26 (June 2011), 4.27 (July 2012) and 4.28 (December 2012). Joint RMS misfits of the P and S-wave travel times are presented in the table 4.5.

Table 4.5: Joint RMS for P and S-waves after inverting with 3Dray_gTI0

year	RMS	year	RMS
May 2005	0.428	June 2011	1.036
July 2012	0.530	Dec. 2012	0.598

Figures 4.29 - 4.32 show the corresponding travel-times vs. offset for each year of P-waves and for the S-waves after the tomographic inversions.

To complete the display of results for each year, Thomsen's parameters are shown in figures 4.33 - 4.36.

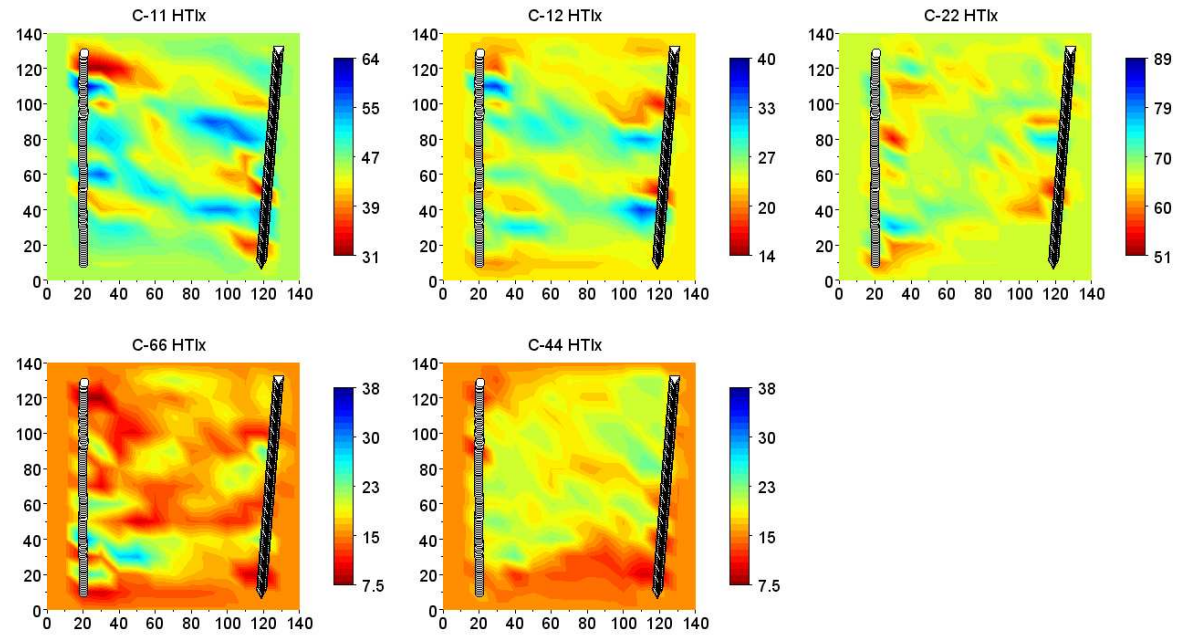

Fig. 4.25: Distribution of parameters of stiffness matrix for May 2005 after inverting the measured data with 3Dray_gTI0.

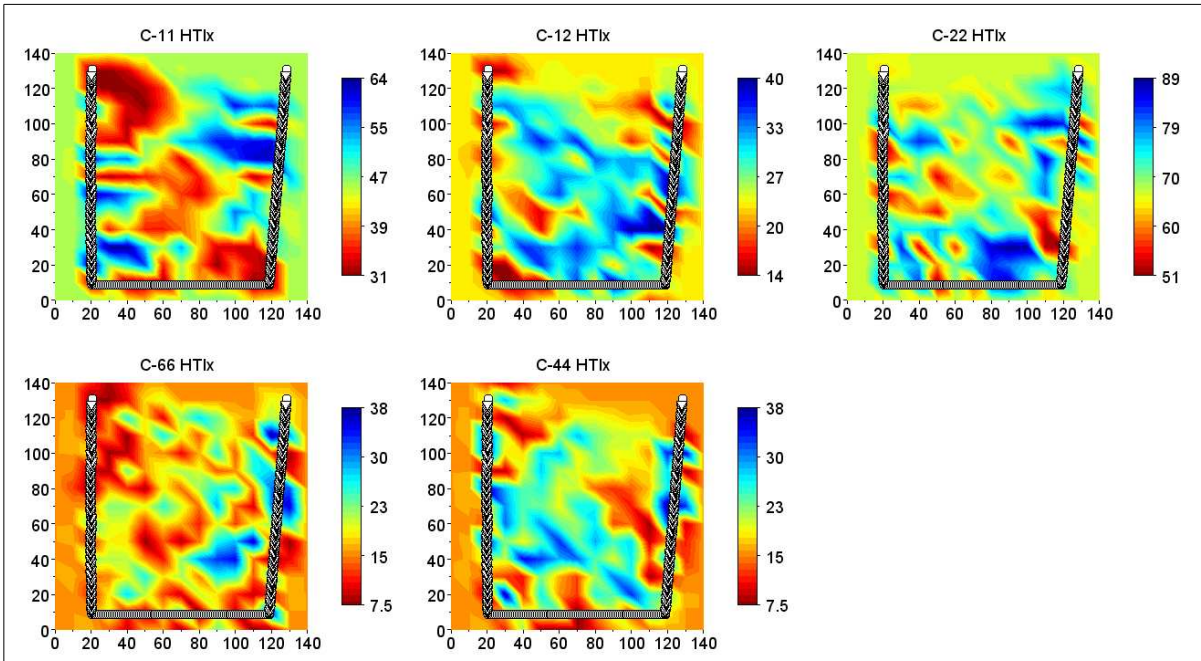

Fig. 4.26: Distribution of parameters of stiffness matrix for June 2011 after inverting the measured data with 3Dray_gTI0.

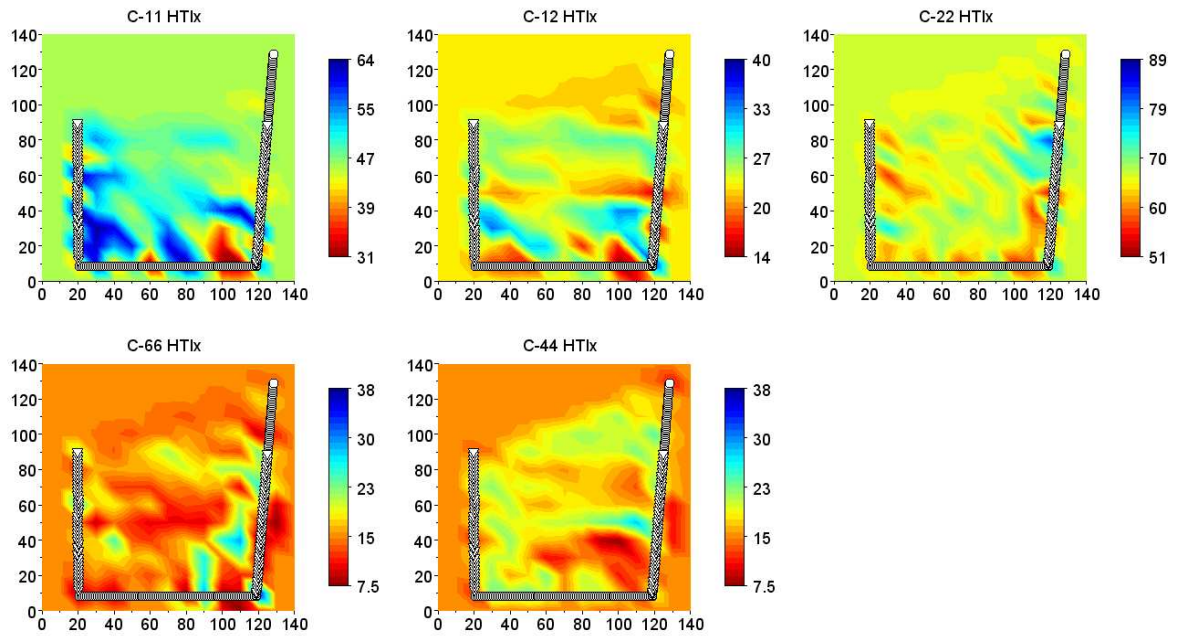

Fig. 4.27: Distribution of parameters of stiffness matrix for July 2012 after inverting the measured data with 3Dray_gTI0.

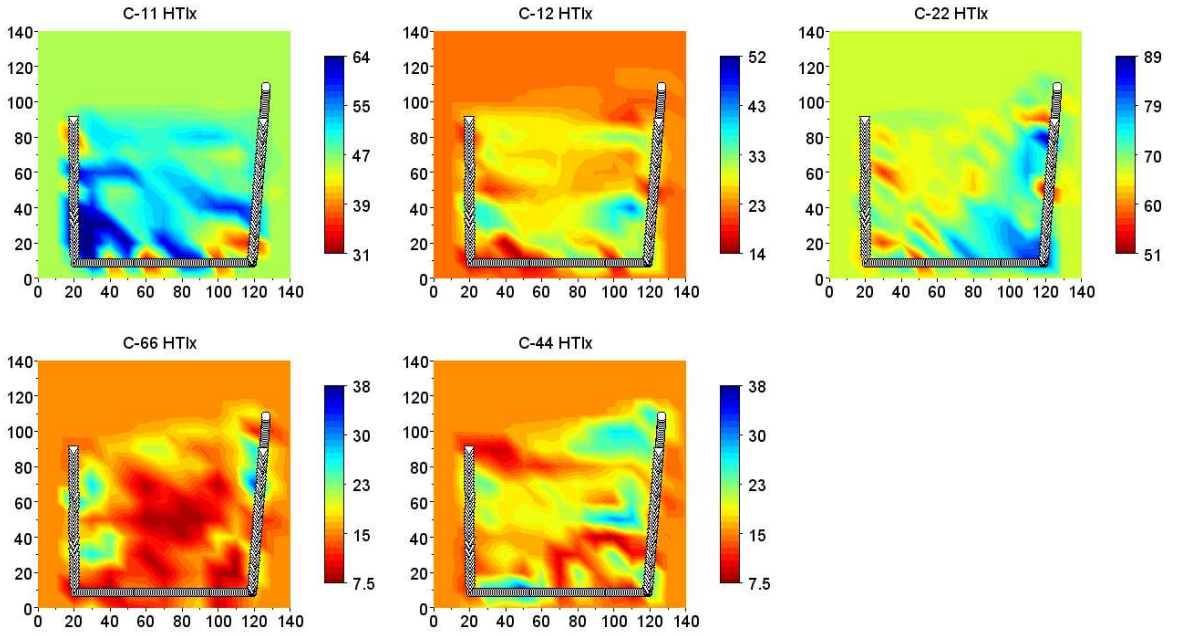

Fig. 4.28: Distribution of parameters of stiffness matrix for December 2012 after inverting the measured data with 3Dray_gTI0.

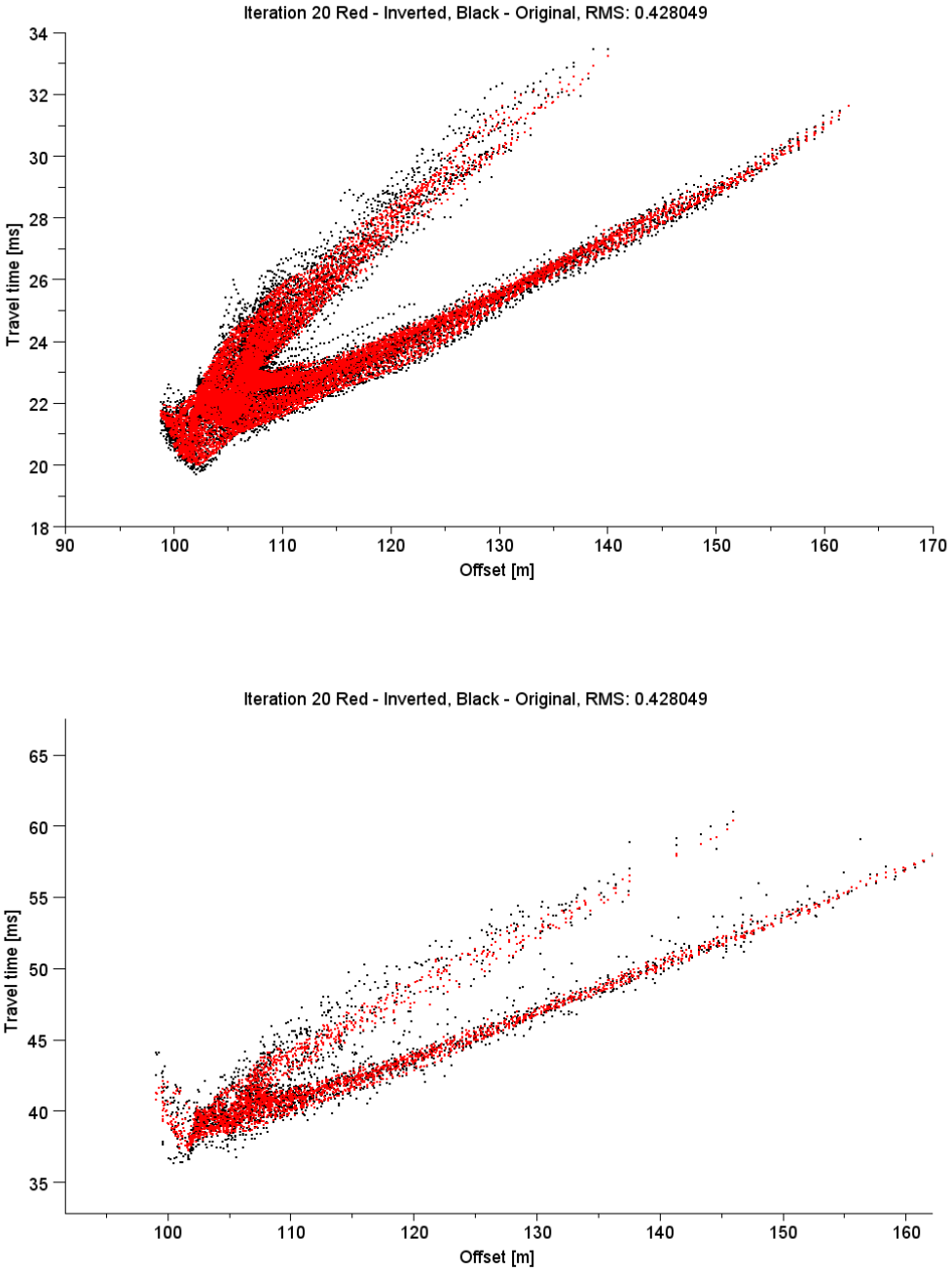

Fig. 4.29: Resulting travel time vs. offset after tomographic inversion. May 2005. Above P-waves, below S-waves. The small 'upward' branch at offset of 100 m for the S-waves represents the measurements along the TG for the very first few meters inside both galleries ABG and MG. The slower velocities (higher value of travel-time) is due to the less clearly defined S-wave arrivals in the recordings.

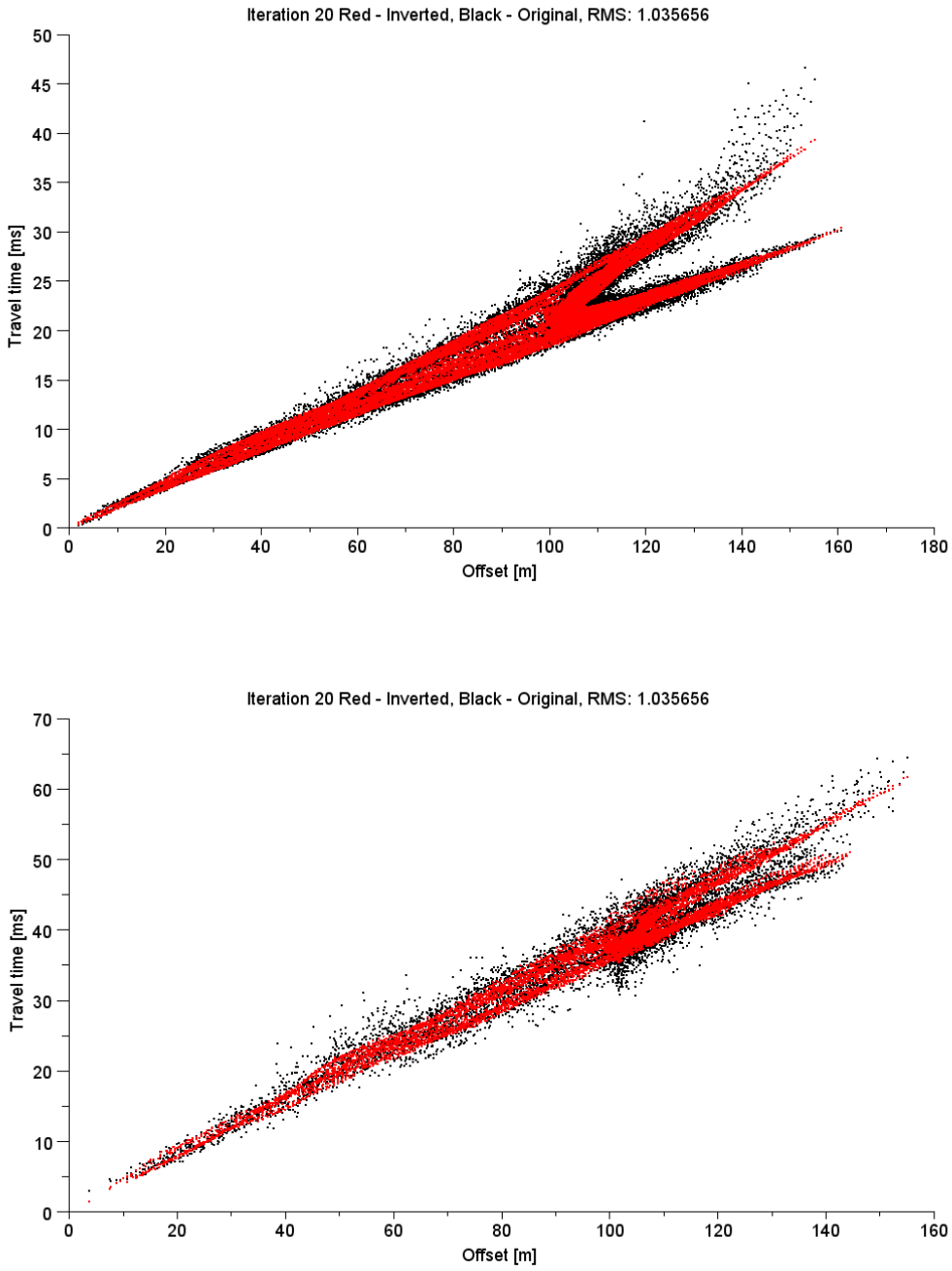

Fig. 4.30: Resulting travel time vs. offset after tomographic inversion. June 2011. Above P-waves, below S-waves. The cloud of points for the P-waves at offsets 140-160 m, at later times the red modelled data is due to higher noise at longer offsets.

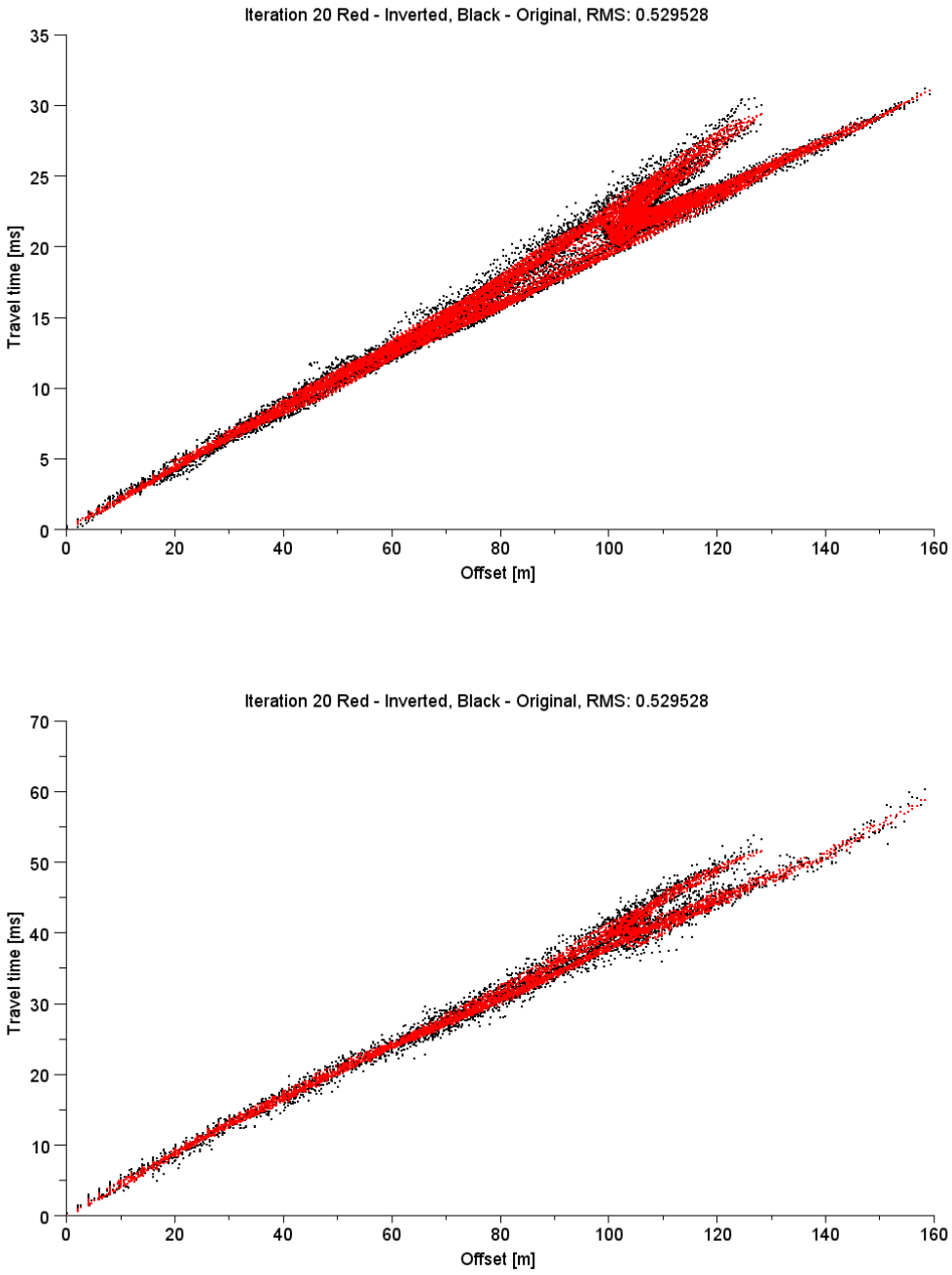

Fig. 4.31: Resulting travel time vs. offset after tomographic inversion. July 2012. Above P-waves, below S-waves.

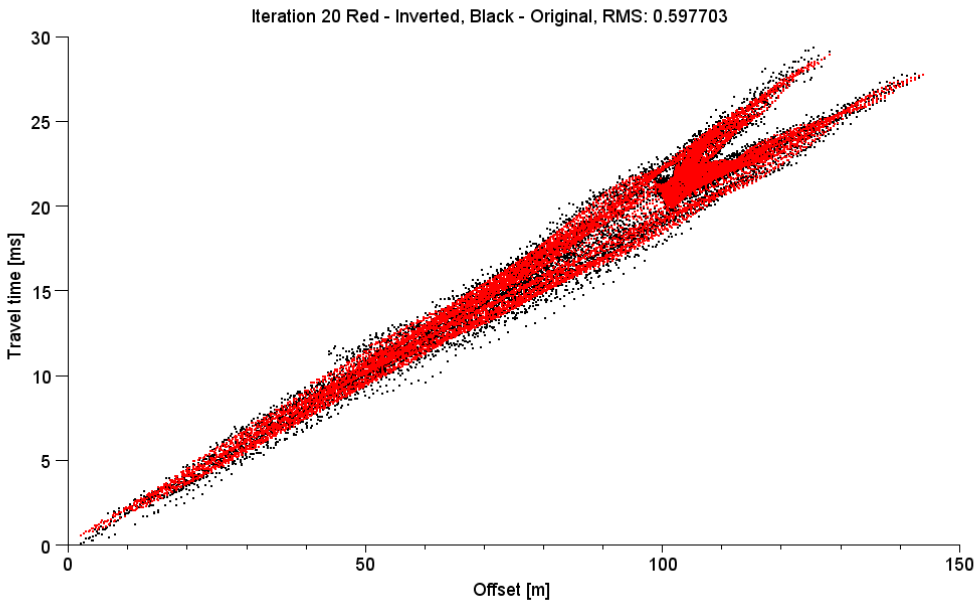

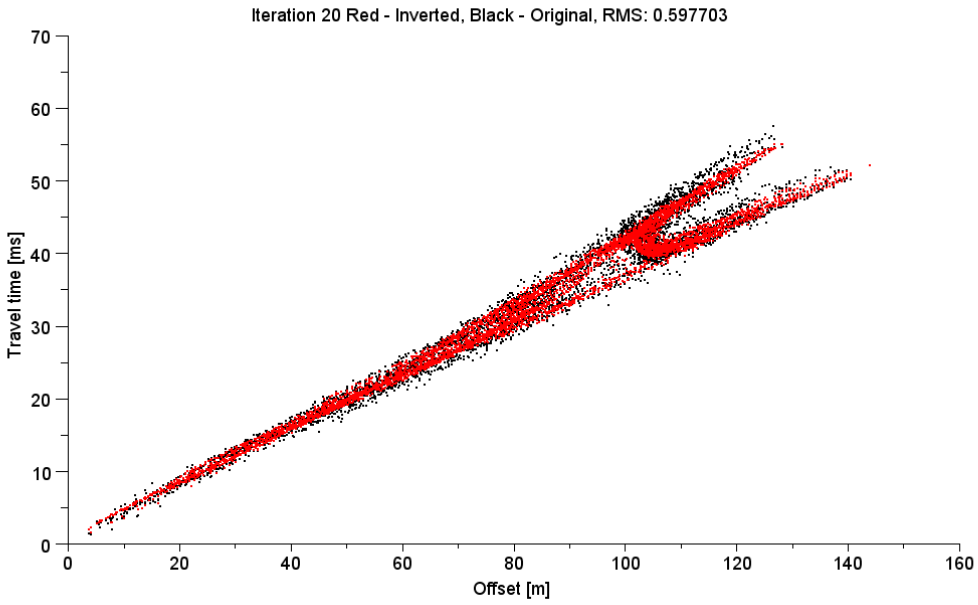

Fig. 4.32: Resulting travel time vs. offset after tomographic inversion. December 2012. Above P-waves, below S-waves.

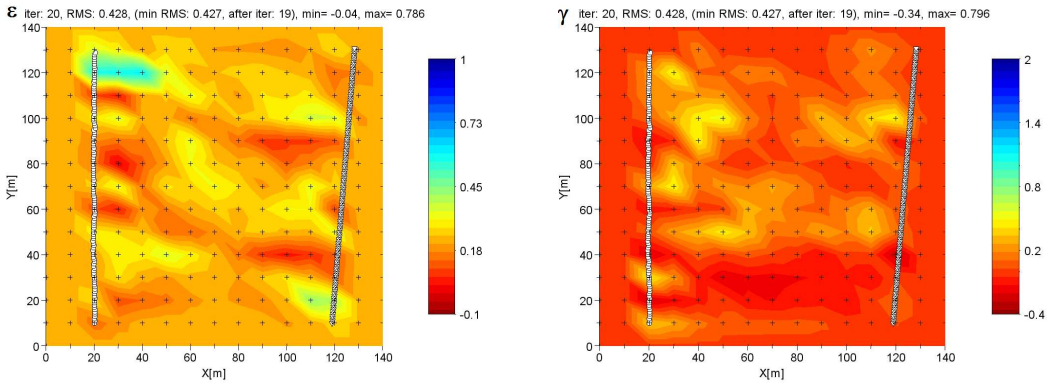

Fig. 4.33: Resulting Thomsen's parameters May 2005, left - parameter ε, right - parameter γ

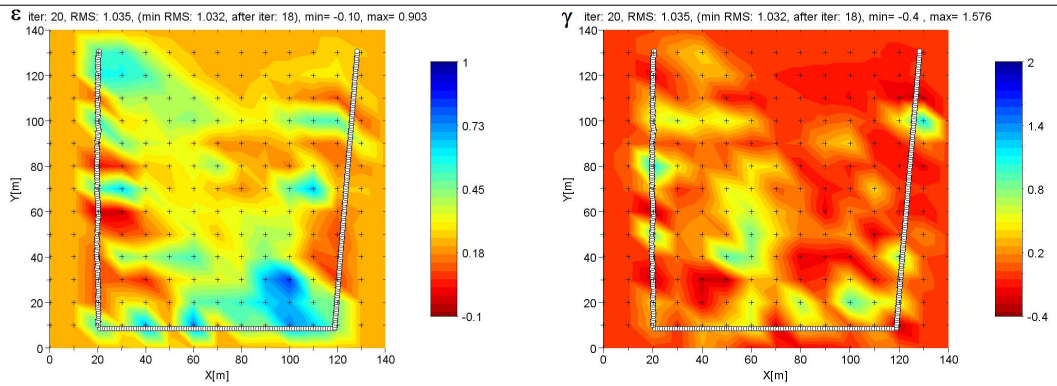

Fig. 4.34: Resulting Thomsen's parameters June 2011, left - parameter ε, right - parameter γ

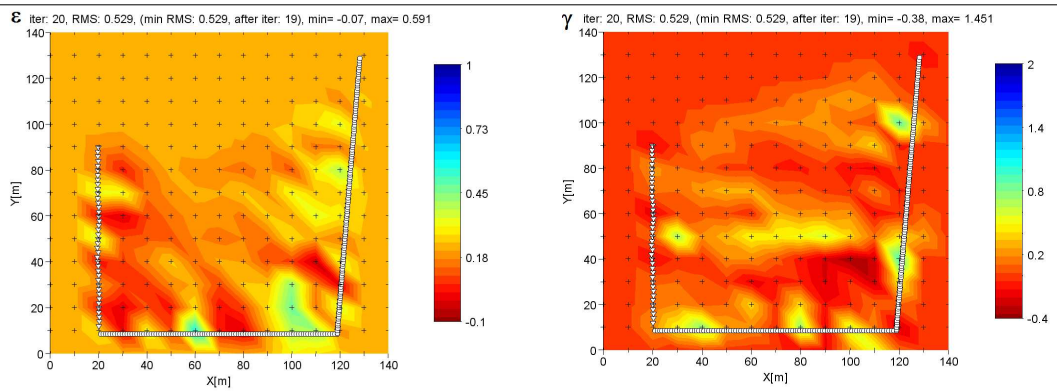

Fig. 4.35: Resulting Thomsen's parameters July 2012, left - parameter ε, right - parameter γ

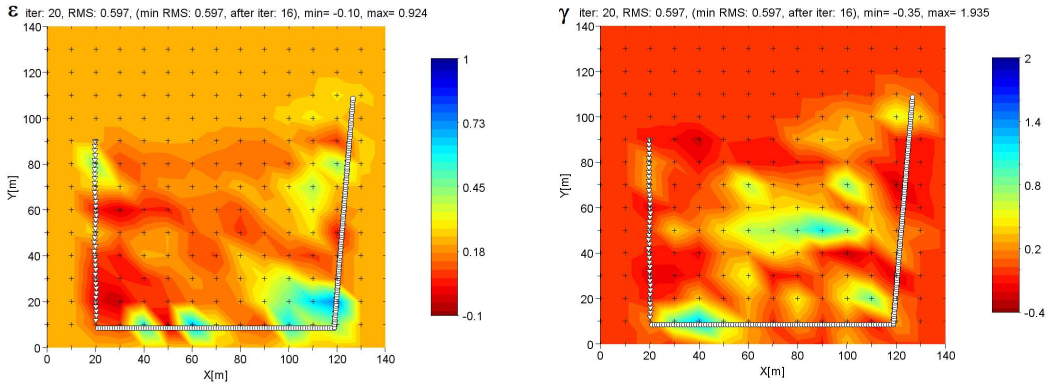

Fig. 4.36: Resulting Thomsen's parameters Dec 2012, left - parameter ε, right - parameter γ

4.2 Electrical resistivity – Real data

4.2.1 Geometry – Equipment

Having validated the theory for the resistivity measurements, we acquired the real data. Data was collected in pole-pole and dipole-dipole configurations. The choice of pole-pole configuration is preferred as it provides the fastest and most natural way of interpretation. Values of measured potentials are always positive (Herwanger, 2001) and the signal-to-noise ratio is generally better than for other configurations. The dipole-dipole data confirmed this assumption. We used Syscal Pro Switch from IRIS Instruments with 48 electrodes. The acquisition is completely automatic once the input file with the set-up is loaded and executed. The instrument uses its own specific cables with placements to attach 24 electrodes every 5 m. The switch box was placed in the middle of the TG and one cable was attached to the electrodes in the right half of TG and the MG, whereas the second cable was connected

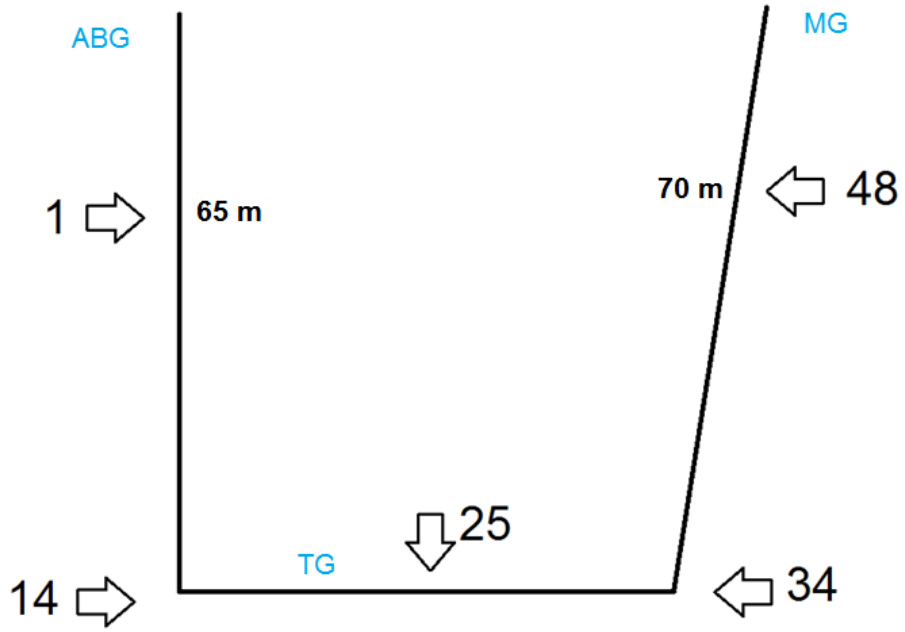

Fig. 4.37: Layout of resistivity measurements with sample electrodes.

to the electrodes in the other half of TG and continued in the ABG (Fig. 4.37). This electrode set-up covered a smaller area than that screened by the seismic method, but it was considered as sufficient to observe anisotropic behaviour.

With this acquisition geometry the cable in the ABG reached 65 m into the gallery and 70 m into the MG. As we were measuring the pole-pole configuration, we had to use two other current electrodes at 'infinite' distance. One of the electrodes was placed some 200 m outside the laboratory on the slope of the mountain. The total distance between the switch box and this electrode was around 950 m. The other 'infinite' electrode was placed 1 km inside the MG.

We measured the resistivity data during three campaigns along with the last three seismic acquisitions in 2011 and 2012. However, in 2011, we measured the potential using small electrodes, implanted only in the concrete. Because the concrete contains supporting metallic frames, the results were not possible to interpret and hence we had to construct new electrodes, that would penetrate the 30-40 cm thick concrete wall and plant them into the limestone underneath. The new electrodes were build from stainless steel and coated with an insulating layer so they would not get in contact with the concrete. There was a little concern about the possible free spaces between the limestone and the concrete, that might be filled with mineralized water running freely when the saturation of the rock is important, therefore creating a conductive layer, but we assumed the effect would be only local and would be affecting only the small offset measurements.

During the data treatment, we decided not to use the small offset measurements up to 25 m, because the inversion program that we used could not model the 3-D effect of the tunnel.

4.2.2 Data treatment

The measurements in LSBB were conducted in the tunnels of finite dimensions. Therefore, the medium was not complete and the current from the injection did not spread to all directions (4π) as it would do in small boreholes. The response of the medium did not follow a distribution from a surface injection either (2π) and therefore we had to quantify possible differences between these three different types of injections. We used Comsol Multiphysics Software to model the potentials produced by an injection inside the tunnel, by a point source buried inside the medium and by a point source on the surface for both isotropic and anisotropic media. Figure 4.38 shows that the values of potentials from the surface injection are as expected twice as big as those coming from an injection within a medium (the current from the surface injection has only half the volume of the medium, compared to the 4π injection, therefore it needs to be double). The potential distribution from the injection on the wall of a finite tunnel (diameter 4 m) has values similar to the 4π injection, but differs for short offsets below 15 m, where it is located between the two configurations. We decided not to use any data with shorter offsets to 25 m.

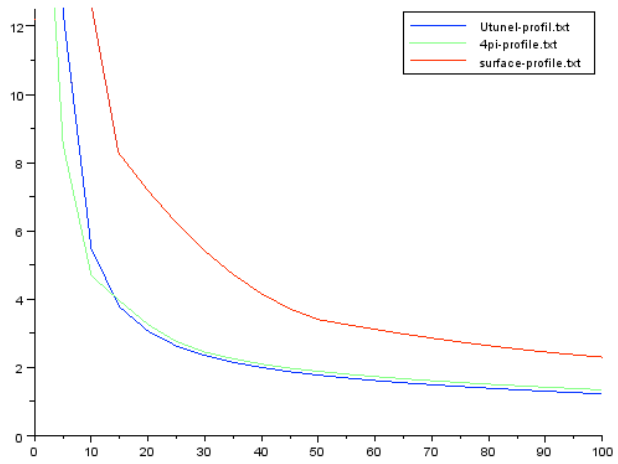

Fig. 4.38: Modelled difference between injections in a tunnel of diameter 4 m (in blue), inside a medium (4π - in green) and on a surface (2π - in red).

As a pre-treatment visualisation tool to check the quality of the data, we plotted the measured apparent resistivities as a function of number of measure. This way, any irregularities such as faulty electrodes, big spikes not consistent with the data would become apparent (Figs. 4.39 and 4.40, top plots).

The resistivity of sane limestone can vary between the order of 10^2 and 10^4 Ω.m (e.g. Wiese, 2012). Fractured limestones, especially with some moisture, filled with soil and weathered remains will have resistivities below those values. The acquired data from July 2012, in the order of measurement, are shown in figure 4.39. At first, these data might look chaotic, but one can clearly see some cyclic behaviour and continuity. The top figure represents all data without any treatment. The middle figure is without the short offset measurements. The bottom figure shows the measured data with some arbitrary modelled data only to show what variations of the data might be expected and to show that for the July 2012 the acquired data are of good quality and the oscillations are normal.

For December 2012 the data is shown in the figure 4.40. Visualisation of all data (top) shows some irregularities and after the examination, one electrode was found faulty and was removed from the following plots and from all data treatment. The bottom figure does not contain the faulty electrode and does not contain either the short-offset measurements.

The comparison between the two successful campaigns in July and December 2012 (Fig. 4.41) shows that the spatial variation of measured resistivities matches very well, however, it was expected that the differences between the two campaigns would be bigger due to the seasonal variations of water content.

It might be difficult to visualise the data and the evolution of apparent resistivities with 1000 values in a row. To help with the visualisation, the variations of apparent resistivities for selected electrodes (summer 2012) are shown in increasing order (Fig. 4.42) and with

respect to the angle of measurement (Fig. 4.43). Variations of all apparent resistivities with respect to the angle for both campaigns are shown in figures 4.44 and 4.45.

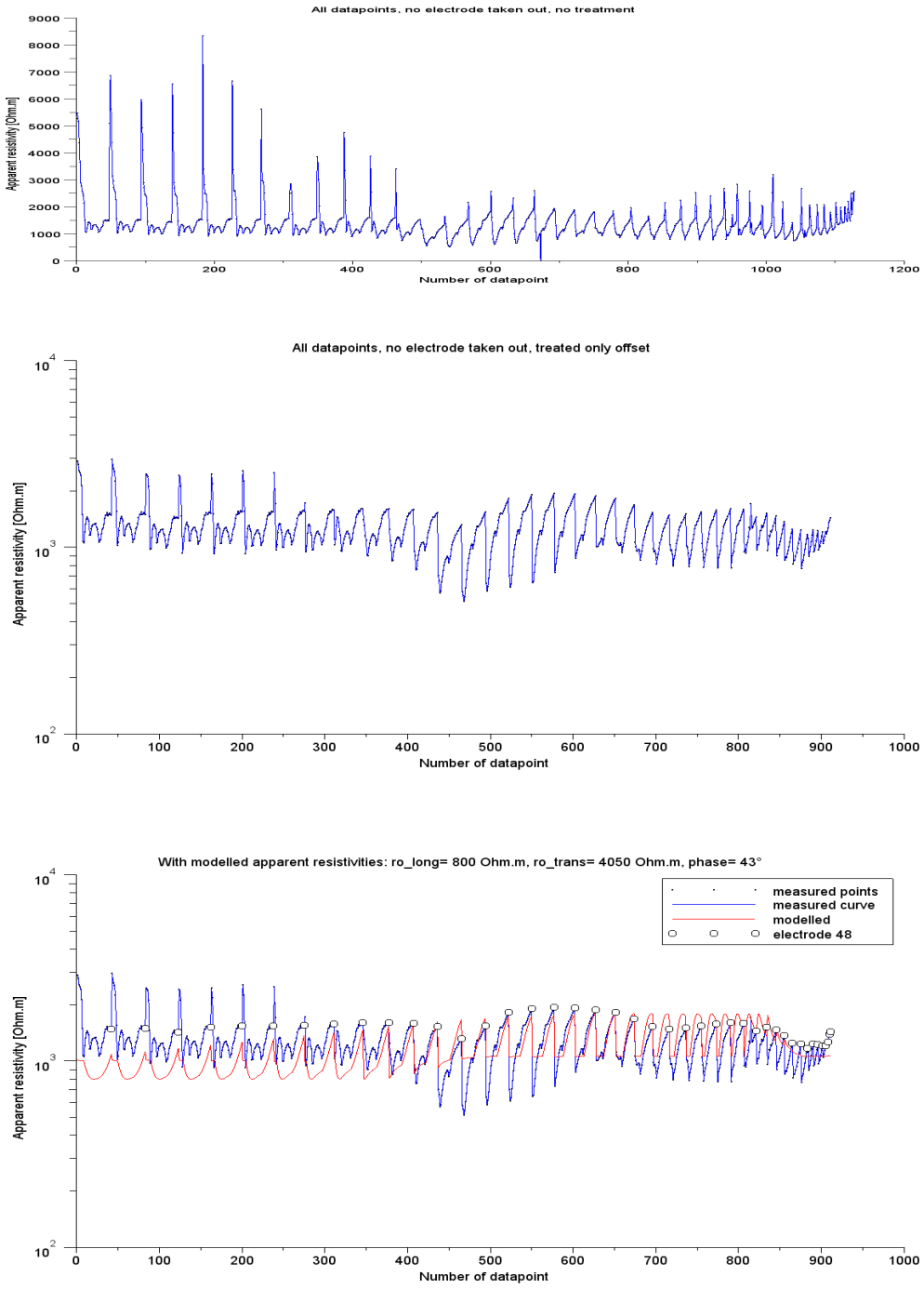

Fig. 4.39: Unfiltered data from July 2012 (top), filtered data without the unaccepted offets smaller than 25 m (middle) and filtered data with expected fit with arbitrary longitudinal and transversal resistivities (based on the minima and maxima found in the figure – bottom). Note the different scales between unfiltered and filtered data.

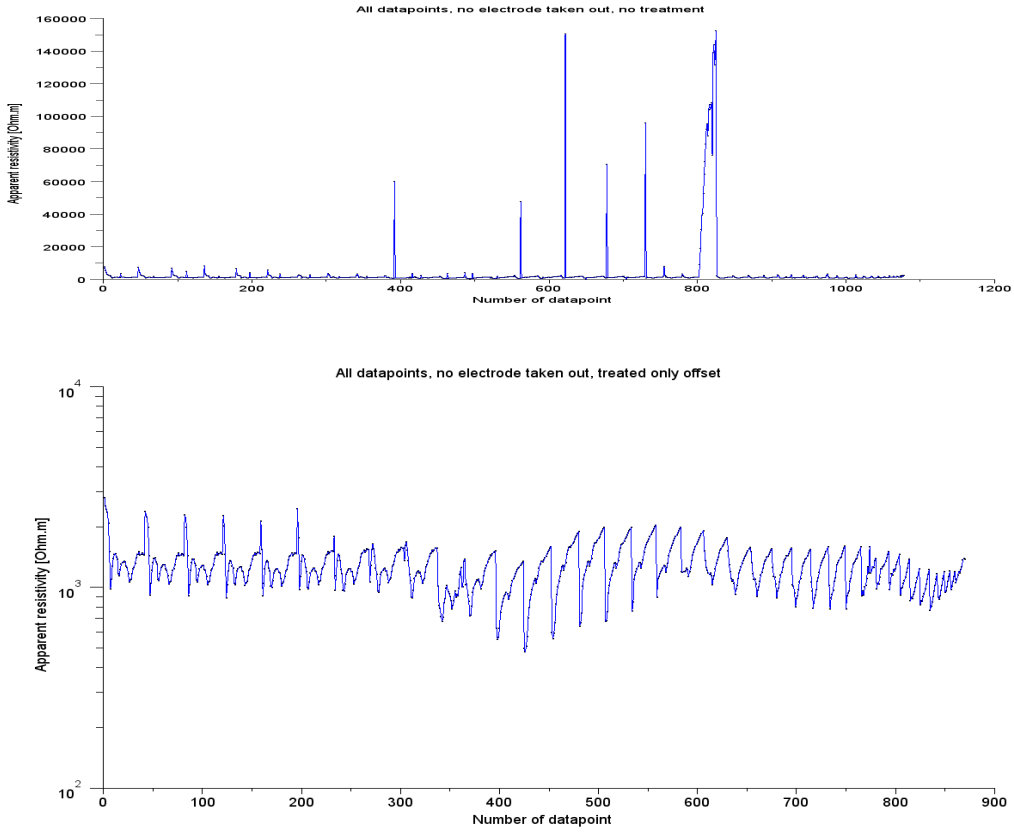

Fig. 4.40: Unfiltered data from December 2012 (top), filtered data without the unaccepted offets smaller than 25 m and without the measurements from faulty electrode (bottom).

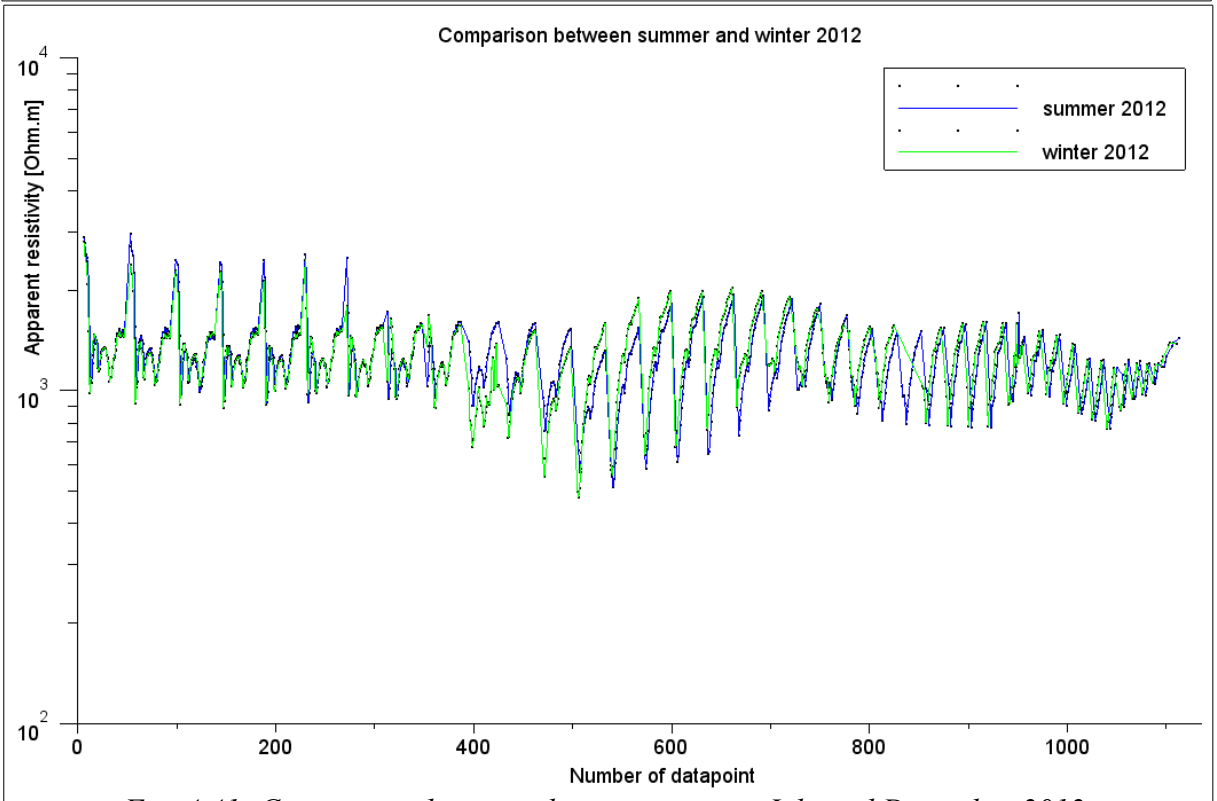

Fig. 4.41: Comparison between the campaigns in July and December 2012.

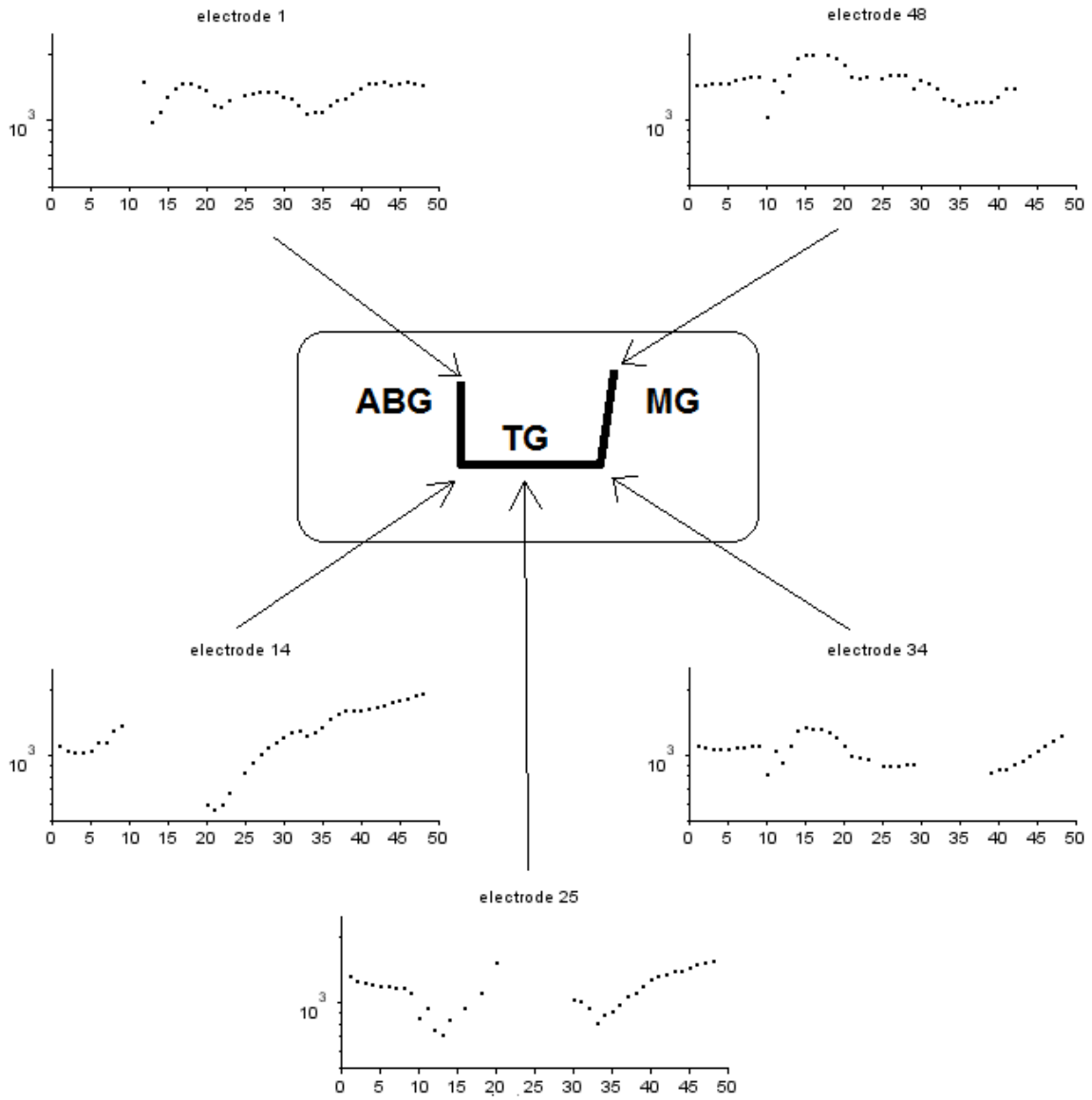

Fig. 4.42:Variations of apparent resistivity for all measurements containing selected electrodes (at the ends and at the corners of ABG and MG and in the middle of TG) in order of increasing number of electrodes. The measurements around the selected electrode are not shown because they were not accepted due to the small offset. Only the results from July 2012 are shown as December 2012 does not differ much.

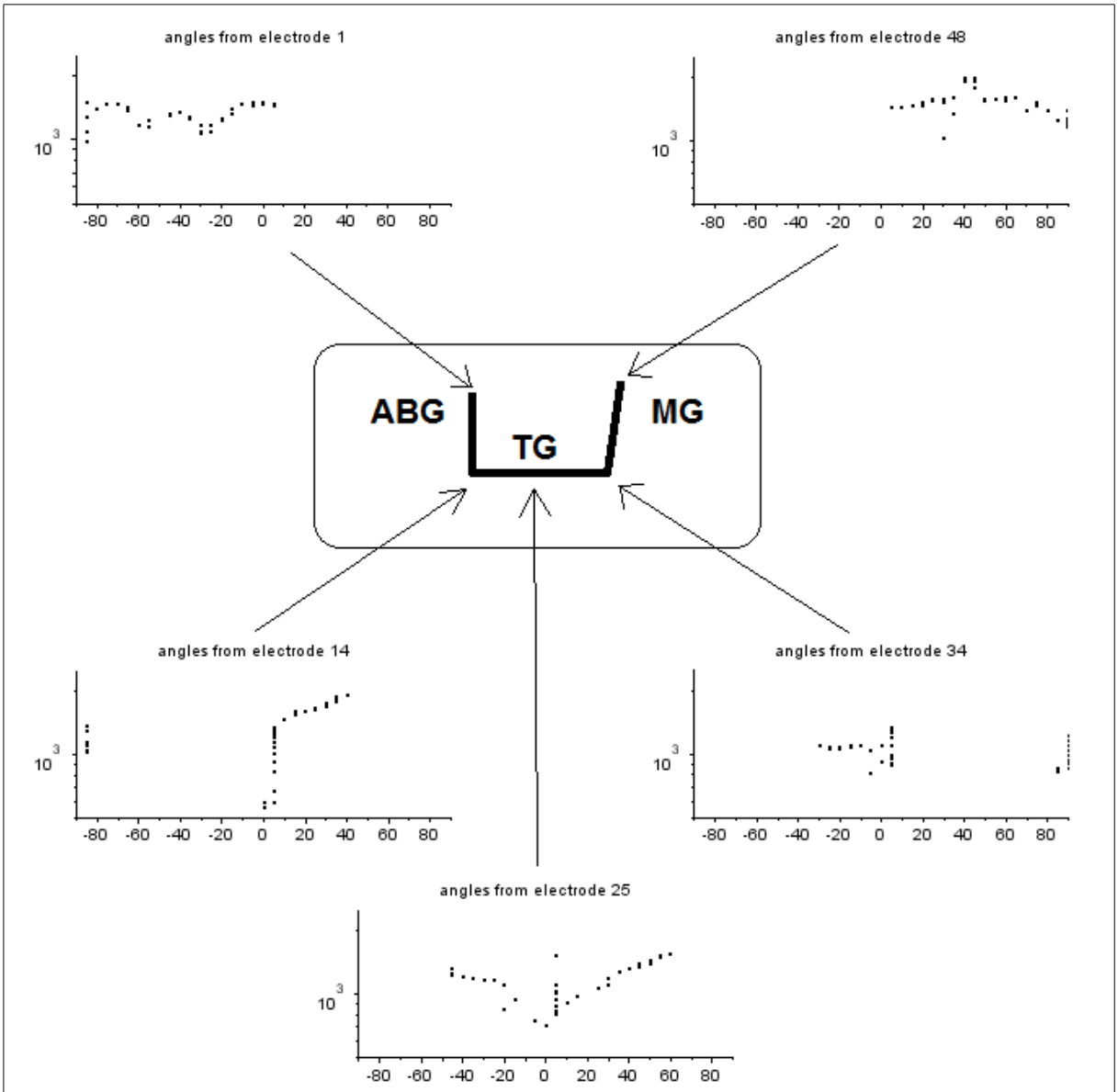

Fig. 4.43: Variations of apparent resistivity for all measurements containing selected electrodes (at the ends and at the corners of ABG and MG and in the middle of TG) with respect to the angle. Only the results from July 2012 are shown as December 2012 does not differ much.

4.2.3 Homogeneous anisotropic Monte-Carlo Markov Chain inversion

Similarly to the seismic data, we first inverted the data using a homogeneous inversion to observe whether the data generally followed some pattern. For the pole-pole configuration, 48 electrodes give 1128 combinations of measurements. The data was treated again as in seismics in two approaches: 1) considering the whole dataset, where each data point was calculated using its own geometry and compared with the measured values and 2) using averaged values for each direction, using bins of ± 2.5°.

These results could be used later as a starting point for tomographic inversions. For both campaigns, the averaged azimuthal resistivities display a curve with two maxima over 180° (Figs. 4.44 and 4.45). It soon became clear that the misfit of modelled versus measured data will never have a minimal optimum value because the ellipsoid of modelled apparent resistivities will have only one maximum over 180° and not two.

As the MCMC inversions were always trying to minimise two maxima with one, the error was always large with many big differences between measured and modelled data. The best result is found close to the central value of apparent resistivity with only small oscillation (red curve in fig. 4.44). At first, we thought that the existance of two maxima was caused by the effect of gallery and having discarded all data from small offset would remedy the problem. This approach proved unsuccessful and the two maxima remained in the data after this treatment. Examining the data further, we found out that none of the available software programs would be able to find the two maxima and therefore conclude successfully the inversion process.

The results for the MCMC inversion for averaged data are not shown because they are similar to the red curve in figures 4.44 and 4.45. Further examination of the data showed that

because of the two maxima, the data could be fitted only locally for some parts of the figure. They could be fitted in the remaining part with another set of input parameters. More detailed explanation is in the figure 4.46 and in the following paragraph.

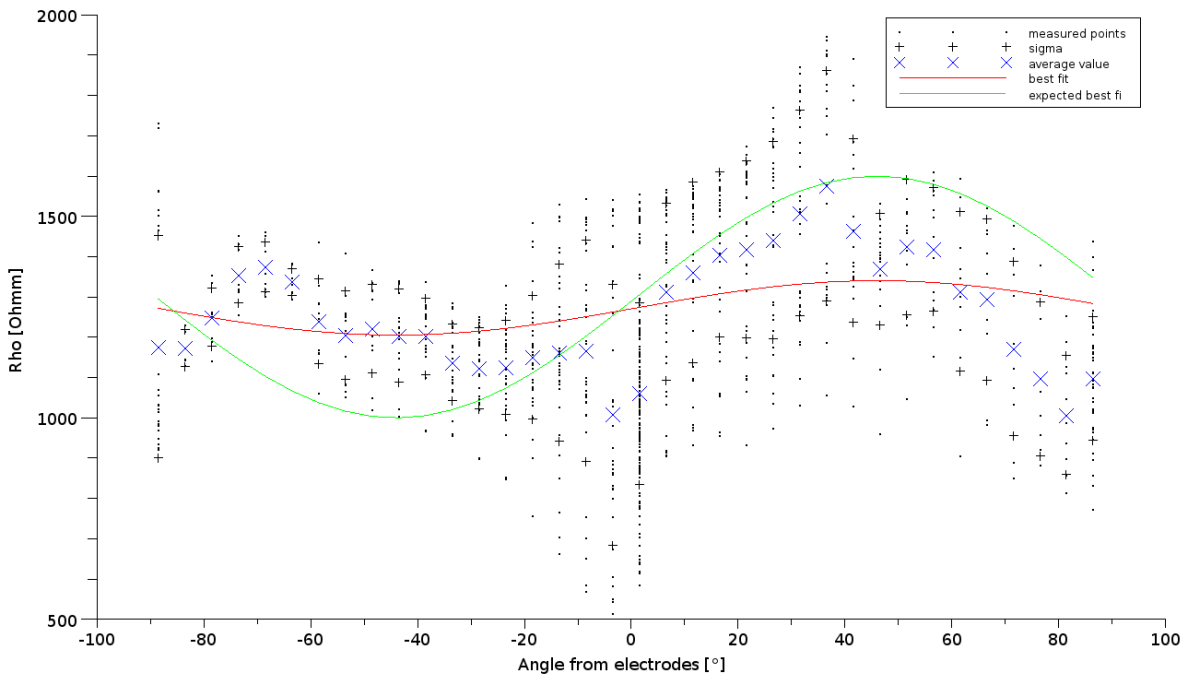

Fig. 4.44: Averaged azimuthal resistivities for July 2012. Red curve shows the best automatic result based on minimising the root mean square error between the averaged measured (blue crosses) and modelled data (red curve). Green curve is the curve with expected amplitude, but cannot be calculated automatically, as it should have two maxima.

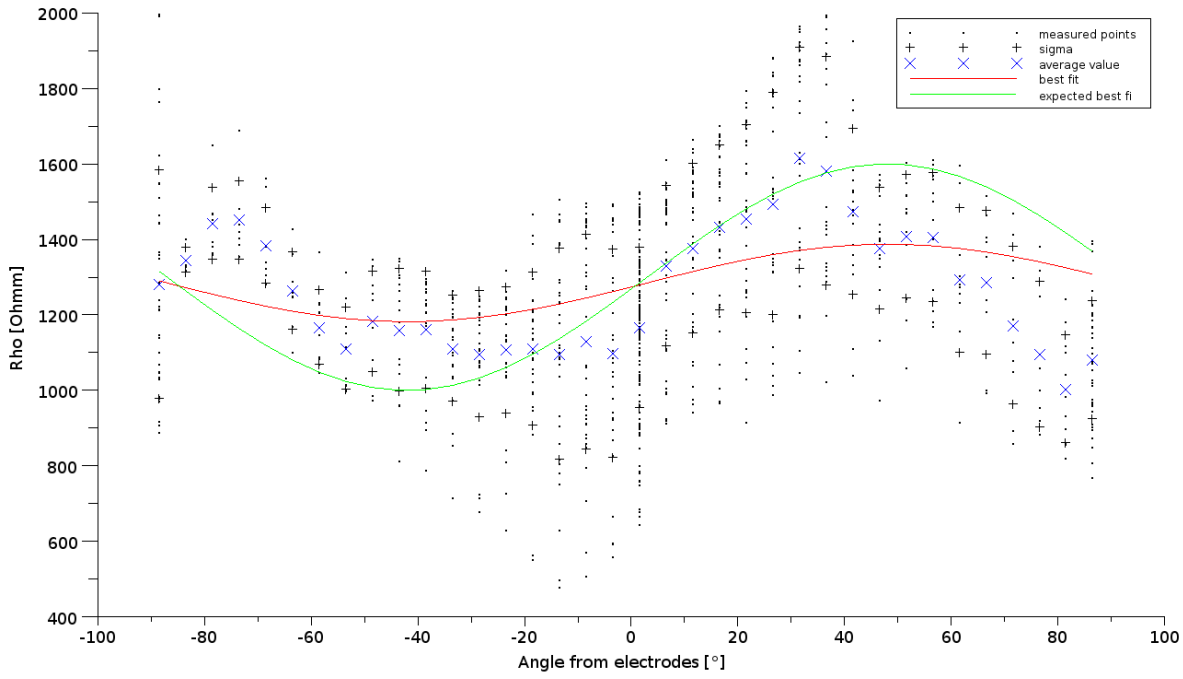

Fig. 4.45: Averaged azimuthal resistivities for December 2012. Red curve shows the best automatic result based on minimising the root mean square error between the averaged measured (blue crosses) and modelled data (red curve). Green curve is the curve with expected amplitude, but cannot be calculated automatically, as it should have two maxima.

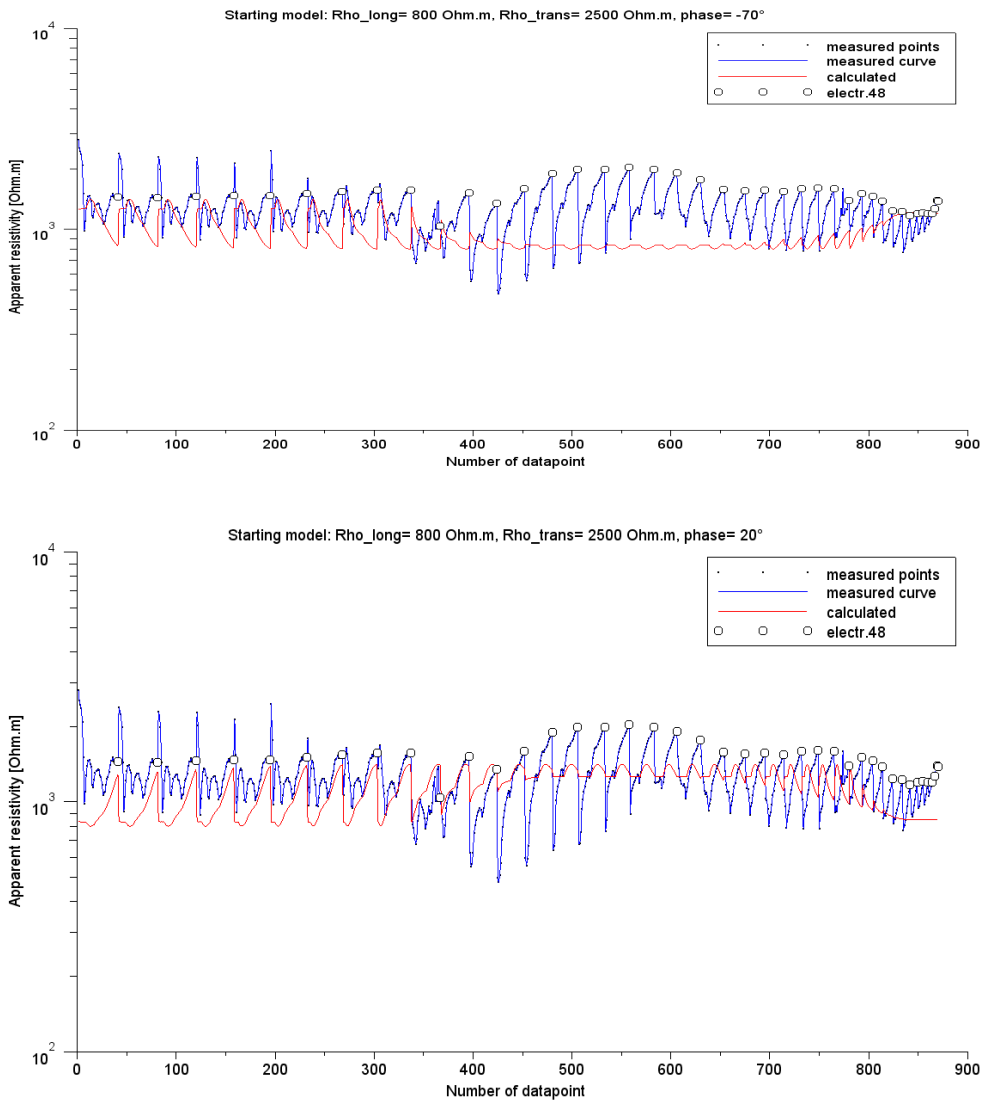

Fig. 4.46: Comparison of two fits with different phases. Top: data with phase φ_0= -70°, bottom: data with phase φ_0= 20°. Top: modelled data (red curve) matches the small maxima at the beginning and matches the variations around the measures 700-800. Bottom: modelled data matches the bigger maxima for the beginning and the middle of the figure. At the end near the measure 800, the variations of maxima and minima of modelled are moving in opposite direction from the measured ones.

Figure 4.46 top, shows the measured and modelled data with a phase angle φ_0=-70°. It can be observed that the red modelled curve is outlining the maxima at the end, between the measures between 700 and 800. The bottom figure is shifted to φ_0=20° (90° from previous) with the same values for transversal and longitudinal resistivities. In this case, the remaining

part of the dataset has matching maxima whereas the data in the position of former fit (top figure), the evolution of maxima is completely opposite (measure 800).

Because of these shifting maxima, the same unsatisfactory result was obtained by running the MCMC on the whole set of measured data (not only on the averaged values) and the best result after 500.000 iterations has very little difference between the transversal and longitudinal resistivities (Fig. 4.47 top and bottom, for July and December 2012

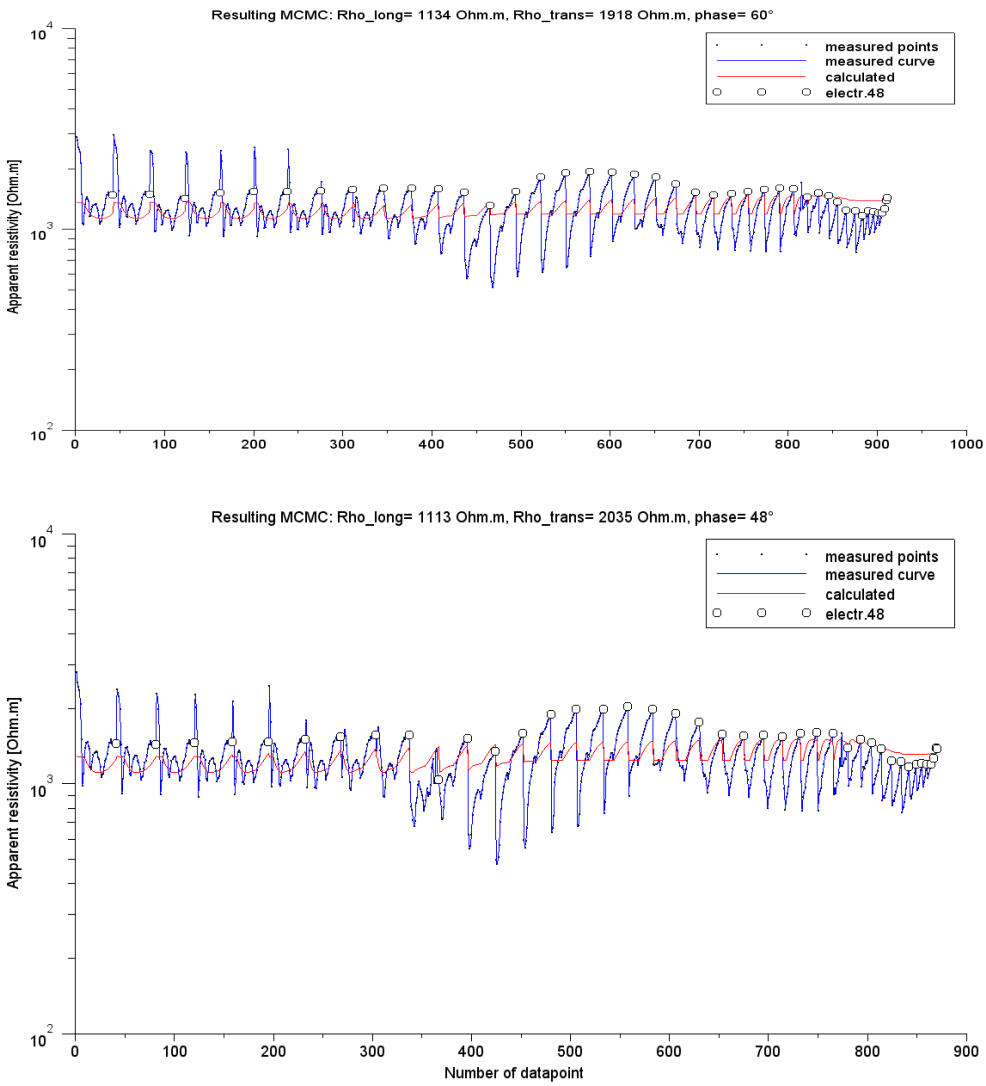

Fig. 4.47: Resulting best parameters from MCMC inversion after 500.000 iterations for July (top) and December 2012 (bottom). Notice the small difference between the transverse and longitudinal resistivities.

respectively). For July, the ρ_T= 1918 Ω.m, ρ_L= 1134 Ω.m and for December ρ_T= 2035 Ω.m, ρ_L= 1113 Ω.m. The minima of the curve correspond to the longitudinal resistivity, therefore $\rho_L \approx$ 1100 Ω.m. The maxima correspond to the mean resistivity ρ_m calculated as a square root of product (ρ_L*ρ_T), $\rho_m \approx$ 1500 Ω.m .

Another puzzling observation of both campaigns, is that for a given azimuth, the apparent resistivities are increasing with offset. This effect can be best seen towards the end of the recording, after the measures 850 for July and after the measure 800 for the December campaign. These measurements are all within the MG, therefore in the same direction, yet

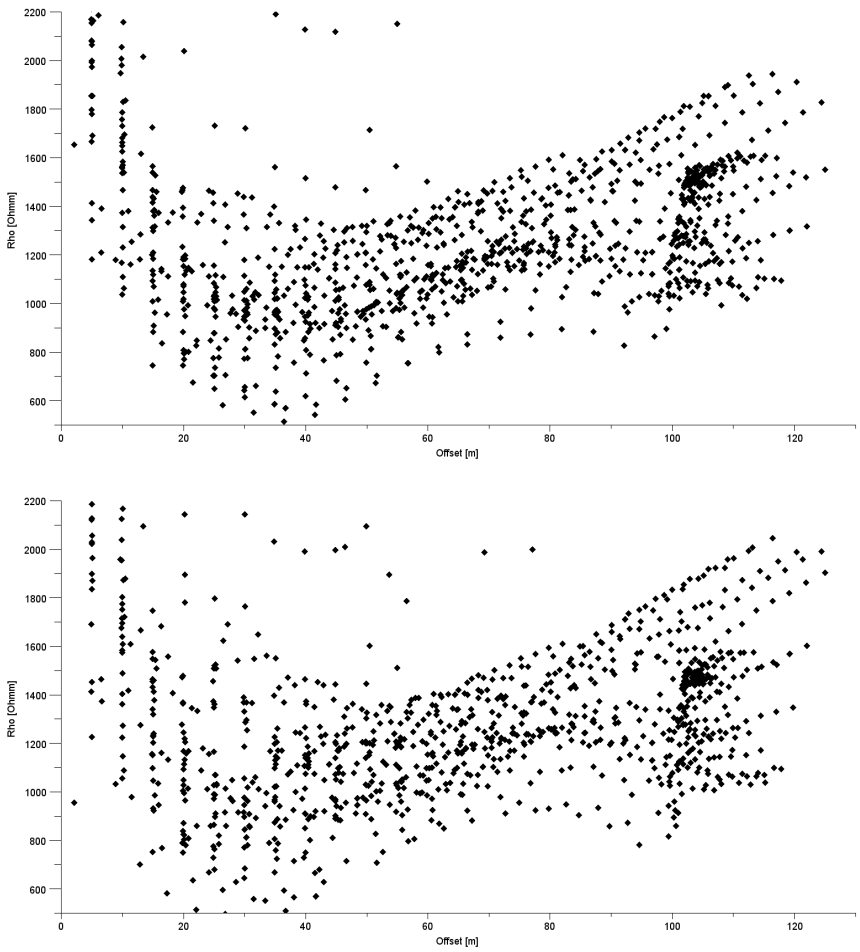

Fig. 4.48: Apparent resistivities with respect to the offset. Top: July 2012 and bottom: December 2012. The high resistivities in the first half of each campaigns come from the effect of the galleries at short offsets.

the apparent resistivities show increasing values towards the last electrode 48 (maxima with dots). The figure 4.48 shows a nice traceable trend at larger offsets for both campaigns.

It is clear that there are two main issues that hamper the interpretation of this data. The first one is the two maxima over 180° and the second is the increasing resistivity with increasing offset.

4.2.4 Anisotropic tomography "3Dres_GQG"

We used a program created by Dr. Zhou from Adelaide University (Zhou et al., 2009). During the inversion, for the calculation of Fréchet derivatives, the program uses the analytic solutions described by Greenhalgh et al. (2009b). The program "3Dres_GQG" tries to find only one maximum and one minimum over 180° and for the same reason as in the Monte-Carlo inversion, the data could not be fit. Additionally we had problems calibrating the program to our needs and the inversion would work with our synthetic models only if the starting parameters were very close to the modelled values.

After a few months of unsuccessful testing, we abandoned this program as we did not have sufficient background and time to fix the problem. Other anisotropic tomography programs were not freely available and the use of Comsol Multiphysics, even though it was promising, shattered on simple geometric transformations and the program stopped responding when the tensor of resistivity was rotated.

4.2.5 Network of conductors

Several publications mention that having several maxima in a resistivity vs. azimuth graph can serve as qualitative measure of number of fracture sets and their orientations (e.g. Boadu et al., 2005; Wishart et al., 2008), but to our knowledge there has been no attempt of quantifying or modelling the different sets of fractures. These measures were obtained at the surface with either azimuthal resistivity surveys (ARS) or square-array configuration, therefore covered the whole 360° of the azimuth. Our acquisition geometry at LSBB inside the tunnels didn't cover the same aperture, but the azimuthal dependence in our data is clearly visible.

Busby (2000) states that a multiple-peaked polar plot may indicate more than one fracture orientation, but without further evidence, it is advised to adopt the isotropic interpretation and the degree of anisotropy might be used only as an estimation of fracture density.

We were investigating these effects and started to model the fractures in LSBB first as a set of parallel conductive wires inside a non-conductive medium. The current was injected at both ends where the wires were connected and angular dependency of apparent resistivity around the source was observed (Fig. 4.49).

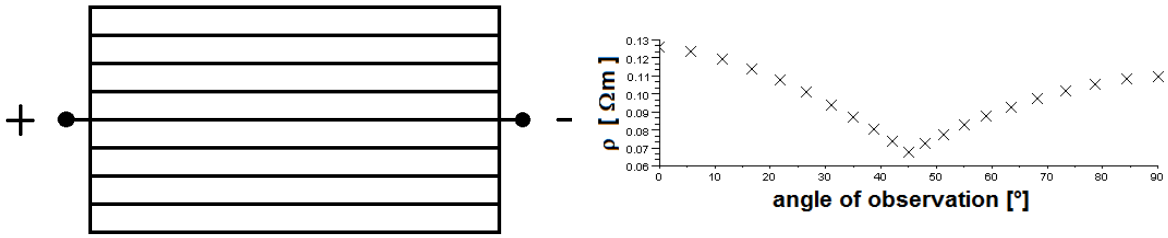

Fig. 4.49: Conceptual modelling of parallel conductive wires inside a non-conductive medium (left). Black dots represent the injection points for the current. On the right, the angular variation of apparent resistivity measured around one of the sources. In the tested model, there were more parallel wires, here only the draft is shown. The values on the vertical axis show relative variations for an arbitrary injection.

We complicated the model further, by crossing the parallel network with another parallel network and created a rectangular mesh, simulating an orthogonal fracture system in an insulating medium where each direction could have different conductivities (σ_1 and σ_2 in later text), thus simulating the anisotropic medium (Fig. 4.50). This way, in addition to the previous angular dependence of apparent resistivity for one set of conductors, also the flow of current was anisotropic. The two maxima were also successfully modelled (Fig. 4.51). Also the increase of apparent resistivities with offset was confirmed (Fig. 4.52).

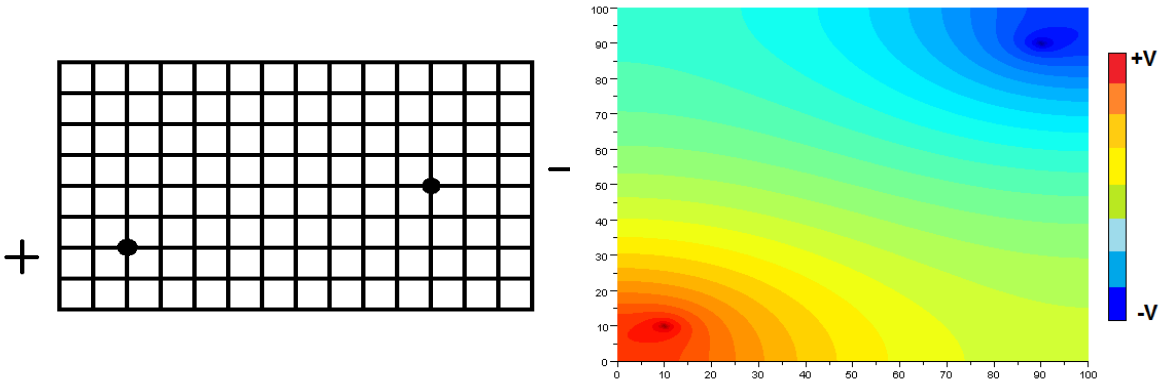

Fig. 4.50: Conceptual modelling of orthogonal fracture system by two sets of parallel conductive wires (left), with a resulting potential distribution (right). Each direction of the wires has different resistivities. Black dots represent the injection points inside a grid.

The network of wires in the rectangular mesh was programmed using Fortran programming language. The distribution of the potential obeys Poisson's equation (3.18). The potential was discretised by being modelled only in the nodes, where the wires crossed. In order to express and solve mathematically the distribution of potential with respect to the current injections, the flow of the current through the nodes of the mesh was modelled using Kirchhoff's law of conservation of current. This law states that, except for nodes of current injection, the sum of all incoming currents into any node must be equal to the sum of all outgoing currents. In other words, sum of all currents must be equal to 0:

$$\sum I = 0 \qquad (4.3)$$

Each node was assigned a number and to express the connections between the nodes they were placed in a square matrix M of size (NxN), where N represents the number of all nodes in the mesh. The i-th line of the matrix contains the connections from node i to all other nodes.

At each position of matrix M_{ii}, the sum of possible entering currents is stored. Each node has four neighbouring nodes (except the borders and corners of the mesh), therefore the

matrix is very sparse, each line with only four additional non-zero entries (three for the border nodes, two for the corner nodes) and at these positions the exiting current is recorded. All spacings between the nodes are considered equal, therefore the only variable in the current flow is the conductivity σ between the considered nodes. All the neighbouring nodes connected by a wire of conductivity σ_1 contain the entry of M_{ij}= - σ_1, with j ≠ i. All the other nodes connected by wire of conductivity σ_2 contain the entry M_{ij}= - σ_2, with j ≠ i. The position M_{ii} contain then the negative sum of all non-diagonal entries of i-th line in order for the sum of each line to be equal to 0:

$$M=\begin{pmatrix} \sigma_1+\sigma_2 & -\sigma_1 & 0 & 0 & -\sigma_2 & 0 & 0 & 0 & \cdots & 0 \\ -\sigma_1 & 2\sigma_1+\sigma_2 & 0 & 0 & 0 & -\sigma_2 & 0 & 0 & \cdots & 0 \\ 0 & -\sigma_1 & 2\sigma_1+\sigma_2 & -\sigma_1 & 0 & 0 & -\sigma_2 & 0 & \cdots & 0 \\ 0 & 0 & -\sigma_1 & \sigma_1+\sigma_2 & 0 & 0 & 0 & -\sigma_2 & \cdots & 0 \\ -\sigma_2 & 0 & 0 & 0 & \sigma_1+2\sigma_2 & -\sigma_1 & 0 & 0 & \cdots & 0 \\ 0 & -\sigma_2 & 0 & 0 & -\sigma_1 & 2\sigma_1+2\sigma_2 & -\sigma_1 & 0 & \cdots & 0 \\ 0 & 0 & -\sigma_2 & 0 & 0 & -\sigma_1 & 2\sigma_1+2\sigma_2 & -\sigma_1 & \cdots & 0 \\ \vdots & \vdots & \vdots & \vdots & \vdots & \vdots & \vdots & \vdots & \ddots & \vdots \\ 0 & 0 & 0 & 0 & 0 & 0 & 0 & 0 & \cdots & \sigma_1+\sigma_2 \end{pmatrix} \quad (4.4)$$

In this way the matrix contains non-zero values only in the primary diagonal, two neighbouring diagonals and two other diagonals at a distance from main diagonal equal the number of nodes in the direction of node numbering. Poisson's equation (3.18) in discretised matrix representation for 2-D medium has the form:

$$M_{ij}U_i=I_j \quad (i,j=1,N) \quad (4.5)$$

The current injection was simulated by imposing a positive potential at the injection point for the positive source and a negative one with the same amplitude at the other injection point. In the matrix this was done by eliminating the respective lines and columns by Gauss elimination process with the current vector I being the right hand side of the equations. The example of the new updated matrix M' with injection simulated at third node

by imposing potential U^+ and sink electrode placed at sixth node by imposing potential U^-.

$$M' = \begin{pmatrix} \sigma_1+\sigma_2 & -\sigma_1 & 0 & 0 & -\sigma_2 & 0 & 0 & 0 & \cdots & 0 \\ -\sigma_1 & 2\sigma_1+\sigma_2 & 0 & 0 & 0 & 0 & 0 & 0 & \cdots & 0 \\ 0 & 0 & 0 & 0 & 0 & 0 & 0 & 0 & \cdots & 0 \\ 0 & 0 & 0 & \sigma_1+\sigma_2 & 0 & 0 & 0 & -\sigma_2 & \cdots & 0 \\ -\sigma_2 & 0 & 0 & 0 & \sigma_1+2\sigma_2 & 0 & 0 & 0 & \cdots & 0 \\ 0 & 0 & 0 & 0 & 0 & 0 & 0 & 0 & \cdots & 0 \\ 0 & 0 & 0 & 0 & 0 & 0 & 2\sigma_1+2\sigma_2 & -\sigma_1 & \cdots & 0 \\ \vdots & \vdots & \vdots & \vdots & \vdots & \vdots & \vdots & \vdots & \ddots & \vdots \\ 0 & 0 & 0 & 0 & 0 & 0 & 0 & 0 & \cdots & \sigma_1+\sigma_2 \end{pmatrix} \quad (4.6)$$

Respective vector of currents, treated as a right hand side of the matrix M, during the Gauss elimination:

$$I' = [\,0 \quad (\sigma_1 U^+ + \sigma_2 U^-) \quad 0 \quad \sigma_1 U^+ \quad \sigma_1 U^- \quad 0 \quad (\sigma_2 U^+ + \sigma_1 U^-) \quad \ldots \, 0\,]^T \quad (4.7)$$

The zero lines and columns are removed from the matrix M', so are the eliminated entries in I' (entries in red colour). Matrix M' therefore has dimension ((N-2)x(N-2)) and the I' has the dimension of (N-2). In order to calculate the potential distribution, the equation below needs to be solved:

$$U_i = (M')^{-1}_{ij} I'_j \quad (i, j = 1, \ldots, N) \quad (4.8)$$

We started with two orthogonal conductor series, creating the chessboard-like structure with segments of 1 m. (Fig. 4.50). Gradually, the angle between the two directions of conductors was changed from 90° to 70°, 50°, 30° and to 10°. The distance between the nodes on each wire of the mesh stayed unchanged (Fig. 4.53)

The peaks of respective modelled apparent resistivities confirm the theory that they should be following the direction of fracture sets. Figures 4.54 to 4.57 show the evolution of peaks from 70° to 10° respectively. At each step, the apparent resistivity was calculated for all azimuths and the two maxima are clearly visible in all cases. Also the space between the

two maxima is getting smaller with decreasing angle between the conductor series, although the spacing does not entirely match the angle between the conductors.

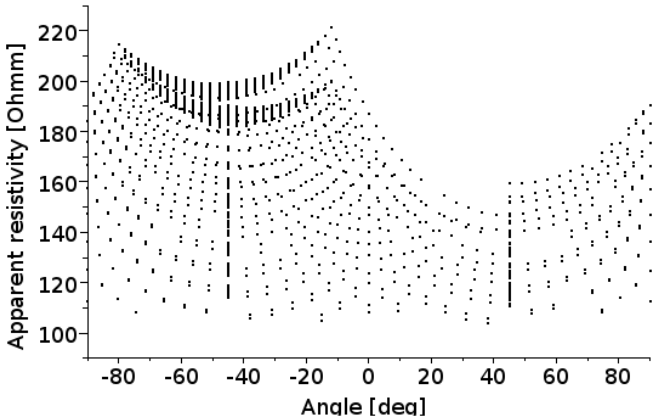

Fig. 4.51: Modelled apparent resistivities with respect to the angle of measurement from a network of perpendicular conductors in a non-conductive matrix. Potential was measured at the nodes of a regular grid, where the conductors crossed. The angle 0° represents direction of one of the conductors .(ρ_1=1 Ωm in direction of 0°, ρ_2=0.33 Ωm in 90°)

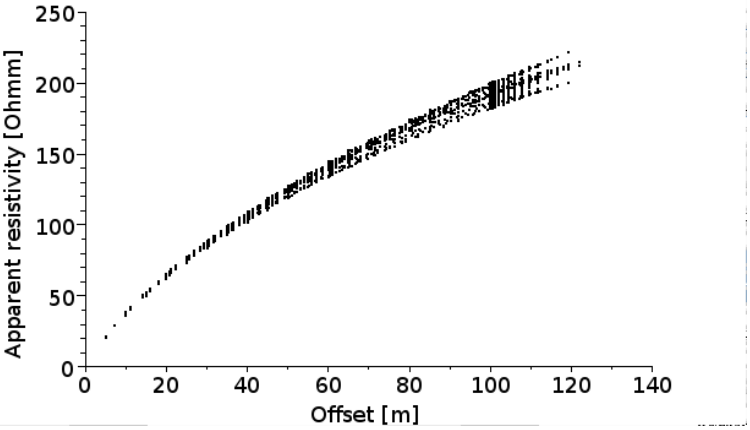

Fig. 4.52: Modelled apparent resistivities as a function of the offset of measurement from a network of perpendicular conductors in a non-conductive matrix. Potential was measured at the nodes of a regular grid, where the conductors crossed.(ρ_1=1 Ωm in direction of 0°, ρ_2=0.33 Ωm in 90°)

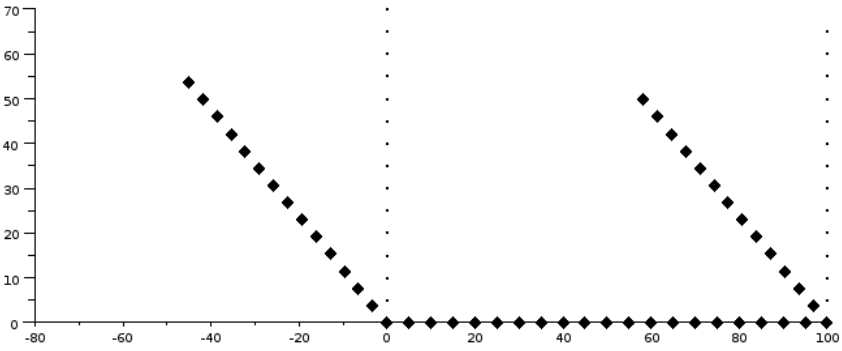

Fig. 4.53: Sketch of skewing the model for the next figures. Small dots represent the original model with fractures in the orthogonal directions, Thick squares represent the new position.

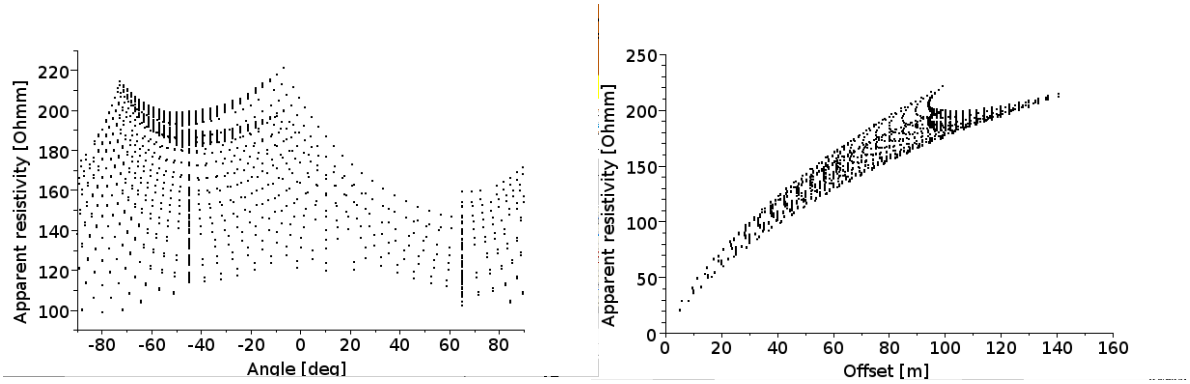

Fig. 4.54: Modelled apparent resistivities with respect to the angle and the offset of measurement from a network of conductors in a non-conductive matrix with an angle of 70° between the conductors. Potential was measured at the nodes of a regular grid, where the conductors crossed.

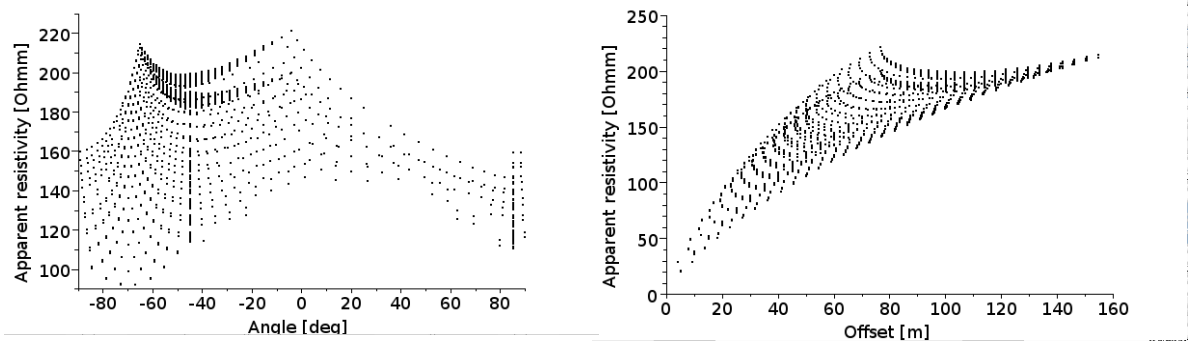

Fig. 4.55: Modelled apparent resistivities with respect to the angle and the offset of measurement from a network of conductors in a non-conductive matrix with an angle of 50° between the conductors. Potential was measured at the nodes of a regular grid, where the conductors crossed.

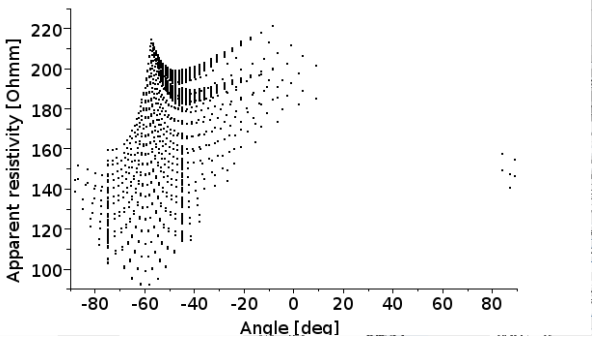

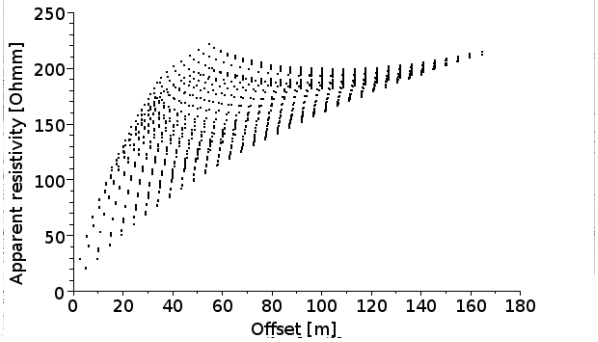

Fig. 4.56: Modelled apparent resistivities with respect to the angle and the offset of measurement from a network of conductors in a non-conductive matrix with an angle of 30° between the conductors. Potential was measured at the nodes of a regular grid, where the conductors crossed.

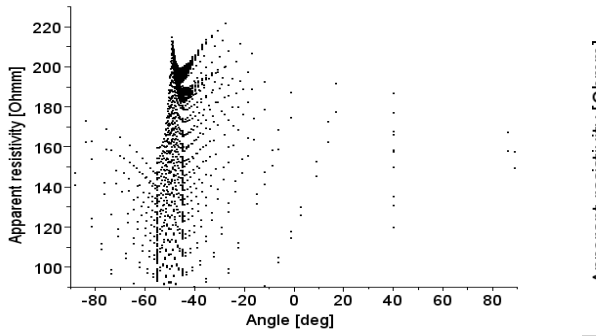

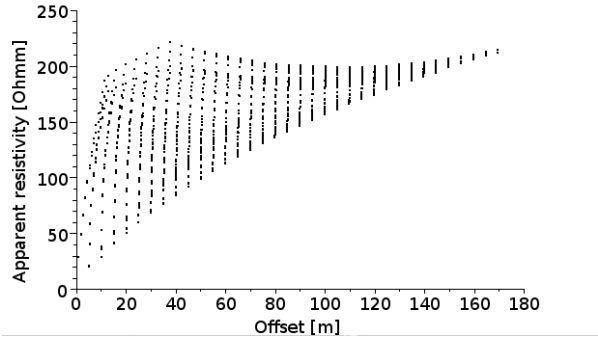

Fig. 4.57: Modelled apparent resistivities with respect to the angle and the offset of measurement from a network of conductors in a non-conductive matrix with an angle of 10° between the conductors. Potential was measured at the nodes of a regular grid, where the conductors crossed.

Because the conductivities / resistivities are limited only to the conductive wires (current not entering the matrix) and the apparent resistivities are calculated under the assumption of homogeneous medium (current entering the matrix), the results need to be calibrated if they want to be used as a quantification tool for real rock. In the shown examples, the real resistivity in one set of conductors is ρ_1=1 Ω.m (direction of 0°) and ρ_2=0.33 Ω.m (90°). However, the apparent resistivity is in the order of 10^2 Ω.m. Further testing is therefore required with different conductivities, different density of conductors, etc.

5 Discussion

Seismic P-wave and S-wave travel-times and electrical resistivity were measured in sub-parallel underground galleries. Standard 2-D seismic tomography resulted in velocities that are unrealistic for the present limestones, mainly in areas with bad ray-coverage. This was interpreted as a sign of anisotropy. Further data treatment confirmed azimuthal variations for both seismic and resistivity data. The properties of studied area were modelled by supposing an HTI rock.

The amount of anisotropy depends on the fracture density in the rocks (e.g. Best et al., 2007; Prasad and Nur, 2003) and on the variations of water content, because the mechanical properties of the fractured rock, with interconnected fractures are influenced by the infill of the fractures (e.g. Rüger and Tsvankin, 1997; Chapman et al., 2003).

The same amount of rainfall in winter does not mean the same impact on the water content and the properties of the massif as would have the same amount of rainfall during a hot dry summer. Nevertheless, the first three campaigns were conducted in spring-summer season and variations of both P- and S-waves velocities are observed. The data acquired in 2011 shows stronger anisotropy (expressed by ε and γ parameters - Fig. 4.34). In order to see, whether the effect was not due to the additional shots in TG, we conducted the inversion also without these shots and the result remained the same (Bereš et al., 2013). To support the non-effect of additional shots, the subsequent campaigns in 2012, with the same shots in TG as in 2011, resulted in variations of properties more similar to the first campaign in 2005.

The maximum P-wave velocity is mainly controlled by the rock matrix, whereas the minimum P-wave velocity is mainly controlled by the fractures and the infill. Therefore it is expected that the seasonal variation in water content will have an impact on the seismic but

also on electric data.

5.1 The seismic data

The interpretation of seismic data is best done by examining the distribution of parameters of stiffness matrix in conjunction with Thomsen's parameters.

5.1.1 Structural interpretation

Looking at the results from 2005 for the parameter c_{11}, which expresses the low velocity perpendicular to fractures, one can clearly see zones of higher and lower velocities. The lower velocities in the symmetry axis direction could be interpreted as:

- wider fracture openings,

- higher density of fractures,

- fractures that are drained more, therefore without any infill

- or zones of different limestones.

Inversion results for all of the campaigns contain the low velocity in the corner of TG and MG. One hypothesis for that might be that the drilling machinery was turning while drilling, therefore causing further disintegration of the rock matrix. All parameters responsible for axial velocities (c_{11}, c_{22} - P-waves, c_{44}, c_{66} -S-waves) support this assumption, except for the year 2011 for fast P and S-waves (c_{22} and c_{44} respectively) and winter 2012 for fast P-waves (c_{22}) - (Fig 4.25 - 4.28).

From the structural knowledge acquired during drilling of the tunnels, all of the fractures inside ABG are oriented within a 30° aperture from 40° - 70° (Thiébaud, 2003). However, looking at the inversions, one has rather the impression of seeing structures that are perpendicular to this expected orientation, in -15° to -35° direction. This direction is the

parallel to the one of the major faults that are not present in the studied area. The faults can be also observed on the surface of the mountain slope where they extrude in forms of cliffs. The same behaviour can be also seen in Thomsen's parameter ε (Fig. 4.33 - 4.36) which represents the ratio between the high and low P-wave velocity. However, the parameter γ, ratio between the high and low S-wave velocities, shows a different pattern. The fast and slow zones are oriented rather in direction of 0°, with the only exception of 2011, where the hint of similar behaviour to the P-waves is visible (-45°).

One hypothesis can be that the zones of low axial velocities could be connected to secondary fractures. However these fractures have not been recorded during the drilling of the tunnels. It is therefore possible that if they exist, they might be not visible to naked eye. The resistivity measurements confirm the existence of secondary fractures.

Another hypothesis might be that the water is preferentially dissolving the limestone in the slower areas between the tunnels, creating wider openings of the fractures.

5.1.2 Hydrological interpretation

A possible way of interpreting the seismic data with respect to water content is to examine the rainfall data (Fig 2.6). It is still not well understood, how the water is circulating in the studied area, or what is the connection between the unmapped collectors and the seepages in the galleries (ongoing research conducted by Ollivier, 2013), especially when the seasons for our campaigns are different. Therefore, at this stage, we considered the water circulation and retention constant for all campaigns. This way, the number of variables that can influence the physical properties is reduced to rainfall and we can examine the correlation between them.

Garry (2007) examined the water collected from seepage inside the ABG and concludes

that its chemical composition points towards relatively short period between the rainfall and circulation 200 m below the surface. If we take for example that the water stays only up to 5 days inside the studied area. There should be no difference between the campaigns as there was virtually no rainfall data for any of them (Table 5.1).

Table 5.1: Cumulative precipitation for all campaigns 5, 10, 20 and 30 days prior the measurements [mm of rainfall]

	5 days	10 days	20 days	30 days
May 2005	0	13	84.5	104
June2011	0	38	91	95.6
July 2012	0	2.6	8.8	15.6
Dec. 2012	0.6	4.6	4.6	62.2

If we supposed the water stayed in the massif up to 10 days, then there are variations for the different campaigns. The biggest rainfall data is for year 2011 and after the inversion, higher variations for the all stiffness parameters are observed and stronger anisotropy is recorded (Fig. 4.34). However, the only problem with this interpretation is that the variations should be smaller for 2011, as the water (a non-compressible fluid) should be filling the voids and thus replacing the air (a compressible fluid). In addition, the water infill should not be affecting the S-wave velocities. The high oscillations for the S-wave parameters (c_{44} and c_{66}) could be expected, due to the experimental mounting of the geophones. The picking of first time arrivals for S-waves was hidden in a lot of noise and it was unclear, when the waves arrived, which in return meant larger uncertainties. However, the oscillations should not be so strong for the P-waves coefficients (c_{11} and c_{22}).

The 20 days water retention influence on the parameters is highly unlikely, because there is a huge difference between the rainfall of 2005 and both 2012 campaigns, yet the seasonal change of stiffness parameters, especially c_{11} is completely opposite with respect to the expectations. More water in 2005 should have increased the values of this parameter.

The 30 days water retention influence on the parameters could be interpreted only if the

campaigns of 2012 are taken into consideration with exactly the same acquisition geometry. For the winter measurement, there is four times the amount of water with a slight increase of the c_{11} (perpendicular to fractures) and visible increase of c_{22} (parallel to fractures) parameters. However the c_{22} should not be affected at all, and if, then only a little.

Therefore it can be concluded that the rainfall does not influence the stiffness of the rock directly and the variations of stiffness parameters are related to perched aquifers and water circulation related to them, such as time of accumulation of water inside the aquifers.

5.1.3 Fracture characterisation

Another possible interpretation of seismic anisotropy can be done in terms of fracture characterisation. For such interpretations, lots of assumptions need to be considered (so far, the fractures are modelled as simplified regular objects; by assuming weak anisotropy; quantification is done in simulated rock models; or small laboratory samples that are not representative of the in-situ rocks; rather homogeneous media), but they can serve as a starting point for future interpretations. In karstified rock, the fractures are irregular, they are not distributed evenly throughout the medium, they can create significant heterogeneities, therefore cannot fulfil any of these assumptions. Therefore, only the interpretation of the results from MCMC inversions can be attempted.

Using equations (3.43) and (3.45) or (3.47) we calculated the fracture densities *e* for each campaign (Table 5.2). The calculated densities should have the same value, because they are independent of any infill in the fractures and these slight variations could result from different acquisition geometries used for each campaign.

Table 5.2: Fracture density e for each campaign calculated from weaknesses Δ_T and ratio V_S^2/V_P^2 of isotropic background matrix (Bakulin et al., 2000a)

year	May 2005	June 2011	July 2012	Dec. 2012
e	0.13	0.09	0.05	0.07

Porosity of lower Cretaceous carbonates at the LSBB site can have different values. Our studied area is situated in the Urgonian facies from Upper Barremian to Aptian. They are characterised by an average porosity of 10%. (Mauffroy, 2010). Fournier et al. (2011) conducted laboratory measurements on samples collected from nearby locations and from our site. According to their results, velocities of non-fractured limestone reach up to 6.2 km/s and decrease with increasing porosity. As the study was conducted on small samples, where anisotropy was not considered, we are comparing their results with our average velocity obtained from Monte Carlo inversion (4.8 km/s). This velocity corresponds to a porosity of about 15% in good agreement with the value published by Mauffroy (2010). Above the MG, Mauffroy (2010) obtained an isotropic seismic tomography image on a vertical plane oriented 40° with respect to the fast direction between the surface and the gallery. She obtained a velocity of 4.8–4.9 km/s which is also in good agreement with our results in this direction. According to the results of their tomography, the total porosity of 13% was calculated.

5.2 The electrical resistivity data

The results for electrical resistivity modelling and inversions with available software were not conclusive as the real data proved to be more complicated than the modelled data. Simultaneous research (Carrière et al., 2013) conducted on the surface near the far end of escape gallery (ca 1600 m WNW of our studied area - fig. 2.1) also confirms the azimuthal anisotropy, however their results do not provide complete cover of all directions, because the vegetation did not allow to conduct measurements in all directions and only bidirectional surveys have been performed. Without a new approach to calculate general anisotropic electrical potential distribution, there is no possible way of modelling the real measured data in LSBB with two peaks over 180° in azimuthal resistivity graphs.

In spite of initial difficulties, we managed to model the two maxima with a network of conductors in a non-conductive matrix (Fig 4.50). Our conceptual modelling is working for a 2-D case for two sets of fractures with different directional conductivities. Future work in this field will include modelling in 3-D. Currently, it is possible to assume the conductors as infinite conductive planes, creating a 2.5-D model and this approach therefore might work as a first approximation.

However, even though we managed to observe the maxima following the azimuthal direction of modelled fractures, there are still some unresolved issues or questions that need answering with this modelling, such as:

- the apparent resistivities increase with offset. This anomaly, however, was observed also for measured and modelled homogeneous data (eq. 3.22). Therefore the increase of apparent resistivity with offset, could be the first indication of more conductive fractures;

- quantification of resulting apparent resistivity in real resistivity. If the medium is homogeneous, and the current density changes gradually, equation 3.22 leads to correct values of potential. However, a conductive network inside non-conductive medium will have different values of potential, because the current flows only through the wires and the current density has only two preferred directions. When placed in a conductive medium, (less conductive than the wires), the potential distribution will depend on conductivity of both, wires and matrix;

- from the mathematical point of view, considering the paradox of anisotropy of a homogeneous medium, it is understood, why the apparent resistivity acts counter-intuitively and what are the extreme values of minima and maxima in terms of longitudinal and transversal resistivities. However, for two fracture sets with specific conductivities, inside a non-conductive or less conductive matrix, what are the minima and maxima for the double

peaked result? In our real case, both of the averaged minima for both campaigns had nearly the same values, whereas the maxima differed. Would the minima always be the same in other case studies, or should they also vary? What do they represent? Is it the longitudinal resistivity of less resistive fracture system, or is it a combination of all four entities?;

- there is one last remark on the positions of the minima and maxima for the modelled data. The maxima should be following the direction of the conductors and the minima should be in between the maxima. For an orthogonal model (Fig. 4.51), we find that the maxima are not exactly at the position of the conductors, but the minima match well the inter-conductor directions. By decreasing the angle between the conductors, the maxima follow more or less their position, however the minima are always in the vicinity of the maxima, which is not completely understood yet (Figs. 4.54 - 4.57). This can be still a minor numerical problem, further research is therefore required.

5.3 Structural interpretation

The higher resistivities on the left side (Fig. 4.39 – 4.41) are for the short offsets within the ABG. They are not repeated in the TG or MG galleries. The reason for that might be that the ABG does not contain the concrete wall with metallic reinforcements and the resistivities are true, whereas in the TG and MG they could be influenced by the metallic grid and therefore could not be real.

The comparison of measured and modelled data (e.g. Fig 4.39 - July 2012), shows that there is also a slight longer wavelength oscillation of real data in the middle of the recording (blue curve goes up and then comes back, comparing to the red one). Is it another effect of the metallic grid, which might be more pronounced in some areas? Or is it the effect of the cavities or water content inside the massif that influence the apparent resistivities?

6 Conclusions and outlook

We were investigating a karstified limestone massif in-situ. Using the tunnels inside a mountain we had access to a block of dimensions 100 m x 100 m. We conducted four seismic campaigns and two electrical ones. The objective was to see, whether there is dependence between the studied anisotropies and seasonal variations of different factors. The main interest was to see the correlation between the water content and measured anisotropy that could result in fracture characterisation.

The seismic results show that variations of physical properties (15-20% seismic anisotropy) are probably connected to the water content, but they cannot be correlated directly to the rainfall. The water circulation within the massif is not completely understood, because of complex structures that are more pronounced than anisotropy caused by the fractures. It is the unknown exact positions and properties of water collectors, in addition to unknown preferential fluid flow that make the interpretation impossible at this stage of research.

Under the assumption of weak anisotropy, a porosity of 10-15% was interpreted. These results have been confirmed by other studies conducted in the studied area. This information needs clarification from undergoing and future studies in order to improve hydrogeophysical interpretation.

For the resistivity measurements, we modelled the fractures in 2-D with a mesh of conductors in a non-conductive medium. The results are promising, however further research and laboratory models need to be tested in order to understand found discrepancies (e.g. differences between the directions of modelled wires and peaks in their graphical representations, quantification of apparent resistivity with respect to non-conductive and less

conductive medium). The increase of apparent resistivity with offset gives first indication of more conductive fracture sets within a less conductive medium. We modelled successfully the two maxima in 180° in azimuthal measurements, confirming two fracture sets.

This thesis was finished before a drilling of a third gallery in the middle of TG and parallel to the ABG and MG, creating a fork structure. Analysis of the drilling log will either confirm our models or will lead to further constraints for future modelling.

Future numerical studies can complicate the resistivity model by adding a third set of conductors, either within a rectangular grid, connecting the nodes in one diagonal, or by modelling the mesh of equilateral triangles. Adding a third dimension for the model is necessary to simulate real 3-D structures. Eventually, the numerical studies can lead to simulation of a conductive matrix surrounding the more conductive wires.

Laboratory research could be started in order to simulate the current entering the matrix and possibly calibrate the modelling giving the relationships between the apparent and real resistivities. Future research will include cooperation with Laboratory FAST (Fluides, Automatique et Systemes Thermiques) of our University, where the current could be studied in a conductive fluid with less conductive bricks in order to simulate a real mesh of orthogonal conductors.

For the electrical resistivity anisotropy, even though it is known for almost a century now, there is a lack of research, probably because the main prospecting method for oil is seismic reflection. It would perhaps be possible to model the two maxima, if the conductivity tensor could be expressed as a 4^{th} rank, similar to the seismic stiffness tensor. In the seismic stiffness tensor, this is observed in the S_{perp}-wave phase velocity function and some cases of non-elliptic P-wave phase velocity function. If this is possible at all, this characterisation might happen with increasing interest and study of anisotropy in resistivity method. If this

however would not be possible, then other algorithms or approaches to the problem need to be invented in order to interpret and quantify the different conductivities and possibly characterise the fractures with the resistivity method. Finite element methods can be helpful, but they require huge amounts of computational power and therefore are not applicable currently.

We tested few existing programs capable of handling anisotropy, we improved the seismic anisotropic tomography program and created several different routines to treat seismic and resistivity data, to visualise the properties and to invert for best suitable parameters. Future work can focus on testing and developing the modelling tool for electrical resistivity by the network of conductors, testing the real laboratory models such as submerged bricks. It would be also desirable for future researchers, to run the inversion of existing seismic data with a more advanced software, such as full waveform inversions, when the software becomes available. Final goal, that was not concluded during this study, is to develop a joint inversion program, that would treat seismic and resistivity data at the same time and characterise the fractures and/or water content by two independent methods.

7 References

Abramowitz M. and Stegun I., 1964. Handbook of Mathematical Functions with Formulas, Graphys and Mathematical Tables. Dover Publications, Inc. New York, ISBN: 0-486-61272-4, 1046 pp

Adam J.M.-C and Lebedev S., 2012, Azimuthal anisotropy beneath southern Africa from very broad-band surface-wave dispersion measurements. Geophys. J. Int. 191, 155–174

Agosta F., Alessandroni M., Antonellini M., Tondi E. and Giorgioni M., 2010, From fractures to flow: A field-based quantitative analysis of an outcropping carbonate reservoir. Tectonophysics 490, 197–213

Aleixo R. and Schleicher J., 2010, Traveltime approximations for q-P waves in vertical transversely isotropy media. Geophysical Prospecting 58, 191–201

Alkhalifah T. and Tsvankin I., 1995, Velocity analysis for transversely isotropic media. Geophysics 60, 1550–1566

Babuška V., Plomerova J. and Vecsey L., 2008, Mantle fabric of western Bohemian Massif (central Europe) constrained by 3D seismic P and S anisotropy. Tectonophysics 462 (1-4), 149-163

Bakulin A., Grechka V. and Tsvankin I., 2000a, Estimation of fracture parameters from reflection seismic data: part I. HTI model due to a single fracture set. Geophysics 65, 1788–1802

Bakulin A., Grechka V. and Tsvankin I., 2000b, Estimation of fracture parameters from reflection seismic data: part II. Fractured models with orthorhombic symmetry. Geophysics 65, 1803–1817

Bereš J., Zeyen H., Sénéchal G., Rousset D. and Gaffet, S., 2013, Seismic anisotropy analysis at the Low-Noise Underground Laboratory (LSBB) of Rustrel (France). Journal of Applied Geophysics 94, 59–71

Best A.I., Sothcott J. and McCann C., 2007, A laboratory study of seismic velocity and attenuation anisotropy in near-surface sedimentary rocks. Geophysical Prospecting 55, 609-625.

Boadu F.K., Gyam J. and Owusu E., 2005, Case History: Determining subsurface fracture characteristics from azimuthal resistivity surveys: A case study at Nsawam, Ghana. Geophysics 70 (5), B35 – B42, 10.1190/1.2073888

Bóna A. Gurevich B., Ball G. and Pervukhina M., 2011, Special section: Seismic anisotropy – Introduction. Geophysics 76 (3), WA1–WA2

Boyd O.S., 2006, An efficient Matlab script to calculate heterogeneous anisotropically elastic wave propagation in three dimensions. Computers & Geosciences 32, 259–264

Bristow J. R., 1960, Microcracks and the static and dynamic elastic constants of annealed and heavily cold-worked metals. British Journal of Applied Physics 11, 81–85

Busby J.P., 2000, The effectiveness of azimuthal apparent-resistivity measurements as a method for determining fracture strike orientations. Geophysical Prospecting 48, 677-695

Carcione J.M., Herman G.C. and ten Kroode A.P.E., 2002, Seismic modeling. Geophysics 67, 1304–1325

Carrière S.D., Chalikakis K., Sénéchal G., Danquigny C. and Emblanch C., 2013, Combining Electrical Resistivity Tomography and Ground Penetrating Radar to study geological structuring of karst Unsaturated Zone, Journal of Applied Geophysics 94, 31–41

Červený V., 1972, Seismic rays and ray intensities in inhomogeneous anisotropic media. Geophysical Journal of the Royal Astronomical Society 29, 1–13

Chapman M., Maultzsch S., Liu E. and Li X.Y., 2003, The effect of fluid saturation in an anisotropic, multi-scale equant porosity model. Journal of Applied Geophysics 54, Issues 3–4, 191-202

Coggon J. H., 1971, Electromagnetic and electrical modeling by the finite-element method. Geophysics 36, 132-155

Cognard-Plancq A.L., Gevaudan C., Emblanch C., 2006. Historical monthly rainfall–runoff database on Fontaine de Vaucluse karst system: review and lessons. Proceedings of 3rd Karst, cambio climatico y aguas submediterraneas, Malaga, Spain, pp. 465–475.

Dey A., and Morrison H. E, 1979, Resistivity modeling for arbitrarily shaped three-dimensional structures. Geophysics 44, 753-780

Dix C.H., 1955, Seismic velocities from surfaces measurements. Geophysics 20, 68–86

Douma H. and Calvert A., 2006, Nonhyperbolic moveout analysis in VTI media using rational interpolation. Geophysics 71, D59– D71.

Fichtner A., Trampert J., Cupillard P., Saygin E., Taymaz T., Capdeville Y. and Villaseñor A., 2013, Multiscale full waveform inversion. Advance Access published April 28, Geophys. J. Int. doi: 10.1093/gji/ggt118

Fournier F., Leonide P., Biscarrat K., Gallois A., Borgomano J. and Foubert A., 2011, Elastic properties of microporous cemented grainstones. Geophysics 76 (6), E211-E226.

Gajewski D. and Pšenčík I., 1990, Vertical seismic profile synthetics by dynamic ray tracing in laterally varying layered anisotropic structures. J. Geophys. Res. 95B, 11301-11315

Gaffet S., Guglielmi Y., Virieux J., Waysand G., Chwala A., Stolz R., Emblanch C., Auguste M., Boyer D. and Cavaillou A., 2003, Simultaneous seismic and magnetic measurements in the Low-Noise Underground Laboratory (LSBB) of Rustrel, France, during the 2001 January 26 Indian earthquake. Geophys. J. Int. 155 (3), 981-990

Garry B., 2007, Etude des processus d'écoulements de la Zone Non Saturée pour la modélisation des aquifères karstiques Expérimentation hydrodynamique et hydrochimique sur le site du Laboratoire Souterrain à Bas Bruit de Rustrel et de Fontaine-de-Vaucluse – PhD Thesis, Université d'Avignon et des Pays de Vaucluse, 218 pp

Golikov P. and Stovas A., 2012, Traveltime parameters in a tilted elliptical anisotropic medium. Geophysical Prospecting 60 (3), 433-443

Grechka V., Contreras P. and Tsvankin I., 2000, Inversion of normal moveout for monoclinic media. Geophysical Prospecting 48, 577-602

Grechka V., and Kachanov M., 2006, Effective elasticity of fractured rocks: A snapshot of the work in progress. Geophysics 71 (6), W45–W58

Grechka V., 2007, Multiple cracks in VTI rocks: Effective properties and fracture characterization. Geophysics 72 (5), D81–D91

Grechka V., 2009a, Applications of seismic anisotropy in the oil and gas industry. European Association of Geoscientists & Engineers, Houten (NL), 171 pp

Grechka V., 2009b, On the nonuniqueness of traveltime inversion in elliptically anisotropic media. Geophysics 74 (5), WB137–WB145

Greenhalgh S.A., Zhou B. and Green A., 2006, Solutions, algorithms and inter-relations for local minimization search geophysical inversion. J. Geophys. Eng. 3, 101–113

Greenhalgh S.A., Zhou B., Greenhalgh M., Marescot L. and Wiese T., 2009a, Explicit expressions for the Fréchet derivatives in 3-D anisotropic resistivity inversion. Geophysics 74 (3), F31-F43

Greenhalgh S.A., Marescot L., Zhou B., Greenhalgh M., and Wiese T., 2009b, Electric potential and Fréchet derivatives for a uniform anisotropic medium with a tilted axis of symmetry. Pure appl. Geophys. 166, 673–699

Gurvich I. I., 1940, Interpretaciya dannykh sejsmorazvedki v sluchae anizotropnoj sredy [Interpretation of seismic-prospecting data in the case of anisotropic medium]. Izvestiya Akademii Nauk SSSR, Seriya Geografii i Geofiziki 5, 108–116 (in Russian)

Herwanger J.V, 2001, Seismic and Electric Crosshole Tomography for Fracture Detection and Characterization, Computational Physics and Geophysics Group, Imperial College of Science Technology and Medicine, London, PhD Thesis, 198 pp

Holcombe H.T. and Jiracek G., 1984, 3-D terrain corrections in resistivity surveys, Geophysics 49, 439–452

Hudson J. A., 1980, Overall properties of a cracked solid. Mathematical Proceedings of Cambridge Philosophical Society 88, 371–384

Hsu C.-J. and Schoenberg M., 1993, Elastic waves through a simulated fractured medium. Geophysics 58, 964–977

Jeanne P., Guglielmi Y. and Cappa F., 2012, Multiscale seismic signature of a small fault zone in a carbonate reservoir: Relationships between VP imaging, fault zone architecture and cohesion. Tectonophysics 554-557, 185–201

Jolly R.N., 1956, Investigation of shear waves, Geophysics 21, 905-938

Lee T., 1975, An integral equation and its solution for some two and three-dimensional problems in resistivity and induced polarization. Geophys. J. 42, 81-95

Masse J.P., 1993, Valanginian-Early Aptian carbonate platform from Provence, Southeastern France, In: Simo J.A., Scott R.W., and Masse J.P. (Eds.), Cretaceous carbonate platforms. A.A.P.G. Memoire 56, 363-374

Maufroy E., 2010, Caractérisation et modélisation numérique de l'effet de site topographique 3D: application à la Grande Montagne de Rustrel, Vaucluse. PhD Thesis, University of Nice, France, 245 pp

Maultzsch S., Chapman M., Liu E. and Li X.Y., 2003, Modelling frequency-dependent seismic anisotropy in fluid-saturated rock with aligned fractures: implications of fracture size estimation from anisotropic measurements. Geophysical Prospecting 51, 381–392

Menke W., 1984, Geophysical data analysis: Discrete inverse theory. Academic Press, London, 260 pp

Moser T. J. 1991, Shortest path calculation of seismic rays. Geophysics 56, 59–67

Musgrave M. J. P., 1970, Crystal acoustics: Introduction to the study of elastic waves and vibrations in crystals: Holden-Day. 303 pp

Neau A., 2005, Tomographie de vitesse entre galeries au LSBB: Analyse et interprétation de données sismiques en transmission. rustrel – provence., master thesis (memoire), universite de Pau et des Pays de l'Adour, 33pp

Ollivier C., 2013, Interepretation couplée de données géologiques, hydrogéologiques et géophysiques et réalisation d'un géomodèle locale de la zone non saturée du karst. Master thesis, Université d'Avignon et des Pays de Vaucluse, 57 pp

Pain C., Herwanger J., Saunders J., Worthington M. and Oliveira C., 2003, Anisotropic resistivity inversion. Inverse Problems 19, 1081–1111

Pal B.P. and Dasgupta S.P., 1984, Electrical potential due to a point current source over an inhomogeneous anisotropic earth. Geophys. Prosp. 32, 943–954

Perineau A., Emblanch C., Danquigny C., Boyer D. and Poupeney J., 2011, Hydrodynamic organisation of the flows in the unsaturated zone of the Fontaine de Vaucluse karst system. First results. EDP Sciences. DOI http://dx.doi.org/10.1051/idust/201101001

Pirson S. J., 1935, Effect of anisotropy on apparent resistivity curves. AAPG Bull. 19, 37-57

Prasad M. and Nur A., 2003, Velocity and attenuation anisotropy in reservoir rocks. SEG Expanded abstracts, 1652-1655

Pridmore D., Hohmann G.W., Ward S.H. and Sill W.R., 1981, An investigation of the finite element method for electrical and electromagnetic modelling data in three dimensions. Geophysics 46, 1009–1024

Robertsson J. O., Bednar B., Blanch J., Kostov C. and van Manen D. J., 2007, Introduction to the supplement on seismic modeling with applications to acquisition, processing and interpretation. Geophysics 72 (5), SM1–SM4

Rüger A., 1997, P-wave reflection coefficients for transversely isotropic models with vertical and horizontal axis of symmetry. Geophysics 62, 713-722

Rüger A. and Tsvankin I., 1997, Using AVO for fracture detection: Analytic basis and practical solutions. The Leading Edge 10, 1429–1434

Schoenberg M., 1980, Elastic wave behavior across linear slip interfaces. J. Acoust. Soc. Am. 68, 1516–1521

Schoenberg M. and Sayers C., 1995, Seismic anisotropy of fractured rock. Geophysics 60, 204–211

Sénéchal G., Rousset D. and Gaffet S., 2013, Ground Penetrating Radar investigation inside a karstified limestone reservoir. Near Surface Geophysics 11, 283-291

Slichter L., 1933, The interpretation of resistivity prospecting method for horizontal structures. Physics 4, 307-322

Staigre J.C., 1983, Nouvelles plongées à la Fontaine de Vaucluse. Spelunca 4, 110-111

Stoneley R., 1949, “The seismological implications of aeolotropy in continental structure,” Monthly Notices of the Royal Astronomical Society. Geophysical Supplement, Vol. 5, No. 8, 343-353

Thiébaud E., 2003, Etude structurale et hydrogéologique du site du Laboratoire Souterrain à Bas Bruit de Rustrel. Master thesis, Université de Franche-Comté, Besançon, France, 50 pp

Thomsen L., 1986, Weak elastic anisotropy. Geophysics 51 (10), 1954-1966

Tryggvason A. and Linde N., 2006, Local earthquake (LE) tomography with joint inversion for P- and S-wave velocities using structural constraints. Geophys. Res. Lett. 33, L07303

Tsvankin I. and Thomsen L., 1994, Nonhyperbolic reflection moveout in anisotropic media. Geophysics 59, 1290–1304

Tsvankin I., 1997a, Reflection moveout and parameter estimation for horizontal transverse isotropy. Geophysics 62 (2), 614-629

Tsvankin I., 1997b, Anisotropic parameters and P-wave velocity for orthorhombic media. Geophysics 62, 1292–1309

Tsvankin. I, Larner K., Gaiser, J. and Grechka V., 2009, Special section: Seismic anisotropy – Introduction. Geophysics 74 (5), WB1–WB2

Tsvankin I., Gaiser J., Grechka V., van der Baan M. and Thomsen L., 2010, Seismic anisotropy in exploration and reservoir characterization: An overview. Geophysics 75 (5), A15-A29

Unz M., 1953, Apparent resistivity curves for dipping beds, Geophysics 18 (1), 116-137

Virieux J., and Operto S., 2009, An overview of full-waveform inversion in exploration geophysics. Geophysics 74 (6), WCC1–WCC26, doi: 10.1190/1.3238367

Warner M., Ratcliffe A., Nangoo T., Morgan J., Umpleby A., Shah N., Vinje V., Štekl I., Guasch L., Win C., Conroy G. and Bertrand A., 2013, Anisotropic 3D full-waveform inversion. Geophysics 78 (2), R59-R80

White J.E. and Sengbush R.L., 1953, Velocity measurements in near-surface formations. Geophysics 18, 54-69

Wiese T., 2012, DC Anisotropic Resistivity Sensitivity and Inversion. PhD thesis, The University of Adelaide, 148 pp

Wiese T., Greenhalgh S. and Zhou B., 2013, Resistivity inversion in 2D anistropic media: Numerical experiments. Geophysical Prospecting, submitted

Winterstein D.F., 1990, Velocity anisotropy terminology for geophysicists. Geophysics 55 (8), 1070-1088

Winterstein D. F. and Meadows M. A., 1991, Shear-wave polarizations and subsurface stress directions at Lost Hills field. Geophysics 56, 1331–1348

Wishart D.N, Slater L.D. and Gates A.E., 2008, Fracture anisotropy characterization in crystalline bedrock using field-scale azimuthal self potential gradient. Journal of Hydrology 358, 35– 45

Xu S. Z., Gao Z. C., and Zhao S. K., 1988, An integral formulation for three-dimensional terrain modeling for resistivity surveys. Geophysics 53, 546-552

Yin C. and Weidelt P., 1999, Geoelectrical fields in layered earth with arbitrary anisotropy. Geophysics 64, 426–434

Zhao S. and Yedlin M.J., 1996, Some refinements on the finite-difference method for 3-D DC resistivity modeling. Geophysics 61 (5), 1301-1307

Zhou B. and Greenhalgh S.A., 2005, 'Shortest path' ray tracing for the most general anisotropic 2D/3D anisotropic media. J. geophys. Eng. 2, 54–63

Zhou B. and Greenhalgh S., 2008, Non-linear traveltime inversion for 3-D seismic tomography in strongly anisotropic media. Geophys. J. Int. 172(1), 383-394

Zhou B., Greenhalgh S. and Green A., 2008, Nonlinear traveltime inversion scheme for crosshole seismic tomography in tilted transversely isotropic media. Geophysics 73 (4), D17–D33

Zhou B., Greenhalgh M. and Greenhalgh S.A, 2009, 2.5-D/3-D resistivity modelling in anisotropic media using gaussian quadrature grids. Geophys. J. Int. 176, 63–80

Zhou B., Greenhalgh S. A., and Hansruedi M., 2012, 2.5-D frequency-domain seismic wave modelling in heterogeneous, anisotropic media using a gaussian quadrature grid technique. Computer and Geosciences 39, 18-33

8 Index of Tables

Table 4.1: Summary of acquisition geometries for each campaign.....64

Table 4.2: Summary of best fitting parameters for simple cosine fit.....70

Table 4.3: Best fitting parameters MCMC after 500.000 iterations, showing results for inversion of all travel time data, for inversions of averaged directional velocities and manual fit with respective standard deviations (σ) for all velocities. In order to compare the two different approaches, the standard deviations are expressed in both [ms] and [km/s], as they have been recalculated with the resulting parameters from the inversion.....78

Table 4.4: Comparison of all parameters of stiffness matrix from MCMC inversion with the best cosine fits for all years.....86

Table 4.5: Joint RMS for P and S-waves after inverting with 3Dray_gTI0.....94

Table 5.1: Cumulative precipitation for all campaigns 5, 10, 20 and 30 days prior the measurements [mm of rainfall].....127

Table 5.2: Fracture density e for each campaign calculated from weaknesses ΔT and ratio VS2/VP2 of isotropic background matrix (Bakulin et al., 2000a).....128

9 Index of Figures

Fig. 1.1: Example of horizontal layering having vertical symmetry axis - VTI medium.....8

Fig. 1.2: Layout of tunnels inside the mountain (green) with the rocket tubes (left bottom), launching centre (centre bottom) and the entry (right bottom). Red ellipse represents the area of interest with two sub-parallel tunnels.....18

Fig. 1.3: Travel-time vs. offset for first campaign in May 2005 P-waves (A), S-waves (B). 18

Fig. 2.1: : Location of the study area and fracture/faults setting. Faults visible at the surface are shown with long red lines (thick lines: major faults, thin lines minor ones). Short red lines indicate fractures visible in the galleries. The red oval represents the investigation zone.....21

Fig. 2.2 Geographical location of LSBB (star) and Fontaine-de-Vaucluse (FdV - dot) on a geological map of the region. 22

Fig. 2.3: Example of seepages inside the tunnels.....24

Fig. 2.4: A) Schematic N-S geological cross section of LSBB site with the zone of interest marked with red segment within the red ellipse; B) Lithostratigraphic succession and porosity variation of the carbonate rocks; C) Representation of the galleries with topographic information superposed (Modified from Maufroy, 2010).....26

Fig. 2.5: Geological cross section of LSBB with permanent water table and schematic seasonal zones filled with water above some impermeable layers that entrap the water. Modified from Sénéchal et al., 2013.....27

Fig. 2.6: Rainfall data recorded at the station: St Saturnin lès Apt, 10 km east from the LSBB site. The arrows represent the dates of four seismic campaigns.Modified from Perineau et al., 2011.....27

Fig. 3.1: Example of difference between the size of signal wavelength and layering.....28

Fig. 3.2: Phase velocity function for P-waves of VTI medium, represented in one quadrant of a section between isotropic axis (vertical) and isotropic plane (horizontal). Red dotted curve represents the perfect ellipse. Blue curve represents an example of another anisotropic phase velocity, with different parameter c13 from the red curve. Both of the anisotropic media have the same maximum and minimum velocities. Green lines represent the isotropic velocities situated at maximum and minimum of the anisotropic examples..36

Fig. 3.3: Phase velocity function for P-waves of VTI medium with respect to angle of departure. Two combinations of parameters are shown, red curve form an exact ellipse, the blue deviates from ellipticity. Maximum and minimum velocities are the same for both of them.....37

Fig. 3.4: Phase velocity function for S-waves of VTI medium, represented in a section of a quadrant of space. Green curve represents the S-waves polarised perpendicular to layering, Yellow curve represents S-wave polarised parallel to layering. Red curves represent the isotropic reference velocity.....37

Fig. 3.5: Potential distribution (coming from 3Dres_QGQ) in a block of 100 x 100 m at four injection points (imposed nominal current) located at the maxima of potentials (red zone, with second current electrode in the infinite distance with negative nominal current) with transversal resistivity of 1000 Ω.m and longitudinal resistivity of 100 Ω.m and angle of rotation of anisotropy of Φ0=-45° from the reference system (angle 0° is parallel to x-axis). 46

Fig. 3.6: Export of working environment from Comsol Multiphysics program with visualisation of modelled potential.....47

Fig. 3.7: Comparison of selected profiles for each of the four modelled injections from figure 3.5 (passing through the injection point), coming from three different forward calculations.....48

Fig. 3.8: Example of a misfit function for two parameters (on the axes). The global minimum in placed in the centre of the searched parameter boundaries (green square). The local minimum on the right side (red triangle) may attract the inversion process if the starting points for the inversion is located at wrong place (indicated with a blue star). In this case, the result would be at wrong combination of parameters 1 and 2.....53

Fig. 3.9: Example of a step in a process of validation of inversion by allowing to update only one parameter c22, with other parameters fixed. Figure shows the result after the inversion. The parameter c22 was inverted, the remainder of parameters (c12=6.8, c11=18, c44=c66=5.6) were unchanged (the brown plots of starting parameters). Note that the inside of the circle contains the updated, correctly found values of the parameter, while at the rims, with no travel-time data, the input parameters stayed unchanged.....55

Fig. 3.10: Polar representations of azimuthal apparent resistivity surveys after removal of the datum for better distinction of the peaks. A) single-peaked ellipse with orientation of fractures in azimuth 120° and B) multiple-peaked ellipse indicating possible direction of two fracture sets in direction 10-20° and 120°. Alternatively depending on interpretation, three fracture sets in directions 0°, 45° and 120°. ρD1 and ρD2 represent measurements with different Wenner offsets. ρD1,D2 is the combination of the two (Busby, 2000).....60

Fig. 4.1: Travel-time vs. offset for first campaign in May 2005.....61

Fig. 4.2: Example of rays coming from 3 shots performed in the ABG, recorded in the MG conducted in May 2005. Missing rays are due to noise at the corresponding receiver.....62

Fig. 4.3: Visualization of angle coverage before additional shots in TG, coming from a) only the shots from the sub-parallel galleries ABG and MG in May 2005, and angle coverage b) with additional shots in TG. The lines represent samples of shot-receiver couples and the angles at the chosen locations.....63

Fig. 4.4: Visualization of record section using the in-house Seg2read program. The first arrivals of P-waves are recorded with pink picks, allowing also the interpreter to choose the uncertainty of his/her pick. The green dashed line represents the onset of the S-waves (not picked in this figure. (The horizontal axis: receiver position number, vertical axis: travel-time (ms).....65

Fig. 4.5: P-wave velocity distribution obtained from 3-D isotropic cross-hole tomography using the real field geometry - cross section in the plane of the galleries. The very high velocities in the upper right and lower left corners and the low velocities in the opposite corners are artefacts due to neglecting anisotropy. The black dots correspond to the positions of shots (left) and receivers (right). Long red arrow: direction of high velocity, short red arrow: direction of low velocity obtained from cosine fit described later. 67

Fig. 4.6: Ray coverage for isotropic tomography. Nray represents density of rays per m2 68

Fig. 4.7: May 2005. Velocities for all rays departing from the shot points within a range of angles of +/- 2.5° (dots), along with averaged velocities (X), standard deviation of averaged velocities (error bars) and with optimum velocity adjustments from cosine fit function (red curve - title of each graph contains the information about the equation of the curve). 0° departure corresponds to the direction perpendicular to the ABG. Top figure velocities P-waves, bottom figure velocities S-waves.....71

Fig. 4.8: June 2011.Velocities for all rays departing from the shot points within a range of angles of +/- 2.5° (dots), along with averaged velocities (X), standard deviation of averaged velocities (error bars) and with optimum velocity adjustments from cosine fit function (red curve - title of each graph contains the information about the equation of the curve). 0° departure corresponds to the direction perpendicular to the ABG. Top figure velocities P-waves, bottom figure velocities S-waves.....72

Fig. 4.9: July 2012. Velocities for all rays departing from the shot points within a range of angles of +/- 2.5° (dots), along with averaged velocities (X), standard deviation of averaged velocities (error bars) and with optimum velocity adjustments from cosine fit function (red curve - title of each graph contains the information about the equation of the curve). 0° departure corresponds to the direction perpendicular to the ABG. Top figure velocities P-waves, bottom figure velocities S-waves.....73

Fig. 4.10: December 2012. Velocities for all rays departing from the shot points within a range of angles of +/- 2.5° (dots), along with averaged velocities (crosses), standard deviation of averaged velocities (error bars) and with optimum velocity adjustments from cosine fit function (red curve - title of each graph contains the information about the equation of the curve). 0° departure corresponds to the direction perpendicular to the ABG. Top figure velocities P-waves, bottom figure velocities S-waves.....74

Fig. 4.11: Best fit for MCMC May 2005 with resulting parameters. P-waves above, S-waves below. Black dots - measured data, red dots - calculated data.....79

Fig. 4.12: Best fit for MCMC June 2011 with resulting parameters. P-waves above, S-waves below. Black dots - measured data, red dots - calculated data.....80

Fig. 4.13: Best fit for MCMC July 2012 with resulting parameters. P-waves above, S-waves below. Black dots - measured data, red dots - calculated data.....81

Fig. 4.14: Best fit for MCMC December 2012 with resulting parameters. P-waves above, S-waves below. Black dots - measured data, red dots - calculated data.....82

Fig. 4.15: Result of MCMC May 2005. Velocity vs. angle dependence with resulting best parameters. P-waves left, S-waves right.....83

Fig. 4.16: Result of MCMC June 2011. Velocity vs. angle dependence with resulting best parameters. P-waves left, S-waves right.....83

Fig. 4.17: Result of MCMC July 2012. Velocity vs. angle dependence with resulting best parameters. P-waves left, S-waves right.....83

Fig. 4.18: Result of MCMC December 2012. Velocity vs. angle dependence with resulting best parameters. P-waves left, S-waves right.....84

Fig. 4.19: Example of possible best fit from visually fitting the fork of velocities (July 2012). P-waves left, S-waves right. Travel-time data fits above, velocity vs. angle below. 85

Fig. 4.20: Example of first parameter distribution after 500.000 iterations with large boundaries in order to choose the smaller boundaries around the best solution (red rectangles). Note the different scales for each parameter. The epsilon represents the RMS of all tested parameter combinations. Vertical scale arbitrary, horizontal scales: tested values for stiffness coefficients [GPa], tested angle ϕ0 [°] and resulting ε – RMS [ms]....87

Fig. 4.21: Histograms of all tested parameters within the chosen tighter boundaries. Top May 2005, bottom June 2011. Circles represent the best results. Note the different scales for each parameter. Vertical scale is arbitrary, horizontal scales: tested values for stiffness coefficients [GPa], tested angle ϕ0 [°] and resulting RMS [ms].....88

Fig. 4.22: Histograms of all tested parameters within the chosen tighter boundaries. Top July 2012, bottom December 2012. Circles represent the best results. Note the different scales for each parameter. Vertical scale arbitrary, horizontal scales: tested values for stiffness coefficients [GPa], tested angle ϕ0 [°] and resulting RMS [ms].....89

Fig. 4.23: Histograms of accepted parameters. Top 2005, bottom 2011. Note the different scales for each parameter. Vertical scale arbitrary, horizontal scales: tested values for stiffness coefficients [GPa], tested angle ϕ0 [°] and resulting RMS [ms].....90

Fig. 4.24: Histograms of accepted parameters. Top July 2012, bottom December 2012. Note the different scales for each parameter. Vertical scale arbitrary, horizontal scales: tested values for stiffness coefficients [GPa], tested angle ϕ0 [°] and resulting RMS [ms]. 91

Fig. 4.25: Distribution of parameters of stiffness matrix for May 2005 after inverting the measured data with 3Dray_gTI0.....95

Fig. 4.26: Distribution of parameters of stiffness matrix for June 2011 after inverting the measured data with 3Dray_gTI0.....95

Fig. 4.27: Distribution of parameters of stiffness matrix for July 2012 after inverting the measured data with 3Dray_gTI0.....96

Fig. 4.28: Distribution of parameters of stiffness matrix for December 2012 after inverting the measured data with 3Dray_gTI0.....96

Fig. 4.29: Resulting travel time vs. offset after tomographic inversion. May 2005. Above P-waves, below S-waves. The small 'upward' branch at offset of 100 m for the S-waves represents the measurements along the TG for the very first few meters inside both galleries ABG and MG. The slower velocities (higher value of travel-time) is due to the less clearly defined S-wave arrivals in the recordings.....97

Fig. 4.30: Resulting travel time vs. offset after tomographic inversion. June 2011. Above P-waves, below S-waves. The cloud of points for the P-waves at offsets 140-160 m, at later times the red modelled data is due to higher noise at longer offsets.....98

Fig. 4.31: Resulting travel time vs. offset after tomographic inversion. July 2012. Above P-waves, below S-waves.....99

Fig. 4.32: Resulting travel time vs. offset after tomographic inversion. December 2012. Above P-waves, below S-waves.....100

Fig. 4.33: Resulting Thomsen's parameters May 2005, left - parameter ε, right - parameter γ.....101

Fig. 4.34: Resulting Thomsen's parameters June 2011, left - parameter ε, right - parameter γ.....101

Fig. 4.35: Resulting Thomsen's parameters July 2012, left - parameter ε, right - parameter γ.....101

Fig. 4.36: Resulting Thomsen's parameters Dec 2012, left - parameter ε, right - parameter γ.....101

Fig. 4.37: Layout of resistivity measurements with sample electrodes.....102

Fig. 4.38: Modelled difference between injections in a tunnel of diameter 4 m (in blue), inside a medium (4π - in green) and on a surface (2π - in red).....104

Fig. 4.39: Unfiltered data from July 2012 (top), filtered data without the unaccepted offets smaller than 25 m (middle) and filtered data with expected fit with arbitrary longitudinal and transversal resistivities (based on the minima and maxima found in the figure – bottom). Note the different scales between unfiltered and filtered data.....106

Fig. 4.40: Unfiltered data from December 2012 (top), filtered data without the unaccepted offets smaller than 25 m and without the measurements from faulty electrode (bottom). 107

Fig. 4.41: Comparison between the campaigns in July and December 2012. 107

Fig. 4.42:Variations of apparent resistivity for all measurements containing selected electrodes (at the ends and at the corners of ABG and MG and in the middle of TG) in order of increasing number of electrodes. The measurements around the selected electrode are not shown because they were not accepted due to the small offset. Only the results from July 2012 are shown as December 2012 does not differ much.....108

Fig. 4.43: Variations of apparent resistivity for all measurements containing selected electrodes (at the ends and at the corners of ABG and MG and in the middle of TG) with respect to the angle. Only the results from July 2012 are shown as December 2012 does not differ much.....109

Fig. 4.44: Averaged azimuthal resistivities for July 2012. Red curve shows the best automatic result based on minimising the root mean square error between the averaged measured (blue crosses) and modelled data (red curve). Green curve is the curve with expected amplitude, but cannot be calculated automatically, as it should have two maxima. 111

Fig. 4.45: Averaged azimuthal resistivities for December 2012. Red curve shows the best automatic result based on minimising the root mean square error between the averaged measured (blue crosses) and modelled data (red curve). Green curve is the curve with expected amplitude, but cannot be calculated automatically, as it should have two maxima. 111

Fig. 4.46: Comparison of two fits with different phases. Top: data with phase φ0= -70°, bottom: data with phase φ0= 20°. Top: modelled data (red curve) matches the small maxima at the beginning and matches the variations around the measures 700-800. Bottom: modelled data matches the bigger maxima for the beginning and the middle of the figure. At the end near the measure 800, the variations of maxima and minima of modelled are moving in opposite direction from the measured ones.....112

Fig. 4.47: Resulting best parameters from MCMC inversion after 500.000 iterations for July (top) and December 2012 (bottom). Notice the small difference between the transverse and longitudinal resistivities.....113

Fig. 4.48: Apparent resistivities with respect to the offset. Top: July 2012 and bottom: December 2012. The high resistivities in the first half of each campaigns come from the effect of the galleries at short offsets.....114

Fig. 4.49: Conceptual modelling of parallel conductive wires inside a non-conductive medium (left). Black dots represent the injection points for the current. On the right, the angular variation of apparent resistivity measured around one of the sources. In the tested model, there were more parallel wires, here only the draft is shown. The values on the vertical axis show relative variations for an arbitrary injection.....117

Fig. 4.50: Conceptual modelling of orthogonal fracture system by two sets of parallel conductive wires (left), with a resulting potential distribution (right). Each direction of the wires has different resistivities. Black dots represent the injection points inside a grid.. .118

Fig. 4.51: Modelled apparent resistivities with respect to the angle of measurement from a network of perpendicular conductors in a non-conductive matrix. Potential was measured at the nodes of a regular grid, where the conductors crossed. The angle 0° represents direction of one of the conductors .(ρ1=1 Ωm in direction of 0°, ρ2=0.33 Ωm in 90°)....121

Fig. 4.52: Modelled apparent resistivities as a function of the offset of measurement from a network of perpendicular conductors in a non-conductive matrix. Potential was measured at the nodes of a regular grid, where the conductors crossed.(ρ1=1 Ωm in direction of 0°, ρ2=0.33 Ωm in 90°).....121

Fig. 4.53: Sketch of skewing the model for the next figures. Small dots represent the original model with fractures in the orthogonal directions, Thick squares represent the new position. 122

Fig. 4.54: Modelled apparent resistivities with respect to the angle and the offset of measurement from a network of conductors in a non-conductive matrix with an angle of

70° between the conductors. Potential was measured at the nodes of a regular grid, where the conductors crossed. 122

Fig. 4.55: Modelled apparent resistivities with respect to the angle and the offset of measurement from a network of conductors in a non-conductive matrix with an angle of 50° between the conductors. Potential was measured at the nodes of a regular grid, where the conductors crossed. 122

Fig. 4.56: Modelled apparent resistivities with respect to the angle and the offset of measurement from a network of conductors in a non-conductive matrix with an angle of 30° between the conductors. Potential was measured at the nodes of a regular grid, where the conductors crossed. 123

Fig. 4.57: Modelled apparent resistivities with respect to the angle and the offset of measurement from a network of conductors in a non-conductive matrix with an angle of 10° between the conductors. Potential was measured at the nodes of a regular grid, where the conductors crossed. 123

10 Résumé étendu français

Nous présentons les résultats d'une thèse effectuée avec le soutien financier du ministère français de l'Enseignement Supérieur et de la Recherche.

Le premier chapitre introduit la problématique ainsi qu'un état de l'art des travaux sur l'anisotropie.

Le deuxième chapitre aborde la géologie du site étudié.

Le troisième chapitre présent la physique, la modélisation ainsi que l'inversion en générale. Il aborde aussi les différentes manières de caractériser les fractures.

Le quatrième chapitre montre les données acquises, leur traitement et les résultats.

Le cinquième chapitre discute des résultats, et des hypothèses d'interprétation sont effectuée.

Enfin, le dernier chapitre conclut la thèse avec les perspectives et suggestions pour l'approfondissement dans ce domaine.

Le site

Nous avons étudié un massif calcaire de dimensions 100 m x 100 m. Comme beaucoup de massifs calcaires, celui-ci est altéré, on parle de massif karstique (ou karst). Le site d'étude se situe au sud de la France sur le plateau d'Albion, qui fait partie des Préalpes françaises (Fig. 2.2).

Les mesures ont été effectuées dans les galeries (système des tunnels – fig 2.1) du Laboratoire Souterrain à Bas Bruit (LSBB), qui est à l'origine un aménagement d'un ancien centre de lancement des missiles nucléaires (Fig. 1.2). Les tunnels se trouvent dans les calcaires de l'Urgonien de 200 m d'épaisseur (Fig. 2.4) dans la zone non-saturée (ZNS), avec le niveau de zone saturée une centaine de mètres en-dessous des galeries (Fig. 2.5). Des failles majeures ne sont pas présentes dans la zone étudiée, seulement les fracturations

mineures d'orientation N30°E.

Nous avons effectué quatre campagnes de mesures sismiques (Mai 2005, Juin 2011, Juillet 2012 et Décembre 2012) et deux campagnes de mesures électriques (Juillet et Décembre 2012).

La théorie

Les propriétés du massif montrent une anisotropie (les propriétés physiques dépendent de la direction d'observation) dans les mesures sismiques autant que dans les mesures électriques.

Les raisons qui mènent à une anisotropie peuvent être différentes. Une des possibles raisons, peut être une alternance de couches sédimentaires avec différentes propriétés se répétant plusieurs fois. Une possible autre raison pour l'anisotropie, valable aussi dans notre cas, est la présence de fractures orientées. Si un milieu contient des fractures qui sont alignées parallèlement, il en résulte une isotropie transversale (Transversal Isotropy - TI). Si le milieu contient des couches ou des fractures horizontales, les propriétés semblent isotropes si elles sont mesurées à la surface, car il n'y a pas de variations visibles dans les mesures, d'où son nom d'isotropie apparente. Si les couches sont horizontales, elles créent une anisotropie avec un axe vertical (VTI : Vertical Transverse Isotropy). Si par contre les fractures ou les couches sont orientées verticalement, elles créent un milieu avec un axe d'isotropie qui est horizontale, donc HTI (Horizontal Transverse Isotropy). Le site étudié est affecté par ce dernier type d'anisotropie.

Ces propriétés peuvent être représentées mathématiquement par des tenseurs, qui relient les impulses (coup de marteau, injection du courant) avec les réponses du milieu (déformations, répartition du potentiel). Il existe plusieurs systèmes d'anisotropie. Les systèmes sont dérivés de ceux utilisés en cristallographie. Par contre, tous les différents systèmes trouvés dans les cristaux (32) ne peuvent pas être retrouvés dans la géologie, dans

les échantillons plus grands. La liste se trouve à la page 31 avec le nombre des coefficients indépendants nécessaires pour décrire une telle anisotropie ainsi que des exemples et les causes qui peuvent créer cette anisotropie. La TI est décrite en plus détail dans le chapitre 3.1.3. Le tenseur des constantes élastiques qui est utilisé pour décrire une VTI est décrit dans l'équation 3.2. Pour un milieu avec une anisotropie transversale horizontale, le tenseur a la forme décrit dans l'équation 3.10. Avec ces tenseurs, on utilise les coefficients de Thomsen, (Éqs. 3.4-3.6) qui peuvent aider l'interprétation des propriétés du milieu. Ces coefficients sont sans dimension et ils décrivent le rapport entre la vitesse rapide et la vitesse lente pour les ondes P (ondes de compression) – coefficient ε (Éq. 3.4) et les ondes S (ondes de cisaillement) – coefficient γ (Éq. 3.5). Le coefficient δ (Éq. 3.6) n'est pas utilisé pour notre étude, il est utilisé pour les données de sismique réflexion. Dans un milieu anisotrope, les ondes S subissent une modification et elles sont séparées en deux types d'ondes S ; S_{paral} dont le mouvement des particules est polarisé parallèlement aux fractures (couches) et l'autre, S_{perp}, dont le mouvement des particules est polarisé perpendiculairement aux fractures (Éqs. 3.17). Les figures 3.2 – 3.4 décrivent le comportement et les variations de la fonction de vitesse de phase de chaque onde par rapport à l'angle de propagation dans un milieu avec une TI. Dans les figures 3.2 et 3.4, la direction de vitesse lente est orientée verticalement, la direction de vitesse rapide est orientée horizontalement. L' angle 0° de la figure 3.3 correspond à la direction de la vitesse lente.

La modélisation

Pour la sismique, l'équation utilisée pour les calculs est l'équation du mouvement (3.7). Elle relie les contraintes (coup de marteau), les mouvements des particules et les propriétés du milieu (exprimées dans les tenseurs des constantes élastiques appelés aussi tenseurs des rigidités (Éq. 3.2 – VTI, 3.10 – HTI)). Pour l'électrique, l'équation utilisée est celle de Poisson (3.18). Elle relie les injections du courant, les potentiels mesurés et les tenseurs de

conductivité (Éq. 3.19 et 3.20).

Le massif étudié est donc modélisé par une approximation d'un milieu de HTI, car les fractures présentes sont orientées verticalement. Nous avons mesuré les temps des premières arrivées des ondes P et S. Puisque l'anisotropie du milieu entraîne les différentes propriétés dans différentes directions, les vitesses des ondes P et S sont dépendantes de la direction de propagation. Cette dépendance est exprimée par les équations 3.17. Chaque coefficient de la matrice des rigidités décrit une propriété. Le coefficient c_{11} décrit la vitesse de propagation de l'onde P dans la direction de l'axe d'isotropie, perpendiculaire aux fractures. Cette vitesse est la vitesse lente. Le coefficient c_{22} décrit la vitesse parallèle aux fractures dans les deux autres directions dans le système référentiel. Le coefficient c_{12} décrit le comportement des ondes dans les directions non-axiales : la non-ellipticité des ondes P et la non-uniformité des ondes S_{perp}. Les coefficients c_{44} et c_{66} décrivent les vitesses des ondes S_{paral}. Le premier, décrit la vitesse rapide dans la direction φ=90°, le deuxième, la vitesse lente dans φ=0°. Par contre le coefficient c_{66} contrôle les vitesses axiales pour S_{perp} et il entre aussi dans le calcul des ondes P.

Les vraies résistivités électriques dans un milieu anisotrope sont masquées par le « paradoxe d'anisotropie ». Le potentiel dans le milieu anisotrope se calcule par l'équation 3.22. En supposant que la résistivité longitudinale réelle ρ_L (celle qui est parallèle aux fractures / couches) est plus petite que la résistivité transversale réelle ρ_T (perpendiculaire aux fractures), on mesure une résistivité apparente dans la direction perpendiculaire (Éq. 3.26) égale à la résistivité longitudinale et en direction parallèle aux fractures on mesure une résistivité apparente moyenne (Éq. 3.25), définie par l'équation 3.23. Donc les valeurs des résistivités apparentes sont contre-intuitives.

La caractérisation des fractures est dérivée des modèles de fractures de Schoenberg (1980) – fractures infinies (linear slip theory) et les fractures de forme circulaire (forme de

pièce de monnaie – penny shape) de Hudson. L'influence des fractures du milieu HTI est modélisée par la matrice des rigidités d'un milieu isotrope et la matrice des faiblesses des fractures (Éq. 3.41). Exprimées en quantités sans dimension, elles décrivent les faiblesses normales et tangentielles Δ_N et Δ_T (Éq. 3.42 et 3.43 respectivement). Elles peuvent aider à quantifier les porosités en examinant les fractures avec et sans eau (Éq. 3.44 – 3.47).

La méthodologie et les résultats

Sismique

Pour les données sismiques, nous avons utilisé les coups de marteau de 4 kg comme la source, avec les geophones plantés dans les murs des galeries qui enregistraient les mouvements horizontaux de la paroi. Les instruments utilisés étaient les boites d'acquisition de système Summit de DMT. En 2005, nous avons effectué les tirs uniquement dans la galerie Anti-souffle (anti-blast gallery - ABG) et nous les avons enregistrés dans la galerie principale (main gallery - MG) (Fig. 4.2). Pour les campagnes suivantes, nous avons ajouté les tirs dans la galerie transversale (TG). Les configurations de toutes les campagnes sont décrites dans le tableau 4.1, un exemple de traitement des enregistrements sismiques est montré dans la figure 4.4, et les différents point de tirs (les coins des galeries et milieu de notre dispositif) sont montrés dans l'annexe, page 161.

Dès que nous avons commencé à traiter les données, deux branches étaient visibles dans le graphique de temps d'arrivée en fonction de distance (Fig. 4.1). Dans un milieu isotrope, les données devraient se trouver sur une ligne. Nous avons traité les données de 2005 avec une tomographie isotrope et les résultats (Fig. 4.5) montrent des zones de vitesse rapide et de vitesse lente. Les directions des vitesses rapides sont bien en accord avec les directions des fractures alignées. Par contre, les vitesses rapides sont beaucoup trop élevées pour un calcaire.

Ensuite, nous avons traité les données avec une approche approximative en supposant

l'ellipticité de vitesse de phase des ondes P (le cas le plus simple d'anisotropie, mais très rare) et des ondes S_{paral} par l'équation 4.1. Par cette approche, nous avons trouvé par la méthode des moindres carrées la vitesse moyenne v_0 et les variations dv (v_0+dv= vitesse maximale, v_0–dv= vitesse minimale). Avec ces deux paramètres, on a aussi trouvé l'angle entre la direction lente (l'axe d'anisotropie) et la direction de la galerie transversale qui correspondent le mieux à toutes les mesures. Les résultats des quatre campagnes sont montrés dans le tableau 4.2 et sur les figures (4.7 - 4.10)

Puisqu'il s'agit d'une méthode approximative, nous avons construit un programme d'inversion basé sur l'algorithme de Monte-Carlo couplée à une chaîne de Markov (MCMC). On initialise le calcul avec les coefficients de la matrice des rigidités sortis de méthode approximative (paragraphe précédent). On compare avec les données mesurées et les résidus sont évaluées. Après, dans la première itération, les coefficients sont choisis au hasard dans un espace pré-défini autour du choix précédent et la somme des résidus est recalculée. Si le résultat est mieux que le précédent, il est accepté dans l'assemblage des résultats. Si le résultat n'est pas mieux que le précédent, il peut toujours être accepté avec certaine probabilité, pour pouvoir sortir d'un minimum local (dans l'espace des résidus – Fig. 3.8). S'il n'est pas accepté, les coefficients du choix précédent sont ajoutés dans l'assemblage des résultats et une nouvelle itération est lancée. Nous avons testé cet algorithme avec toutes les données et aussi avec les vitesses moyennes en fonction de l'angle de départ. Les résultats sont présentés sur les figures 4.11 - 4.18. Les histogrammes des coefficients testés pendant l'inversion sont montrés sur les figures 4.21 - 4.22. On observe que les temps d'arrivée résultants des calculs par une inversion automatique n'expliquent pas bien les données mesurées. Il est possible de faire un ajustement manuel, en examinant les branches des figures, mais ce résultat est très dépendant de l'utilisateur (Fig. 4.19). Les coefficients finaux des inversions de tous les temps d'arrivée, des vitesses et ceux trouvés par l'ajustement

manuel sont représentés dans le tableau 4.3. La comparaison de MCMC avec l'approximation de cosinus est montrée dans le tableau 4.4.

Nous avons testé plusieurs algorithmes de tomographie anisotrope, mais à la fin nous avons choisi un programme développé par Zhou et Greenhalgh (2008), qui pouvait traiter aussi les milieux avec une forte anisotropie et pas seulement utiliser l'approximation de faible anisotropie. Nous avons modifié le programme et ajouté la matrice de covariance des données. La matrice est construite à partir des incertitudes qui étaient attribuées visuellement pendant le 'picking' des temps d'arrivée des ondes. Le résultat est trouvé par un processus itératif. Les paramètres initiaux ont été choisis à partir des résultats de MCMC et répartis dans un maillage de 10m x 10m. Les résultats et la somme des résidus joints pour les ondes P et S se trouvent dans le tableau 4.5. La répartition des paramètres après l'inversion est montrée sur les figures 4.25 – 4.28. Les représentations de temps d'arrivée en fonction de la distance sont montrées sur les figures 4.29 – 4.32. Les paramètres de Thomsen pour toutes les campagnes sont présentés sur les figures 4.33 - 4.36.

Résistivité électrique

Les mesures ont été effectuées dans la TG et les premiers 70 mètres de ABG et MG. Nous avons utilisé les instruments de IRIS Instruments – Syscal Pro avec 48 électrodes. Ce système d'acquisition utilise ses propres câbles avec points d'attachement pour 24 électrodes chaque 5 m. De cette manière on pouvait placer l'instrument au milieu de TG et un câble dans la moitié droite de TG continuant 65 m dans ABG, l'autre câble dans l'autre moitié de la TG continuant 70 m dans MG (Fig. 4.37). Pour mesurer et visualiser l'anisotropie, la configuration pôle-pôle est la plus convenable. Pour pouvoir effectuer les mesures en cette configuration, nous avons placé deux électrodes à "l'infini": l'une sur la côte de la montagne à quelques centaines de mètres devant l'entrée du LSBB (à une distance de 950 m), l'autre 1 km dans MG. Pour 48 électrodes, nous avons obtenu 1128 mesures par campagne. Pour

visualiser les résultats, nous avons calculé la résistivité apparente de chaque mesure en appliquant le facteur de géométrie correspondant à la configuration pôle-pôle et nous les avons affiché en fonction du nombre de mesure croissant (Fig. 4.39 haut). Cette visualisation permet de voir s'il n'y a pas de mesures erronées (Fig. 4.40 haut). La comparaison des deux campagnes est fournie sur la figure 4.41. On voit également, que les données modélisées (courbes rouges) suivent les variations de résistivité comme les valeurs mesurées (Fig. 4.39 et 4.40 bas).

Pour traiter les données, nous avons utilisé le programme développé de nouveau par Dr. Zhou (Wiese et al., 2013), et nous avons vérifié le calcul du problème direct en comparant les résultats avec deux calculs indépendants, celui utilisant la fonction analytique (Éq. 3.22) et finalement celui provenant du logiciel Comsol Multiphysics. Le résultat de la comparaison est dans la figure 3.7.

Pour visualiser les données à partir de quelques injections, nous avons regroupé les données en fonction du nombre croissant des électrodes (Fig. 4.42) et en fonction de l'angle de mesure (Fig. 4.43). Les figures 4.44 et 4.45 montrent l'évolution de toutes les résistivités apparentes en fonction de l'angle de mesure pour les deux campagnes. Sur les figures on voit deux maxima à +40° et -70°. La courbe rouge est le résultat d'ajustement automatique par moindres carrées. Cet algorithme essaie d'ajuster un seul maximum et c'est pourquoi le meilleur résultat se trouve autour de la valeur moyenne avec petites variations. On attendrait plutôt une variation comme celle montrée par la courbe verte.

Après avoir étudié plusieurs cas, on s'est aperçu qu'aucune méthode couramment utilisée ne peut modéliser les données obtenues au LSBB, car la fonction anisotrope qui gouverne le calcul permet d'avoir seulement un maximum par 180°. Ceci se voit bien sur la figure 4.46 où nous présentons d'abord un calcul anisotrope avec une direction de résistivité maximale de -70° par rapport à la direction de TG, puis avec une direction de +20°. On voit

clairement que dans le premier cas, les maxima de la courbe modélisée (rouge) suivent les maxima vers la fin de l'enregistrement (à partir de la mesure 800). Dans le deuxième cas, les maxima modélisés suivent les maxima mesurés au début et au milieu de l'enregistrement, mais pour les mesures autour de 800, le comportement est complètement opposé.

Les résultats de la méthode MCMC sont présentés sur la figure 4.47. Le même comportement est observée que sur les figures 4.44 et 4.45 et les maxima des courbes modélisées sont centrés près de la valeur moyenne.

A cause des deux maxima, nous n'avons pas pu utiliser la tomographie électrique. De plus, le programme utilisé ne pouvait pas inverser la bonne solution sauf si elle se trouvait très proche des paramètres initiaux.

Nous avons aussi remarqué que les résistivités apparentes augmentent avec la distance (Fig. 4.48).

On n'a pas eu l'accès à d'autres logiciels libres, et en plus puisque les algorithmes d'inversion existants ne sont pas capables de maîtriser les deux maxima, nous avons construit un modèle, où nous avons simulé les fractures par des fils électriques conducteurs dans un milieu isolant. Tout d'abord, une seule direction était modélisée (Fig. 4.49) et nous avons observé la présence de deux maxima (seulement un quadrant est visualisé). Nous avons compliqué davantage le modèle avec un deuxième système de fils, créant un maillage rectangulaire, où nous pouvions assigner des conductivités différentes (inverse des résistivités) pour les deux systèmes de fils. De cette manière, la conductivité électrique pouvait elle aussi être anisotrope (Fig. 4.50).

La modélisation a suivi la loi de Kirchhoff, sur la conservation du courant ; en dehors des sources de courant, la somme des courants entrant et sortant d'un nœud est égale a zéro (Éq. 4.3). Pris en compte toutes les nœuds du maillage de notre modèle, les courants sont exprimés sous la forme de matrice M (Éq. 4.4).

Les injections de courant ont été modélisées en fixant le potentiel dans les nœuds d'injections, éliminant les lignes et les colonnes respectives de la matrice par une élimination de Gauss, avec le vecteur du courant comme côté droit de la matrice (Éqs. 4.6 et 4.7). La distribution de potentiel était calculée par inversion de la matrice finale M' (Éq. 4.6) et en multipliant avec le vecteur de courant I' (Éq. 4.8)

Les deux maxima étaient modélisés et aussi l'augmentation de résistivité apparente en fonction de la distance (Fig. 4.51 et 4.52) . Nous avons successivement diminué l'angle entre les deux systèmes de fils (Fig. 4.53) et nous avons observé le rapprochement des maxima pour des angles différents de 70°, 50°, 30° et 10° sur les figures respectives (4.54 – 4.57).

La discussion

Le dégré d'anisotropie dépend de la densité de fractures et de leur contenu. L'effet d'infiltration de la pluie pendant l'été n'est pas le même que durant l'hiver.

Les effets de variations de teneur en eau se manifestent dans les coefficients de matrice des rigidités. La vitesse d'ondes dans le plan d'isotropie (la vitesse maximale) n'est pas influencée, car le signal passe surtout dans la roche. La vitesse dans la direction d'axe d'isotropie (la vitesse minimale) est influencée, car les ondes passent par la roche et par les fractures. Dans le cas de fractures vides remplies d'air (fluide compressible), la vitesse des ondes à travers celles-ci est moins élevée par rapport à la vitesse dans les fractures remplies d'eau (fluide in-compressible). Donc c'est la vitesse minimale qui change avec le contenu de la fracture. Pour l'anisotropie électrique, les fractures remplies d'eau minéralisées sont plus conductrices que les fractures sans fluide. Donc, avec un remplissage des fractures, on devrait observer l'augmentation du dégré d'anisotropie électrique et la diminution du dégré d'anisotropie sismique.

L'interprétation des résultats sismiques (Fig : 4.25 - 4.36) du point de vue structurale se fait en examinant la distribution des paramètres de la matrice des rigidités et avec les

paramètres de Thomsen. Dans les figures montrant la vitesse lente – paramètre c_{11} (direction de l'axe d'isotropie), les zones de vitesse moins élevée peuvent se traduire en :

- fractures plus épaisses
- densité de fractures plus importante
- fractures sans eau
- ou bien des zones de calcaire différent.

Du point de vue hydrologique, les variations sont causées par des teneurs en eau différentes. Nous avons corrélé les variations de pluie avec les variations des paramètres et le dégré d'anisotropie, mais nous avons conclu, que le stockage de l'eau est beaucoup plus compliqué et que la pluie n'influence pas directement les variations des propriétés physiques de la roche.

Pour la caractérisation des fractures, nous avons interprété la densité des fractures (tableau 5.2) et à partir de ce résultat nous avons interprété une porosité de 10-15 %. Ce résultat corrèle bien avec les interprétations précédentes effectuées sur le site. Les études actuelles et futures vont clarifier de quelle porosité il s'agit pour améliorer une interprétation hydrologique.

L'interprétation des résultats électriques mène vers la conclusion qu'il y a plusieurs systèmes de fractures, mais pour le moment nous ne sont pas encore en mesure de les quantifier. Notre modèle conceptuel, permet de modéliser les deux maxima pour deux systèmes de fractures, mais il faudrait encore avancer dans la quantification de ces modèles, car pour le moment le courant ne passe que par les fractures (les fils conducteurs) et ne passe pas par la matrice rocheuse qui en principe est aussi conductrice grâce à la porosité. Cela a pour effet des résistivités apparentes qui n'ont rien à voir avec la réalité. Il est conseillé de modéliser numériquement trois systèmes de fractures pour voir si on va observer trois maxima et si leurs directions dans la représentation angulaire correspondent bien à la

direction réelle.

La conclusion et les perspectives

Nous avons observé les variations de propriétés élastiques pendant quatre campagnes qui sont reliées avec les variations de teneur en eau. Par contre, ces variations ne peuvent pas être reliées avec la pluie.

Nous avons interprété une porosité de 10-15 %. Cette valeur est confirmée par d'autres études effectuées sur le site.

Dans le cas de la résistivité électrique, nous avons numériquement modélisé deux systèmes de fractures. La recherche va continuer avec une modélisation, où le courant va pouvoir passer aussi dans le milieu et ne va pas être confiné dans des fils électriques. La modélisation du flux de courant dans un fluide conducteur avec des briques moins conductrices peut mener à une simulation des fractures orthogonales réelles. Ce type d'expérience va être dirigé avec la coopération du laboratoire FAST (Fluides, Automatique et Systèmes Thermiques) de notre Université.

Nous avons testé, amélioré et créé différents programmes et routines pour traiter les données sismiques et électriques, visualiser les résultats et inverser les paramètres recherchés. Le travail devrait continuer avec la modélisation numérique, des expériences avec des fluides conducteurs et devrait mener vers la création d'un programme d'inversion conjointe des données sismiques et électriques.

11 Annexe

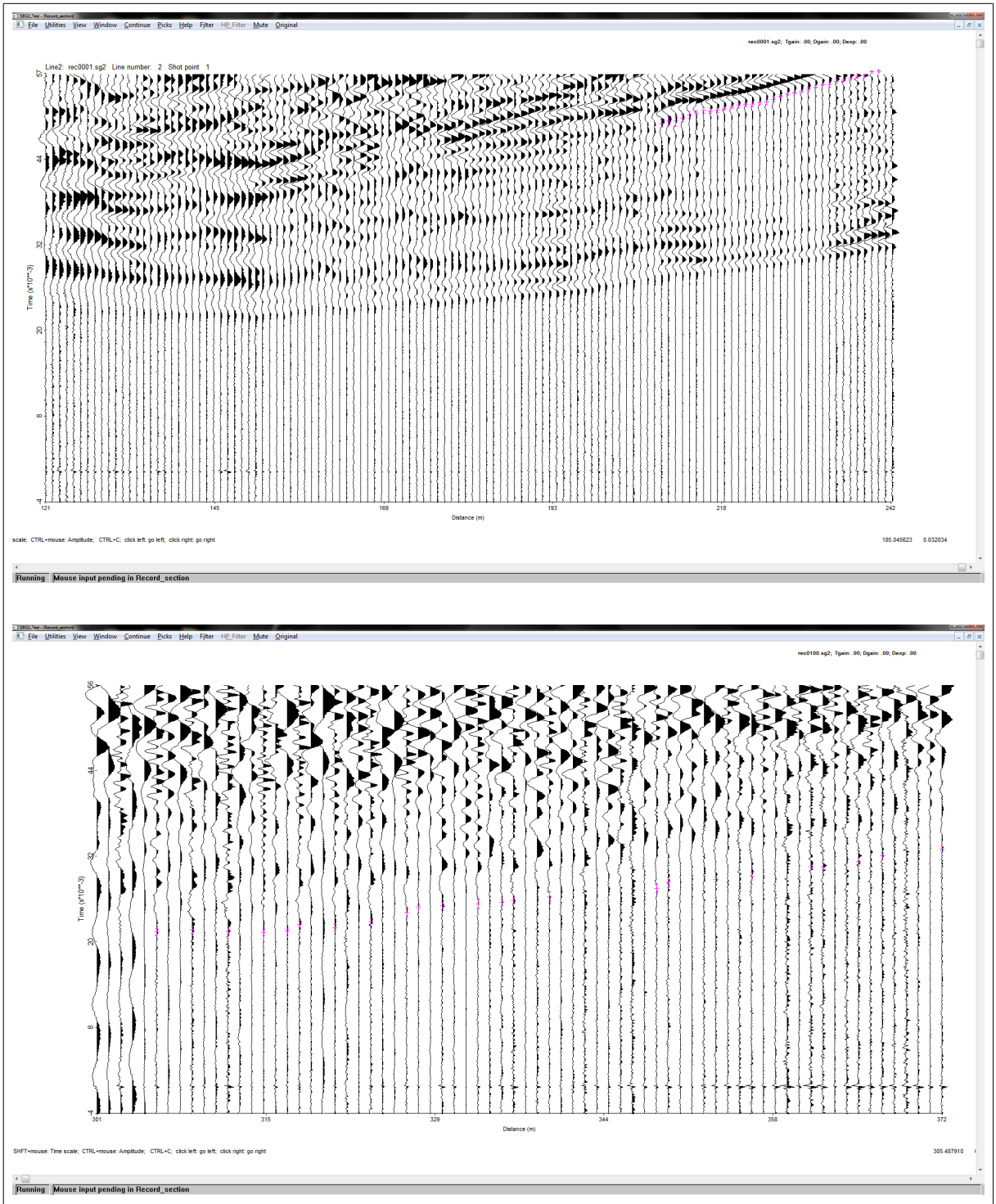

Shot in corner of MG and TG, geophones in ABG. Above May 2005 (50 Hz geophones), below June 2011 (10 Hz geophones).

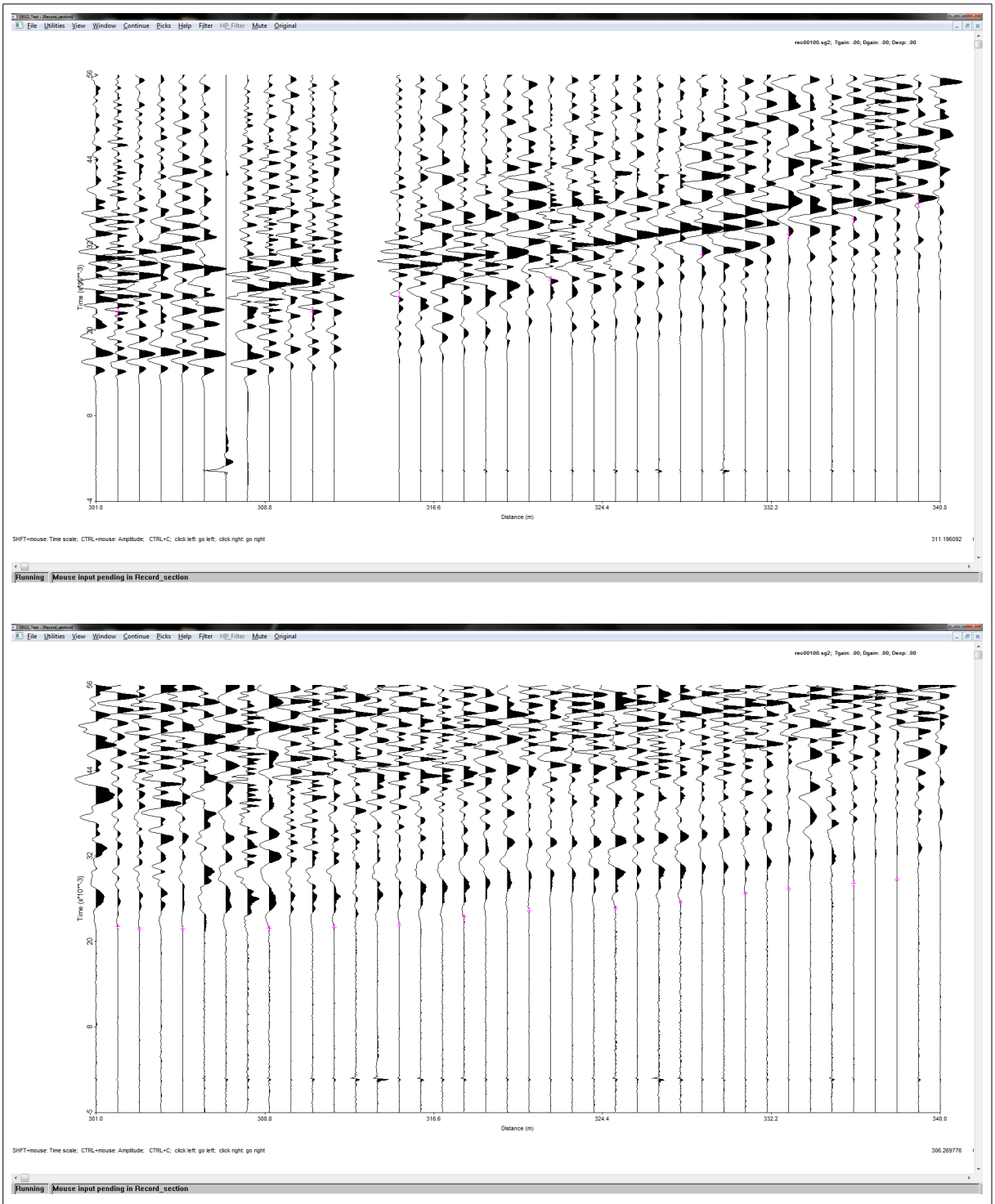

Shot in corner of MG and TG, geophones in ABG. Above July 2012, below December 2012, (50 Hz geophones).

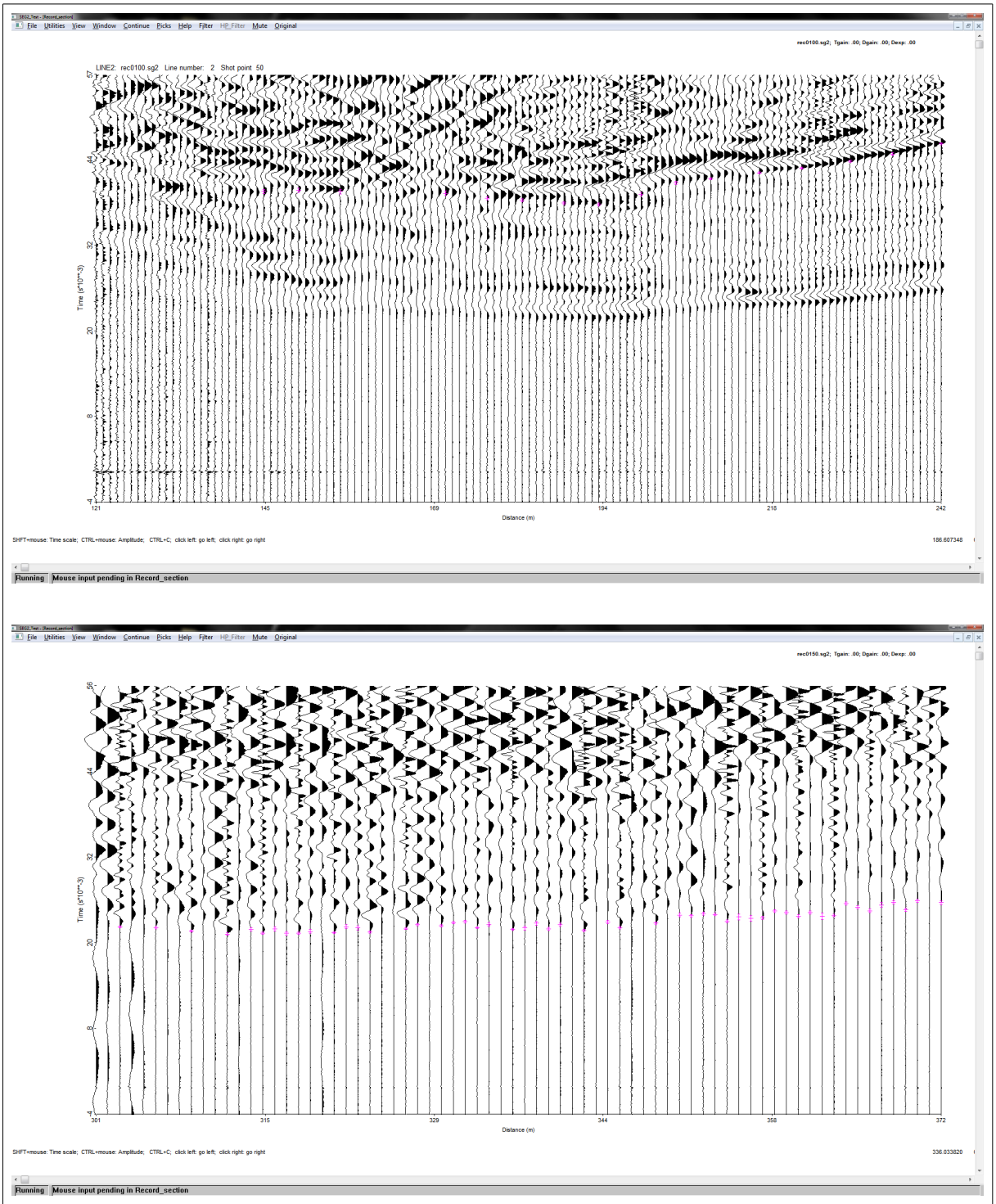

Shot at 50 m into MG, geophones in ABG. Above May 2005 (50 Hz geophones), below June 2011 (10 Hz geophones).

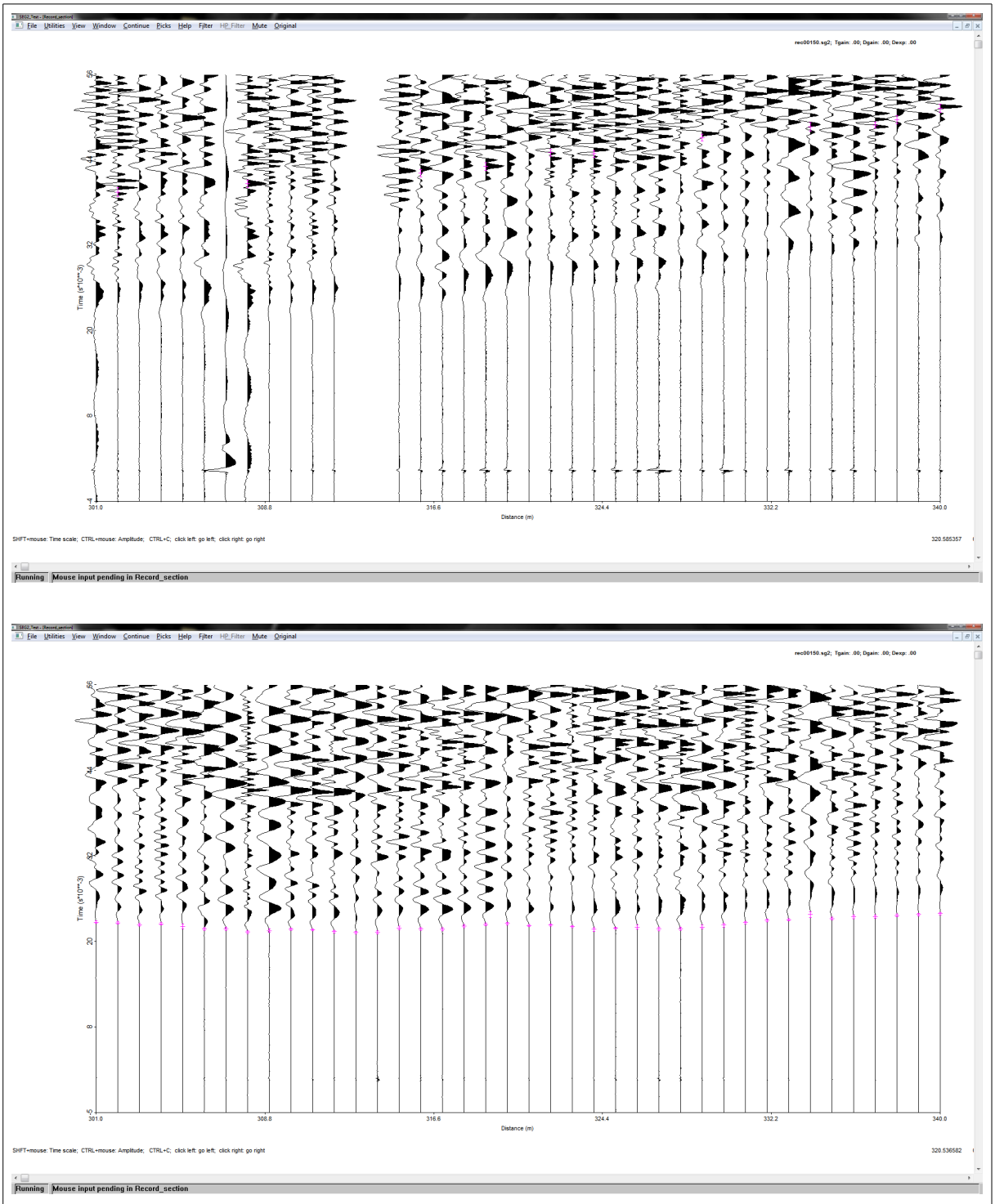

Shot at 50 m into MG, geophones in ABG. Above July 2012, below December 2012, (50 Hz geophones).

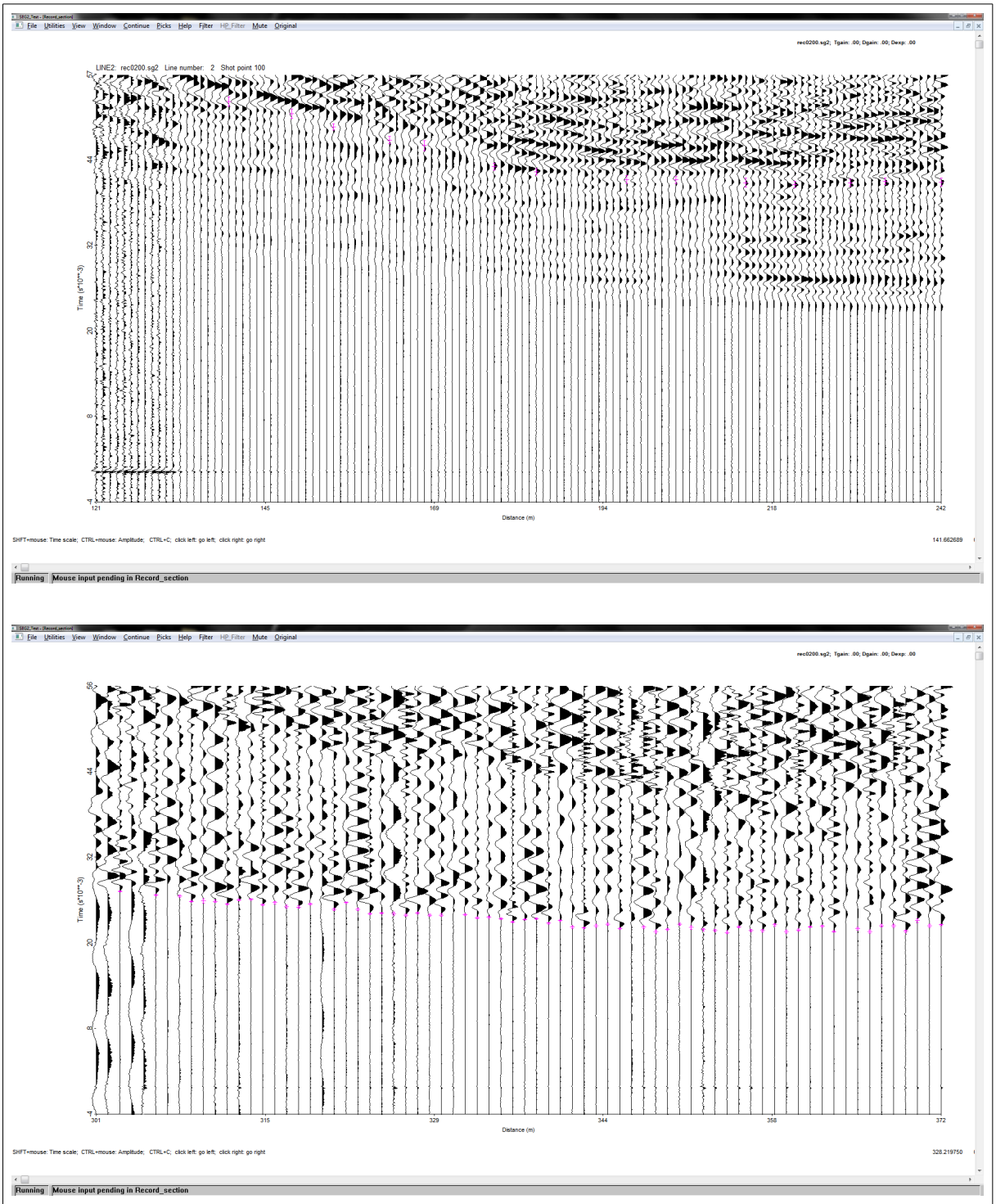

Shot at 100 m into MG, geophones in ABG. Above May 2005 (50 Hz geophones), below June 2011 (10 Hz geophones).

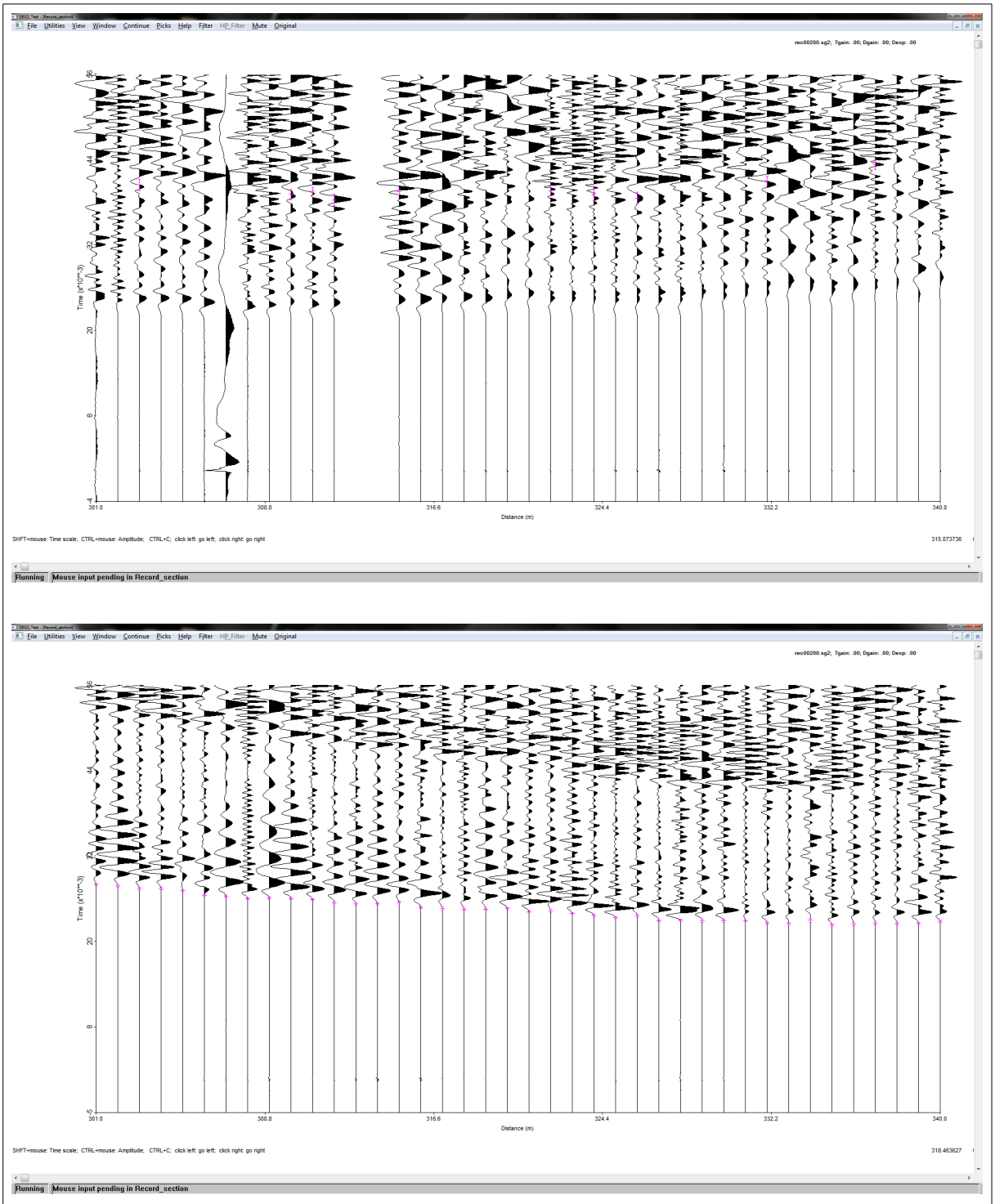

Shot corner 100 m into MG, Geophones in ABG. Above July 2012, below December 2012, (50 Hz geophones).

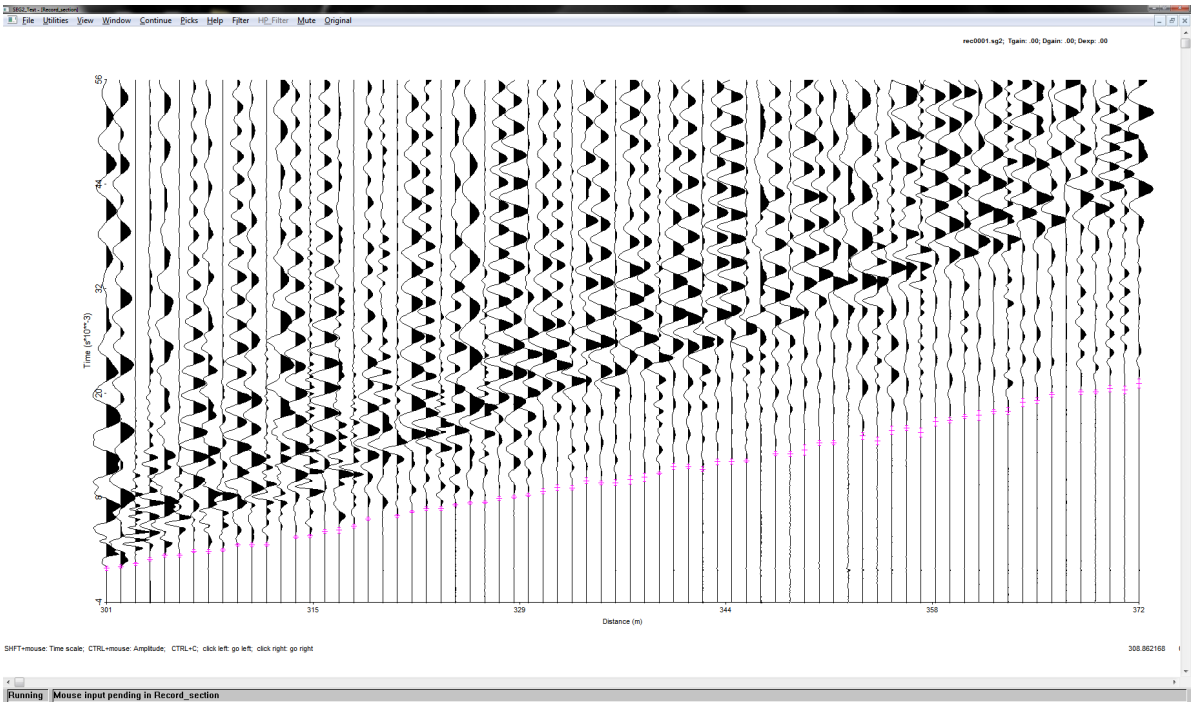

Shot in corner of ABG and TG, geophones in ABG. June 2011, (10 Hz geophones).

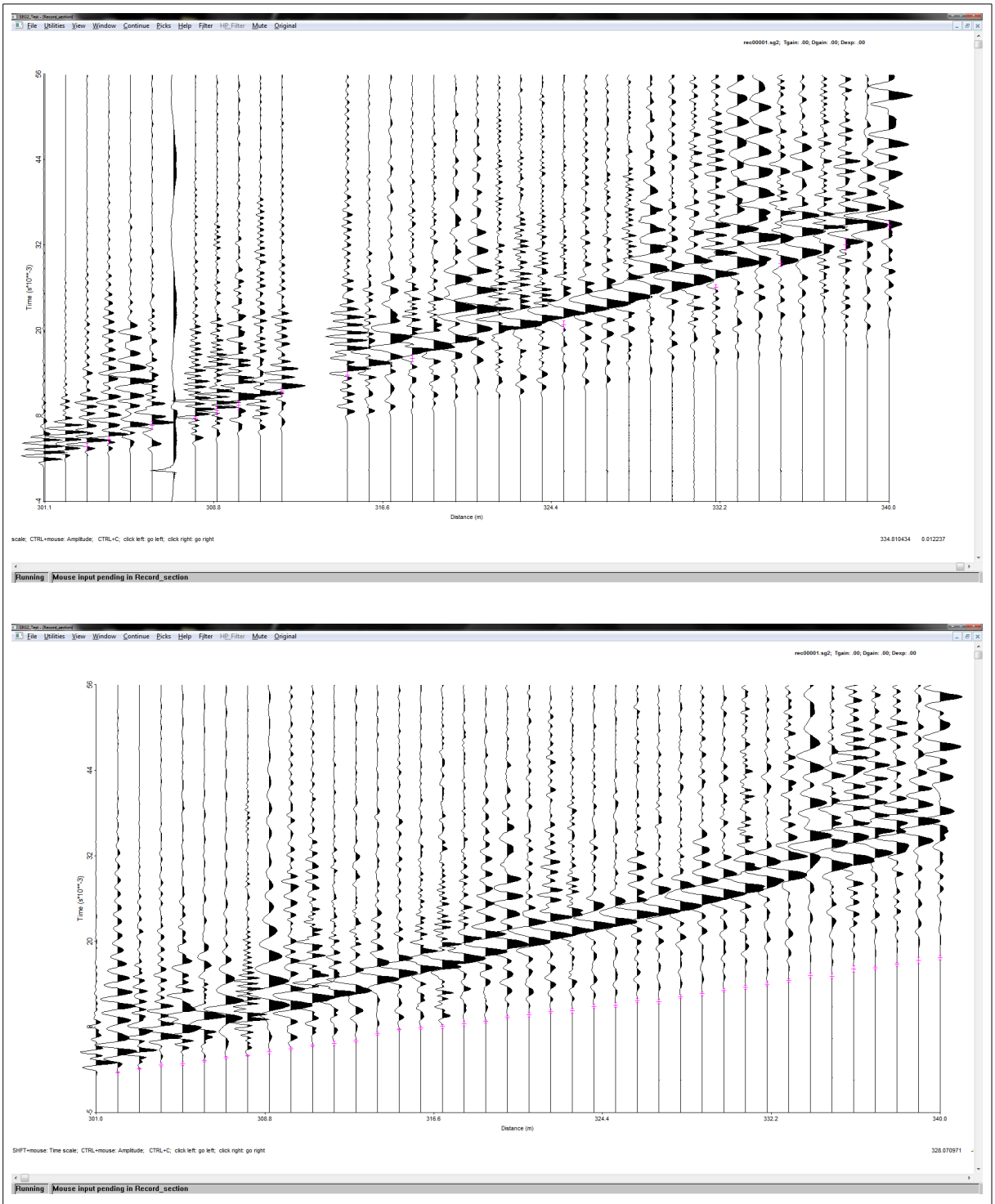

Shot in corner of ABG and TG, geophones in ABG. Above July 2012, below December 2012, (50 Hz geophones).

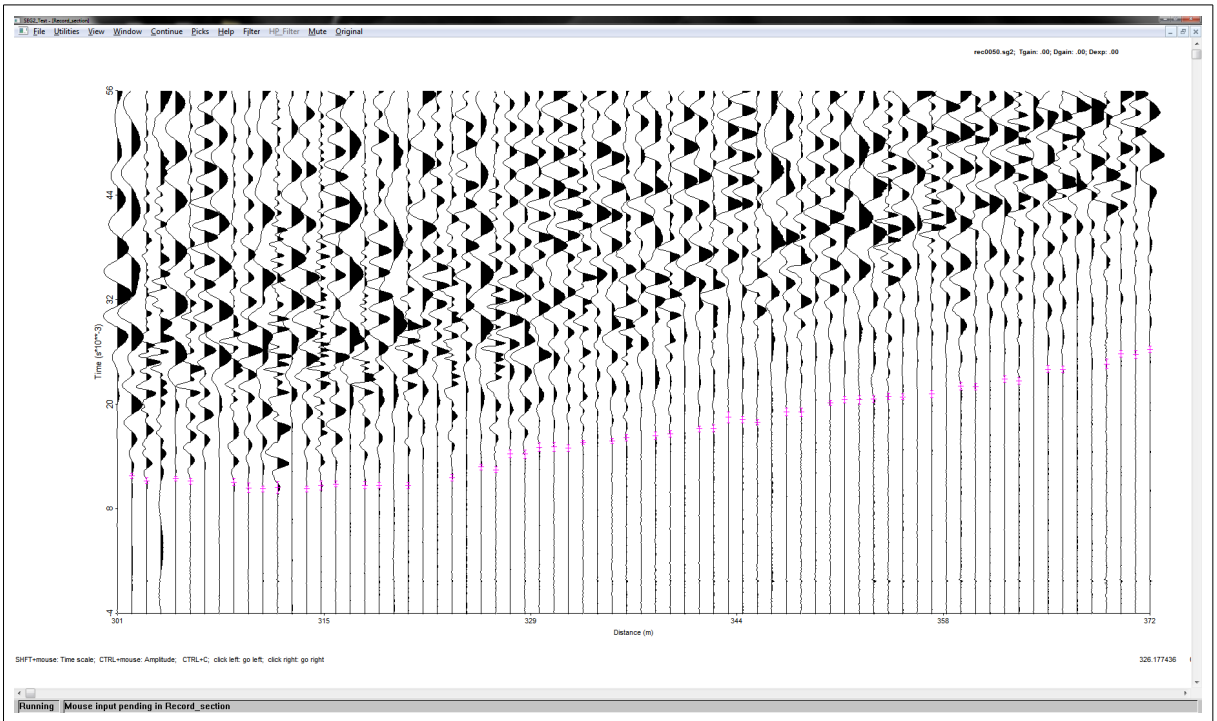

Shot at 50 m of TG, geophones in ABG. June 2011, (10 Hz geophones).

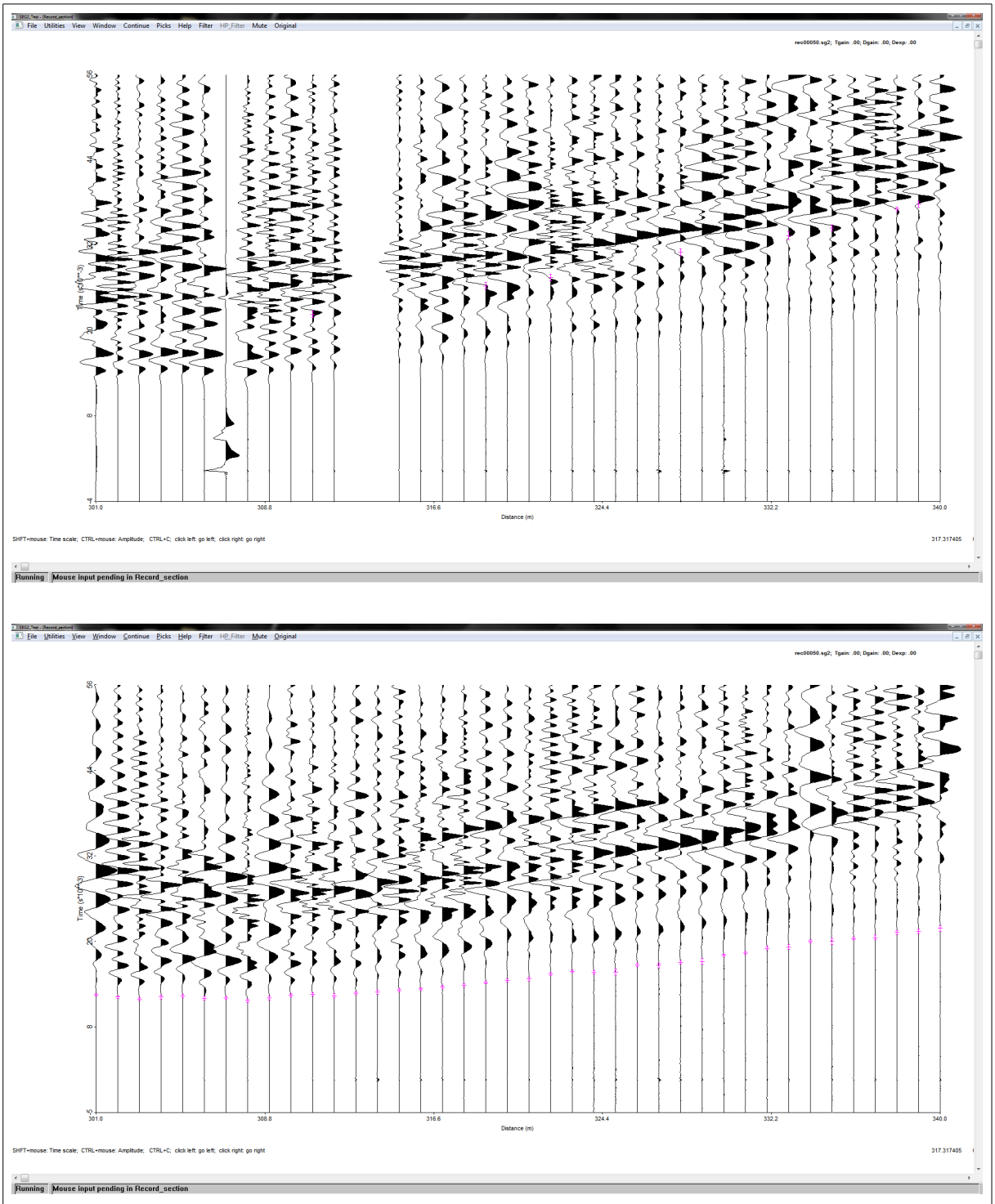

Shot at 50 m of TG, geophones in ABG. Above July 2012, below December 2012, (50 Hz geophones).

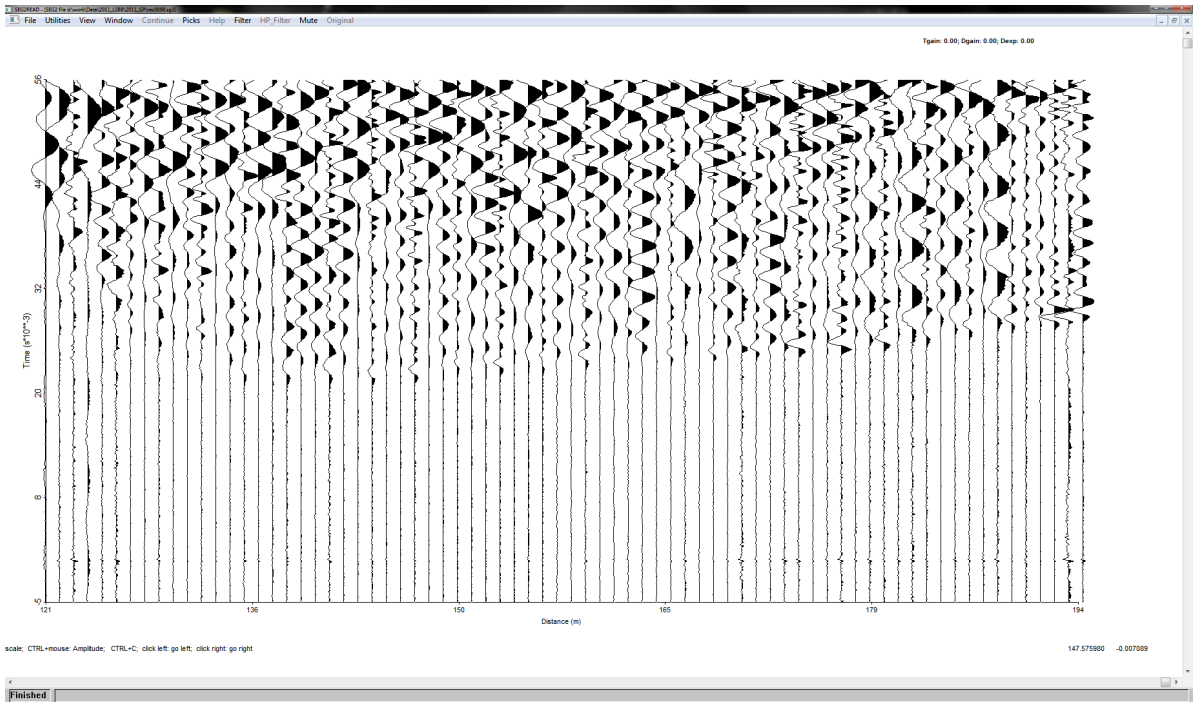

Shot in corner of ABG and TG, geophones in MG. June 2011, (10 Hz geophones).

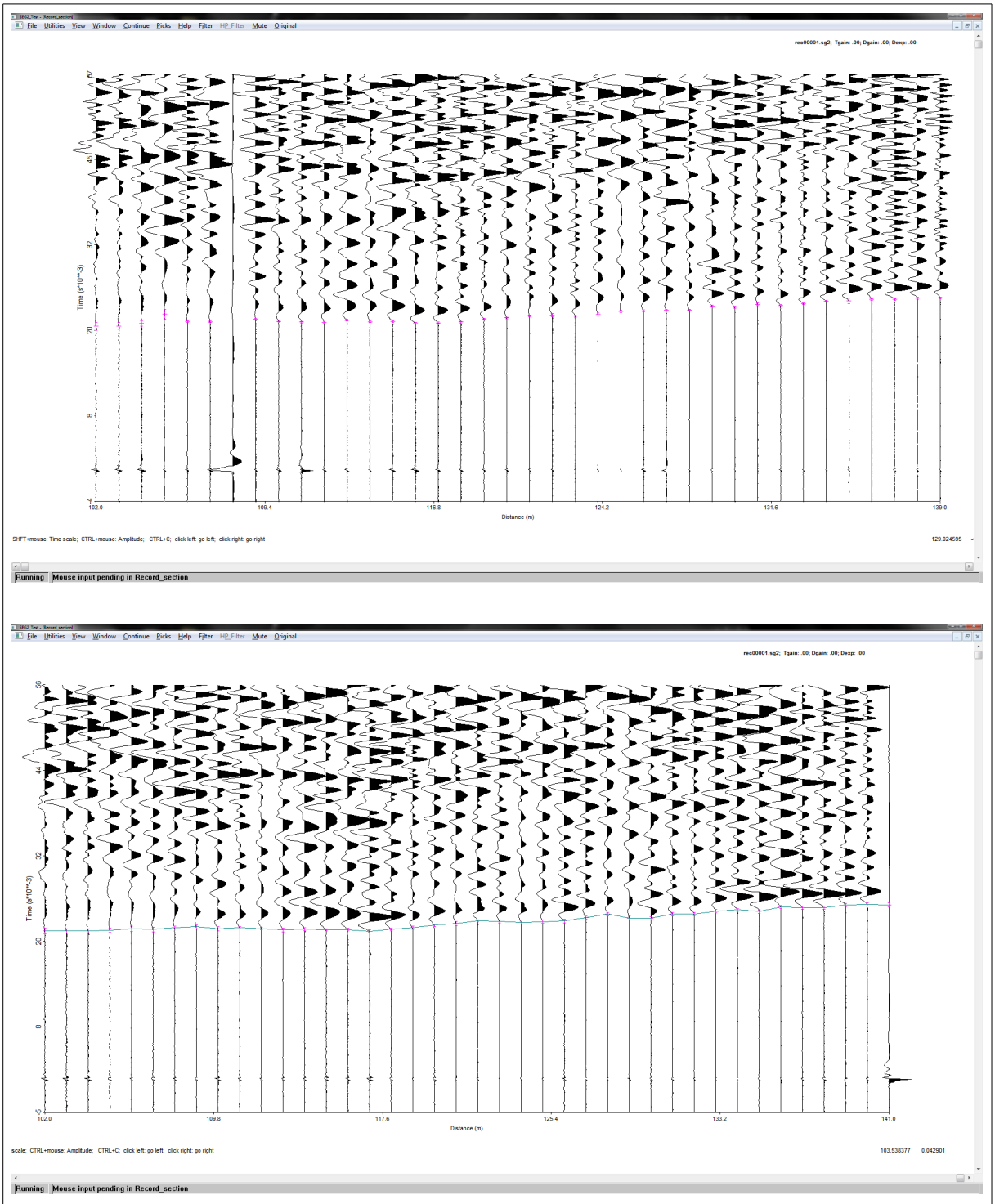

Shot in corner of ABG and TG, geophones in MG. Above July 2012, below December 2012, (50 Hz geophones).

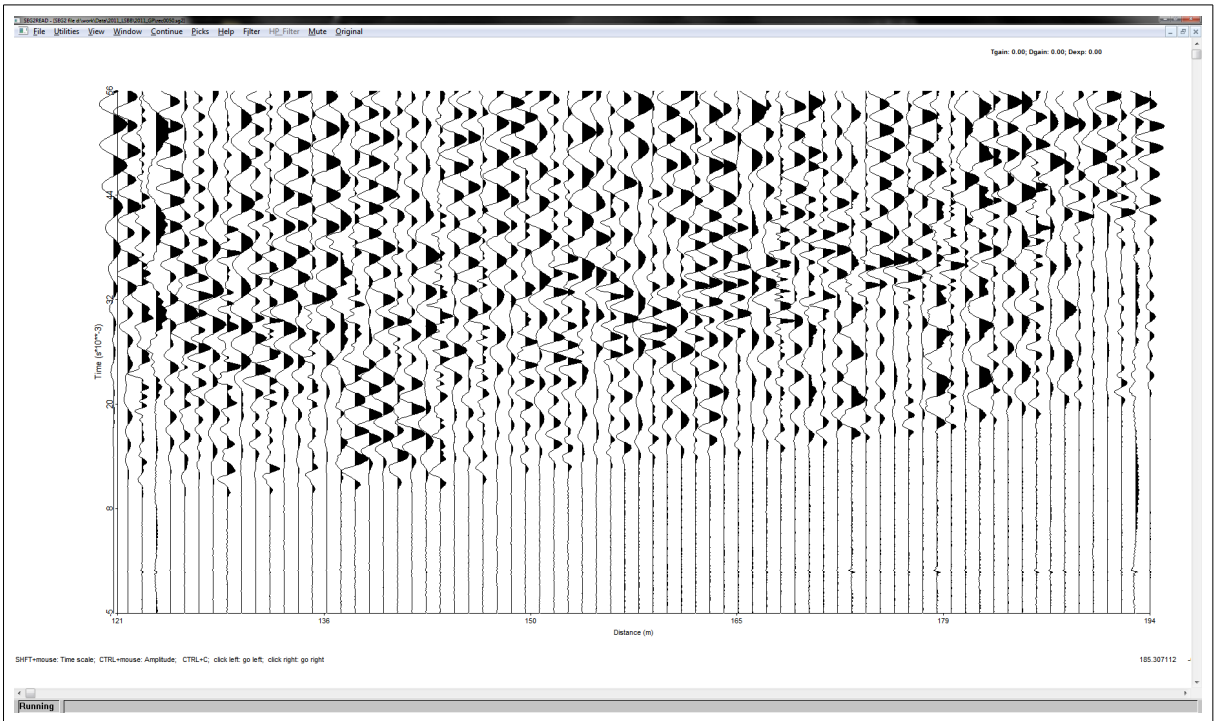

Shot at 50 m of TG, geophones in MG. June 2011, (10 Hz geophones).

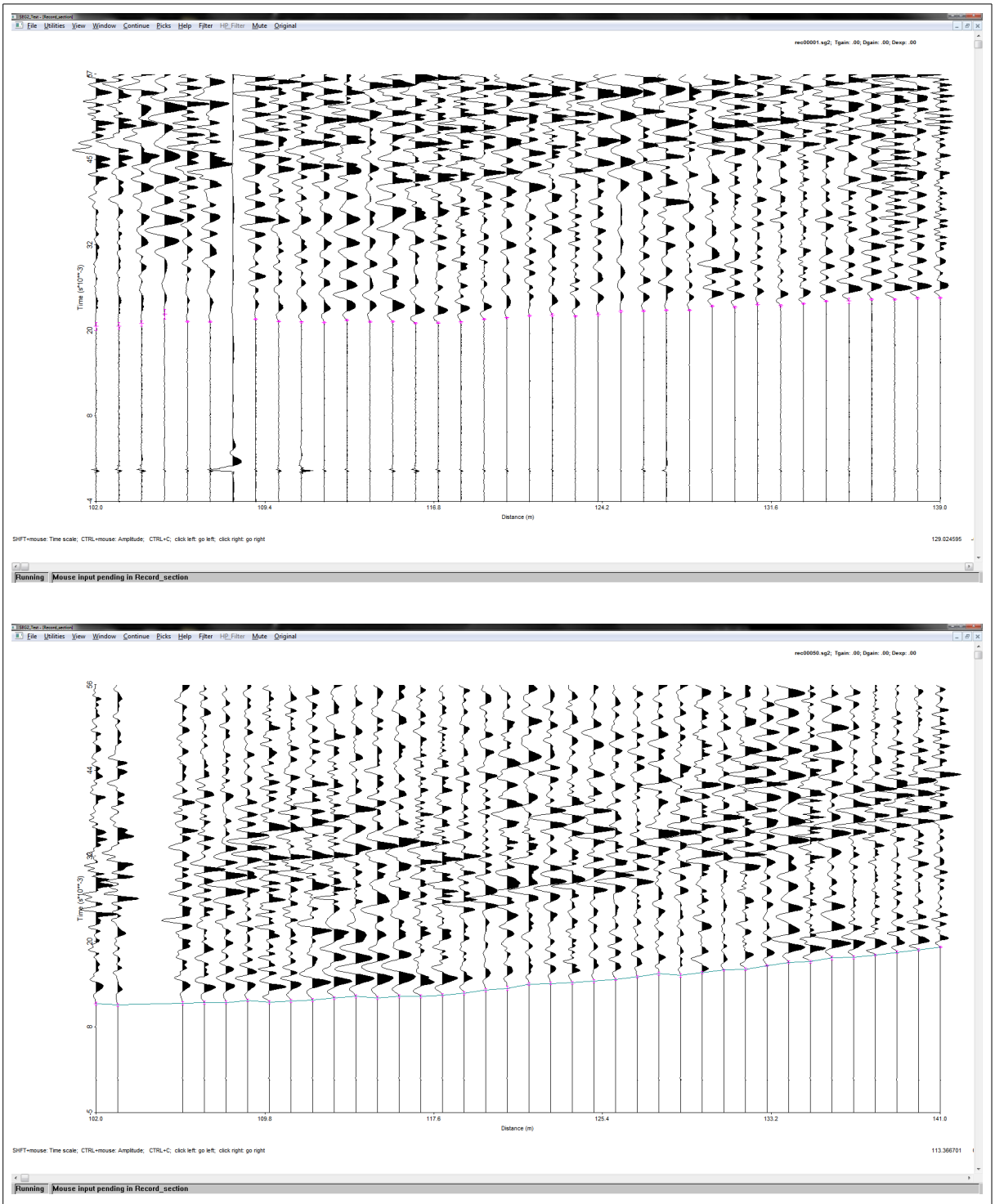

Shot at 50 m of TG, geophones in MG. Above July 2012, below December 2012, (50 Hz geophones).

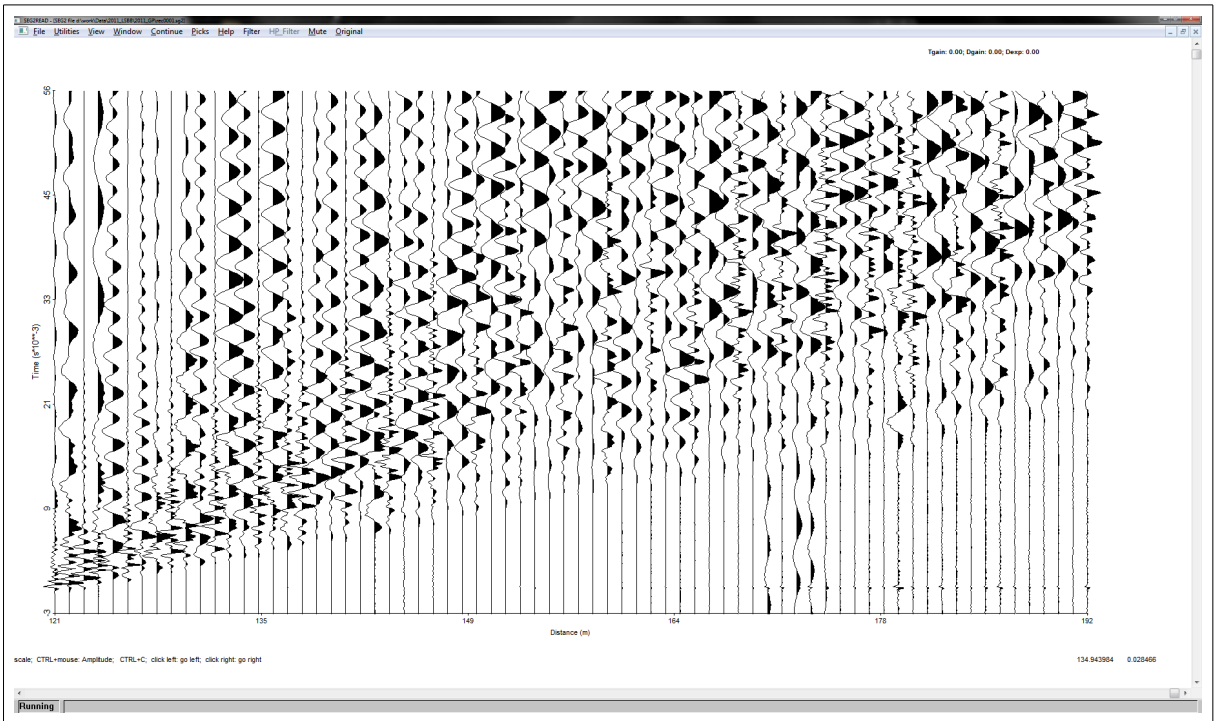

Shot in corner of TG and MG, geophones in MG. June 2011, (10 Hz geophones).

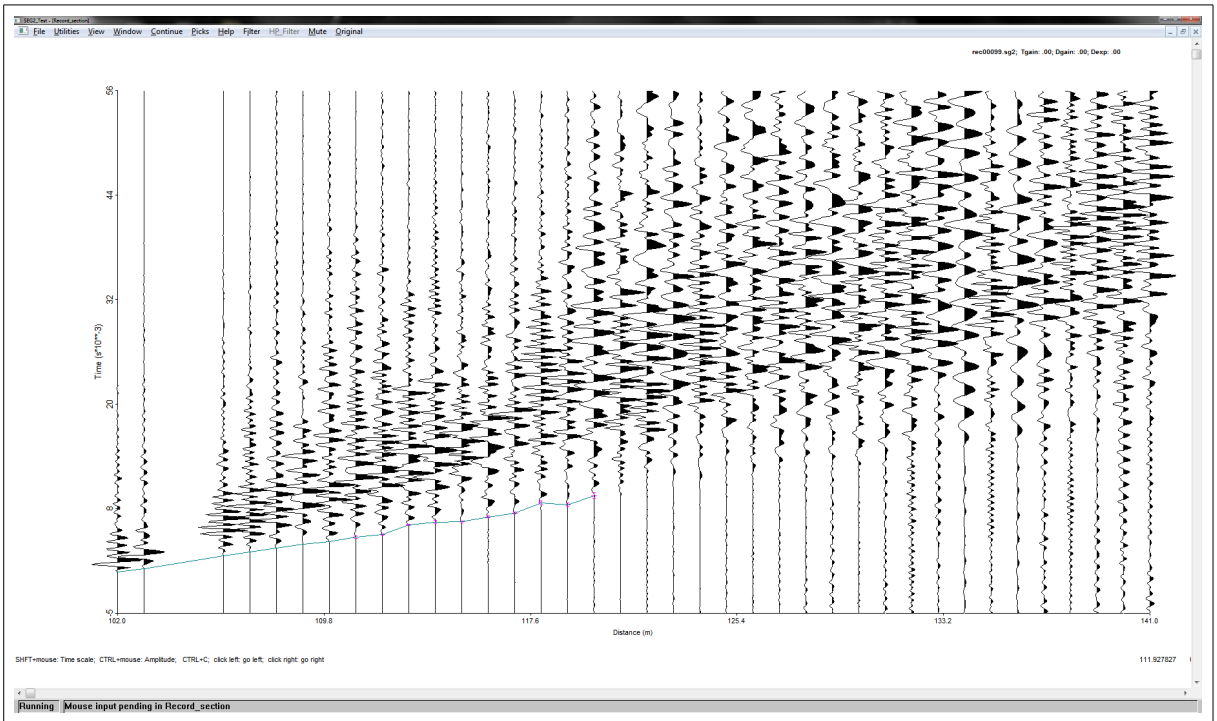

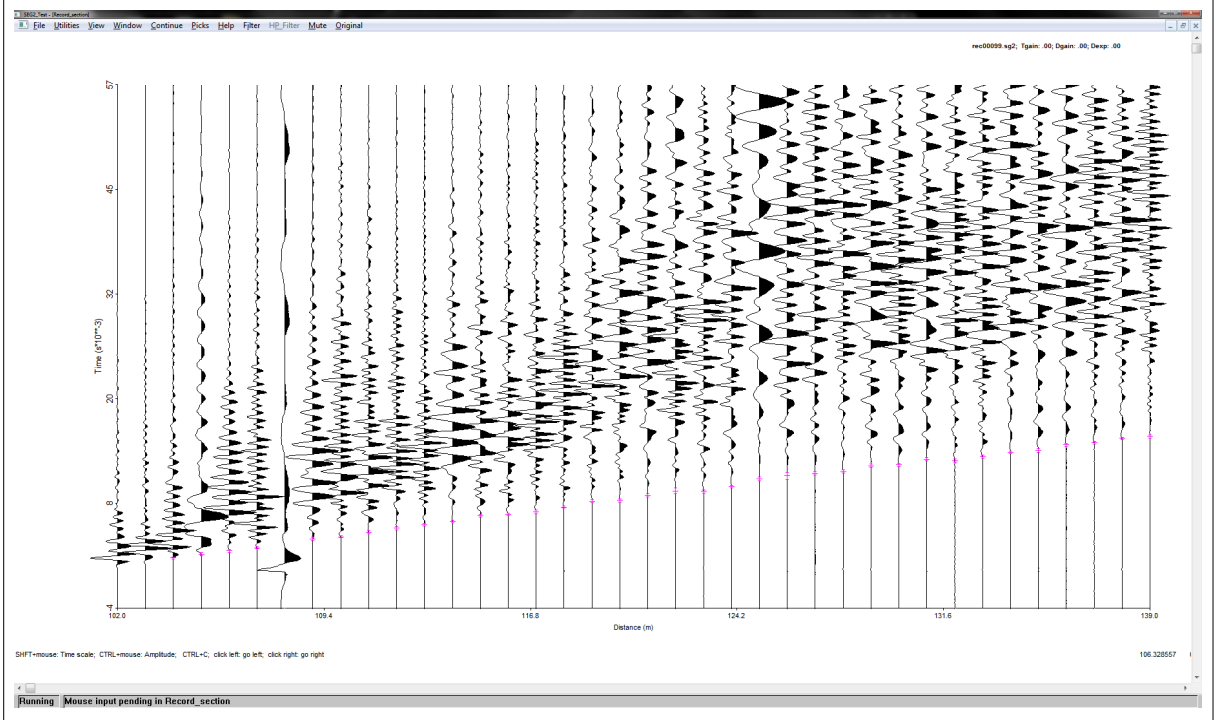

Shot in corner of TG and MG, geophones in MG. Above July 2012, below December 2012, (50 Hz geophones).

12 Appendix

Journal of Applied Geophysics 94 (2013) 59–71

Contents lists available at SciVerse ScienceDirect

Journal of Applied Geophysics

journal homepage: www.elsevier.com/locate/jappgeo

Seismic anisotropy analysis at the Low-Noise Underground Laboratory (LSBB) of Rustrel (France)

Ján Bereš [a], Hermann Zeyen [a,*], Guy Sénéchal [b], Dominique Rousset [b], Stéphane Gaffet [c]

[a] UMR 8148 IDES, CNRS-Université Paris-Sud XI, Bât. 504, cedex F-91405 Orsay, France
[b] FR 2952, IPRA, Université de Pau et des Pays de l'Adour, Cedex BP 1155F-64013 Pau France
[c] UMR GEOAZUR 6526, UNS/CNRS/OCA, 250, rue Albert Einstein—Bât. 4, Sophia-Antipolis—F-06560 Valbonne, France

ARTICLE INFO

Article history:
Received 24 November 2012
Accepted 16 April 2013
Available online 29 April 2013

Keywords:
Horizontal transverse isotropy
Seismic anisotropy
Cross-hole tomography
Hydro-geophysics
Karst
Time lapse

ABSTRACT

Seismic anisotropy of a fractured karstic limestone massif in sub-parallel underground galleries is studied. As the fractures are mostly vertically oriented, the seismic properties of the massif are approximated by horizontal transverse isotropy (HTI). Several data inversion methods were applied to a seismic dataset of arrival-times of P and S-waves.

The applied methods include: isotropic tomography, simple cosine function fit, homogeneous Monte-Carlo anisotropic inversion for the parameters of horizontal transverse isotropy and anisotropic tomography for tilted transversely isotropic bodies. All methods lead to the conclusion that there is indeed an anisotropy present in the rock massif and confirm the direction of maximum velocity parallel to the direction of fracturing. Strong anisotropy of about 15% is found in the studied area. Repeated measurements show variations of the P-wave parameters, but not of the S-wave parameters, which is reflecting a change in water saturation.

© 2013 Elsevier B.V. All rights reserved.

1. Introduction

In May 2005 and June 2011 seismic data were acquired between two nearly parallel sub-horizontal underground galleries approximately 100 m apart. These galleries form part of the LSBB (Laboratoire Souterrain à Bas Bruit; Low Noise Underground Laboratory), a system of underground tunnels in southern France built for the command of French nuclear forces that was converted into a research laboratory in 1998. The data served in the first place for a tomographic study of the site. However, soon it became clear that we have to deal with important anisotropy of seismic velocities. In this publication, we present an analysis of the acquired data in terms of quasi-P-wave (qP) and quasi-S-waves (qS) velocities and anisotropy distribution. In the following, we will omit the letter q for brevity. If the anisotropy is due to sub-parallel rock fracturing, the mechanical properties of the rock should depend on the water content in those fractures. Acquisition of seismic data in two different years with different water content should then show different anisotropy magnitudes. Therefore, we will present also a time lapse analysis of the data from both years.

The laboratory is located in a karstic limestone massif containing fractures and faults with a predominant N30°E direction, (Thiébaud, 2003) (simplified sketch in Fig. 1). The properties of the investigated part of the massif are influenced mostly by minor fractures, major faults are not present. However, the rock is intensely deformed by subvertical and subparallel cracks. Different types of limestone are present and observable at the surface. Sub-horizontal alternations of massive banks and friable layers (dipping with 25° in N120–130° direction) are interrupted by sub-vertical reef structures striking in E–W to WNW–ESE direction (Thiébaud, 2003).

2. Data acquisition

In 2005, 120 sledge hammer blasts carried out against the vertical wall of one of the sub-horizontal galleries ("anti-blast gallery", Fig. 1) were recorded by 12,250 Hz geophones fixed in horizontal position on the wall of the opposite sub-horizontal but not parallel gallery ("main gallery"), recording horizontal movements with the aim of doing a cross-hole tomography. Shot as well as station separation was 1 m (i.e. shot profile of 120 m and geophone profile of 122 m length). In the South, along the transversal gallery (Fig. 2), the two galleries are 100 m apart from each other, at the northern end of the measurements the distance increases to 108 m. In this way, we covered an azimuthal range of about 100°, from −50° to +50°, defining the zero azimuth as the direction perpendicular to the anti-blast gallery. This setup is similar to horizontal cross borehole measurements, with one difference that the boreholes start within the massif and not at the surface. Fig. 2a shows the position of shots and receivers as well as the rays of three example shots. The data quality allowed us to pick some 22,500 P-wave first arrival times (Fig. 3) and additional 2700 S_{paral}-wave arrivals (S-waves polarised parallel

* Corresponding author. Tel.: +33 169154909.

0926-9851/$ – see front matter © 2013 Elsevier B.V. All rights reserved.
http://dx.doi.org/10.1016/j.jappgeo.2013.04.008

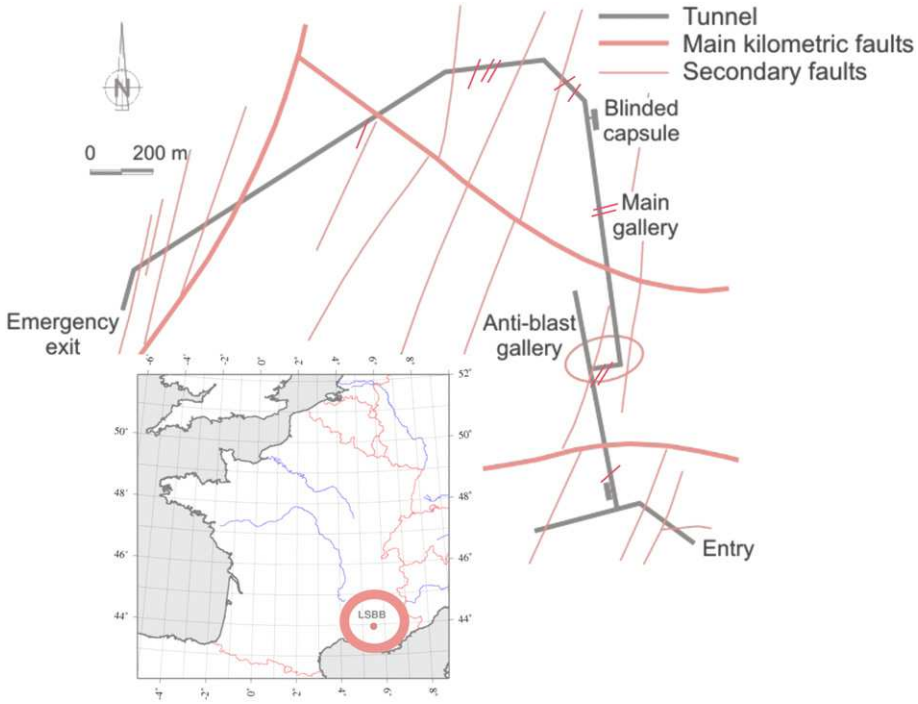

Fig. 1. Location of the study area and fracture/faults setting. Fractures visible at the surface are shown with long red lines (thick lines: major faults, thin lines minor ones). Short red lines indicate faults visible in the galleries. The red oval represents the investigation zone.

to the fractures) for the measurements of the year 2005. The arrivals of the S_{prp}-waves (polarised normal to the fractures—after Rüger, 1997) were not possible to pick as the y cannot be distinguished behind the S_{paral}-waves. These data were acquired during a period with significant water content in the massif.

In 2011, a second campaign was conducted, where shots were executed not only in the anti-blast gallery but also in the transversal gallery (Fig. 2b), extending in this way the angle coverage from 100° to almost 140°. Other parameters remained unchanged. More than 26,000 P-wave first arrival times and 6500 S_{paral}-wave arrivals were picked. This dataset was acquired during a dry period.

3. Data Analysis

3.1. Isotropic Cross Hole Tomography

Fig. 3 shows all measured P-wave and S_{paral}-wave arrival times from May 2005 as function of offset. For an isotropic and homogeneous velocity distribution, one should expect all points lying on a straight line. The scatter of the arrival times shows that the rocks must be inhomogeneous in the area. As a first step, we did standard isotropic cross-hole tomography using the code pstomo_eq (Tryggvason and Linde, 2006). Since the galleries are not parallel and do not have the same slope, we had to use a 3D programme that takes the real geometry into consideration. The resulting model (Fig. 4) explains the data well with a standard deviation of 0.29 ms, however, it shows clear artefacts (red ellipse areas), especially in the NE and SW corners, where velocities that are unrealistically high for limestones (e.g. Fournier et al., 2011; Jeanne et al., 2012). This result can be explained by the fact that rays travelling in SW–NE direction have smaller travel-times than those travelling in NW–SE direction. The tomographic inversion algorithm gives realistic velocities in the centre, where the ray density is highest (Fig. 5). However, it tries to compensate the travel time differences in the areas that are less well constrained due to smaller ray density. This result indicates presence of anisotropy. It is well known that P-wave travel-times corresponding to an anisotropic medium may be explained also by a more complicated isotropic velocity distribution, but, the resulting velocities are then usually not geologically meaningful (e.g. Grechka, 2009). Also the two well distinguished branches in Fig. 3 indicating two different velocities can be explained by anisotropy.

3.2. Cosine Function Fit

Therefore, as a first test of anisotropy, we fitted the observed travel-times to a simple cosine function assuming seismically homogeneous material (i.e. straight rays):

$$t(d,\varphi) = \frac{d}{v_0 + dv \cdot \cos[2(\varphi - \varphi_0)]} \quad (1)$$

where t is the measured travel time [ms], d the offset [m] taking into account the 3D coordinates of shot and receiver points, ϕ the angle of ray departure ($\phi = 0°$ is perpendicular to the wall of the anti-blast gallery), v_0 the average velocity [km/s], dv the amplitude of anisotropy [km/s] and ϕ_0 the direction of the high velocity direction with respect to the direction perpendicular to the anti-blast gallery.

The resulting best fitting parameters for P-waves and S_{paral}-waves are given in Table 1. The overall data misfit (fourth column in Table 1 for each year) corresponds to 60% travel time variance reduction with respect to the best fitting isotropic model and >99% with respect to the measured data. σ represents the standard deviation calculated as:

$$\sigma = \sqrt{\frac{1}{N-1}\sum_{i=1}^{N}\left(t_{calculated} - t_{measured}\right)^2} \quad (2)$$

We also calculated the average velocity for all rays departing within bins of 5° and plotted these data for both years for P- and S-waves of both years as function of departure angle (Fig. 6) together with the best fitting cosine approximations. Bigger uncertainty bars for the year 2011 are due to a different experimental mounting of the

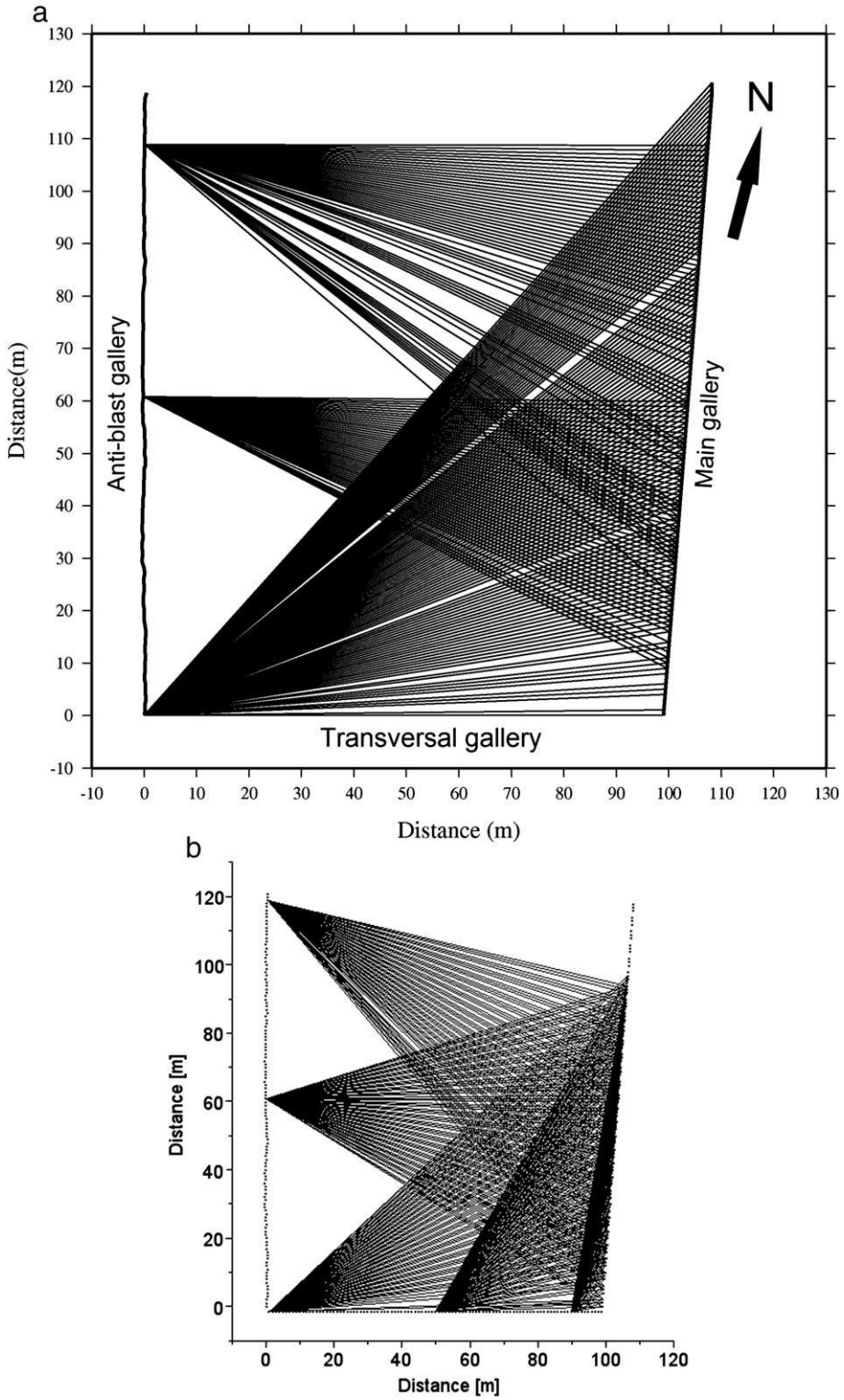

Fig. 2. a) Example of rays from 3 shot points (May 2005). b) Example of rays from 5 shot points (June 2011). Missing rays are due to noise at the corresponding receiver.

geophones on the walls which produced some additional noise due to geophone vibrations after the first arrival.

3.3. Monte Carlo Inversion of Anisotropic Stiffness Coefficients

In order to determine more precisely the anisotropic seismic properties of the rock massif, we developed a Monte Carlo programme based on the Markov chain algorithm. In the most general case, 21 independent stiffness coefficients are needed to describe anisotropic seismic velocity distribution (e.g. Grechka, 2009). Grechka and Kachanov (2006), examined the media with penny shaped cracks and came to conclusion that when the cracks are not co-planar, resulting anisotropy is orthorhombic. The number of independent stiffness coefficients for such a medium decreases to nine.

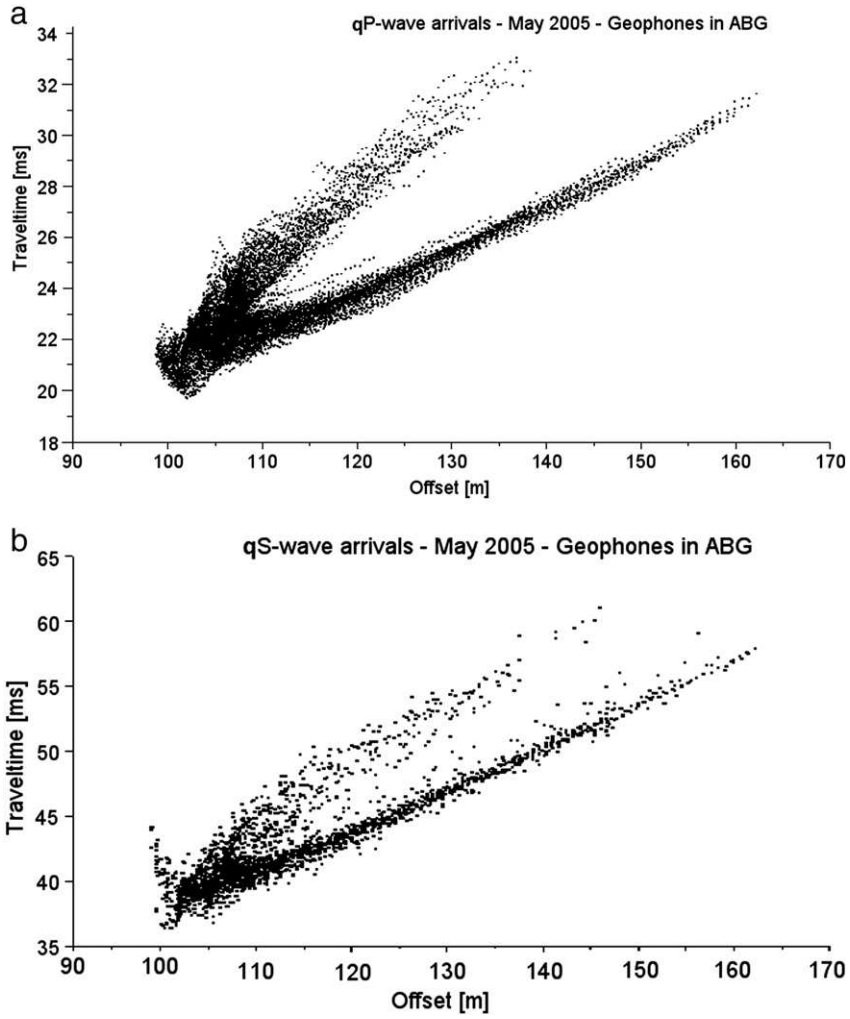

Fig. 3. a) Travel times vs. offset of all measured P-wave arrival time in 2005. b) Travel times vs. offset of all measured S-wave arrival times in 2005.

However, in the plane, perpendicular to the plane of fractures, in this case, the symmetry is equivalent to transverse isotropy where the number of independent stiffness coefficients decreases furthermore to five The third dimension does not influence the velocities in the two studied dimensions, and the third orthorhombic plane and its respective coefficients have no effect on studied dimensions. If the fractures would not be oriented vertically, but with an important angle, using this simplification of transversely isotropic medium, would lead to an error of the maximum velocity. The real velocity would be higher if the velocity in direction of the unused orthorhombic axis was higher, and smaller in the other case. As Grechka and Kachanov (2006) state, there is virtually no effect on the stiffness matrix if the crack faces are corrugated or not.

Therefore, the massif is considered as a medium with an isotropy plane parallel to the principal fracture planes (Tsvankin et al., 2010) containing the maximum velocity. The minimum velocity is parallel to the symmetry axis perpendicular to the fractures. In the studied area, sub-vertical cracks lead to a horizontal transversely isotropic medium approximation (HTI).

This simplification leads to a reduction of the number of coefficients to five stiffness coefficients and the angle of direction of the symmetry axis. The coefficients stem from the matrix of stiffness coefficients expressed in Voigt notation (Winterstein, 1990), and derived from the stress–strain relationship:

$$\tau_i = C_{ij} \cdot \varepsilon, \tag{3}$$

$$C^{(HTI)} = \begin{bmatrix} c_{11} & c_{12} & c_{12} & 0 & 0 & 0 \\ c_{12} & c_{22} & c_{23} & 0 & 0 & 0 \\ c_{12} & c_{23} & c_{22} & 0 & 0 & 0 \\ 0 & 0 & 0 & c_{44} & 0 & 0 \\ 0 & 0 & 0 & 0 & c_{66} & 0 \\ 0 & 0 & 0 & 0 & 0 & c_{66} \end{bmatrix} \tag{4}$$

For HTI, the stiffness coefficients are connected to velocities in the following way (modified from Grechka's VTI coefficients, 2009):

$$V_p^2 = \frac{1}{2\rho}\left\{F + \sqrt{\left[(c_{11}-c_{66})\cos^2(\phi)-(c_{22}-c_{66})\sin^2(\phi)\right]^2 + 4(c_{12}+c_{66})^2\cos^2(\phi)\sin^2(\phi)}\right\} \tag{5}$$

$$V_{Sprp}^2 = \frac{1}{2\rho}\left\{F - \sqrt{\left[(c_{11}-c_{66})\cos^2(\phi)-(c_{22}-c_{66})\sin^2(\phi)\right]^2 + 4(c_{12}+c_{66})^2\cos^2(\phi)\sin^2(\phi)}\right\} \tag{6}$$

$$V_{Sparal}^2 = \frac{1}{\rho}\left\{c_{66}\cos^2(\phi) + c_{44}\sin^2(\phi)\right\} \tag{7}$$

where

- Vs_{prp} stands for S wave velocity, for which particle movement with respect to fractures depends on propagation direction, polarised normal to fractures, (Rüger, 1997);

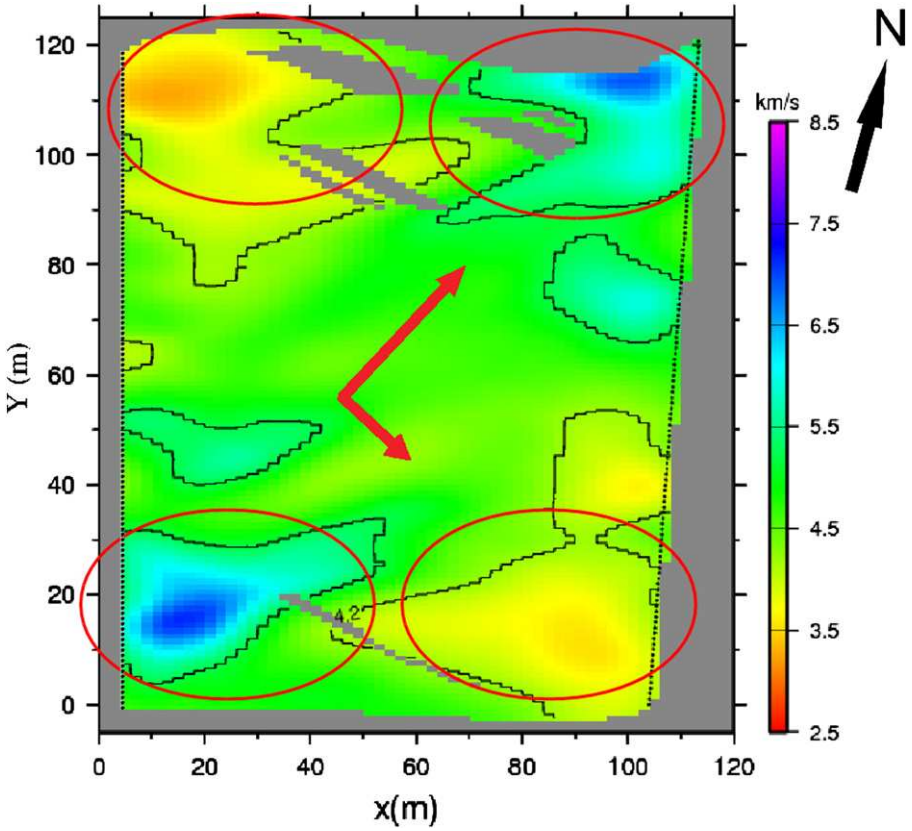

Fig. 4. P-wave velocity distribution obtained from 3D isotropic cross-hole tomography using the real field geometry. The very high velocities in the upper right and lower left corners and the low velocities in the opposite corners are artefacts due to neglecting anisotropy. The black dots correspond to the positions of shots (left) and receivers (right). Big red arrow: direction of high velocity, small red arrow: direction of low velocity obtained from cosine fit described later.

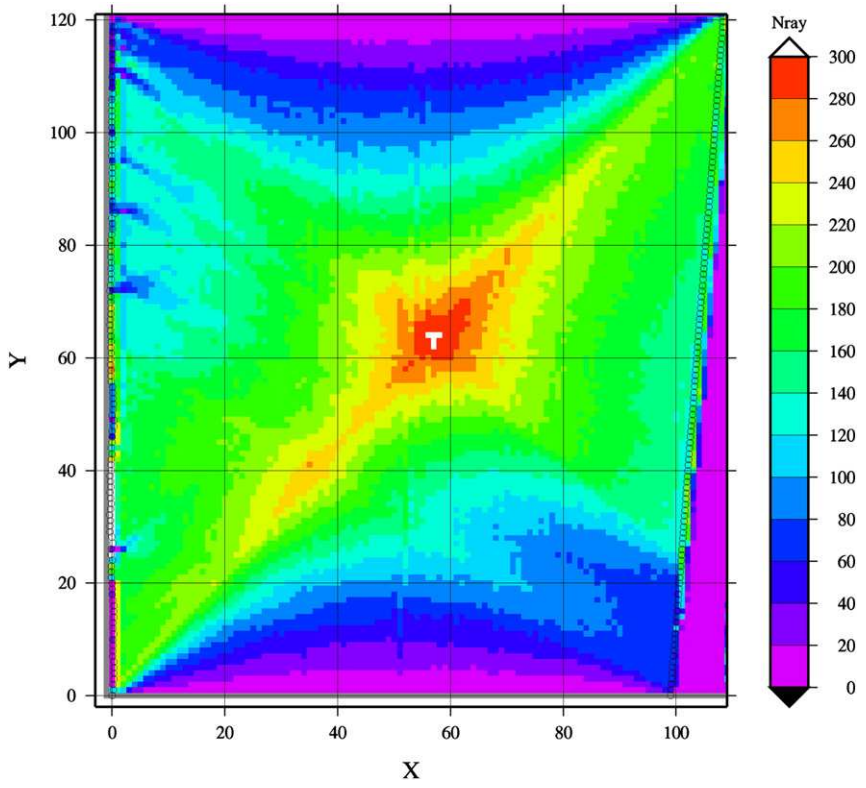

Fig. 5. Ray coverage for isotropic tomography. N ray represents density of rays per m^2.

Table 1
Summary of best fitting parameters for simple cosine fit.

Wave type	2005				2011			
	v_0 [km/s]	dv [km/s]	ϕ_0[°]	σ [ms]	v_0 [km/s]	dv [km/s]	ϕ_0 [°]	σ [ms]
P	4.69 ± 0.03	0.45 ± 0.02	43 ± 3	0.98	4.63 ± 0.03	0.61 ± 0.04	40 ± 2	1.14
S_{paral}	2.61 ± 0.01	0.17 ± 0.01	43 ± 3	1.37	2.61 ± 0.02	0.13 ± 0.03	35 ± 6	3.45

- Vs_{paral} stands for S wave velocity, with particle movement always parallel to fractures;
- $F = (c_{11} + c_{66})\cos^2(\phi) + (c_{22} + c_{66})\sin^2(\phi)$;
- ρ is the rock density taken here as 2500 $kg.m^{-3}$;
- ϕ represents the angle between propagation direction and isotropy axis

In the coordinate system of anisotropy, we define the direction of the isotropy axis and therefore also of low velocity as X_{HTI}. The isotropy plane of high velocity is then parallel to Y_{HTI} and Z_{HTI}. This coordinate system is rotated with respect to the one of the underground laboratory, where the X-axis is defined perpendicular to the anti-blast gallery, by an angle ϕ_0 in the X–Y plane. The Z axis of the laboratory and the anisotropy coordinate systems are the same due to the essentially 2D configuration of the data acquisition. This angle of rotation is one of the unknowns in the inversion.

Although it is common to express anisotropy in reflection seismics in terms of Thomsen's parameters (Thomsen, 1986) or Thomsen's type parameters derived for HTI media (Rüger, 1997; Tsvankin, 1997), we are inverting for the stiffness coefficients as they provide the direct physical information about the medium. If only P-wave information were available, Thomsen's parameters ε and δ could be uniquely resolved, whereas the stiffness coefficients c_{12} and c_{66} would be linearly dependent. However, the joint inversion of P and S-wave arrivals allows a unique resolution of all five stiffness parameters necessary for HTI anisotropy and the rotation angle. Thomsen's parameters

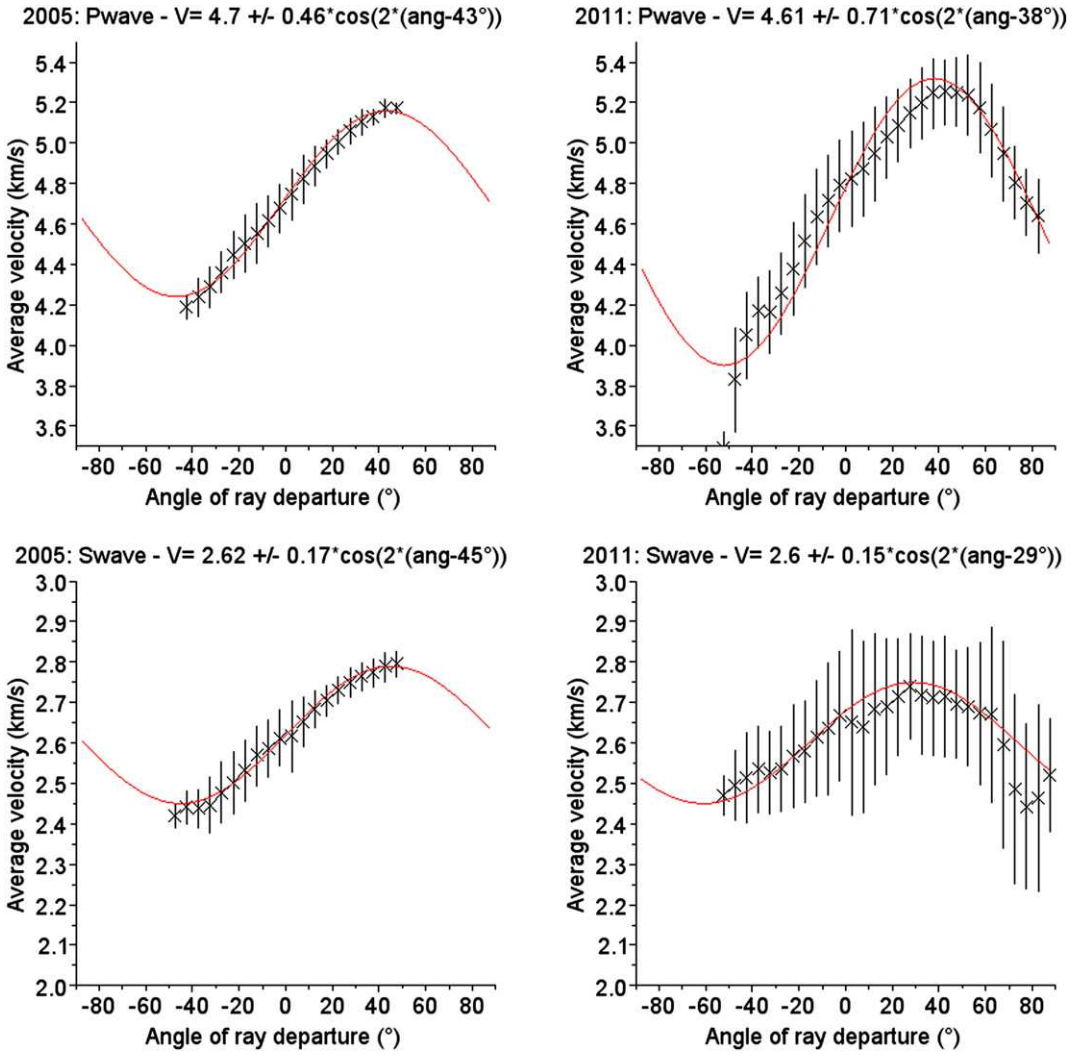

Fig. 6. Average velocities for all rays departing from the shot points within a range of angles of ± 2.5°, with optimum velocity adjustments from cosine fit function. 0° departure corresponds to the direction perpendicular to the anti-blast gallery. Error bars correspond to standard deviation of average velocities. Left column 2005, right column 2011. First row velocities P-waves, second row velocities S-waves.

Table 2
Summary of best fitting parameters for Monte Carlo inversion (units of coefficients: $[(km/s)^2 \cdot (g/cm^3)]$).

Parameters	2005	2011	
		All shots	Without transverse gallery
c_{11}	44.9	36.9	37.1
c_{22}	65.9	67.6	69.2
c_{12}	25.4	23.3	23.8
c_{44}	19.3	18.3	19.7
c_{66}	14.8	15.3	15.4
ϕ_0[°]	−43.9	−53.1	−52.7
Vp min [km/s]	4.23	3.84	3.85
Vp max [km/s]	5.13	5.2	5.26
Vs min [km/s]	2.43	2.47	2.48
Vs max [km/s]	2.78	2.71	2.81
RMS [ms]	0.47	0.91	0.82

can then easily be calculated from the stiffness parameters, as well as the velocities in the direction of the symmetry axis, V_{P0} and V_{S0}.

Apart from the angle of rotation ϕ_0, the independent coefficients needed to be calculated for this model are in Voigt notation: c_{11}, c_{22}, c_{12}, c_{66} and c_{44} (Grechka, 2009). Coefficients c_{11} and c_{22} are the coefficients that relate to the velocities of P-waves parallel to the anisotropy axes, where c_{11} is related to the minimum velocity and c_{22} to the maximum velocity. The coefficients c_{44} and c_{66} are mainly controlled by the S velocities, although c_{66} enters also the equation for P velocities where, it is related to c_{12}, leading to a strong linear dependency between these two parameters in the absence of S-wave travel times.

During the inversion, beginning with an arbitrary starting model, the programme modifies randomly all parameters at the same time within a predefined model space and with a Gaussian probability-density function around each actual model parameter. The fit of the new model measured in a least squares sense with respect to measured and calculated travel-times is compared with the one of the former model. If the new model fits the data better than the former model, it is introduced in an assemblage of accepted models and the following model is searched around the new model (i.e., the centre of the probability-density function is shifted from the former to the new model); if not, the new model is rejected and the former model is repeated in the mentioned assemblage. The area was supposed to be homogeneous, i.e. no ray bending was considered and we inverted only for the average stiffness parameters. As output, the programme gives a list of all coefficient combinations with their respective misfits (root mean square—RMS of the differences between measured and calculated travel-times). The best fitting model after 500,000 iterations is displayed in Table 2 and Fig. 7.

The inversions for both years correspond quite well to their cosine approximations for both wave types. Fig. 8 displays the histogram of inverted parameters for all models yielding a fit within 10% of the best solution.

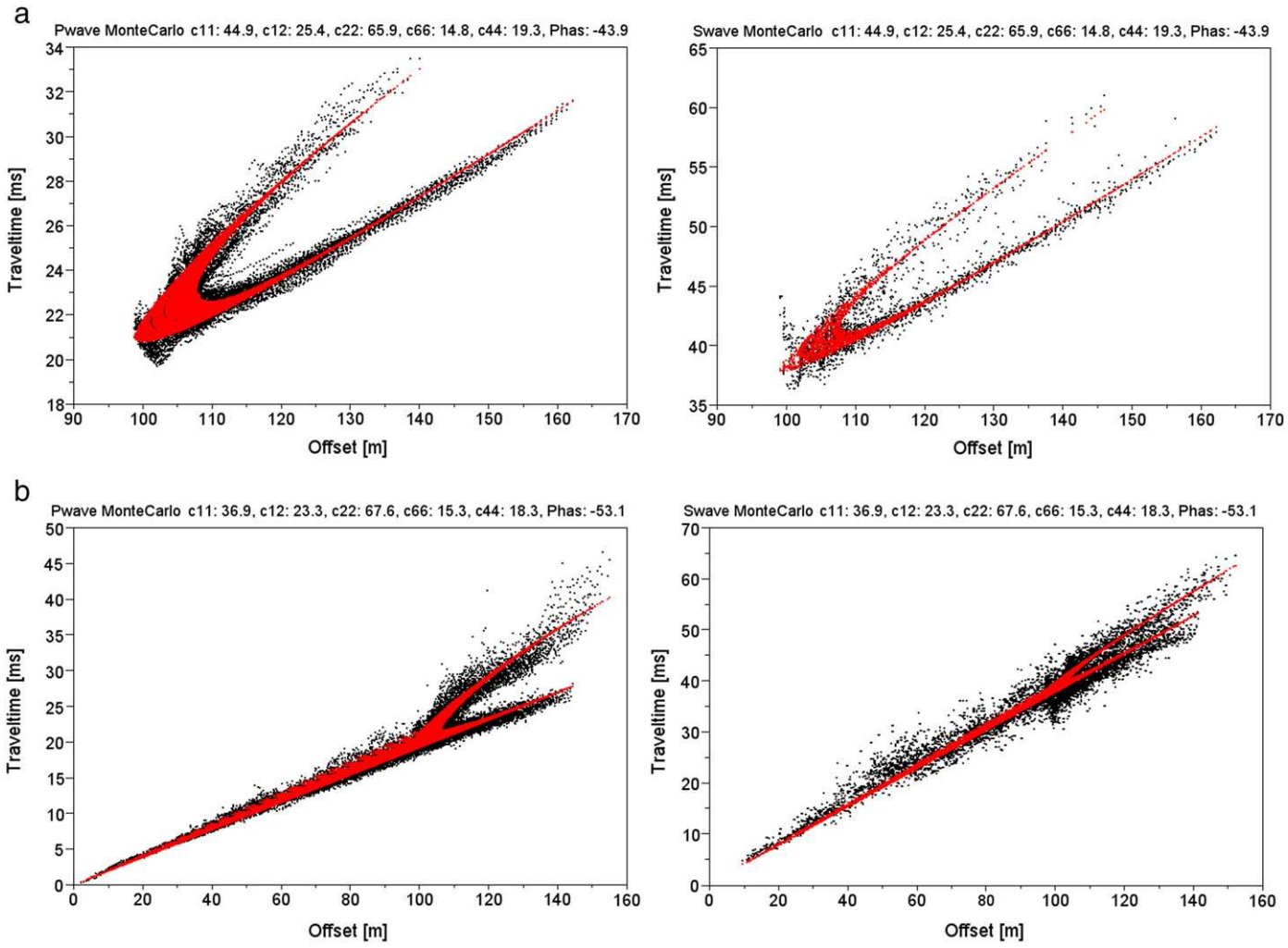

Fig. 7. Travel-times measured (black) and modelled (red) (Monte Carlo approach). Upper row shows results for 2005, lower row those for 2011; left column: P waves, right column: S waves.

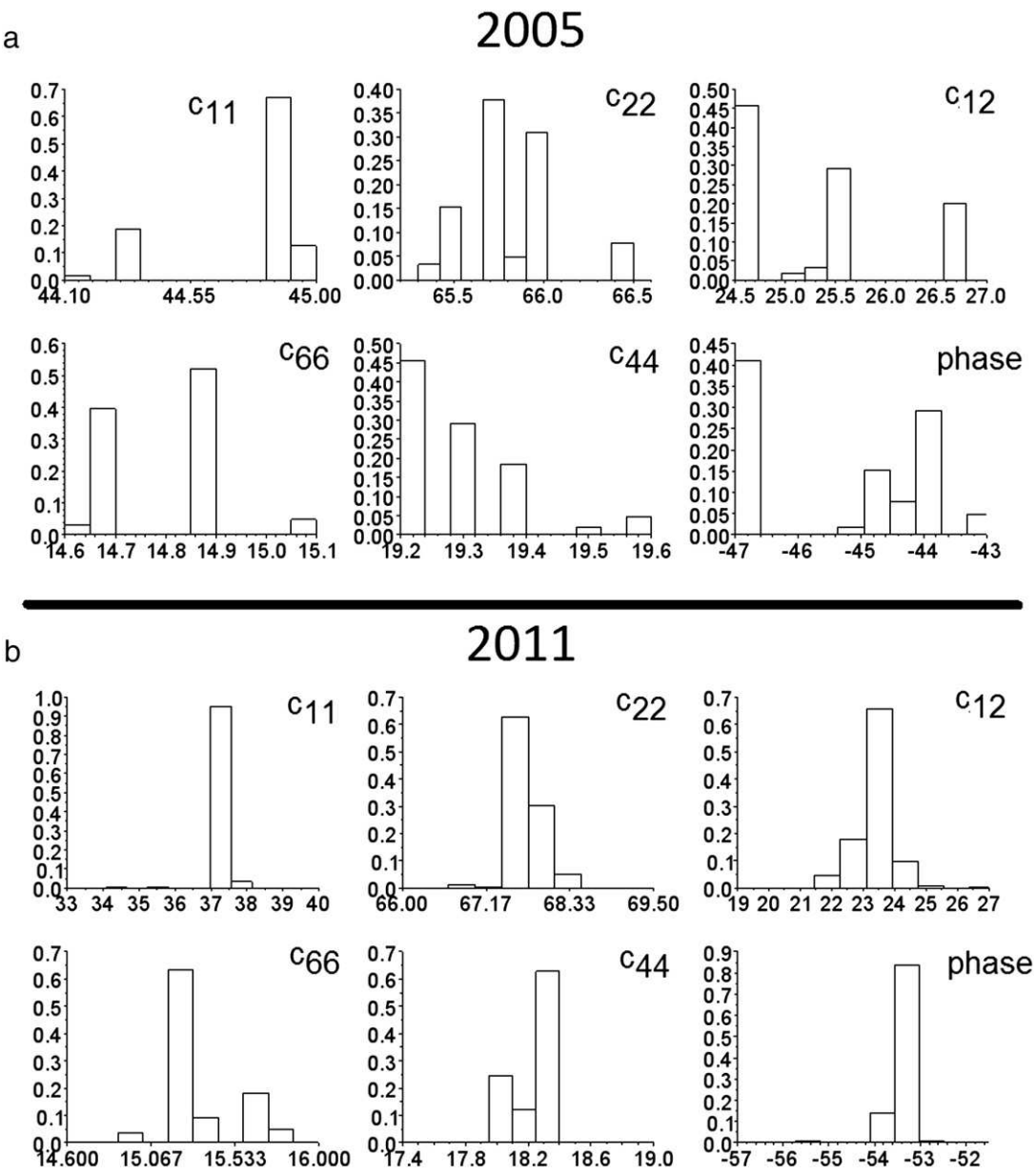

Fig. 8. Histogram of all inverted parameters for models within 10% of the best solution for Monte-Carlo anisotropic inversion.

3.4. Anisotropic Tomography

The previous results show that the approximation of the rock by an HTI medium explains most of the data, however the spread of the measured travel-times around the synthetic ones shows that the area is not homogeneous. Therefore, we used the 3D seismic anisotropy tomography programme "3Dray_gTI0" (Zhou and Greenhalgh, 2008), designed for tilted transversely isotropic media (TTI) in order to invert for the distribution of stiffness parameters. Tilting in 3D is done using 2 rotational angles in spherical coordinates. Since we are dealing with an HTI medium, the first rotation angle of the symmetry axis is set to 90° with respect to a VTI model being the reference model of 3Dray_gTI0. The second angle was fixed as previously obtained from the Monte-Carlo inversion. As the massif is rather homogeneous and the direction of the fractures does not show important changes in the studied area, we did not invert for the angles because the sensitivity of velocity with respect to the angle is very small around the optimum angle and small changes in angles would not affect the result but make the inversion rather unstable (Golikov and Stovas, 2012).

We modified the programme to our needs, implementing a data co-variance matrix that allows for taking account of variable data uncertainties for the model construction (Menke, 1984). These data uncertainties were measured during picking of arrival times and depend on visually determined data quality. P-wave picks have in average smaller uncertainties than S-wave picks.

The inversion is non-linear and it is therefore done by a series of iterations. The parameters of the starting model were set to the output values of the homogeneous Monte-Carlo anisotropic inversion on a 10 × 10 m grid. After 20 iterations, the model stabilized. The resulting parameters are shown in Figs. 9 and 10. Fig. 11 shows the corresponding travel times of P-waves and for the S-waves. In average, the result is similar to the Monte-Carlo results. Joint RMS misfits of the P and S travel times are 0.46 ms and 1.30 ms for 2005 and 2011, respectively.

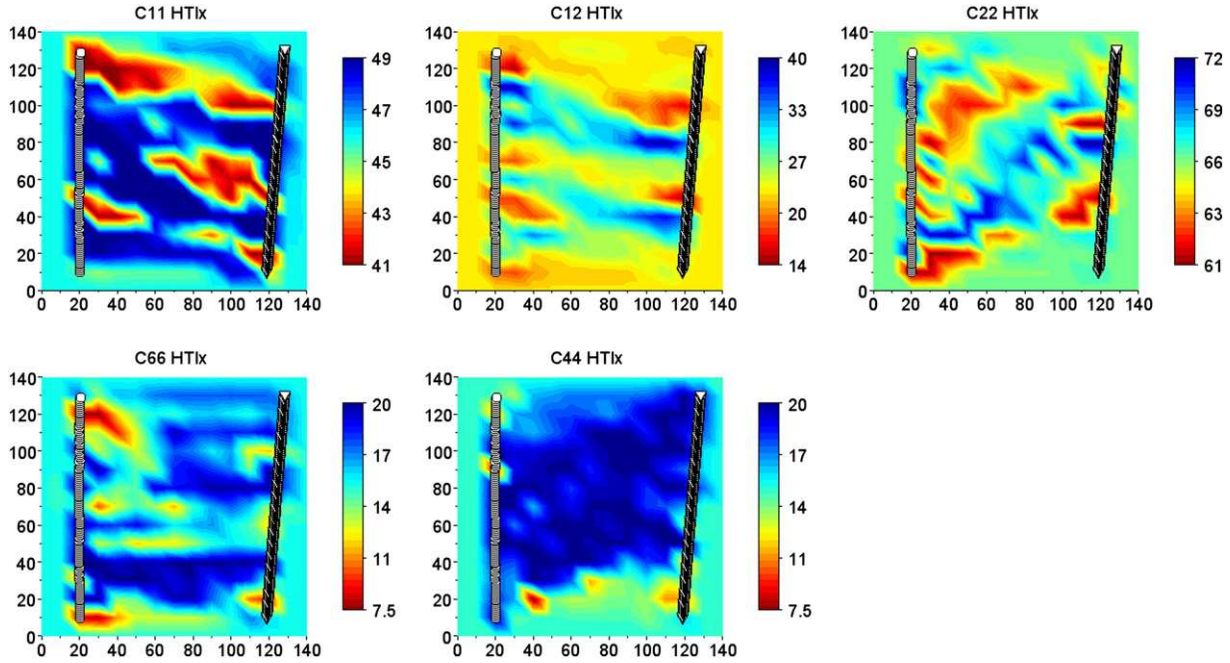

Fig. 9. Results May 2005: Parameter variations were allowed within fixed boundaries (limits of the colour bars) considered to be physically possible.

The degree of resulting anisotropy is best displayed through the distribution of Thomsen's parameter ε, δ and γ (modified from Thomsen, 1986).

$$\varepsilon = \frac{c_{22} - c_{11}}{2c_{11}} \tag{8a}$$

$$\gamma = \frac{c_{44} - c_{66}}{2c_{66}} \tag{8b}$$

$$\delta = \frac{(c_{12} + c_{66})^2 - (c_{11} - c_{66})^2}{2c_{11}(c_{11} - c_{66})} \tag{8c}$$

The parameter ε is a measure of the difference of coefficients c_{11} and c_{22}, and therefore of the difference between P-velocities in the directions of the principal anisotropy axes. It controls the near-vertical anisotropy. The parameter γ is a measure of the difference of coefficients c_{44} and c_{66}, and therefore of the difference between S velocities in the directions of the principal anisotropy axes. Both are intuitive to understand and vanish in anisotropic media (modified for HTI from Grechka, 2009). The combination of stiffness coefficients in δ is chosen in such way that it includes coefficient c_{12} without the coefficient c_{22} and becomes useful for near horizontal propagation of elastic waves (modified for HTI from Thomsen, 1986).

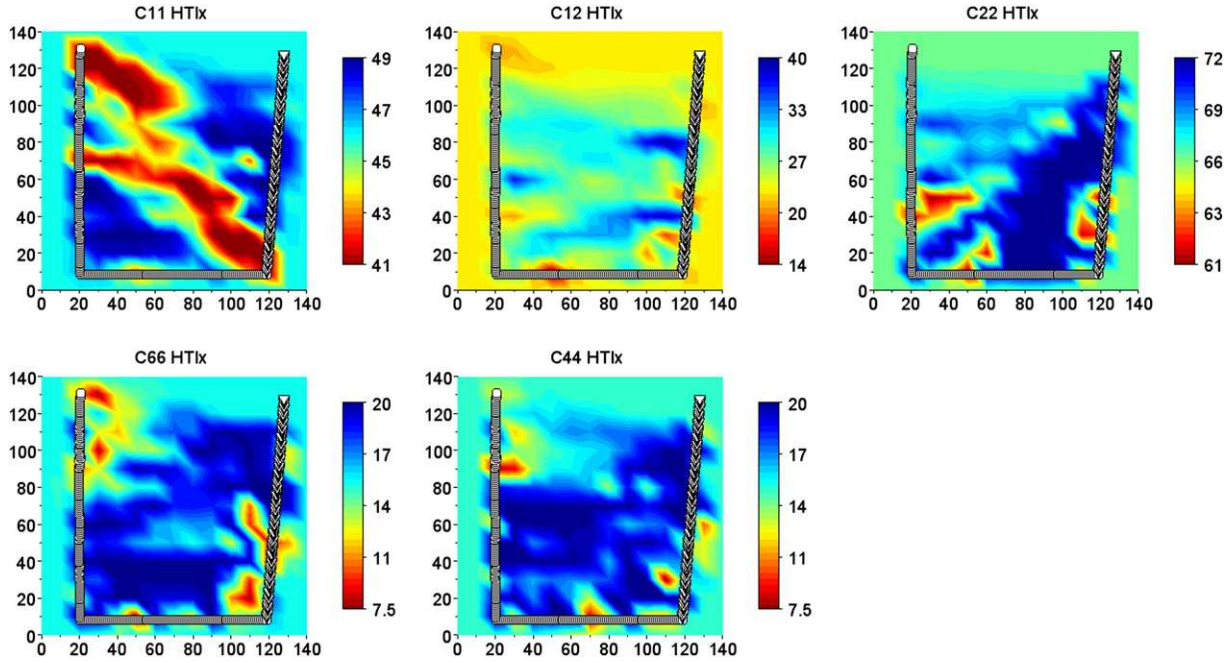

Fig. 10. Results June 2011: Parameters variations were allowed within fixed boundaries (limits of the colour bars) considered to be physically possible.

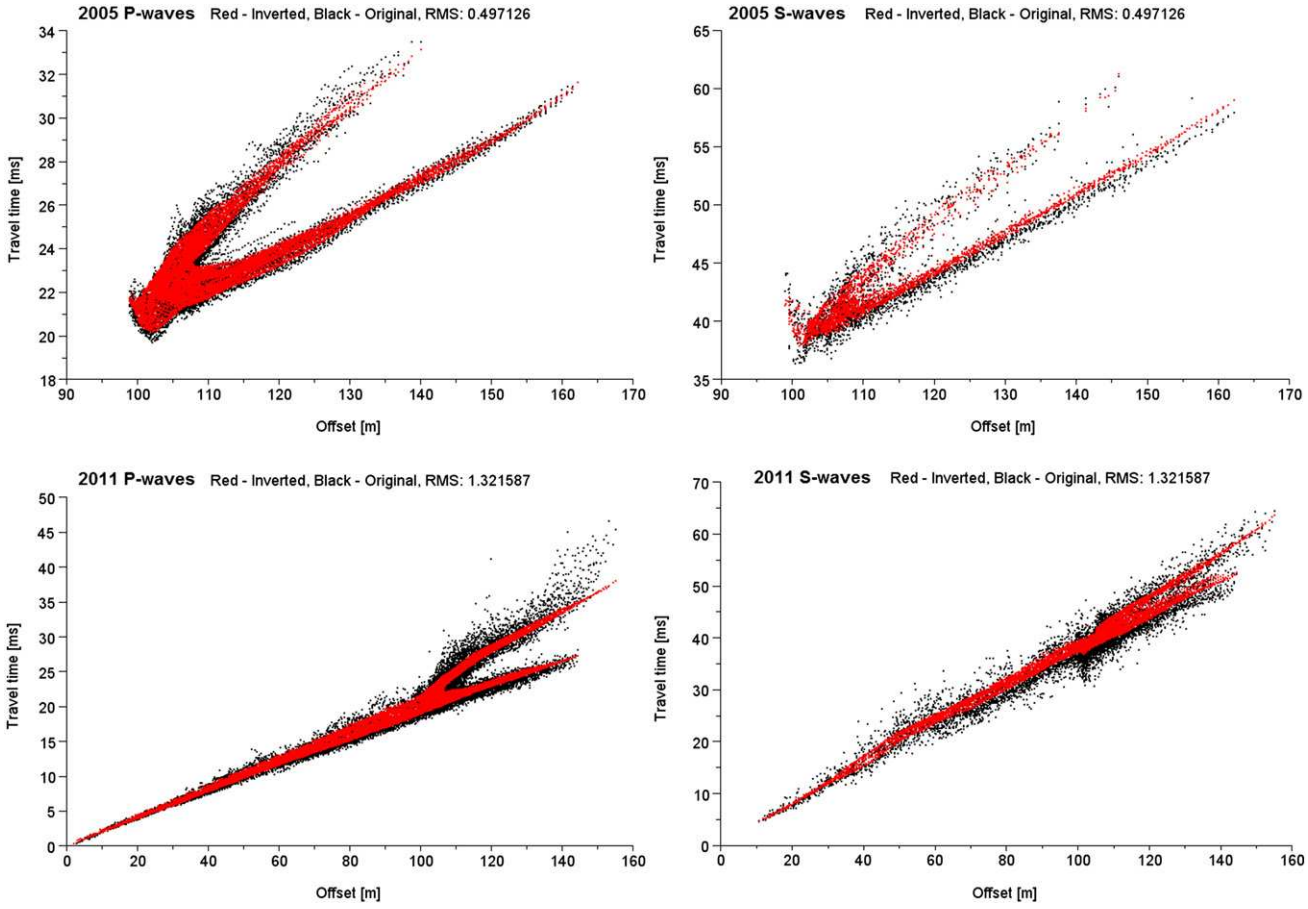

Fig. 11. Results anisotropic tomography offset vs. travel-time. Top row May 2005; bottom row June 2011. Left column: graphs for P-waves; right column graphs for S-waves.

In addition to Thomsen's parameters, we calculated the velocities averaged over all angles at each grid node in order to see the importance of lateral velocity variations. Figs. 12 and 13, show the distribution of these averaged velocities and the coefficients ε, δ and γ. It is interesting that the structures observed on these maps generally do not show the same directions as the fractures. It seems that they are more related to variable rigidity in the limestones than to fracturing. The direction of reef structures observed at the surface striking between N90° and N110°, corresponds well with the directions of average velocities.

4. Discussion and Conclusions

Seismic P-wave and S-wave travel-times in sub-parallel underground galleries were measured. Standard 2D seismic tomography resulted in velocities that are unrealistic for the present limestones, mainly in areas with bad ray-coverage. This was interpreted as a sign of anisotropy of the rock massif. Data was therefore treated by several anisotropic approaches. The seismic velocities were modelled by simple cosine fit and two independent anisotropic inversion schemes. They all give similar results in terms of high and low velocities and the direction of maximum velocity corresponds well with the direction of the main fracture systems observed between the two galleries, as has to be expected.

An independent confirmation of the anisotropy would be obtained, if we could quantify the S-wave splitting. However, using the coefficients obtained, it is easy to calculate (Eq. (7)) that for our offsets of 100–150 m arrivals of both S-waves are so close to each other that they are near resolution limit (1 to 1.5 periods of arrival time differences).

The amount of anisotropy depends on the fracture density in the rocks (e.g. Best et al., 2007; Prasad and Nur, 2003), on the wave type and on the filling of the fractures: For P-waves, anisotropy should be weaker for water-saturated rocks than for dry rocks due to strong variation of compressibility. This change in anisotropy should be principally due to a change in minimum velocity, which is strongly affected by the fractures, whereas the maximum velocity is mainly controlled by the rock matrix. In contrast, S-waves should hardly react on the amount of saturation, since the rigidity is near zero as well for air as for water. We observed much stronger anisotropy for P-waves in June 2011 (dryer period) than in May 2005 (wetter period), whereas no significant variation of S-wave anisotropy was observed between the two measurements. In order to be sure that this difference is not related to integrating additional shot points in 2011, we inverted the 2011 data also without the travel times from the shots in the transverse gallery. The results were the same within a few percent (Table 2). The observed variations fit thus well to a difference in rock saturation between spring 2005 and summer 2011. Similar results were obtained in the study conducted by Schubnel et al. (2006). Depending on fracture density, velocities of saturated samples are larger than the velocities of dry samples. The higher the fracture density, the bigger is the difference between the dry and the saturated samples. Although their study was conducted on a different rock type (granite), their normalized results could be used for comparison with our data. Velocity in slow direction could be as small as 40% of the maximum velocity for a crack density equal to 1, where crack density q is defined as $q = \frac{1}{V}\sum r_i^3$, r being the crack radius, N total number of cracks embedded in a representative volume V. For crack density equal to 0.1 the slow velocity reaches 80% of the maximum velocity. In 2011, being the dryer period, the slow

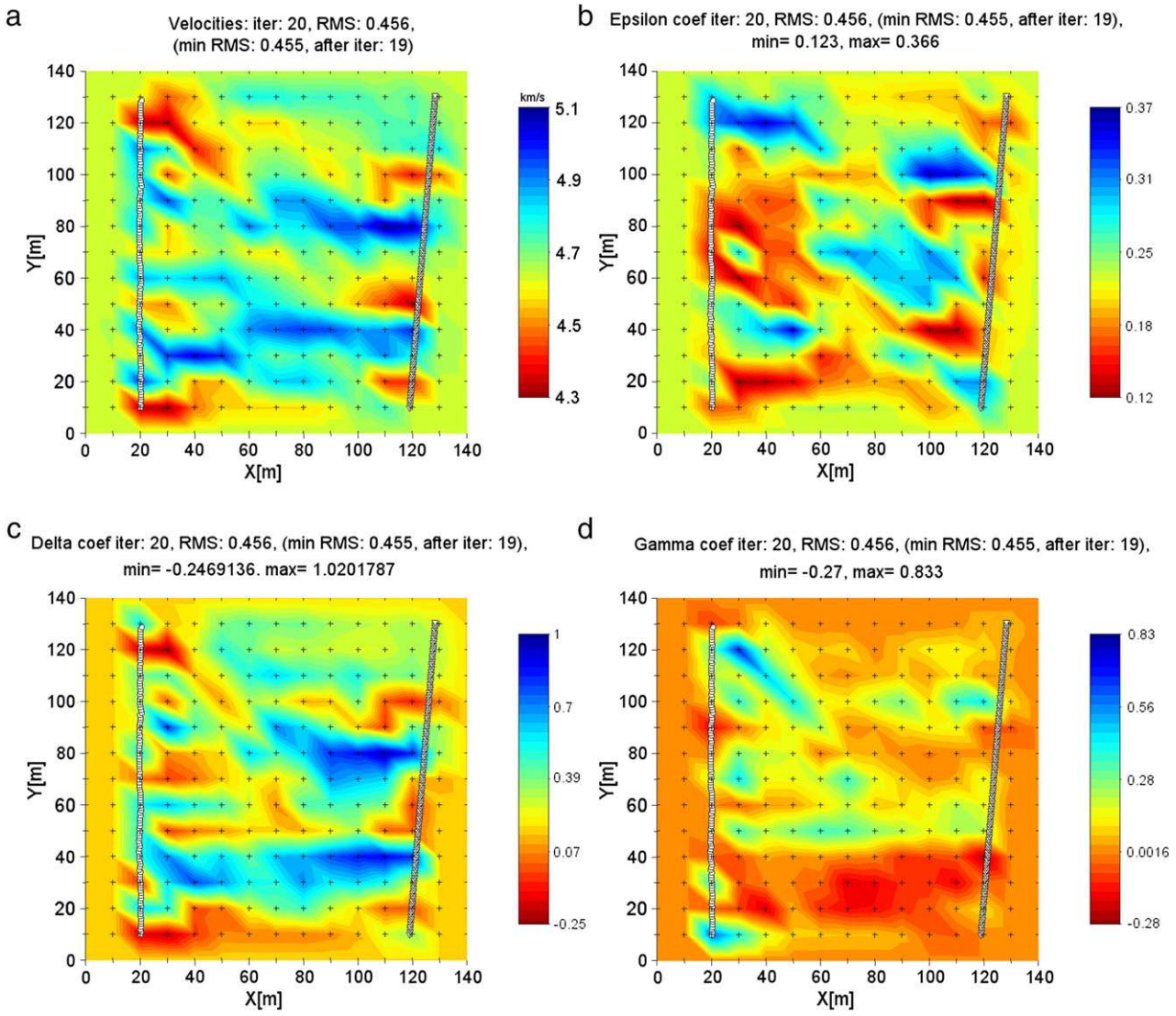

Fig. 12. Results 2005: a) Average velocity, b) Thomsen's parameter ε, c) Thomsen's parameter δ and d) Thomsen's parameter γ.

velocity in our case reaches 73% of the maximum velocity, therefore if anisotropy is only due the cracks in our massif, their density could be slightly above 0.1. According to Bakulin's equation 18 based on S-wave velocities (Bakulin et al., 2000), the crack density has a value q = 0.10 in 2005 and q = 0.08 in 2011. The crack density should be equal for both campaigns and this slight variation can result from different geometries during acquisition in both years and/or uncertainties during picking of travel times. Bakulin's equation 17 based on P-wave velocities gives clearly different values for 2005 (0.06, i.e. 40% less than for S-waves), whereas values are similar to those of S-waves in 2011 (0.07). This confirms the interpretation of nearly dry fractures in 2011 and partly saturated ones in 2005, since for S-waves, the corresponding coefficient Δ_T is independent of saturation, whereas for p-waves, Δ_N becomes zero for water saturated fractures and gives an apparent fracture density of zero.

Porosity of lower cretaceous carbonates at the LSBB site can have different values. Our studied area is situated in the Urgonian facies from Upper Barremian to Aptian. They are characterised by an average porosity of 10%. (Mauffroy, 2010). Fournier et al. (2011) conducted laboratory measurements on samples collected from nearby locations and from our site. According to their results, velocities of unfractured limestone reach up to 6.2 km/s and decrease with increasing porosity. As the study was conducted on small samples, where anisotropy was not considered, we are comparing their results with our average velocity obtained from Monte Carlo inversion (4.8 km/s). This velocity corresponds to a porosity of about 15% in good agreement with the value published by Mauffroy (2010). Above the main gallery, Mauffroy (2010) obtained an isotropic seismic tomography image on a vertical plane oriented 40° with respect to the fast direction between the surface and the gallery. She obtained a velocity of 4.8–4.9 km/s which is also in good agreement with our results in this direction. According to the results of their tomography, a porosity of 13% was calculated.

If velocity variations are only due to anisotropy, Thomsen's coefficient ε should be inversely proportional to the averaged velocities. Increase of anisotropy should be due to an increase of fracture density and therefore to a reduction mainly of the minimum velocity. Comparing the distributions in Figs. 12 and 13, one can see in general an anti-correlation between ε and average velocities. Deviations from this show again that part of the velocity variations must be related also to material changes.

Acknowledgements

The authors acknowledge partial financing by project GUTEC of the PIR-PACEN du CNRS. The field work in the galleries would not have

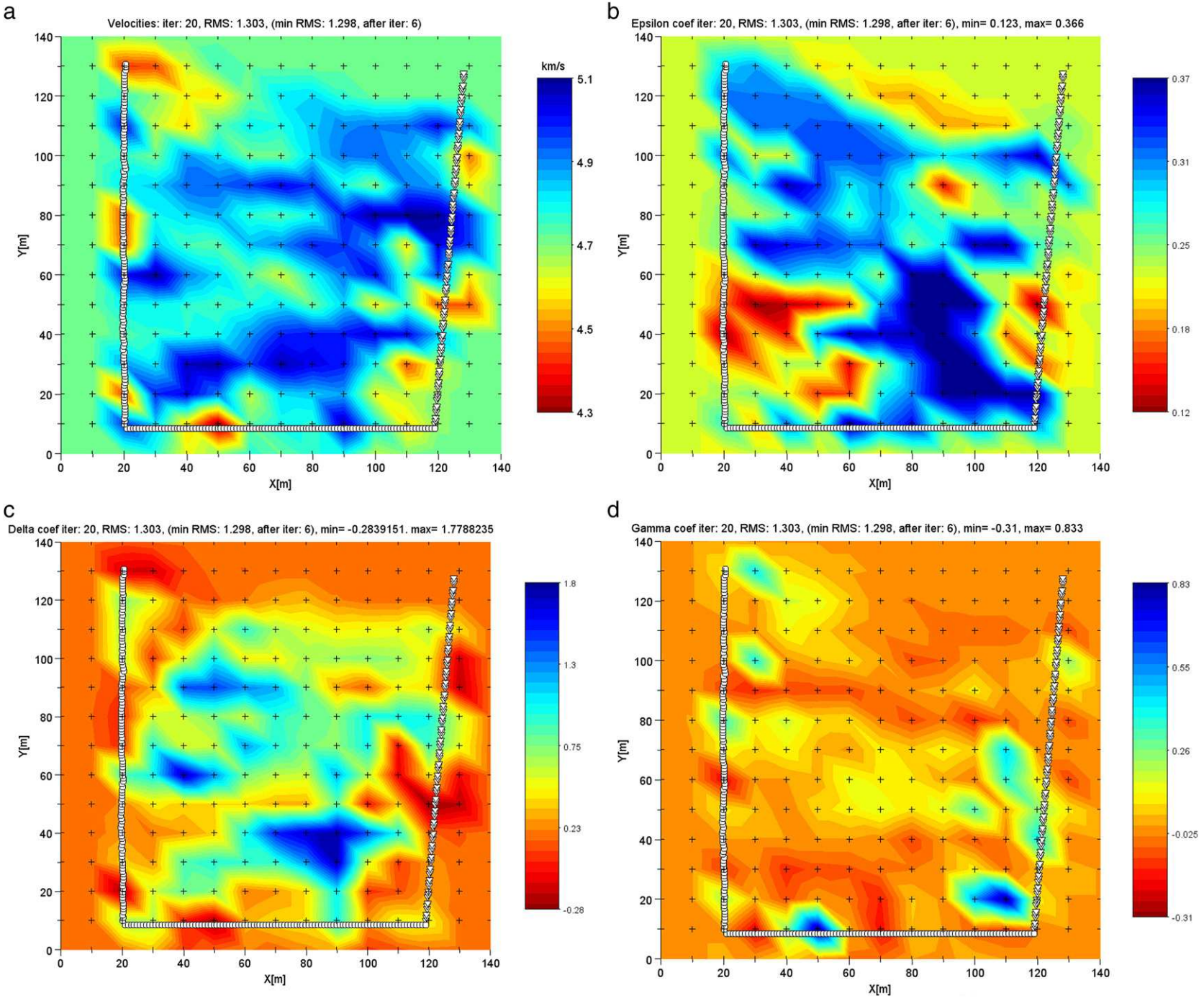

Fig. 13. Results 2011: a) Average velocity, b) Thomsen's parameter ε, c) Thomsen's parameter δ and d) Thomsen's parameter γ.

been possible without the support of the technical staff. We thank an anonymous reviewer for his thoughtful suggestions.

References

Bakulin, A., Grechka, V., Tsvankin, I., 2000. Estimation of fracture parameters from reflection seismic data: part I. HTI model due to a single fracture set. Geophysics 65, 1788–1802.

Best, A.I., Sothcott, J., McCann, C., 2007. A laboratory study of seismic velocity and attenuation anisotropy in near-surface sedimentary rocks. Geophysical Prospecting 55 (5), 609–625.

Fournier, F., Leonide, P., Biscarrat, K., Gallois, A., Borgomano, J., Foubert, A., 2011. Elastic properties of microporous cemented grainstones. Geophysics 76 (6), E211–E226.

Golikov, P., Stovas, A., 2012. Traveltime parameters in a tilted elliptical anisotropic medium. Geophysical Prospecting 60 (3), 433–443.

Grechka, V., 2009. Applications of Seismic Anisotropy in the Oil and Gas Industry. European Association of Geoscientists & Engineers, Houten (NL) (171 pp.).

Grechka, V., Kachanov, M., 2006. Effective elasticity of fractured rocks: a snapshot of the work in progress. Geophysics 71 (6), W45–W58.

Jeanne, P., Guglielmi, Y., Cappa, F., 2012. Multiscale seismic signature of a small fault zone in a carbonate reservoir: relationships between VP imaging, fault zone architecture and cohesion. Tectonophysics 554–557, 185–201.

Mauffroy, E., 2010. Caractérisation et modélisation numérique de l'effet de site topographique 3D: application à la Grande Montagne de Rustrel, Vaucluse. PhD thesis Thesis University of Nice, France (245 pp.).

Menke, W., 1984. Geophysical Data Analysis: Discrete Inverse Theory. Academic Press, London (260 pp.).

Prasad, M., Nur, A., 2003. Velocity and attenuation anisotropy in reservoir rocks. SEG Expanded abstracts, pp. 1652–1655.

Rüger, A., 1997. P-wave reflection coefficients for transversely isotropic models with vertical and horizontal axis of symmetry. Geophysics 62, 713–722.

Schubnel, A., Benson, P., Thompson, B., Hazzard, J., Young, R., 2006. Quantifying damage, saturation and anisotropy in cracked rocks by inverting elastic wave velocities. Pure and Applied Geophysics 163 (5–6), 947–973.

Thiébaud, E., 2003. Etude structurale et hydrogéologique du site du Laboratoire Souterrain à Bas Bruit de Rustrel. Master thesis Université de Franche-Comté, Besançon, France (50 pp.).

Thomsen, L., 1986. Weak elastic anisotropy. Geophysics 51 (10), 1954–1966.

Tryggvason, A., Linde, N., 2006. Local earthquake (LE) tomography with joint inversion for P- and S-wave velocities using structural constraints. Geophysical Research Letters 33, L07303.

Tsvankin, I., 1997. Reflection moveout and parameter estimation for horizontal transverse isotropy. Geophysics 62 (2), 614–629.

Tsvankin, I., Gaiser, J., Grechka, V., van der Baan, M., Thomsen, L., 2010. Seismic anisotropy in exploration and reservoir characterization: an overview. Geophysics 75 (5), A15–A29.

Winterstein, D.F., 1990. Velocity anisotropy terminology for geophysicists. Geophysics 55 (8), 1070–1088.

Zhou, B., Greenhalgh, S., 2008. Non-linear traveltime inversion for 3-D seismic tomography in strongly anisotropic media. Geophysical Journal International 172 (1), 383–394.